Simulations of active galactic nuclei feedback with cosmic rays and magnetic fields

---

Kristian Ehlert
Leibniz-Institut für Astrophysik Potsdam (AIP)

Kumulative dissertation
zur Erlangung des akademischen Grades
doctor rerum naturalium (Dr. rer. nat.)
in der Wissenschaftsdisziplin Theoretische Astrophysik

Eingereicht an der Mathematisch-Naturwissenschaftlichen Fakultät
Institut für Physik und Astronomie
der Universität Potsdam
und
dem Leibniz-Institut für Astrophysik Potsdam (AIP)

Potsdam, den 28.08.2022

Betreuer: Prof. Dr. Christoph Pfrommer/Prof. Dr. Matthias Steinmetz

1. Gutachter: Prof. Dr. Christoph Pfrommer
Leibniz-Institut für Astrophysik Potsdam/Universität Potsdam

2. Gutachterin: Prof. Dr. Debora Sijacki
University of Cambridge

3. Gutachter: Prof. Dr. Mateusz Ruszkowski
University of Michigan

Zusammenfassung

Das zentrale Gas in der Hälfte aller Galaxienhaufen weist kurze Kühlzeiten auf. Dies sollte zu hohen Sternentstehungs- und Massenkühlungsraten führen. Bei ungehinderter Kühlung würden jedoch viel mehr Sterne entstehen als beobachtet. Stattdessen wird vermutet, dass das kondensierende Gas durch das zentrale Schwarze Loch akkretiert wird, das einen aktiven Galaxienkerne antreibt, der den Haufen heizt. Der genaue Heizmechanismus ist noch unklar. Ein vielversprechender Mechanismus geht von Protonen der kosmischen Strahlung aus, die an selbst erzeugten magnetischen Fluktuationen, d.h. Alfvénwellen, streuen. Die kontinuierliche Dämpfung der Alfvénwellen heizt das Gas.

Für eine große Anzahl von Galaxienhaufen wurden stationäre Lösungen gefunden, bei denen Kühlen durch Alfvénwellenheizen ausgeglichen wird. Um die Modellierungsannahmen zu überprüfen, untersuchen wir die CR-Injektion in magnetohydrodynamischen 3D-Simulationen von Jets in einem idealisierten Cluster mit dem Code AREPO. Wir simulieren die Entstehung und Entwicklung von Gasblasen durch energetische Ausflüsse in einer turbulenten, magnetische Atmosphäre. Darüberhinaus ist die Dynamik des Jets und das Heizen eng verknüpft mit der soweit unklaren Zusammensetzung des Jets. Die Wechselwirkung von Elektronen mit dem kosmischen Mikrowellenhintergrund führt zu beobachtbaren Signaturen, die vom Inhalt der Blasen abhängen. Diese jüngsten Beobachtungen lieferten Beweise für unterdichte Blasen mit einer relativistischen Füllung, wobei vereinfachende Modellannahmen für die Blasen angenommen wurden. Indem wir die Beobachtungen mit unseren Simulationen reproduzieren, bestätigen wir die Gültigkeit ihrer Modellannahmen und damit die wichtige Erkenntnis, dass Jets eine niedrige (Impuls-)Dichte haben.

Außerdem haben die Geschwindigkeits- und Magnetfeldstruktur der Haufenatmosphäre tiefgreifende Auswirkungen auf die Blasenentwicklung und Heizprozesse. Da Geschwindigkeits- und Magnetfelder physikalisch gekoppelt sind, zeigen wir, dass numerische Simulationen dazu beitragen können, die jeweiligen Beobachtungsdaten in direkte Verbindung zu setzen, um sie dadurch besser abschätzen zu können. Schließlich implementieren wir das derzeit bevorzugte Akkretionsmodell, *cold accretion*, in AREPO und untersuchen die Rückkopplung durch leichte Jets in einem explizit kühlenden magnetisierten Haufen. Während die Selbstregulierung unabhängig vom Akkretionsmodell, der Jetdichte und der Jeteffizienz erreicht wird, ist die Morphologie des kalten Gases bei Simulationen mit leichten Jets Beobachtungen am ähnlichsten.

Summary

The central gas in half of all galaxy clusters shows short cooling times. Assuming unimpeded cooling, this should lead to high star formation and mass cooling rates, which are not observed. Instead, it is believed that condensing gas is accreted by the central black hole that powers an active galactic nuclei jet, which heats the cluster. The detailed heating mechanism remains uncertain. A promising mechanism invokes cosmic ray protons that scatter on self-generated magnetic fluctuations, i.e. Alfvén waves. Continuous damping of Alfvén waves provides heat to the intracluster medium.

Previous work has found steady state solutions for a large sample of clusters where cooling is balanced by Alfvénic wave heating. To verify modeling assumptions, we set out to study cosmic ray injection in three-dimensional magnetohydrodynamical simulations of jet feedback in an idealized cluster with the moving-mesh code AREPO. We analyze the interaction of jet-inflated bubbles with the turbulent magnetized intracluster medium. Furthermore, jet dynamics and heating are closely linked to the largely unconstrained jet composition. Interactions of electrons with photons of the cosmic microwave background result in observational signatures that depend on the bubble content. Those recent observations provided evidence for underdense bubbles with a relativistic filling while adopting simplifying modeling assumptions for the bubbles. By reproducing the observations with our simulations, we confirm the validity of their modeling assumptions and as such, confirm the important finding of low-(momentum) density jets.

In addition, the velocity and magnetic field structure of the intracluster medium have profound consequences for bubble evolution and heating processes. As velocity and magnetic fields are physically coupled, we demonstrate that numerical simulations can help link and thereby constrain their respective observables. Finally, we implement the currently preferred accretion model, *cold accretion*, into the moving-mesh code AREPO and study feedback by light jets in a radiatively cooling magnetized cluster. While self-regulation is attained independently of accretion model, jet density and feedback efficiencies, we find that in order to reproduce observed cold gas morphology light jets are preferred.

Contents

1 Introduction

Galaxy clusters are the largest virialized structures in the universe. Their outskirts are currently still in the process of forming and they accrete matter from the cosmic web. The total mass of galaxy clusters is dominated by dark matter, which makes up 85% of their total mass. In the optical, clusters appear as mostly empty space on scales $\sim 3\,\mathrm{Mpc}$ populated with up to $\sim 10^3$ galaxies making up a mere 2% of the cluster mass. However, vast amounts of gas are revealed by the observer through an X-ray telescope. This gas is smoothly filling intergalactic space. It makes up the remaining 13% of mass and is termed the intracluster medium (ICM). Due to the vast depth of the potential well of a cluster, the gas emits at X-ray energies via thermal bremsstrahlung and metal line cooling. For roughly half of all observed clusters it would take only $\sim 1\,\mathrm{Gyr}$ to radiate away energy equivalent to all thermal energy within their center ($r \lesssim 10 - 50\,\mathrm{kpc}$ for a typical Perseus-like cluster). Therefore this subclass is termed cool-core (CC) clusters. Cooling gas would condense and move to the center so that thermal pressure decreases and causes more material to flow inwards, i.e. the formation of a *cooling flow* (Fabian, 1994). Consequently, one would expect uninhibited mass cooling rates of $\sim 1,000\,\mathrm{M}_\odot$. However, observed cold gas and star formation rates are orders of magnitude below this value. Moreover, strong line emission expected as the gas cools below 0.7 keV from FeXVII is not observed (Peterson et al., 2001; Tamura et al., 2001). The end product of cooling in the form of star formation and molecular gas can be observed but generally contains much less mass than expected (McNamara and Nulsen, 2012). The failure to find a large reservoir of cold gas, lead people to look into the possibility of gas heating.

Early X-ray images of the center of the Perseus and Cygnus A clusters revealed cavities near the central radio source (Böhringer et al., 1993; Carilli et al., 1994). These cavities (or *bubbles*) correspond to gas injected by a jet originating from an active galactic nuclei (AGN) that is powered by accretion onto a supermassive black hole (SMBH). The detailed composition of these bubbles remains unknown. To make them appear as cavities, one requires gas with temperatures above the observed X-ray band ($\sim 10\,\mathrm{keV}$) or a non-thermal component made up of magnetic fields and/or cosmic rays (CRs). Due to buoyancy hot, under-dense bubbles rise buoyantly in cluster atmospheres. The total enthalpy, i.e. the pV work plus the internal energy that provides pressure supporting the cavities can be readily computed from X-ray measurements of the ICM thermal pressure and the cavity volume. The mechanical power of a bubble can then be approximated by dividing the enthalpy by the bubble age, which is usually approximated by the bubble rise time. A correlation between mechanical power and X-ray cooling luminosity is observed for systems ranging from giant ellipticals to galaxy clusters (e.g. Bîrzan et al., 2008), where mechanical power exceeds cooling power in almost all cases. Consequently, jets could provide sufficient energy to limit cooling to observed levels. In addition, this correlation implies that there seems to be a tight loop regulating feedback. The cluster cools and gas flows onto the accretion disk of the central supermassive black hole (SMBH). When the inwards moving gas reaches the black hole a jet is launched, that heats the ICM. The ICM will in turn eventually start cooling again and initiate the next cycle of feedback.

However, the detailed heating mechanism remains unknown. Proposed mechanisms include jet-induced weak shocks (David et al., 2001), mixing of hot bubble material with the ICM (Yang and Reynolds, 2016), sound waves (Fabian et al., 2003), gravity waves (Reynolds et al., 2015) and decaying turbulence (Zhuravleva et al., 2014). In addition, there may be a large population of CR protons accelerated in internal shocks that could stream out of the bubble and transfer thermal energy via the streaming instability (Loewenstein et al., 1991). The streaming instability leads CRs to scatter on self-generated Alfvén waves that limits their bulk velocity to the Alfvén velocity. The waves are damped by plasma instabilities, which leads to a net transfer of energy from CRs to the ICM, i.e. the CRs heat the ICM. Jacob and Pfrommer (2017a) construct a steady-state model where CR heating balances ratiative cooling. They find solutions in all their tested 39 CC clusters that match the observed temperature and density profiles. Building on these promising results, we wanted to loosen the strict constrains imposed by the model and focus on the details of CR injection for our first project in Chapter 3. Here, we study the injection of cosmic rays from jet-inflated bubbles in a turbulent magnetized Perseus-like cluster atmosphere in three-dimensional magnetohydrodynamic (MHD) simulations with the moving-mesh code AREPO.

Identifying the heating mechanism depends crucially on the unknown bubble content. Free electrons in the ICM may Compton up-scatter cosmic microwave background (CMB) photons, which impacts the observed CMB photon flux density. This effect is termed the Sunyaev-Zel'dovich (SZ) signal. Photons are redistributed from part of the spectrum below the so called crossover frequency above this frequency. However, relativistic bubble electrons that are much hotter than the bulk ICM modulate the spectrum less effectively, which makes observations of the CMB sensitive to the exact electron filling. This effect has been observed for bubbles in MS 0735.6+7421 (Abdulla et al., 2019). We test modeling assumptions and constrain the expected signal from the kinetic SZ effect in Chapter 4. The latter may help to break the inherent degeneracy of jet inclination angle and bubble age, which is a potential source of uncertainties for bubble composition measurements.

Many details of AGN feedback in clusters depend on the velocity and magnetic field in the ICM. The velocity structure of the ICM can directly be estimated from high resolution X-ray spectra (Hitomi Collaboration, 2016). Magnetic field structure and strength can be constrained from radio polarization measurements. Specifically, the interaction of linearly polarized synchrotron emission from a background AGN with the ICM leads to a rotation of the wave polarization plane, i.e. Faraday rotation. The wave length dependent difference in polarization angle, the *Faraday rotation measure*, is proportional to the magnetic field strength along the line-of-sight. Therefore, observations of Faraday rotation measure are a powerful tool to estimate the magnetic field strength on small areas of the sky. We expand on the inherent link between velocity and magnetic fields in clusters and suggest that challenging observations of them should be treated as complementary to each other for gaining deeper insights into the state of the ICM in Chapter 5.

With the advent of ALMA (Atacama Large Millimeter/submillimeter Array), detailed observations of cold molecular carbon oxygen (CO) filaments and their kinematics in the core of clusters became available (Russell et al., 2019). These and observations of Hα filaments enable us to gain more insight into the details of cooling and accretion onto the SMBH (Olivares et al., 2019). Widely employed classical Bondi accretion assumes a smooth, spherically symmetric, non-rotating gas distribution whereas cluster centers appear to harbor clumpy multiphase gas. It is now believed that thermally unstable gas condenses out of the ICM and gets accreted onto the SMBH via *chaotic cold accretion* (Sharma et al., 2012; Gaspari et al., 2013). In Chapter 6, we therefore study self-regulated AGN feedback in a Perseus-like cluster with chaotic cold accretion. Furthermore, we study trends of observational signatures like cold filament morphology for varying jet densities, accretion models and accretion parameters.

The outline of this thesis is as follows. An introduction to the observational windows of ICM physics in galaxy clusters is given in Section 2.1. In Section 2.2, we expand on the cluster properties leading to the current understanding of the cooling flow problem, the present magnetic and velocity fields and cosmic rays in cluster. We then turn to details of AGN jet physics in CC clusters in Section 2.3 and their fueling process via accretion in Section 2.4. Numerical methods employed throughout the thesis implemented in the moving-mesh MHD code AREPO are discussed in Section 2.5. Publications alluded to above follow in Chapters 3, 4, 5 and 6. We conclude this thesis in Chapter 7 with a discussion of our work and an outlook for future work.

AGN feedback in cool core clusters

2

This chapter introduces the reader to CC clusters and the cooling flow problem. In addition, it provides a background of AGN jets and black hole accretion in the paradigm of AGN feedback. Finally, we discuss main features of the simulation techniques employed throughout the thesis.

2.1 Observational windows to clusters

Information on the thermodynamic properties of the ICM can be gained from X-ray and SZ observations, which are discussed in Section 2.1.1 and 2.1.2, respectively. In Section 2.1.3, we turn to the non-thermal component of the ICM, i.e. magnetic fields and cosmic rays, and how radio observations help us reveal their characteristics.

2.1.1 X-ray

While stars in galaxies are visible in the optical, the gas contained in the deep potential well of a cluster is discernible in X-rays (see Figure 2.1). The ICM is almost fully ionized and therefore harbors a plasma of electrons, protons, and heavier ions. The deflection of an electron due to electrostatic interaction with a proton leads to the emission of a bremsstrahlung photon and is observable as a flat spectrum with an exponential decline at X-ray frequencies. The *thermal* bremsstrahlung emissivity (due to a *thermal* electron population) scales with observed photon frequency ν and electron temperature T_e as

$$j_\mathrm{X}(\nu, T) \propto g(\nu, T) n_\mathrm{e} n_\mathrm{i} \sqrt{k_\mathrm{B} T_\mathrm{e}} e^{-h\nu/k_\mathrm{B} T_\mathrm{e}}, \tag{2.1}$$

where $g(\nu, T)$ is the quantum mechanical Gaunt correction factor, n_e is the electron number density and n_i is the ion number density. In addition to hydrogen and helium the ICM contains small traces of highly ionized heavy metals. Interactions of free electrons with the ions may excite bound electrons to higher energy levels. During de-excitation a photon is emitted with energy corresponding to the difference in energy of the two levels. These are detectable as metal emission lines at characteristic energies in the spectrum.

As bremsstrahlung is a two body process, we define the emission measure via $\mathrm{EM} = \int n_\mathrm{e} n_\mathrm{i} \mathrm{dV}$,[1] which resembles the bremsstrahlung luminosity, when we neglect the (weak) temperature dependence, which can in practice be approximately realized by choosing an appropriate frequency band. Assuming a smooth gas distribution and making additional assumptions of the emitting volume, a radial density profile can be computed. Typical densities are in the range $n \approx (10^{-4}...10^{-3})\,\mathrm{cm}^{-3}$. As can be seen from Equation 2.1, the emission will decrease exponentially for energies $h\nu$ larger than $k_\mathrm{B} T_\mathrm{e}$. Thus, the observed shape of the continuum allows for the computation of the temperature. In addition, the relative intensity of emission lines is sensitive to temperature. Observed temperatures in clusters are of order $T \approx (10^7...10^8)\,\mathrm{K}$.

2.1.2 Sunyaev-Zel'dovich effect

The universe is filled with black body ration at 2.725 K termed cosmic microwave background (CMB). It formed when hydrogen recombined at redshift $z \approx 1100$. Remnant thermal radiation from the Big

---

[1] where V is the emitting volume of the source

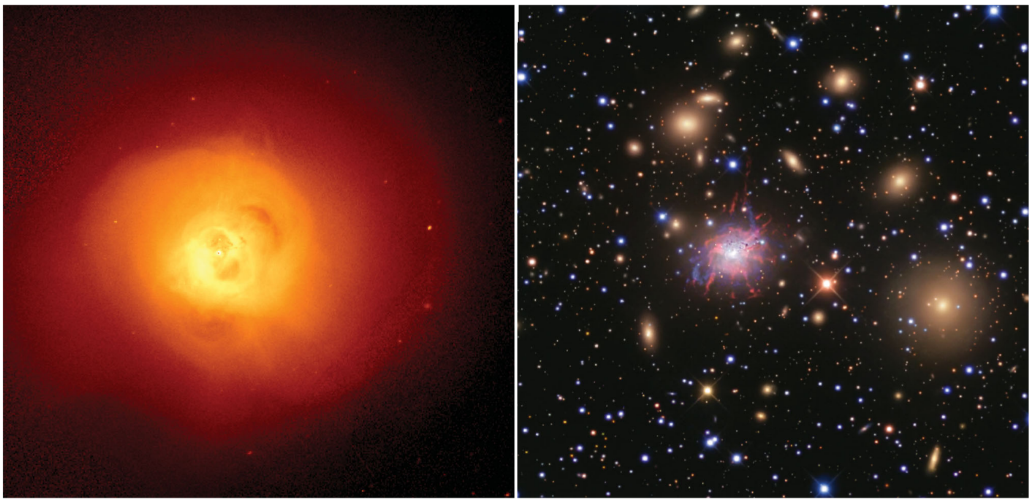

Figure 2.1: Chandra X-ray (left) and optical (right) observation of the center of the Perseus cluster (adopted from Fabian et al. (2011b)). The images are 11.8 arcmin ≈ 260 kpc from north to south. Optical observation from Blackbird Observatory. AGN bubbles are visible as X-ray cavities. The central galaxy NGC 1275 shows pronounced Hα emission.

Bang stopped scattering on free electrons as hydrogen recombined (via 2-photon recombination) and the universe therefore became transparent to the CMB. However, expansion of the universe causes the temperature to decrease. In clusters "hot" ICM electrons can transfer some of their energy onto "cold" CMB photons via inverse Compton (IC) scattering. Assuming that the cluster is at rest with respect to the CMB rest frame, this leads to a distortion of the CMB spectrum, i.e. reducing the signal below $\nu_0 \approx 217\,\mathrm{GHz}$ and increasing the signal above ν_0. Below ν_0 clusters will appear as holes in CMB sky, above ν_0 they show as bright spots, which makes observations of the so called Sunyaev-Zel'dovich (SZ) a powerful tool in finding and characterizing clusters.

To compute the amplitude of the SZ effect, we integrate the typical energy gained by a photon in a Compton interaction ($k_\mathrm{B}T_\mathrm{e}/m_\mathrm{e}c^2$) with the differential cross section of the interaction, $\mathrm{d}\tau = n_\mathrm{e}\sigma_\mathrm{T}\mathrm{d}l$, where σ_T is the Thompson cross section, over the length of the photon path length though the cluster D, i.e.

$$y = \int_0^D \frac{k_\mathrm{B}T_\mathrm{e}}{m_\mathrm{e}c^2} n_\mathrm{e}\sigma_\mathrm{T}\mathrm{d}l \approx 7\times 10^{-5}\left(\frac{T_\mathrm{e}}{6\,\mathrm{keV}}\right)\left(\frac{n_\mathrm{e}}{10^{-3}\,\mathrm{cm}^{-3}}\right)\left(\frac{D}{3\,\mathrm{Mpc}}\right), \tag{2.2}$$

where we assumed characteristic temperate and density values typical for massive clusters (and which are averaged along the line-of-sight through the cluster centre). The amplitude in SZ emission corresponds to an integral of the electron pressure $P_\mathrm{e} = k_\mathrm{B}T_\mathrm{e}n_\mathrm{e}$ along the line-of-sight. This in combination with density profiles obtained from X-ray measurements represents an alternative method to measure cluster temperatures.

2.1.3 Radio

Synchrotron radiation

Relativistic electrons with energy $\epsilon = \gamma m_\mathrm{e}c^2$ gyrating around a magnetic field produce synchrotron radiation. Emission is concentrated into a forward cone with half angle $\simeq \gamma^{-1}$. Most astrophysical sources are optically thin at radio synchrotron frequencies, the spectrum of the emission is then given by a superposition of the radiation from single electrons. Usually the CR population in the ICM is described by a power law energy distribution

$$n(\epsilon)\mathrm{d}\epsilon = \epsilon^{-p}\mathrm{d}\epsilon, \tag{2.3}$$

where p is the power law index. It is related to the radio spectral index[2] α via

$$p = 1 - 2\alpha, \tag{2.4}$$

where diffusive radio emission in clusters usually shows steep spectra with $\alpha \lesssim -1$. The resulting radio spectrum depends on the physics of the acceleration mechanism and the electron synchrotron and IC energy losses. An estimate of the characteristic lifetime t_{age} of synchrotron emitting electrons ($\gamma = 10^4$, GeV energy) can therefore be estimated as (e.g., Miley, 1980)

$$t_{\mathrm{age}} \approx 3.2 \times 10^{10} \frac{B^{1/2}}{B^2 + B_{\mathrm{CMB}}^2} \left[(1+z)\nu\right]^{-1/2}, \tag{2.5}$$

where B is the magnetic fields strength, z is the source redshift, B_{CMB} the equivalent magnetic field strength of the CMB ($B_{\mathrm{CMB}} = 3.25(1+z)^2\,\mu$G) and ν is the observing frequency in MHz. Magnetic field strengths are given in μG. The corresponding lifetime in a galaxy cluster with $B > 2\mu$G is approximately $t_{\mathrm{age}} \lesssim 200\,$Myr for emission at frequency $\nu = 200\,$MHz. Typical gas bulk velocities of $v \lesssim 300\,\mathrm{km\,s^{-1}}$ could transport CRs to scales of $v \cdot t_{\mathrm{age}} \lesssim 100\,$kpc.

Radio emission in clusters

Clusters often host numerous AGN jets that emit radio synchrotron emission, i.e. radio galaxies. Their sizes range from a few kpc (Capetti et al., 2020) up to Mpc (Cantwell et al., 2020) scales extending well beyond their host galaxy. Jets located in the outskirts of clusters show morphologies reminiscent of their strong ram-pressure interaction with the ICM classified as wide-angle, narrow angle or head-tail radio sources (for recent examples see Gendron-Marsolais et al., 2020; O'Neill et al., 2019; Botteon et al., 2021, respectively). However, central radio galaxies in CC clusters are less disturbed. Here, radio emission can be observed filling X-ray cavities.

In addition, clusters may show diffuse radio emission not directly related to radio galaxies (Feretti et al., 2012). Synchrotron emission from GeV electrons interacting with μG magnetic fields are observed in the form of (1) centrally located diffuse sources in merging clusters (radio halos), (2) smaller sized radio halos in CC clusters (radio mini halos), (3) highly polarized extended sources in cluster outskirts (radio relics), (4) AGN fossil plasma that is reignited by merger driven compression (radio phoenix) and (5) fossil radio plasma that is passively evolving after the AGN switched off (AGN relics) (van Weeren et al., 2019). These phenomena prove the presence of magnetic fields and cosmic rays in the ICM. More details on magnetic fields in clusters will be given in Section 2.2.2 and 2.2.4, respectively. A short discussion of radio mini halos follows, as they may provide an observational marker of CR feedback in CC clusters (see Section 2.2.4).

Radio mini halos

Radio mini halos are found in CC clusters with sizes of $\sim 100-400\,$kpc. These scales require in-situ acceleration as CR propagation is unable to reach these scales as discussed above. As discussed in Section 2.2.4, the transport of CRs in CC clusters is likely confined by self-generated Alfvén waves, via the streaming instability. Assuming streaming, the diffusion coefficient is $\kappa \sim v_{\mathrm{s}} L_{\mathrm{gradient}}$, where v_{s} is the streaming velocity and L_{gradient} is the gradient length of the CRs. Hence, CRs can diffuse in their life time t_{age} to $\sqrt{x^2} \sim \sqrt{2\kappa t_{\mathrm{age}}}$. Therefore, the emission does not directly originate from the central AGN. Giacintucci et al. (2017) find a radio mini halo in 80% of their CC clusters in their sample and no mini halos in non-cool-core (NCC) clusters. However, the large dynamical range between central sources and large-scale emission complicates classification and many faint mini halos likely fall below the detection limit of current telescopes (van Weeren et al., 2019). Deepest imaging exists for the mini halos found in the Perseus cluster. Here, detailed observations of the Perseus mini radio

---

[2] The radiative flux density F_ν usually scales as a power-law with frequency, i.e. $F_\nu \propto \nu^\alpha$. The spectral index α corresponds to the power law index.

halo at 230 – 470 MHz show substructure in the form of filaments (Gendron-Marsolais et al., 2017), which suggests that when observed at high resolution and signal-to-noise, mini halos are not fully diffuse. These structures may hint towards localized sites of particle acceleration, local magnetic fields or a non-uniform distribution of source electrons.
The origin of radio mini halos may be due to re-accelerated electrons (leptonic origin) (Gitti et al., 2002) or secondary electrons (hadronic origin) (Pfrommer and Enßlin, 2004). The later are formed when CR protons interact with thermal protons to produce pions which decay into secondary electrons, positrons, neutrinos and gamma rays in the form;

$$\pi^{\pm} \rightarrow \mu^{\pm} + \nu_{\mu}/\bar{\nu}_{\mu} \rightarrow e^{\pm} + \nu_e/\bar{\nu}_e + \nu_{\mu} + \bar{\nu}_{\mu} \tag{2.6}$$

$$\pi^{0} \rightarrow 2\gamma \tag{2.7}$$

Thus, the detection of gamma rays would help constrain the origin of the radio emission. However, so far only upper limits exist for observations of diffuse gamma rays in mini halos. The most constraining observations exist for Perseus due to its high mass, vicinity and mini-halo brightness (Ackermann et al., 2014; Ahnen et al., 2016). The current gamma ray upper limits cannot directly exclude the hadronic model. However, they can be used to put a constraint on the minimum cluster magnetic field strength (Pfrommer, 2008), provided the radio emission is of hadronic origin. In Perseus, gamma ray observations currently limit the magnetic field strength to $\sim 5\,\mu$G (Brunetti et al., 2017), which is still well below observed values from observations of the Faraday rotation measure that find $25\,\mu$G (Taylor et al., 2006).

On the other hand, turbulent re-acceleration of primary electrons may power mini halos. Sloshing motions usually observed in the center of CC clusters could provide the source of the turbulence. Large-scale radio halos are presumably powered by merger-induced turbulent re-acceleration. Therefore, mini halos may just correspond to scaled down version of radio halos, which is supported by recent observations. The mini halo in CL1821+643 shows a transitional behavior, as it seems to switch off while the radio halo lightens up (Bonafede et al., 2014; Kale and Parekh, 2016). In PSZ1G139.61+24.20, Savini et al. (2018) find a possible co-existence of a radio mini halo and radio halo.

Faraday rotation measure

The polarization plane of light traveling through a magnetised plasma, e.g. the ICM, is changed by the wavelength-dependent Faraday rotation effect. The observed polarization plane χ at location $x = 0$ is related to the intrinsic polarization position angle of the polarized emission χ_0 at $x = L$, via

$$\chi(\lambda) = \chi_0 + \lambda^2 \frac{\mathrm{e}^3}{2\pi {m_\mathrm{e}}^2 c^4} \int_0^L \mathrm{d}x\, n_\mathrm{e}(x) B_x(x), \tag{2.8}$$

where B_x is the magnetic field component along the line of sight. The change in position angle of the radiation can thus be written as $\chi(\lambda) - \chi_0 = \lambda^2 \mathrm{RM}$. The proportionality constant given by the integral over density and magnetic field component along the line-of-sight is termed *Faraday rotation measure* (RM). Although χ_0 is unknown a priori, it can be computed by measuring the polarization angle χ at different wavelengths λ. Freshly injected electrons in jets or young radio bubbles provide ideal sources for polarized light. As background sources, they can be used to probe magnetic field strength and structure of a foreground galaxy cluster (Clarke, 2004) as discussed in Section 2.2.2.

2.2 Properties of cool core clusters

Early simulations of cosmological structure formation of cold dark matter (CDM) found that density profiles of CDM halos can be fitted by the simple formula (Navarro et al., 1995, 1997)

$$\frac{\rho(r)}{\rho_\mathrm{crit}} = \frac{\delta_\mathrm{c}}{(r/r_\mathrm{s})(1 + r/r_\mathrm{s})^2}, \tag{2.9}$$

where $\rho_{\rm crit} = 3H^2/8\pi G$ is the critical density of the universe, $\delta_{\rm c}$ is a characteristic density and $r_{\rm s}$ is the scale radius. The profile is referred to as Navarro-Frank-White (NFW) profile after the author names of the paper proposing it. The observed electron number density of CC clusters is usually well approximated by a *double beta profile* given by

$$n_{\rm e}(r) = n_0 \left[1 + \left(\frac{r}{r_{\rm c,0}}\right)^2\right]^{-3\beta_0/2} + n_1 \left[1 + \left(\frac{r}{r_{\rm c,1}}\right)^2\right]^{-3\beta_1/2}, \tag{2.10}$$

where typical values are $\beta_{0,1} = 1$, $(n_0, n_1) = (0.1, 0.01)\,{\rm cm}^{-3}$ and $(r_{\rm c,0}, r_{\rm c,1}) = (10, 100)\,{\rm kpc}$. At low redshift, CC clusters are observed to be in a quiescent state and to first order can be assumed to be in hydrostatic equilibrium, which gives an estimate of their temperature profiles. In contrast to density, temperature profiles in clusters vary more slowly as the temperature declines typically by a factor of three towards the center and towards the outskirts. Central temperatures reach $k_{\rm B}T \sim 1 - 2{\rm keV}$.

A characteristic quantity is a timescale on which the ICM would cool away its current total central energy, i.e. the cooling time. When only considering bremsstrahlung, the cooling time $t_{\rm cool}$ is given by

$$t_{\rm cool} = \frac{\epsilon_{\rm th}}{\dot{\epsilon}_{\rm brems}} = 2.8 \left(\frac{k_{\rm B}T}{2\,{\rm keV}}\right)^{1/2} \left(\frac{n_{\rm e}}{10^{-2}\,{\rm cm}^{-3}}\right)^{-1} {\rm Gyr}, \tag{2.11}$$

where values below $t_{\rm cool} < 1{\rm Gyr}$ are reached in dense centers ($n_{\rm e} \sim 0.1\,{\rm cm}^{-3}$) of CC clusters, while NCC clusters show $t_{\rm cool} > 3\,{\rm Gyr}$.

2.2.1 Cooling flow problem

The ICM loses energy by the emission of X-ray radiation in the dense central region of the cluster, which is accompanied by a loss in thermal pressure. Gas at higher altitudes is compressed and moves inwards leading to further cooling. In addition, inhomogeneities in the gas are expected to form cold clumps and stars. The result is a massive cooling flow, which in the case of CC clusters should be observable in nearby clusters due to their low cooling times. Models predict uninhibited mass cooling rates of $\sim 1{,}000\,{\rm M}_\odot\,{\rm yr}^{-1}$ with significant star formation (Fabian, 1994). However, the highest star formation rates in a local BCG reach a maximum at a comparatively low rate of $\sim 125\,{\rm M}_\odot\,{\rm yr}^{-1}$ in A1835 (McNamara et al., 2006). This could be brought in accordance with the cooling flow model if the cold gas was hidden in some form. An overabundance of low mass stars has been evoked to lower expected HI emission from young stars to observed values, possibly due to a reduced Jeans mass in high-pressure environments of BCGs (Fabian et al., 1982). However, most observations show evidence for a uniform initial mass function (IMF) in a variety of different objects (Fabian (2012), but see Van Dokkum and Conroy (2010); Cappellari et al. (2012)).

The lack of detection of crucial strong emission lines, when gas cools below 0.7 keV with XMM-Newton, indicated a strong deviation from the standard cooling flow model (Peterson et al., 2001; Tamura et al., 2001). This signified a severe deficit of cooling gas in the cluster core at one third of the temperature of the hot ambient cluster atmosphere (Peterson et al., 2003). The inability to find a repository of cold gas and/or stars, lead to the conclusion that something is preventing the gas from reaching such low temperatures in the first place. While dynamical friction and thermal conduction of heat from the outer cluster atmosphere have been discussed as possible heating mechanisms (Soker, 2003), it is now widely accepted that AGN jets represent the main source of heat for the ICM (McNamara and Nulsen, 2012).

The main idea is that cold gas is accreted by the black hole, which in combination with black hole spin powers jets that inflate bubbles, i.e. X-ray cavities. In a study of the brightest 55 galaxy clusters, all clusters with $t_{\rm cool} < 3\,{\rm Gyr}$ (except for Ophiuchus, which undergoes a merger) show bubbles in their atmospheres (Fabian, 2012). This implies a duty cycle of > 95 %, which suggests a tight coupling between heating and cooling. Crucially, the estimated kinetic power of the jet is sufficient to balance the observed energy losses due to X-ray radiation (Bîrzan et al., 2004).

2.2.2 Magnetic fields

Giant radio halos and radio mini halos prove the presence of volume filling magnetic fields in clusters and the dense cores of CC systems, respectively. Two popular models for the origin of magnetic field in clusters exist (Ryu et al., 2012). In the first, initial seed magnetic fields are generated in the early universe. Alternatively, galactic magnetic fields are expelled into the ICM via galactic winds or AGNs. In clusters, magnetic fields are then amplified by adiabatic compression and a small scale dynamo based on turbulence, which are both powered by minor and major mergers (Subramanian, 2016).

Magnetic field strengths can be estimated by measuring the Faraday rotation measure from background polarized radio sources (see Section 2.1.3). Ideally multiple sources can be found behind a single cluster to resolve the large scale structure of the magnetic field. The Coma cluster provides such an environment, where Bonafede et al. (2010) compare simulated realizations of the magnetic field in the cluster to data derived from seven patches in the cluster with background sources. They find that the power spectrum of the magnetic field is well approximated by a Kolmogorov power spectrum with maximum scale of 34 kpc. The magnetic field reaches values of $\sim 5\,\mu$G in the center. In denser environments of cool core clusters, generally larger field strengths are observed (Carilli and Taylor, 2002). In Hydra A, Kuchar and Enßlin (2011) find a central magnetic field strength of $36\,\mu$G and determine a lower limit for the maximum scale of the field at 8 kpc. In addition, their computed spectrum is consistent with a Kolmogorov-like power law, which confirms the finding of other groups (Vogt and Enßlin, 2005a; Guidetti et al., 2008; Vacca et al., 2012). While Faraday RM represents a powerful tool to analyze magnetic fields in cluster, intrinsic uncertainties of the method limit determination of the magnetic field strength to factors of a few (Newman et al., 2002; Johnson et al., 2020).

2.2.3 Turbulent velocity fields

The details of heating by AGN jets in galaxy clusters depend crucially on the velocity structure of the ICM. They have an impact on jet dynamics (Mendygral et al., 2012), heating by decaying turbulence crucially depends on the magnitude of turbulent velocities (Zhuravleva et al., 2014), etc. Possible sources of bulk motions and/or turbulence in clusters include large scale structure formation, sloshing motions due to mergers, subhalo infall and AGN jets themselves (for further details see Simionescu et al., 2019).

First estimates of the velocity dispersion of the ICM became feasible with the X-ray satellite *XMM-Newton*. Although the ICM is generally optically thin, at some energies resonant scattering can make the gas optically thick. Small scale turbulence will weaken the effect and reduce the optical depth (Gilfanov et al., 1986). Other lines unaffected by turbulence are used to estimate the magnitude of resonance scattering and a comparison with the former allows an estimate of the magnitude of turbulence (Churazov et al., 2010). The method has been applied to X-ray bright galaxies as found in the core of clusters on scales $\lesssim 10$ kpc, which find velocities on the order of hundreds of km s^{-1} (Werner et al., 2009; De Plaa et al., 2012; Ogorzalek et al., 2017). In a smooth cluster potential drawing a direct connection between surface brightness fluctuations and velocity fluctuations allowed Zhuravleva et al. (2014) to estimate the velocity structure of the Perseus cluster including its power spectrum.

Most importantly, spectral lines can be used to determine turbulent velocities. Lines are broadened due to uncertainties in the energy of the involved atomic states, i.e. the *natural line width* (which is a small effect). In addition, the Doppler shift affects gas with a thermal distribution, i.e. *thermal broadening* and turbulent velocities, i.e. *line-of-sight velocity broadening*. Most recently, the X-ray satellite *Hitomi* with its unprecedented high spectral resolution was able to measure a line-of-sight velocity dispersion of $\sigma \sim 100$km s^{-1} in the bulk of the cluster and $\sigma \lesssim 200$ km s^{-1} toward the central AGN as well as near a remnant bubble (Hitomi Collaboration, 2016, 2018).

2.2.4 Streaming cosmic rays

Cosmic rays are charged particles moving nearly at the speed of light with energies between 1 MeV and 10^{21} eV (Grenier et al., 2015). Cosmic ray protons with energies in the range $1-3$ GeV comprise most of the cosmic ray energy. Strong energetic losses of CR electrons and lower abundances limit the dynamical impact of CR electrons. We therefore focus on CR protons here. For brevity, we will refer to CR protons as CRs in the following sections. By studying the evolution of spallation processes leading to observed element abundances of CRs, it was determined that cosmic rays reside in the Galaxy on timescales that depend on their energy. Specifically, CRs at 1 GeV stay confined for $10-20$ Myr. This is significantly longer than the time it takes to cross the disk of the Galaxy ($d \sim 10$kpc) traveling at the speed of light $d/c \approx 0.03$ Myr. While tangled magnetic fields may confine CRs for some time, the expected energy dependence on the confinement time would be smaller than observed. The confinement time of CRs decreases with energy, which allows us to conclude that the acceleration timescale is much smaller than the confinement time. In addition, CRs show a high degree of isotropy, which decreases for higher CR energies. Consequently, it appears that a fraction of thermal gas particles is accelerated on short timescales and now propagates diffusively through the disk with a diffusion coefficient κ that increases with CR energy, $\kappa \sim 10^{28-29}\,\mathrm{cm}^2\mathrm{s}^{-1}$ at 1 GeV (Zweibel, 2013).

Streaming instability

CRs are confined to gyrate around magnetic fields due to the Lorentz force. The corresponding cyclotron frequency is given by $\Omega = eB_0/(\gamma m_\mathrm{p} c)$, where B_0 is the magnetic field strength. As noted above, long confinement times cannot be due to gyration around magnetic field lines. Furthermore, the acceleration process of CRs cannot be responsible for their confinement, otherwise the oldest CRs would stay confined the longest. Therefore, it becomes necessary to study how CRs interact with magnetic field fluctuations. The angle subtended by the CR velocity and the magnetic field is called pitch angle θ, i.e. $\cos(\theta) = \mu = \boldsymbol{v}_\mathrm{cr} \cdot \boldsymbol{B}/|\boldsymbol{v}_\mathrm{cr}||\boldsymbol{B}|$. Assume a CR is gyrating around the magnetic field that has has a small transverse perturbation in form of an Alfvénic wave with a wavelength of size the CR's gyro radius. The perpendicular component of these Alfvénic fluctuations exerts a Lorentz force on the CR that is directed opposite to its drifting motion along the mean magnetic field. This causes the parallel component of the CR velocity (with respect to the mean magnetic field) to decrease, and the perpendicular component to increase because particle energy is conserved for the stationary magnetic field in the reference frame of the Alfvén wave. The previously described interaction is therefore called *pitch angle scattering*. For pitch angle scattering to be most effective, the wavelength of Alfvén waves (projected along the mean magnetic field) should match the CR's gyro orbit r_G. The resulting resonance condition is given by (Kulsrud, 2005)

$$0 = k_\mathrm{res}(\mu v - v_\mathrm{A}) \mp \Omega, \tag{2.12}$$

where $\omega = k v_\mathrm{A}$ is the dispersion relation for Alfvén waves. If $r_{\delta B} \ll r_\mathrm{G}$, the Lorentz force varies on very small scales such that its effect averages out. If $r_{\delta B} \gg r_\mathrm{G}$, the CR will just gyrate along the slowly evolving magnetic field fluctuations.

Self-confinement of CRs

But what is the source of these magnetic field fluctuations in the ICM and do they have the properties required to realize resonant scattering? While scattering on fluctuations in the MHD turbulent cascade or on magnetosonic waves are theoretically possible, the most promising mechanism relies on Alfvén waves that are generated by the CRs themselves via the *streaming instability* (Kulsrud and Pearce, 1969; Zweibel, 2013). The growth rate Γ of Alfvén waves due to a power-law distribution of CRs with $f \propto p^\alpha$ can be computed from employing perturbation analysis of the Vlasov Equation and is given by (Kulsrud and Cesarsky, 1971)

$$\Gamma = \frac{\pi}{4}\Omega_0 \frac{\alpha - 1}{\alpha} \frac{n_\mathrm{cr}(> p_\mathrm{min})}{n_\mathrm{i}} \left(\frac{v_\mathrm{d}}{v_\mathrm{A}} - 1\right), \tag{2.13}$$

where $\Omega_0 = \gamma\Omega$ is the non-relativistic proton gyrofrequency, $n_{\rm cr}(> p_{\rm min})$ is the number density of CRs with critical momentum $p_{\rm min} = ZeB/ck$ that can resonate with a wave of wavenumber k, $n_{\rm i}$ is the ion density of the ambient plasma, $v_{\rm d}$ is the drift speed of the CRs relative to the gas and $v_{\rm A}$ is the Alfvén velocity. Note, the CR density decreases with CR energy such that self-confinement becomes less efficient for high energy CRs. The streaming instability causes waves to grow until pitch angle scattering isotropizes the CR distribution in the frame of the waves, i.e. $v_{\rm d} \sim v_{\rm A}$.

From this, one could conclude that CRs are always confined to stream at the Alfvén speed. However, Alfvén waves are subject to damping processes, which reduce confinement. In addition, bulk motion at faster drift velocities, i.e. super-Alfvén streaming, becomes possible. The most relevant damping processes in galaxy clusters are non-linear Landau damping and turbulent damping (Zweibel, 2013). Non-linear Landau damping occurs when two parallel propagating MHD waves A & B with slightly different speeds interact to form a beat wave. Thermal particles with parallel velocities identical to the wave's phase speed $v_{\|} = (\omega_{\rm A} - \omega_{\rm B})/(k_{\rm A} - k_{\rm B})$ interact with the beat wave. Thermal particles extract energy from the wave when they are slower than the wave and add energy to the wave when they are faster (Lee and Völk, 1973). For Maxwellian plasmas, usually $\partial f/\partial v < 0$ in the range $v_{\|} = v_{\rm A}$, such that wave damping dominates. In addition, waves are damped by shearing due to small scale perpendicular magnetic field structures associated with the MHD turbulence cascade (Farmer and Goldreich, 2004), which is termed turbulent damping. In cluster environments, damping mechanisms for CRs at $E > 100\,\mathrm{GeV}$ start to dominate excitation such that an alternative scattering mechanism would be required at these energies to confine CRs (Zweibel, 2013). Crucially, assuming steady state between Alfvén wave damping and excitation, GeV CRs are self-confined to stream at nearly the Alfvén speed in the ICM (Jacob and Pfrommer, 2017a). Note, only Alfvén waves that travel in the same direction as the CRs are amplified. Therefore, CRs stream down their pressure gradient and due to weak damping their speed is limited to the Alfvén velocity. The propagation speed of the CRs, i.e. streaming velocity $\boldsymbol{v}_{\rm st}$ is then given by

$$\boldsymbol{v}_{\rm st} = -\mathrm{sgn}\,(\boldsymbol{b} \cdot \nabla P_{\rm cr})\, \boldsymbol{v}_{\rm A}, \tag{2.14}$$

where $\boldsymbol{b}$ is a unit vector pointing along the magnetic field.

In the picture of *self*-confinement, we now assume that streaming CRs are the main source of magnetic field fluctuations. CRs that are initially faster than the Alfvén speed generate Alfvén waves. Frequent scattering on these waves isotropizes the CR distribution, i.e they are confined to the wave speed. Consequently, these interactions without collisions occur on microscopic scales that are much smaller than the kpc scales we are interested in. We can therefore use the Vlasov equation to describe the conservation of phase space density ($df/dt = 0$) in the absence of collisional processes like spallation as

$$\frac{\partial f}{\partial t} + \boldsymbol{v}_{\rm cr} \cdot \nabla f + \frac{\mathrm{d}\boldsymbol{p}}{\mathrm{d}t} \cdot \nabla_{\boldsymbol{p}} f = 0, \tag{2.15}$$

where $\boldsymbol{v}_{\rm cr}$ is the total velocity of CRs and $f(\boldsymbol{x},\boldsymbol{p},t)$ is the CR distribution function, which gives the probability for a CR to be at position $\boldsymbol{x}$ with momentum $\boldsymbol{p}$ (in units of mc) at time t. The distribution function can be expanded in inverse powers of the scattering frequency ν, $f = f_0 + f_1 + f_2 + ...$, where $f_x \sim O(\nu^{-x})$. We then study the CR distribution under the influence of the Lorentz force due to magnetic fluctuations. In the limit of frequent scattering, we can average over pitch angle and assume $f_0 \gg f_1$, i.e. the distribution function is isotropic in the wave frame plus a small isotropy f_1. When retaining second order terms $O(\nu^{-2})$, we obtain the equation of CR transport (Schlickeiser, 1989),

$$\frac{\partial f_{\rm p}}{\partial t} + (\boldsymbol{v} + \boldsymbol{v}_{\rm st}) \cdot \nabla f_{\rm p} = \nabla \cdot \left[\kappa_{\rm p} \boldsymbol{b} \left(\boldsymbol{b} \cdot \nabla f_{\rm p}\right)\right] + \frac{1}{3} p \frac{\partial f_{\rm p}}{\partial p} \nabla \cdot (\boldsymbol{v} + \boldsymbol{v}_{\rm st}) + \frac{1}{p^2} \frac{\partial}{\partial p}\left[p^2 \Gamma_{\rm p} \frac{\partial f_{\rm p}}{\partial p}\right] + Q_{\rm p}, \tag{2.16}$$

where $f_{\rm p}(\boldsymbol{x}, p, t)$ is the CR distribution function (isotropic in momentum space), $\boldsymbol{v}$ is the gas velocity, $\kappa_{\rm p}$ is the spatial diffusion coefficient, $\Gamma_{\rm p}$ is the momentum diffusion coefficient and $Q_{\rm p}$ is a CR source function. Note, the equation uses a mixed frame of reference. While the spatial coordinates are measured in the laboratory frame, momenta are defined with respect to the CR rest frame. The physical interpretation of the equation identifies the left-hand side as the total time derivative, including

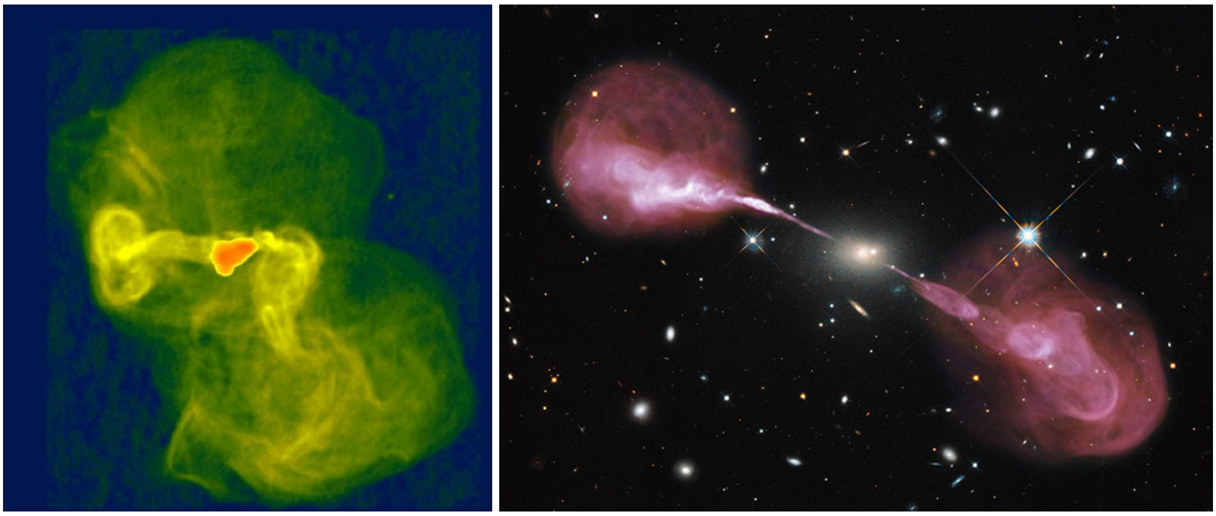

Figure 2.2: On the left, VLA radio observations of M87 (adopted from Owen et al. (1999)), which represents a FRI radio galaxy. On the right, VLA radio observations of Hercules A in 3C 348 combined with HST optical data (adopted from nasa.gov (2012)), which is a typical FRII radio galaxy.

advection in the wave frame. On the right-hand side, the terms describe diffusive transport along magnetic field lines, adiabatic deceleration/acceleration, second-order Fermi acceleration (diffusion in momentum space) and sources/sinks of the CR distribution.

Alfvén heating

In the frame of the Alfvén waves, there are no electrical fields such that particles conserve energy as they scatter in pitch angle. However, in the frame of the gas a changing magnetic field induces an electrical field. Consequently, there is a net transfer from the CRs to the gas with volumetric heating rate, i.e. *Alfvénic heating rate* $\mathit{\Gamma}_{\mathrm{A}}$ given by (Kulsrud, 2005)

$$\mathit{\Gamma}_{\mathrm{A}} = -\boldsymbol{v}_{\mathrm{A}} \cdot \nabla P_{\mathrm{cr}}, \tag{2.17}$$

where ∇P_{cr} is the pressure gradient of the CRs.

2.3 Jets from active galactic nuclei

Active galactic nuclei are compact regions at the center of galaxies that emit non-thermal radiation. They are powered by an accretion disk surrounding a *supermassive black hole*. A fraction of AGNs show highly collimated bipolar outflows that are visible as jets in radio observations. Jets terminate in large-scale underdense X-ray cavities that buoyantly rise as bubbles in the cluster atmosphere. They are believed to heat CC clusters. Here, we discuss the observational evidence that led to this conclusion and review candidates for the currently unknown heating mechanism in CC cluster. We start out by summarizing our understanding of jets.

2.3.1 Jet launching

AGN black holes are surrounded by orbiting gas. When gas is allowed to cool on the inflow timescale, it settles onto an accretion disk. Gas can lose angular momentum due to magnetic torques via the magnetorotational instability and flows towards the event horizon of the black hole. However, cooling of the gas is inhibited in this simple model when the accretion rate exceeds the Eddington limit, i.e. $\dot{M} \gtrsim \dot{M}_{\mathrm{Edd}}$. Assuming spherical symmetry, the Eddington accretion rate is given by balancing radiation pressure and gravity, $\dot{M}_{\mathrm{Edd}} = 4\pi G M m_{\mathrm{p}}/(\sigma_{\mathrm{T}} c)$. Here, radiation is trapped by inflowing gas and the disk thickens due to strong radiation pressure.

Therefore, properties of accretion disks and outflows depend on the mass accretion rate of the disk. These are usually divided into two regimes. For low accretion rates $\dot{M} \lesssim 0.05 - 0.1\dot{M}_{\mathrm{Edd}}$, the currently favored model of accretion disk suggests that the disk is optically thin but geometrically thick (Blandford et al., 2019). SMBH in CC clusters are mostly observed in this state. Here, the surface density of the disc is very low such that the gas decouples into a two temperature electron-ion plasma. While ions at $\sim 10^{12}\,\mathrm{K}$ supply the pressure, electrons at $10^{9-11}\,\mathrm{K}$ provide most of the radiation. Here, ions are unable to cool on the inflow timescale, an *advection dominated accretion flow* (ADAF) forms where heat generated by viscosity will be advected inwards instead of radiating away (Ichimaru, 1977). General relativistic magnetohydrodynamical (GRMHD) simulations show that the disk can sustain large-scale poloidal magnetic flux (De Villiers et al., 2003). The disk carries the flux inwards and jets are launched when the magnetic field reaches the spinning SMBH. This launching mechanism is termed Blandford-Znajek (BZ) process (Blandford and Znajek, 1977). Increasing spin values leads to higher jet powers (McKinney, 2006).

When the disk is accreting at a significant fraction of the Eddington accretion rate, strong thermal emission leads to an optically thick and geometrically thin disk (Shakura and Sunyaev, 1973). These sources are generally termed quasars and outshine their host galaxy in the optical, which distinguishes them from radio galaxies. Interestingly, roughly 10% of observed quasars are believed to host a radio jet (Ivezić et al., 2002; Kellermann et al., 2016). GRMHD simulations by Liska et al. (2019) suggest that they may also be launched by the BZ mechanism.

Fanaroff-Riley Classes

A popular classification of jets introduced by Fanaroff and Riley (1974) is based on their radio morphology. While FRI radio galaxies show a brighter center, FRIIs are edge-brightened. While differences may be linked to their internal engines (Hardcastle and Croston, 2020), the reason is generally attributed to a combination of jet power and environmental density. FRII jets are thought to remain relativistic throughout and terminate in a bright internal shock (hotspot). On the other hand, FRI jets decelerate on kpc scales. Powerful jets in less dense environments tend to show FRII morphology, while lower power jets in dense environment appear as FRI jets (Tchekhovskoy and Bromberg, 2016). While newly detected low power FRII jets challenge this idea (Mingo et al., 2019), there are large uncertainties when converting from radio luminosity to jet power (Croston et al., 2018). In addition, these FRII jets appear to reside in less dense environments in agreement with the initial model (Mingo et al., 2019). Prominent examples of a FRI and FRII radio galaxy are shown in Figure 2.2.

2.3.2 Observational evidence for AGN feedback

Jet energy estimates

A major finding regarding AGN feedback in clusters concerns the observed mechanical jet power and central cooling luminosity. Observations of jet inflated bubbles provide a unique opportunity to estimate mechanical feedback provided by jets. The energy required to inflate a bubble of volume V against thermal pressure P plus the internal energy $PV/(\gamma - 1)$ required to stabilize the bubble is given by its enthalpy H;

$$H = PV + \frac{PV}{\gamma - 1} = \frac{\gamma}{\gamma - 1} PV = \begin{cases} 2.5\,PV, & \text{for } \gamma = 5/3, \\ 4\,PV, & \text{for } \gamma = 4/3, \end{cases} \tag{2.18}$$

where γ is the adiabatic index of the cavity plasma. The value of γ depends on the relativistic ($\gamma = 4/3$) or non-relativistic ($\gamma = 5/3$) composition of the bubbles. Note, that Equation (2.18) corresponds to a lower limit of jet energy as it misses expected additional energy sinks like sound waves (Fabian et al., 2006), weak shocks (Mathews et al., 2006), thermal conduction (Kim and Narayan, 2003), leaking CRs (Guo and Oh, 2008), and others. Bubbles need to contain gas with temperatures $T > 20\,\mathrm{keV}$ to appear as cavities in X-ray observations such that a relativistic filling appears more likely. More details on our current understanding of the bubble composition are discussed in Section 2.3.3.

Cooling in clusters is usually characterized by the X-ray luminosity. To obtain a corresponding jet luminosity, one divides the mechanical energy by the age of the bubble. Popular approximations of bubble age include bubble rise time at the speed of sound, bubble rise time due to buoyancy or the time required to refill the displaced volume of the rising bubble, where these time scales agree within factors of $2-4$ (Bîrzan et al., 2004). When comparing resulting jet luminosities to corresponding cooling luminosities in clusters, cooling luminosities are of order $4PV$ in many clusters (Rafferty et al., 2006). Observations are biased against identifying bubbles in less dense cluster outskirts, such that bubbles can be missed. However, bubbles in the dense center of strong cooling cluster should be readily observable. Remarkably, all strong cool clusters have observed cavity powers where cooling luminosities are equal to at most $L_X \lesssim 1\,PV$ (McNamara and Nulsen, 2012). Interestingly, McDonald et al. (2019) find the thermodynamic profiles of the center of the Phoenix cluster consistent with a steady-state cooling flow. They suggest that its SMBH is undersized relative to cluster mass, which provides insufficient feedback to heat the cluster.

Details of heating

The observed correlation between jet luminosity and cooling luminosity suggests that AGN heating is tightly coupled to cooling in CC clusters. Furthermore, Hudson et al. (2010) show that 44% of the HIFLUGCS sample have $t_{\mathrm{cool}} < 1\,\mathrm{Gyr}$. This high fraction of CC clusters means that a successful model for heating in clusters needs to be able to reproduce short cooling times and therefore limit "unregulated" over-heating. This makes AGN feedback a prime candidate. In addition, radial profiles of cooling time smoothly decline from a few Hubble timescales in the outskirts ($\sim 200-300\,\mathrm{kpc}$) towards central cooling times of $10^8\,\mathrm{yr}$ (Voigt and Fabian, 2004). Thus, feedback needs to be gentle to sustain these weak cooling flows on long timescales.

Note, cooling in the ICM does not necessarily imply a temperature reduction. Radiative losses of gas in a fixed volume lead to a drop in temperature. However, in clusters, cooling gas will be compressed by gas at higher altitudes due to gravity and thereby heated. It therefore becomes more instructive to look at entropy instead of temperature to study heating and cooling. The specific entropy S is given by

$$\rho T \frac{\mathrm{d}S}{\mathrm{d}t} = \mathcal{H} - \mathcal{R}, \tag{2.19}$$

where ρ is the gas density, T is its temperature, $\mathcal{H}$ is the heating rate per unit volume and R is the power radiated away per unit volume. This is equivalent to

$$\frac{\mathrm{d}}{\mathrm{d}t} \ln K = \frac{1}{t_{\mathrm{heat}}} - \frac{1}{t_{\mathrm{cool}}}, \tag{2.20}$$

where $K = kT/n_{\mathrm{e}}^{\gamma-1}$ is the entropy index and n_{e} is the electron number density.[3] The cooling time t_{cool} is given by

$$t_{\mathrm{cool}} = \frac{P}{(\gamma-1)\mathcal{R}}, \tag{2.21}$$

which corresponds to the timescale required to radiate away the thermal energy of the cluster. The heating time t_{heat} is analogously given by

$$t_{\mathrm{heat}} = \frac{P}{(\gamma-1)\mathcal{H}}. \tag{2.22}$$

Measurements of entropy index K provide an alternative path of excluding the presence of strong cooling flows in clusters. While models of unimpeded cooling flows predict declining entropy profiles towards the center, observed entropy profiles show a central plateau. Crucially, jet power correlates with central entropy in CC clusters (Pfrommer et al., 2012). It appears that cooling gas triggers

---

[3] The entropy index is related to the proper thermodynamic entropy via $s = c_V \ln(K/K_0)$, where s is the specific entropy and c_V is the specific heat at constant volume (see Pfrommer, 2022, for more details).

the AGN to initiate heating. It is therefore required for the jet to act on smaller timescales than the cooling time. By using cavity buoyancy time as a proxy for cavity age, (Rafferty et al., 2008) shows that cavities are indeed younger than central ICM cooling times. Even the most massive jet outburst shows this gentle mode of heating where the AGN compensates for potential energy lost due to cooling (Vantyghem et al., 2014).

2.3.3 Lobe composition

The particle content of lobes and bubbles provides crucial information for jet dynamics and constrains heating mechanisms. Early polarization observations established that the pressure contribution from internal thermal electrons is low in FRII lobes (Scheuer, 1974). In the past, assumptions about the proton fraction and magnetic field strength were required to infer the electron density from the measured synchrotron radiation. Here, usually energy equipartition between magnetic field and radiating particles was assumed (Beck and Krause, 2005). However, observations of the inverse-Compton emission from lobes and hotspots of FRII sources directly constrain the number of electrons. The magnetic field strength can then be computed from synchrotron observations. The combined energy density due to magnetic fields and electrons is in agreement with estimates of the external ICM pressure. At the tip of the lobe, lobes can be overpressured with regard to the ICM. Therefore, protons are not expected to be energetically dominant in these source (Croston et al., 2018). However, they could still be present at the same level as electrons.

On the other hand, determining the content of FRI lobes is more difficult as thermal emission usually dominates inverse-Compton emission here. When assuming energy equipartition between electrons and magnetic field strengths, lobes appear significantly underpressued with regard to the external medium. Here, an energetically dominant proton population seems plausible in stark contrast to FRII sources (Croston et al., 2018). The appearance of the lobes as X-ray cavities and polarization observations rule out thermal protons similar to the surrounding medium. Recently, Abdulla et al. (2019) used the SZ effect to measure the thermal content of bubbles in cluster MS 0735.6+7421. They varied the filling of bubbles in their model and compared the resulting SZ signal to their observations. They conclude that the bubbles are either pressure supported by gas with temperatures $T \sim 1000\,\mathrm{keV}$ or a non-thermal pressure component. Consequently, it appears that the pressure of FRI lobes is dominated by high-energy particles. The idea is that entrainment of external material slows down the lobes, which is then heated inside the lobes (Croston and Hardcastle, 2014).

2.3.4 Heating mechanisms

Initially, the conduction of heat from hot cluster outskirts to strongly cooling centers was discussed as the main heating source in CC clusters. However, conductivity needs to be fine-tuned (Guo et al., 2008), sometimes requires a conductivity exceeding the theoretical maximum value (Zakamska and Narayan, 2003) and solutions are not locally stable on scales larger than the Field length (Kim and Narayan, 2003). Thermal conduction may however play a role in combination with jet feedback (Voit et al., 2015). While the most relevant heating mechanism for AGN feedback in CC clusters remains uncertain, a plethora of possible mechanisms exist, of which the most promising are introduced in the following.

Weak shocks

Weak shocks are readily observed (Forman et al., 2007; Blanton et al., 2011) and detected in simulations of self-regulated AGN feedback (Mathews et al., 2006). Due to limited heating expected from a single weak shock, a continuous input of weak shocks is required to heat a cluster core (McNamara and Nulsen, 2012). In NGC 5813, Randall et al. (2011) find three pairs of cavities from distinct outbursts and identify two related episodes of shock formation, which provides evidence for continuous shock injection with sufficient heating to balance cooling. In addition, Li et al. (2017) identify dissipation of weak shocks as the main heating mechanism in their simulations. Here, weak shocks dissipate most of their energy within 30 kpc. Then, adiabatic processes and mixing redistribute the heat throughout the core. In addition, simulations by Martizzi et al. (2019b) find weak shock dissipation to be a crucial source of heat.

Turbulence

Zhuravleva et al. (2014) analyzed surface brightness fluctuations in Virgo and Perseus. They interpret a significant fraction of them as due to turbulence. If dissipated in the ICM, turbulence can provide sufficient heating to offset cooling in these clusters. However, it appears that turbulence is unable to propagate energy throughout the cluster to balance heating at each radius (Fabian et al., 2017; Bambic et al., 2018b). In addition, Yang and Reynolds (2016) find that turbulent heating makes up a mere percent level contribution to heating in their hydrodynamical simulations. Finally, simulations of driven turbulence to balance heating find resulting ICM velocities inconsistent with velocity measurements by *Hitomi* (Mohapatra and Sharma, 2019).

Sound waves

Ripples are seen in X-ray observations of the Perseus and Centaurs cluster, which are reminiscent of sound waves. Dissipation of these waves can provide energy to heat the core of Perseus (Fabian et al., 2006; Sanders and Fabian, 2008). However, the observational signature of sound wave-like features corresponds generally to only a 10% increase in surface brightness, which limits their detection to the brightest clusters (Graham et al., 2008). In addition, jet simulations by Bambic and Reynolds (2019) find efficient production of sound waves ($E_\mathrm{s} \lesssim E_\mathrm{jet}/3$), which suggests that the contribution from sound waves to heating may be significant. However, details of sound waves transport requires the treatment of plasma instabilities present in the outer ICM, which is weakly collisional. The physics of which are a topic of active research (Kunz et al., 2020; Drake et al., 2021). Finally, similarly to sound waves, alternatively internal gravity waves could be excited by rising bubbles, propagate through the cluster center and dissipate their energy to provide heating (Zhang et al., 2018).

Bubble mixing

Mixing of hot bubble material with the surrounding ICM is discussed as a viable heating mechanism especially in the direct surroundings of the bubbles (Fabian, 2012). Alternatively, jets that possess wide opening angles would spread their ram pressure over a large area and therefore show limited penetration power through the ICM. Bubbles would then deposit their energy close to their origin and heat larger volumes. A similar mechanism can be envisioned for jets with significant levels of precession (Sternberg et al., 2007). The efficient heating of wide jets has been demonstrated in hydrodynamical simulations (Gilkis and Soker, 2012; Hillel and Soker, 2016). The analysis of heating sources in simulations by Yang and Reynolds (2016) identify mixing as one of the main heating mechanisms in combination with weak shock dissipation. However, as no simple model exists for mixing, the amount of heating due to mixing is infered indirectly. The authors assume a strict balance between heating and cooling within the jet cones, where the residual source of heat is attributed to mixing.

Cosmic ray heating

As noted in Section 2.3.3, relativistic protons may provide substantial pressure support to bubbles. Escaping CRs could heat the ICM via streaming. Streaming CRs excite Alfvén waves and scatter on these waves. The damping of Alfvén waves leads to a net transfer of CR energy to heat (Wentzel, 1971). Jacob and Pfrommer (2017a) find steady state solutions for a large sample of clusters where CR heating balances cooling in the center and thermal conduction stabilizes cluster outskirts. In Jacob and Pfrommer (2017b), they confront the expected radio and gamma ray emission from the CRs with observations. They find that a subclass of clusters exceeds limits given by radio observations. These clusters host a radio mini halo and show excess star formation compared to their full sample. They postulate radio micro halos clusters with ongoing CR heating. After the heating reservoir due to CRs is exhausted, a phase of cooling follows with increased star formation, reconciling their results with observations. They suggest that the mini halos could be powered by hadronic processes. Simulations of self-regulated AGN feedback identify CRs as an efficient heating mechanism (Wang et al., 2020). Recently, Beckmann and Dubois (2022) report that jets dominated by CR energy lead to a buildup of Gamma ray emission over time that is inconsistent with observations. However, jets that contain 10% of their energy in CRs remain within limits set by observations.

2.3.5 Jet bubble - ICM interaction

In order to understand the details of AGN feedback in clusters, it becomes crucial to study jet evolution in the ICM. The observed metallicity distribution in clusters provides strong evidence for significant mass transport by jets. The metallicity generally peaks in the BCG but its distribution is much broader than expected from direct enrichment (Rebusco et al., 2005). The detection of cold metal-rich gas along bubbles and radio sources in multiple clusters provides strong evidence for effective uplift of central gas by jets (Simionescu et al., 2008; Kirkpatrick and McNamara, 2015). The metallicity is enriched up to levels detected in the BCG and can reach heights of 100s kpc as observed in Hydra A and MS0735 (Simionescu et al., 2009; McNamara and Nulsen, 2012).

The latter provides strong evidence for the longevity of bubbles in the ICM. In early simulations, bubbles disrupted too efficiently (Churazov et al., 2001). However, the addition of viscosity (Guo, 2015) and magnetic fields (Ruszkowski et al., 2007) resolves the issue. In addition, jet-inflated bubbles are more stable than bubbles set up by hand (Sternberg and Soker, 2008b). Bourne and Sijacki (2017) show that too little resolution elements at the interface between jet-ICM can lead to significant numerical mixing. Dedicated refinement schemes can provide an efficient solution for codes with adaptive mesh refinement. In addition, a low density jet with pressure dominated by CRs has a lower inertia compared to a jet dominated by kinetic energy and therefore decelerates more quickly. Jets expand more laterally due to CR pressure which leads to the displacement of more ICM gas (Guo and Mathews, 2011). The resulting wider X-ray cavities show morphologies in agreement with observations of central X-ray cavities. Finally, bulk motions due to mergers, substructure, etc. can significantly displace and distort bubbles. This leads to faster disruption of bubbles (Mendygral et al., 2012; Bourne and Sijacki, 2017).

2.4 Fueling of active galactic nuclei

AGN jets are fueled by accretion onto a disk surrounding black holes. The disk gas is assumed to loose angular momentum due to the magnetorotational instability (Balbus and Hawley, 1998) and moves inwards towards the event horizon. As discussed in Section 2.3.1, jets are presumably launched here with an unknown contribution from black hole spin, however many details remain inconclusive (Blandford et al., 2019). Based on this model, Talbot et al. (2021, 2022) track the spin evolution of their black hole and extract part of its spin energy to power the jet. However, to at least partially resolve dynamics in the vicinity of the black hole, cells are refined down to 0.01 pc in this region. This limits run times to a few tens of Myr. Consequently, we omit spin evolution in our model for now as we are interested in the long term evolution of the ICM. Here, we introduce two popular models of large scale accretion used in cluster simulations, i.e. Bondi and cold accretion. While the model of Bondi accretion is based on an analytical solution to accretion onto a point mass, cold accretion is based on observations of condensing gas that is assumed to sink onto the central black hole.

2.4.1 Bondi accretion

The traditional description of accretion is *Bondi accretion*, which is based on a model of spherically symmetric accretion onto a stationary (with respect to the ambient medium) point mass (Bondi,

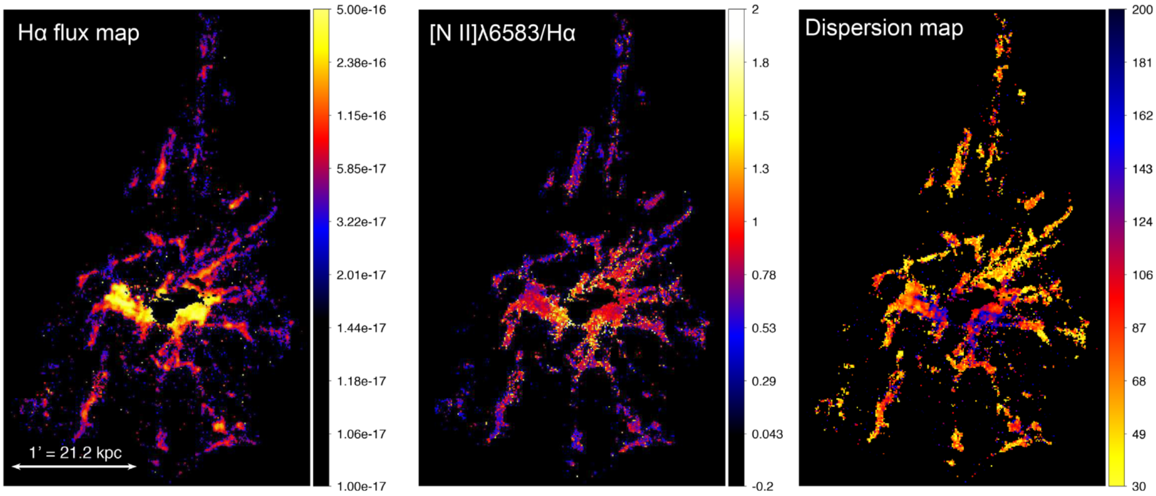

Figure 2.3: Observations of the cold ionized gas of the central part of NGC 1275 from Gendron-Marsolais et al. (2018a). From left to right, we reproduce Hα emission in units of $\mathrm{erg\,s^{-1}cm^{-2}pixel^{-1}}$, line ratio of [NII] at 6583Å and Hα and velocity dispersion in $\mathrm{km\,s^{-1}}$. Images taken with the optical imaging Fourier transform spectrometer SITELLE at the Canada-France-Hawaii Telescope. The orientation of the filaments suggests that they are influenced by bubble dynamics.

1952). Combining equations of mass and momentum conservation, a steady solution for an adiabatic flow ($\gamma = 5/3$) can be determined with accretion rate $\dot{M}$ given by

$$\dot{M} = \frac{\pi \rho G^2 M^2}{c_\mathrm{s}^3}, \tag{2.23}$$

where ρ and c_s are the density and sound speed of the ambient medium, respectively. Assuming non-adiabatic effects like thermal conduction or radiative cooling with $1 < \gamma < 5/3$, the initially subsonic flow becomes supersonic at the so called Bondi radius r_B, defined as

$$r_\mathrm{B} = \frac{2GM}{c_\mathrm{s}^2}, \tag{2.24}$$

where M is the mass of the central object. Note, when balancing kinetic and thermal energy of the gas, it becomes apparent that r_B corresponds to the radius where gas with $v \leq v_\mathrm{s}$ is accreted by the central object. Therefore, resolving the hydrodynamic state of the gas within the Bondi radius gives crucial information on the nature of accretion. Recently, these observations became feasible. They find density scaling as $\rho \propto r^{-1}$ within the Bondi radius, which is flatter than the expected scaling of $r \propto r^{-3/2}$ (Wang et al., 2013; Russell et al., 2015). Outflows in the form of winds may be the reason for this strong reduction in accretion rate (Li et al., 2013). Consequently, expected fueling due to Bondi accretion are insufficient to power the observed jets in these systems. Theoretically, a contribution from the black hole spin would suffice (Tchekhovskoy and McKinney, 2012). Note, that the electron mean free path in the ICM is then on scales of the Bondi radius, e.g. for NGC 1600 $\lambda_\mathrm{mfp} \approx 0.1\,\mathrm{kpc}$ and $r_\mathrm{B} \sim 0.4\,\mathrm{kpc}$.[4] Therefore, direct treatment of plasma effects becomes necessary, which limits significance of these results. Alternatively, the inflow rate may be significantly increased by cold gas accretion, which is motivated by observations of cold gas found in clusters, which we will discuss next.

2.4.2 Observations of cold filaments

While classical cooling flows are inhibited by AGN feedback, significant quantities of molecular gas, Hα emitting ionized gas and star formation are observed in central galaxies of CC clusters compared

---

[4] The mean free path is given by $\lambda_\mathrm{mfp} \sim \frac{1}{\pi n \ln \Lambda}\left(\frac{k_\mathrm{B}T_\mathrm{e}}{Ze^2}\right)^2 \sim 1.4\times 10^{22}\left(\frac{n}{10^{-3}\,\mathrm{cm}^{-3}}\right)^{-1}\left(\frac{k_\mathrm{B}T_\mathrm{e}}{1\,\mathrm{keV}}\right)^2$ cm. We assume $n = 0.04\,\mathrm{cm}^{-3}$ and $T = 1.1\,\mathrm{keV}$ within the Bondi radius based on Runge and Walker (2021).

to nearby elliptical galaxies (McNamara and Nulsen, 2012). Star formation is observed below an entropy threshold of $K \lesssim 30\,\mathrm{keV\,cm^2}$ or equivalently cooling times of $t_{\mathrm{cool}} \lesssim 5\times10^8\,\mathrm{yr}$ (Cavagnolo et al., 2008). While the origin of this sharp threshold is unclear, it implies a strong link between star formation and the thermodynamics of its atmosphere (Donahue and Voit, 2022).

The morphology of the cold gas ranges from a disky to filamentary appearance extending up to $\sim 70\,\mathrm{kpc}$ from the cluster center with many clusters displaying a combination of both (Russell et al., 2019). Coinciding jets appear to entrain the gas (Dasyra et al., 2015) and uplift it in their wakes (Russell et al., 2016). Cooling ICM gas is assumed to become unstable to the thermal instability (TI), which leads to catastrophic cooling down to observed temperatures. Theoretically, gas with cooling time t_{cool} smaller than its free fall time t_{ff} is volatile to the thermal instability (Mccourt et al., 2012), i.e. $t_{\mathrm{cool}}/t_{\mathrm{ff}} \lesssim 1$. Here, t_{ff} is defined as

$$t_{\mathrm{ff}} = \sqrt{\frac{2r}{g}}, \tag{2.25}$$

where $g = \mathrm{d}\Phi/\mathrm{d}r$ is local acceleration due to gravity. The minimum of this ratio, i.e. $\min(t_{\mathrm{cool}}/t_{\mathrm{ff}})$ should therefore provide insights into the presence of the TI in observed clusters. However, observations find cold gas filaments in clusters with somewhat larger ratios, e.g. $t_{\mathrm{cool}}/t_{\mathrm{ff}} = 8-23$ (Olivares et al., 2019), $t_{\mathrm{cool}}/t_{\mathrm{ff}} = 10-25$ (Pulido et al., 2018) or $t_{\mathrm{cool}}/t_{\mathrm{ff}} = 10-35$ (Hogan et al., 2017). As $t_{\mathrm{cool}}/t_{\mathrm{ff}}$ is computed from projected quantities, local large density perturbations can lead to condensation for larger values of the globally measured $t_{\mathrm{cool}}/t_{\mathrm{ff}}$ (Choudhury et al., 2019). In addition, deprojection effects of X-ray data may lead to overestimation of $t_{\mathrm{cool}}/t_{\mathrm{ff}}$ by a factor of a few (Sarkar et al., 2021). In general, Voit (2021) suggests that observations are only sensitive to the global ratio, which can lead to higher ratios as long as entropy fluctuations lower the ratio locally.

The exact triggering mechanism of the instability remains uncertain. Random motions of overdense/underdense blobs in the gas could locally attain critical values of $t_{\mathrm{cool}}/t_{\mathrm{ff}}$ leading to condensation. On the other hand, purely cooling time in observations by Hogan et al. (2017) seems to govern the onset of thermal instability in their clusters' atmospheres. Therefore, they propose that AGN-driven uplift of partially cooled gas may trigger the instability. The detection of molecular gas preferentially in the wake of bubbles supports this hypothesis (McNamara et al., 2014) (see Figure 2.3). In addition, Martz et al. (2020) analyze a sample of five CC clusters, which lack appreciable Hα and star formation, even though they find ratios of cooling time to freefall time of $20 \lesssim \min(t_{\mathrm{cool}}/t_{\mathrm{ff}}) \lesssim 50$, which is within range quoted above for observed apparently TI unstable clusters. Crucially, they find little indication for the presence of radio bubbles in these clusters, which supports the idea that bubbles are required to form cold gas.

2.4.3 Chaotic cold accretion

The condensing gas is expected to sink to the center of the cluster. Collisions of these cold gas clumps can cause the partial cancellation of angular momentum, which leads to it being eventually accreted by the SMBH. This form of accretion is termed *(chaotic) cold accretion* (CCA) (Gaspari et al., 2013). The gas is assumed to accrete on the free fall time, which gives an accretion rate in the form of

$$\dot{M}_{\mathrm{cold}} = \epsilon \frac{M_{\mathrm{cold}}}{t_{\mathrm{ff}}}, \tag{2.26}$$

where ϵ is a free parameter that captures incomplete momentum cancellation and small scale feedback effects. We implement a model of chaotic cold accretion in AREPO as part of this thesis (see Section 6).

Detailed observations and literature analysis by Mckinley et al. (2022) of the center of Centaurus A find observed feeding of the black hole consistent with simulations of CCA coupled to AGN feedback by Gaspari and Sądowski (2017).

2.4.4 Simulations of self-regulated AGN feedback

To study details of AGN feedback in CC clusters, hydrodynamical simulations are required to follow the evolution of the interplay between accretion and AGN jet feedback. They are generally able to reproduce the main characteristics of observed CC clusters, e.g. thermodynamic profiles in agreement with observed CC clusters (Yang and Reynolds, 2016). In addition, Wang et al. (2020) find that Alfvén heating can balance cooling in clusters. A jet regulated by cold accretion can induce turbulence that is in agreement with velocity measurements by *Hitomi* (Prasad et al., 2018). Interestingly, for sufficiently resolved accretion regions, Bondi and cold accretion appear to give very similar results on simulated scales (Meece et al., 2017). Furthermore, magnetic fields appear crucial in simulations of self-regulated feedback as purely hydrodynamical simulations give rise to unobserved long-lived massive cold disks (Li and Bryan, 2014). Here, the inclusion of magnetic fields leads to stronger coupling between the hot and cold phase through magnetic pressure and tension forces inhibiting formation of such disks (Wang et al., 2021).

2.5 AREPO

We employ the moving-mesh code AREPO (Springel, 2010) that solves the equations of magnetohydrodynamics (MHD) on an unstructured mesh using a finite volume approach. This approach combines the Lagrangian property, most notably present in smoothed particle hydrodynamics (SPH) codes, with features of finite-volume Eulerian mesh codes. This way the user profits from the main advantages of both SPH techniques (e.g., intrinsic adaptivity, low advection errors) and fixed mesh codes (e.g., better convergence for smooth flows, good shock capturing). The code features local timestepping and second order convergence (Pakmor et al., 2016b). In the following, we detail the MHD solver and CR solver of AREPO that are crucial for the simulations performed and analyzed in this thesis.

2.5.1 Magnetohydrodynamic solver

The Euler equations describing ideal MHD can be expressed as a system of hyperbolic conservation laws in the form

$$\frac{\partial \boldsymbol{U}}{\partial t} + \nabla \cdot \boldsymbol{F} = 0, \tag{2.27}$$

where $\boldsymbol{U}$ and $\boldsymbol{F}$ are given by

$$\boldsymbol{U} = \begin{pmatrix} \rho \\ \rho \boldsymbol{v} \\ \rho e \\ \boldsymbol{B} \end{pmatrix} \qquad \boldsymbol{F}(\boldsymbol{U}) = \begin{pmatrix} \rho \boldsymbol{v} \\ \rho \boldsymbol{v}\boldsymbol{v}^{\mathrm{T}} + P\boldsymbol{1} - \boldsymbol{B}\boldsymbol{B}^{\mathrm{T}} \\ \rho e \boldsymbol{v} + P\boldsymbol{v} - \boldsymbol{B}(\boldsymbol{v}\cdot\boldsymbol{B}) \\ \boldsymbol{B}\boldsymbol{v}^{\mathrm{T}} - \boldsymbol{v}\boldsymbol{B}^{\mathrm{T}} \end{pmatrix}. \tag{2.28}$$

Here, $P = P_{\mathrm{gas}} + B^2/2$ is the total gas pressure and $e = u + \frac{1}{2}v^2 + \frac{1}{2\rho}B^2$ is the total energy per unit mass, adopting the Heaviside-Lorentz unit system. The closure is given by the equation of state $P = (\gamma - 1)\rho e$.

The flux is computed across interfaces by solving Riemann problems along the normal of the interface (Pakmor et al., 2011). Time integration is based on Heun's method, which is a second order Runge-Kutta variant. Here, fluxes are estimated by using the values of primitive values both at the beginning and at the end of the timestep. Theoretically, two expensive computations of the original and updated mesh would be required for a single timestep. However, when assuming a constant velocity of the mesh generating points over the timestep, the new mesh can be recycled at the next timestep. Intermediate timesteps are then extrapolated based on spatial derivatives as in a MUSCL-Hancock scheme (Pakmor et al., 2016b). Gradients are estimated by employing a least-square gradient estimate. As values at the center of mass ϕ_i, ϕ_j and distances between a neighbouring pair of cells i, j are known, the method minimizes the error when linearly extrapolating values between all neighbours via the gradient estimates $\langle \nabla\phi \rangle_i, \langle \nabla\phi \rangle_j$ (Pakmor et al., 2016b). A Riemann solver is then used to compute the flux exchanged during a timestep using the Harten-Lax-van Leer-Discontinuities (HLLD) Riemann solver (Miyoshi and Kusano, 2005) as detailed in Pakmor et al. (2011). To correctly capture any signal present in the simulation, the maximum timestep is limited by the maximum signal speed, which corresponds to the fastest magneto-acoustic waves in the system plus the velocity of the cell (when working in the cell frame).

An additional complication arises in MHD solvers as magnetic fields are divergence free, i.e.

$$\nabla \cdot \boldsymbol{B} = 0, \tag{2.29}$$

according to Maxwell's equations. In theory, the MHD equations in differential form introduce no divergence for an initially divergence-free field. However, discretization errors in MHD simulations introduce divergences that have to be addressed. A Powell eight-wave scheme is employed here (Powell et al., 1999). Additional source terms are added to the momentum, induction and energy equation, which encode passive advection of $\nabla \cdot \boldsymbol{B}/\rho$ with the flow. This keeps the divergence error small by suppressing further growth (Pakmor and Springel, 2013).

2.5.2 Cosmic ray solver

As described above, there is strong evidence for the presence of CRs in AGN bubbles. To study their impact on the gas via their pressure and Alfvén heating, we make use of the CR module of AREPO, which will be described in the following. For this, we will describe a treatment of CRs as a fluid first.

Fluid description of CRs

The small scale, continuous scattering of CRs on Alfvén waves (see Section 2.2.4) makes a fluid description possible. The Lorentz force on the gas due to the CR current density can be interpreted as an effective pressure of the CRs exerting force $-\nabla_\perp P_{\mathrm{cr}}$ on the gas (Zweibel, 2013). Analogously to hydrodynamics, the three moments of the CR distribution function f are defined as the CR number density n_{cr}, CR pressure P_{cr} and CR energy density ϵ_{cr}, given by

$$n_{\mathrm{cr}} = 4\pi \int_0^\infty p^2 f_{\mathrm{p}} \mathrm{d}p \tag{2.30}$$

$$P_{\mathrm{cr}} = \frac{4\pi m_{\mathrm{p}} c^2}{3} \int_0^\infty \beta p^3 f_{\mathrm{p}} \mathrm{d}p \tag{2.31}$$

$$\epsilon_{\mathrm{cr}} = 4\pi \int_0^\infty p^2 E_{\mathrm{p}} f_{\mathrm{p}} \mathrm{d}p, \tag{2.32}$$

where $\beta = p/\sqrt{1+p^2}$ is the dimensionless CR velocity and E_{p} is the kinetic energy of a CR particle given by

$$E_{\mathrm{p}}(p) = \left(\sqrt{1+p^2} - 1\right) m_{\mathrm{p}} c^2. \tag{2.33}$$

Closure is provided by the equation of state

$$P_{\mathrm{cr}} = (\gamma_{\mathrm{cr}} - 1)\epsilon_{\mathrm{cr}}, \tag{2.34}$$

where $\gamma_{\mathrm{cr}} = 4/3$ is the CR adiabatic index. With the help of these definitions the evolution equation of the CR energy density can be derived.

First, we multiply Equation (2.16) by E_{p} and integrate over the CR momentum p to obtain (Pfrommer et al., 2017)

$$\frac{\partial \epsilon_{\mathrm{cr}}}{\partial t} + \nabla \cdot \left[(\boldsymbol{v} + \boldsymbol{v}_{\mathrm{st}})(P_{\mathrm{cr}} + \epsilon_{\mathrm{cr}}) - \kappa_\epsilon \boldsymbol{b} (\boldsymbol{b} \cdot \nabla \epsilon_{\mathrm{cr}}) \right] = (\boldsymbol{v} + \boldsymbol{v}_{\mathrm{st}}) \cdot \nabla P_{\mathrm{cr}} + \Gamma_\epsilon + \bar{Q}_\epsilon, \tag{2.35}$$

where κ_{cr} is the momentum-space averaged diffusion coefficient given by

$$\kappa_{\epsilon} = \frac{\int_0^{\infty} p^2 E_{\mathrm{p}}\, \kappa_{\mathrm{p}} \left(\boldsymbol{b} \cdot f_{\mathrm{p}}\right) \mathrm{d}p}{\int_0^{\infty} p^2 E_{\mathrm{p}} \left(\boldsymbol{b} \cdot \nabla f_{\mathrm{p}}\right) \mathrm{d}p} \tag{2.36}$$

$\bar{Q}_{\epsilon}$ is the net source of kinetic energy density of CR defined as

$$\bar{Q}_{\epsilon} = 4\pi \int_0^{\infty} p^2 E_{\mathrm{p}} Q_{\mathrm{p}} \mathrm{d}p \tag{2.37}$$

and Γ_{cr} is the energy gain per unit time of CRs due to second-order Fermi acceleration

$$\Gamma_{\epsilon} = -4\pi m_{\mathrm{p}} c^2 \int_0^{\infty} \beta p^2 \Gamma_{\mathrm{p}} \frac{\partial f_{\mathrm{p}}}{\partial p} \mathrm{d}p > 0 \quad \text{for} \quad \frac{\partial f_{\mathrm{p}}}{\partial p} < 0. \tag{2.38}$$

The second term on the left hand-side of Equation (2.35) can be interpreted as the advective transport of the CR enthalpy ($H_{\mathrm{cr}} = P_{\mathrm{cr}} + \epsilon_{\mathrm{cr}}$) with total velocity ($\boldsymbol{v} + \boldsymbol{v}_{\mathrm{st}}$) and anisotropic diffusive transport of CR energy density. The right-hand side captures (from left to right) the volume work of the CR pressure gradient on the background plasma ($\boldsymbol{v} \cdot \nabla P_{\mathrm{cr}}$) and generation of Alfvén waves ($\boldsymbol{v}_{\mathrm{st}} \cdot \nabla P_{\mathrm{cr}}$). Γ_{ϵ} corresponds to the energy gain of CRs due to second-order Fermi acceleration and $\bar{Q}_{\epsilon} = \Gamma_{\mathrm{cr}} + \Lambda_{\mathrm{cr}}$ encompasses additional gains and losses of CR energy density.

Implementation in AREPO

The main implementation details of CRs in AREPO are described in Pfrommer et al. (2017), while the modeling of CR diffusion is explained in Pakmor et al. (2016a). The module focuses on (energetically dominant) $\sim$ 1GeV CRs and therefore evolves purely their energy density without further spectral information.

To incorporate CRs into the code, the Euler equations are, analogously to the MHD implementation, expressed as a system of hyperbolic conservation laws including a source term:

$$\frac{\partial \boldsymbol{U}'}{\partial t} + \nabla \cdot \boldsymbol{F}' = \boldsymbol{S}, \tag{2.39}$$

where conserved variable $\boldsymbol{U}'$, flux function $\boldsymbol{F}'(\boldsymbol{U}')$ and source term $\boldsymbol{S}$ are given by

$$\boldsymbol{U}' = \begin{pmatrix} \rho \\ \rho \boldsymbol{v} \\ \epsilon \\ \epsilon_{\mathrm{cr}} \\ \boldsymbol{B} \end{pmatrix}, \quad \boldsymbol{F}' = \begin{pmatrix} \rho \boldsymbol{v} \\ \rho \boldsymbol{v}\boldsymbol{v}^{\mathrm{T}} + P\mathbf{1} - \boldsymbol{B}\boldsymbol{B}^{\mathrm{T}} \\ (\epsilon + P)\boldsymbol{v} - \boldsymbol{B}(\boldsymbol{v} \cdot \boldsymbol{B}) \\ \epsilon_{\mathrm{cr}} \boldsymbol{v} + (\epsilon_{\mathrm{cr}} + P_{\mathrm{cr}})\boldsymbol{v}_{\mathrm{st}} - \kappa_{\epsilon} \boldsymbol{b}(\boldsymbol{b} \cdot \nabla \epsilon_{\mathrm{cr}}) \\ \boldsymbol{B}\boldsymbol{v}^{\mathrm{T}} - \boldsymbol{v}\boldsymbol{B}^{\mathrm{T}} \end{pmatrix}, \quad \boldsymbol{S} = \begin{pmatrix} 0 \\ \mathbf{0} \\ P_{\mathrm{cr}} \nabla \cdot \boldsymbol{v} - \boldsymbol{v}_{\mathrm{st}} \cdot \nabla P_{\mathrm{cr}} + \Lambda_{\mathrm{th}} + \Gamma_{\mathrm{th}} \\ -P_{\mathrm{cr}} \nabla \cdot \boldsymbol{v} + \boldsymbol{v}_{\mathrm{st}} \cdot \nabla P_{\mathrm{cr}} + \Lambda_{\mathrm{cr}} + \Gamma_{\mathrm{cr}} \\ \mathbf{0} \end{pmatrix}, \tag{2.40}$$

where the adopted system of units is Heaviside-Lorentz. P is the total pressure, i.e.

$$P = P_{\mathrm{th}} + P_{\mathrm{cr}} + \frac{\boldsymbol{B}^2}{2}. \tag{2.41}$$

ϵ corresponds to the total energy density *excluding* CRs given by

$$\epsilon = \epsilon_{\mathrm{th}} + \frac{\rho \boldsymbol{v}^2}{2} + \frac{\boldsymbol{B}^2}{2}. \tag{2.42}$$

Analogously to the MHD solver, the Euler equations are solved by reconstructing the primitive variables at cell interfaces via Runge-Kutta time integration and least-square gradient estimates (Pakmor et al., 2016b). The exchanged fluxes across an interface are obtained by employing the Harten-Lax-van Leer-Discontinuities (HLLD) Riemann solver Pakmor et al. (2011). Concerning the maximum timestep in the simulation, we need to account for the newly introduced effective adiabatic index γ_{eff}, where $\gamma_{\mathrm{eff}}P = \gamma_{\mathrm{th}}P_{\mathrm{th}} + \gamma_{\mathrm{cr}}P_{\mathrm{cr}}$, which modifies the speed of fast and slow magneto-acoustic modes.

Studies that are part of this thesis and include CRs (Ehlert et al., 2018, 2019) emulate streaming via anisotropic CR diffusion and Alfvén heating (Sharma et al., 2009). As discussed in Sharma et al. (2009), pitch angle scattering of CRs limits their drift velocity to the Alfvén speed, i.e. $v_{\mathrm{d}} - v_{\mathrm{A}} = c^2/\nu L_{\mathrm{cr}}$, where $L_{\mathrm{cr}} = P_{\mathrm{cr}}/\nabla P_{\mathrm{cr}}$ is the CR gradient length and ν is the CR pitch-angle scattering rate (Kulsrud, 2005). In addition, CRs diffuse along magnetic field lines with diffusion coefficient $\tilde{\kappa} = c^2/(3\nu) \sim (v_{\mathrm{s}} - v_{\mathrm{A}})L_{\mathrm{cr}}$, which makes the effect of diffusion negligible compared to streaming in the strong scattering limit. Here, an effective diffusion coefficient can be approximated as $\kappa_{\mathrm{cr,A}} \sim L_{\mathrm{cr}}v_{\mathrm{A}}$. The inclusion of explicitly streaming CRs (Thomas and Pfrommer, 2019) is left for future work.

The CR energy density equation is solved by passively advecting CR energy density with the flow. In addition, the adiabatic source term $P_{\mathrm{cr}}\nabla\cdot\boldsymbol{v}$ is calculated by employing Gauss' divergence theorem and exchanging respective fluxes across interfaces. Non-adiabatic source terms and active CR transport are treated after evolving the homogeneous system by one timestep via the so called method of operator splitting. First, we account for CR diffusion followed by computing hadronic and Coulomb losses (Pfrommer et al., 2017). We now summarize implementation details of CR diffusion. Followed by some details on the computation of CR losses.

Anisotropic diffusion

The equations governing CR diffusion are usually solved with an explicit time-integration scheme (Booth et al., 2013; Hanasz et al., 2013). In the case of CR diffusion, these suffer from severely limiting timestep sizes that scale quadratically with linear dimension of a resolution element. Therefore a semi-implicit solver motivated by Sharma and Hammett (2011) is employed. To avoid expensive global timesteps, the scheme is adopted for local timesteps. In addition, the solver ensures that CR only diffuse from high abundance to low abundance regions in agreement with the entropy condition $\Delta S \gtrsim 0$ by employing a flux limited scheme as suggested in Sharma and Hammett (2007). Implementation details are given in Pakmor et al. (2016a), which include required adaptations for unstructured moving meshes. A brief overview follows.

The part of the evolution equation of CR energy density governing CR diffusion is given by

$$\frac{\partial \epsilon_{\mathrm{cr}}}{\partial t} - \nabla\cdot\left[\kappa_\epsilon \boldsymbol{b}(\boldsymbol{b}\cdot\nabla\epsilon_{\mathrm{cr}})\right] = 0. \tag{2.43}$$

We integrate over the volume and apply Gauss' theorem to obtain (in discretized form)

$$\frac{\partial \epsilon_{\mathrm{cr},i}}{\partial t} - \frac{1}{V_i}\sum_j \kappa_{ij}\left(\boldsymbol{b}_{ij}\cdot\nabla\epsilon_{\mathrm{cr},ij}\right)\boldsymbol{b}_{ij}\cdot\boldsymbol{n}_{ij}A_{ij} = 0, \tag{2.44}$$

where the sum runs over all interfaces j of cell i, $\boldsymbol{n}$ is the normal vector of the interface and A_{ij} is its area. Solving this equation, requires knowledge of the magnetic field and CR gradient at the interface. For this, gradients of quantities are estimated first at cell corners by using least-square fits to interpolate/extrapolate values and corresponding gradients from values given at the center of mass of adjacent cells. Here, *extrapolation* is unstable and requires special treatment as discussed below. Values at interfaces are then generally computed via weighted averages (Pakmor et al., 2016a). The magnetic field is computed following the outlined procedure.

The calculation of the CR energy density gradient is done separately for the part of the gradient that lies normal to the surface of the interface $\nabla\epsilon_{\mathrm{cr,n}}$ and the part parallel to the interface. The parallel component is again split while only the component that is parallel to the magnetic field in the interface $\nabla\epsilon_{\mathrm{cr,t}}$ is retained as the perpendicular component cancels out. $\nabla\epsilon_{\mathrm{cr,t}}$ is estimated from values of all corners that were not previously marked as problematic (where extrapolation was required). To ensure that CRs only diffuse from regions with higher CR energy density to lower CR energy density, $\nabla\epsilon_{\mathrm{cr,t}}$ is limited by a generalized van Leer limiter (van Leer, 1984).

On the other hand, two different methods exist to compute the gradient directed normal to the interface $\nabla\epsilon_{\mathrm{cr,n}}$. The simple normal gradient is estimated by interpolating from the values at the center of mass of both neighbouring cells only. If the position of center of mass and mesh-generating point overlap, this estimate is quite accurate. However, in general this method will slightly underestimate the true normal gradient. The full normal gradient is estimated analogously to the magnetic field by taking weighted averages of the interpolated value estimates at the corners. Here, extrapolated values are replaced with the simple normal gradient estimate.

Time integration is done separately for fluxes associated with the two CR gradient components $\nabla\epsilon_{\mathrm{cr,n}}$ and $\nabla\epsilon_{\mathrm{cr,t}}$. The non-linearity inherent in the computation of $\nabla\epsilon_{\mathrm{cr,t}}$ necessitates the usage of a explicit time integration. Thus, CR energy with fluxes associated with gradients in the interface are advanced with an explicit Euler time integrator. In a second step, CR energy with fluxes associated with gradients normal to the interface are advanced with an implicit backward Euler scheme. Consequently, the method is termed semi-implicit time integration and allows solving CR diffusion on a local timestep (Pakmor et al., 2016a).

Collisional loss processes

CRs propagating through a plasma lose energy during high impact parameter interaction with thermal electrons and excitations of quantized plasma oscillations in low impact interactions. The later also lead to a transfer of CR energy to the thermal gas. These two loss terms are summarized as Coulomb losses. In addition, CRs collide inelastically with thermal protons to produce pions and heat the gas in the process. These processes are referred to as hadronic losses.

Hadronic losses only affect the high-momentum regime and are then approximately independent of momentum, which leaves the CR spectrum largely invariant. On the other hand, Coulomb losses increase for decreasing CR momenta and more strongly affect CRs with small momenta. Consequently, a spectral treatment is required. Here, we compute an equilibrium distribution of CRs where CR injection balances both forms of losses. This is valid on timescales that are longer than timescales of considerable variability during the injection process (Pfrommer et al., 2017). In the following, we briefly summarize the derivation of this equilibrium CR distribution.

The kinetic energy loss of a proton with $\gamma \ll m_{\mathrm{p}}/m_{\mathrm{e}}$ due to Coulomb losses is given by (Gould, 1972)

$$-\left(\frac{\mathrm{d}E_{\mathrm{p}}(p)}{\mathrm{d}t}\right)_{\mathrm{Coul}} = \frac{4\pi e^4 n_{\mathrm{e}}}{m_{\mathrm{e}}\beta c}\left[\ln\left(\frac{2m_{\mathrm{e}}c^2\beta p}{\hbar\omega_{\mathrm{pl}}}\right) - \frac{\beta^2}{2}\right] \equiv \frac{A_{\mathrm{Coul}}}{\beta}, \tag{2.45}$$

where $\omega_{\mathrm{pl}} = \sqrt{4\pi e^2 n_{\mathrm{e}}/m_{\mathrm{e}}}$ is the plasma frequency. To ease computation of the CR equilibrium distribution later, the term βp in the Coulomb logarithm is replaced by its mean value for the spectrum $\langle\beta p\rangle = 3P_{\mathrm{cr}}/(m_{\mathrm{p}}c^2 n_{\mathrm{rc}})$. Additionally, a CR cooling timescale due to Coulomb losses is defined as

$$\tau_{\mathrm{cr}} = \frac{\epsilon_{\mathrm{cr}}}{|\mathrm{d}\epsilon_{\mathrm{cr}}/\mathrm{d}t|_{\mathrm{Coul}}}. \tag{2.46}$$

CR protons that exceed the kinematic threshold of $p_{\mathrm{thr}}m_{\mathrm{p}}c = 0.78$ GeV/c collide inelastically with thermal protons to mainly form pions. Neutral pions decay to gamma rays whereas charged particles produce pions that decay into secondary electrons, positrons and neutrinos as detailed in Equation (2.6). About 1/6 of the energy of these charged pions ends up in secondary electrons and positrons. The hadronic losses of the CR population is independent of the exact CR proton momentum and given by

$$-\left(\frac{\mathrm{d}E_{\mathrm{p}}}{\mathrm{d}t}\right)_{\mathrm{hadr}} = n_{\mathrm{N}}\sigma_{\mathrm{pp}}K_{\mathrm{p}}m_{\mathrm{p}}c^3(\gamma-1)\theta(p-p_{thr}) \equiv A_{\mathrm{hadr}}(\gamma-1)\theta(p-p_{\mathrm{thr}}), \tag{2.47}$$

where $\sigma_{\mathrm{pp}} = 44.2\,\mathrm{mbarn}$ is the total pion cross section (Pfrommer and Enßlin, 2004) (assuming a CR distribution with spectral index $\alpha = 2.2$), K_{p} is the inelasticity of the hadronic reaction (Mannheim and Schlickeiser, 1994) and $n_{\mathrm{N}} = n_{\mathrm{e}}/(1 - X_{\mathrm{He}}/2)$ is the target nuclear density in the ICM assuming a primordial composition of $X_{\mathrm{He}} = 0.24$. The Heaviside distribution θ is unity for positive values of its argument and zero otherwise. The respective CR cooling timescale due to hadronic losses is then given by

$$\tau_{\mathrm{hadr}} \equiv \frac{\epsilon_{\mathrm{cr}}}{|\mathrm{d}\epsilon_{\mathrm{cr}}/\mathrm{d}t|_{\mathrm{hadr}}}. \tag{2.48}$$

To compute the Coulomb and hadronic loss rates, we estimate an equilibrium spectrum. We look for steady solutions of the Fokker Planck equation, i.e. $\partial f/\partial t = 0$, governing the evolution of the CR spectrum by considering (i) injection due to a power law spectrum in momentum, (ii) hadronic and Coulomb losses and (iii) CR energy escape from the system. By assuming a sufficiently extended environment, we can neglect energy escape from the system. In addition, hadronic and Coulomb losses are assumed to occur continuously on timescales τ_{hadr} and τ_{Coul}, rather than catastrophically. Finally, hadronic and Coulomb losses are neglected in the low- and high-momentum regimes, respectively. This results in a CR steady-state equilibrium spectrum for both regimes. They are combined asymptotatically at the intersection momentum where hadronic and Coulomb losses match to obtain the final CR spectrum.

We then compute the corresponding equilibrium hadronic and Coulomb loss rates Λ_{hadr} and Λ_{Coul}, respectively. The CR energy density is depreciated due to these losses as

$$\frac{\mathrm{d}\epsilon_{\mathrm{cr}}}{\mathrm{d}t} = \Lambda_{\mathrm{hadr}} + \Lambda_{\mathrm{Coul}} = -\lambda_{\mathrm{cr}} n_{\mathrm{e}} \epsilon_{\mathrm{cr}}, \tag{2.49}$$

or equivalently

$$E_{\mathrm{cr}}(t) = E_{\mathrm{cr}}(t_0)\mathrm{e}^{-\lambda_{\mathrm{cr}} n_e t}, \tag{2.50}$$

where $\lambda_{\mathrm{cr}} = 1.022 \times 10^{-15}\,\mathrm{cm}^3\,\mathrm{s}^{-1}$ (Pfrommer et al., 2017).

Finally, we need to compute the gains of the thermal gas due to these collisional loss processes. Coulomb interactions lead to the acceleration of thermal particles. Therefore, Coulomb losses are completely transformed into heating of the gas. On the other hand, most hadronic losses escape the system in the form of gamma rays and neutrinos. Only 1/6 of the remaining energy ends up in secondary electrons whose fate depends on the electrons' Lorentz factor. Mildly relativistic electrons with $\gamma_{\mathrm{e}} \lesssim 200$ eventually thermalize their energy via Coulomb collisions while losses of highly relativistic electrons with $\gamma_{\mathrm{e}} \gtrsim 1000$ are dominated by synchrotron emission and Compton scattering. The mean energy of secondary electrons in hadronic processes is $\langle E_{e^\pm} \rangle = m_{\pi^\pm} c^2/4 = 35$ MeV $= 68\, m_{\mathrm{e}} c^2$, which means that losses due to Coulomb collisions dominate. Therefore, the collisional heating rate is given by $\Gamma_{\mathrm{th}} = -\Lambda_{\mathrm{Coul}} - \Lambda_{\mathrm{hadr}}/6 = \lambda_{\mathrm{th}} n_e \epsilon_{\mathrm{cr}}$, which results in a gain of thermal energy in the form

$$E_{\mathrm{th}}(t) = E_{\mathrm{cr}}(t_0)\left(1 - \mathrm{e}^{-\lambda_{\mathrm{th}} n_e t}\right), \tag{2.51}$$

where $\lambda_{\mathrm{th}} = 4.02 \times 10^{-16}\,\mathrm{cm}^3\,\mathrm{s}^{-1}$.

By definition, this description is valid if CR injection balances non-adiabatic cooling processes. In addition, it provides a good approximation for freely cooling CRs in the absence of injection at late times. However, deviations from equilibrium will introduce errors. Especially for a fresh CR injection event, where initial Coulomb losses are expected to be substantially higher than captured by the outlined treatment (Pfrommer et al., 2017). Here, spectral treatment of CR protons is required in space and time as in Girichidis et al. (2020), which is deferred to future work.

2.6 Thesis overview

This thesis focuses on studying different aspects of AGN jet feedback in CC clusters. These are

- details of CR heating by a single jet injection event in Chapter 3 published as Ehlert et al. (2018). In addition, we study the effect of magnetic fields on bubble stability. The conception of the study was developed by CP, RW and me. The setup for the simulation was done by myself and RW. I ran the simulations, analyzed them and prepared the manuscript. CP and RW assisted with the preparation of the manuscript. All contributed to the discussion and interpretation.

- testing modeling assumptions of jet inflated bubbles to constrain bubble composition with observations of the Sunyaev-Zel'dovich effect in Chapter 4 published as Ehlert et al. (2019). The conception of the study was developed by CP and me. The setup for the simulation was done by myself and RW. I ran the simulations and analyzed them. The analysis was partly based on old script from a former study of CP (Pfrommer et al., 2005). I prepared the manuscript. CP and RW assisted with the preparation of the manuscript. All contributed to the discussion and interpretation.

- demonstrating the link between magnetic and velocity structures to encourage the usage of numerical simulations to exploit this relation in their respective observables in Chapter 5 published as Ehlert et al. (2021). The conception of the study was developed by CP, RW and me. The setup for the simulation was done by myself. I ran the simulations and analyzed them. The mock X-ray observations with XRISM were performed by RW. I prepared the manuscript. CP and RW assisted with the preparation of the manuscript. All contributed to the discussion and interpretation.

- implementation of cold accretion in AREPO to study the dependence of accretion model, jet efficiency and jet density on simulations of self-regulated feedback in Chapter 6 submitted to MNRS and posted on arXiv as Ehlert et al. (2022). The conception of the study was developed by CP, RW and me. The setup for the simulation was done by myself. I implemented the new accretion model, ran the simulations, analyzed them and prepared the manuscript. CP and RW assisted with the preparation of the manuscript. All contributed to the discussion and interpretation.

Simulations of the dynamics of magnetised jets and cosmic rays in galaxy clusters

3

This chapter is an adapted version of the paper *Simulations of the dynamics of magnetised jets and cosmic rays in galaxy clusters* published as Ehlert et al. (2018).

Part of this work has been presented in my master thesis (Ehlert, 2017). However, substantial additional work detailed in the following was required before publication. The master thesis analyses the influence of jet power and lifetime on jet morphology, stability and resulting CR distribution. However, we realized that the jet energy is the crucial parameter while finishing up the thesis. To make this a main point in our paper, all simulations had to be rerun with refined parameters and analyzed. Most figures had to be redesigned from scratch to fit this new focus. Generally, we added a subset of runs with a ten times higher mass resolution than previously published in the master thesis, which required extensive testing. In addition, we added an analysis of our CR distributions with regard to varying the acceleration threshold and jet energies to the appendix.

3.1 Abstract

Feedback processes by active galactic nuclei in the centres of galaxy clusters appear to prevent large-scale cooling flows and impede star formation. However, the detailed heating mechanism remains uncertain. One promising heating scenario invokes the dissipation of Alfvén waves that are generated by streaming cosmic rays (CRs). In order to study this idea, we use three-dimensional magneto-hydrodynamical simulations with the AREPO code that follow the evolution of jet-inflated bubbles that are filled with CRs in a turbulent cluster atmosphere. We find that a single injection event produces the CR distribution and heating rate required for a successful CR heating model. As a bubble rises buoyantly, cluster magnetic fields drape around the leading interface and are amplified to strengths that balance the ram pressure. Together with helical magnetic fields in the bubble, this initially confines the CRs and suppresses the formation of interface instabilities. But as the bubble continues to rise, bubble-scale eddies significantly amplify radial magnetic filaments in its wake and enable CR transport from the bubble to the cooling intracluster medium. By varying the jet parameters, we obtain a rich and diverse set of jet and bubble morphologies ranging from Fanaroff-Riley type I-like (FRI) to FRII-like jets. We identify jet energy as the leading order parameter (keeping the ambient density profiles fixed), whereas jet luminosity is primarily responsible for setting the Mach numbers of shocks around FRII-like sources. Our simulations also produce FRI-like jets that inflate bubbles without detectable shocks and show morphologies consistent with cluster observations.

3.2 Introduction

The hot, X-ray emitting gas in cool-core (CC) clusters is expected to cool on time scales $\lesssim 1$ Gyr. The absence of observed large-scale cooling flows and low star formation rates suggests an efficient heating process that balances cooling (Peterson and Fabian, 2006). The observed X-ray cavities in the centres of clusters, which correspond to low density, hot bubbles inflated by jets from active galactic nuclei (AGN), contain sufficient energy to heat the intracluster medium (ICM, Bîrzan et al., 2004, 2008). The correlation between jet power and cluster cooling rate supports the now established idea of heating through an AGN that is powered by a supermassive black hole (SMBH) found in the centre of every cluster (McNamara and Nulsen, 2007, 2012). The exact mechanisms by which AGNs heat clusters in a volume-filling fashion remains however unclear.

Proposed models for heating clusters include AGN-initiated weak shocks (Fabian et al., 2003; Li et al., 2017; Martizzi et al., 2019a), sound waves (Sanders and Fabian, 2008; Fabian et al., 2017), gravity waves (Reynolds et al., 2015; Bambic et al., 2018a), or mixing of hot bubble material with the ambient medium (Hillel and Soker, 2016). Thermal conduction is likely relevant in the outskirts of the cluster core but is locally unstable to thermal perturbations (Kim and Narayan, 2003; Soker, 2003) and thus unable to provide the global solution. However, anisotropic thermal conduction renders the ICM unstable to thermal buoyancy instabilities (in particular the heat-flux driven instability in the core region of CC clusters, Quataert, 2008), facilitating mixing of the AGN energy input and thereby increasing the coupling efficiency of feedback energy (Yang et al., 2016; Kannan et al., 2017). Earlier models that suggest energy dissipation of strong shocks and turbulence volumetrically are challenged by velocity measurements of the X-ray satellite *Hitomi*. *Hitomi* inferred velocities in the ICM of the Perseus cluster of $\approx 150\ \mathrm{km\ s^{-1}}$ (Hitomi Collaboration, 2016). Kinetic energy is quickly dissipated before it could reach cooling regions that are distant from the bubbles (Fabian et al., 2017).

As lobes of FRI-type jets (Fanaroff and Riley, 1974) rise buoyantly in the CC cluster atmosphere, their pressure content reaches equilibrium with the ambient ICM. These lobes contain at most a small admixture of thermal pressure, implying a dominant non-thermal pressure component with CR protons being the likely candidate (e.g., Morganti et al., 1988; Croston et al., 2008, 2018). After CRs have diffused from the lobes into the ICM, these CRs can excite Alfvén waves via the streaming instability (Kulsrud and Pearce, 1969; Zweibel, 2013). The process of scattering on the waves confines the CR population to move macroscopically close to the Alfvén speed in the ICM (Wiener et al., 2013). The dissipation of the Alfvén waves through damping processes such as non-linear Landau or turbulent damping effectively transfers CR energy to thermal heat (Wentzel, 1971; Guo and Oh, 2008). This provides a promising alternative heating mechanism in CC clusters (Loewenstein et al., 1991; Guo and Oh, 2008; Pfrommer, 2013). Assuming steady state, a combination of central CR heating and thermal conduction at larger radii can balance radiative cooling in a large sample of CC clusters, suggesting a stable, self-regulated cycle of CR heating and radiative cooling (Jacob and Pfrommer, 2017a,b). Idealised three-dimensional (3D) simulations show that self-regulated CR feedback can smoothly heat the centres of clusters (Ruszkowski et al., 2017). The model depends crucially on the interplay between CR transport and AGN bubble dynamics.

Simulations of AGN bubbles are able to reproduce the general morphology of observed X-ray cavities (e.g., Churazov et al., 2001; Reynolds et al., 2001; Brüggen and Kaiser, 2001) and explain the absence of radio synchrotron emission of so called ghost cavities (Enßlin and Brüggen, 2002; Brüggen et al., 2002). In these earlier simulations, the bubbles are modelled as low-density cavities. Subsequent hydrodynamical (HD) simulations started inflating bubbles self-consistently via a subgrid jet model (Sternberg and Soker, 2008b). On these scales, the jet is assumed to be sufficiently slow such that non-relativistic HD can be used (but see Perucho et al., 2017). A propagating jet introduces significant heating through the dissipation of the accompanying bow shock (e.g., Reynolds et al., 2002; Brüggen and Kaiser, 2002).

However, first simulations showed a discrepancy between short disruption times of HD bubbles (Churazov et al., 2001; Brüggen et al., 2002) and observed long-lived bubbles in the outskirts of cluster cores (e.g., Fabian et al., 2000, 2011a). The issue can be alleviated with the addition of viscosity (Reynolds et al., 2005; Sijacki and Springel, 2006), magnetic fields (Ruszkowski et al., 2007; Bambic et al., 2018a), or modelling the stage of bubble inflation (Sternberg and Soker, 2008b). Jets dominated by kinetic energy form radially elongated cavities at large radii. This is in contrast to observed, light jets that are energetically dominated by CRs and lose momentum more quickly because of the lower jet inertia. The CR pressure causes the jet to expand laterally and to displace more ICM at smaller cluster-centric radii, naturally producing wider cavities near cluster centres in agreement with X-ray observations (Sijacki et al., 2008; Guo and Mathews, 2011). This holds when CR diffusion is added (Ruszkowski et al., 2008). Lobes inflated by jets in cosmological cluster simulations show deviations from the initial jet axis due to bulk motions of the ICM and substructure (Heinz et al., 2006; Morsony

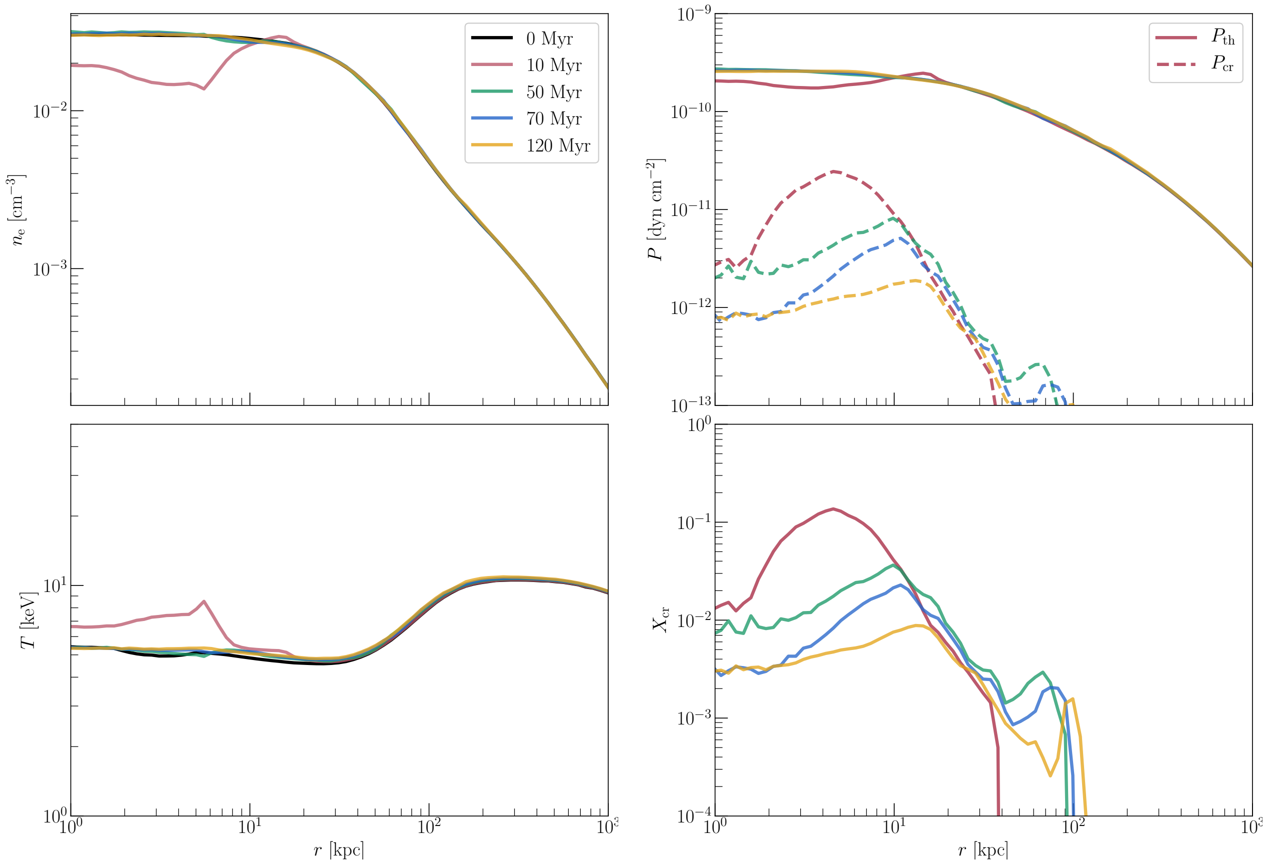

Figure 3.1: Radial profiles of the gas for the initial conditions at 0 Myr (black) and the fiducial model at stated times. The number density n_e is volume-weighted, the temperature T is mass-weighted and the CR pressure P_{cr} as well as the thermal pressure P_{th} are both volume-weighted. The CR-to-thermal pressure ratio X_{cr} is obtained by dividing both volume-weighted quantities. The propagating jet is visible as a low-density and hot feature close to the cluster centre at 10 Myr. The CRs are distributed within the inner 100 kpc and their profile drops off steeply at larger radii.

et al., 2010; Mendygral et al., 2012).

To explore the feasibility of Alfvén-wave heating in CC clusters, we simulate a single AGN jet event leading to the formation and evolution of CR-filled bubbles in a turbulent, magnetised ICM. We focus on the resulting CR distribution due to anisotropic diffusion as well as on the consequences for cluster magnetic fields. By varying jet power and lifetime, we study general trends of the CR distribution, lobe morphology and mixing efficiency.

The outline of our paper is as follows: in Section 3.3, we describe our initial conditions, numerical modelling, and detail the different types of simulations. The general evolution of the jet and subsequent formation of the bubble is analysed in Section 3.4. In Section 3.5, we discuss the stabilisation of the bubble due to magnetic fields and the influence of the bubble on the external magnetic fields and mixing efficiency. The CR distribution and relevance of Alfvén heating is the topic of Section 3.6. In Section 3.7, we focus on the influence of jet power and jet lifetime on bubble morphology, magnetic field structure and CR distribution, in particular in light of the FRI/FRII dichotomy. We briefly summarise our results in Section 3.8. In Appendix 3.9.1, we detail our procedure for generating turbulent magnetic fields. Finally, in Appendices 3.9.2 and 3.9.3, we perform a resolution study and assess how varying parameters of our subgrid CR cooling models impact our results.

3.3 Methods and simulation models

Here, we introduce our numerical set-up of the cluster model and the adopted magnetic structure of the ICM. We employ magneto-hydrodynamical (MHD) simulations with the moving-mesh code AREPO (Springel, 2010) that evolves thermodynamic quantities of the gas on an unstructured moving mesh defined by the Voronoi tessellation of a set of discrete points that initially obey a quasi-Lagrangian distribution. Of particular importance for this work are our models for launching AGN jets and CR transport, which we describe in detail here. An overview of our simulation models closes this section.

3.3.1 Initial conditions

By analogy with Weinberger et al. (2017), we model the cluster density distribution with a Navarro-Frenk-White (NFW) profile (Navarro et al., 1996, 1997) with virial radius[1] $R_{200,\mathrm{c}} = 2.12$ Mpc, virial mass $M_{200,\mathrm{c}} = 10^{15}\ \mathrm{M}_\odot$, and concentration parameter $c_\mathrm{NFW} = 5$. The electron number density n_e is modelled after the Perseus galaxy cluster and based on a double-beta profile fit to the de-projected density distribution from X-ray observations (Churazov et al., 2003). In addition, the number density is scaled in order to retain a gas fraction of 16% within $R_{200,\mathrm{c}}$:

$$\begin{aligned} n_\mathrm{e} = 26.9\times10^{-3}\left[1+\left(\frac{r}{57\ \mathrm{kpc}}\right)^2\right]^{-1.8}\ \mathrm{cm}^{-3} \\ +\, 2.8\times10^{-3}\left[1+\left(\frac{r}{200\ \mathrm{kpc}}\right)^2\right]^{-0.87}\ \mathrm{cm}^{-3}. \end{aligned} \tag{3.1}$$

The pressure in each cell is obtained from the assumption of hydrostatic equilibrium and the restriction that the pressure vanishes at a radius of 3 Mpc. Initially, we adopt a Cartesian mesh with a box size of 1.5 Mpc that we iteratively refine to ensure similar mass content per cell. This yields an adaptive mesh with smoothly increasing cell sizes towards larger radii.

Gravity is treated as a static background provided by a NFW dark matter distribution, neglecting the effects of self-gravity and the gravitational interactions with the SMBH. We show radial profiles of the initial conditions of the electron number density n_e, temperature T, and thermal pressure P_th in Fig. 3.1 (note that there are no CRs in the initial conditions).

To mimic a realistic ICM, we generate a Gaussian-distributed, turbulent magnetic field $\boldsymbol{B}$ (see Appendix 3.9.1, for details). First, we lay down our initial magnetic field on a Cartesian mesh, which needs to have a resolution that is smaller than the smallest (Lagrangian) cell size of our high-resolution initial conditions, $\Delta x = 700$ pc.[2] Fourier transforming such a large Cartesian grid is numerically not feasible. Thus, for our high-resolution simulation we set up three nested meshes, with resolutions decreasing from the cluster centre. Generally, the magnetic field meets the following requirements:

1. $\boldsymbol{B}$ is divergence-free: $\nabla\cdot\boldsymbol{B} = 0$;
2. $\boldsymbol{B}$ follows a Kolmogorov spectrum in the inertial range for wave numbers larger than the injection scale k_inj, and a random white noise power spectrum for $k < k_\mathrm{inj}$;
3. $\boldsymbol{B}^2$ is scaled at each radius to obtain a constant average magnetic-to-thermal pressure ratio of $X_{B,\mathrm{ICM}}$;
4. $\boldsymbol{B}$ fields on different nested meshes do not interconnect.

The resulting cluster magnetic field is then interpolated from this nested mesh onto our adaptive, smoothly varying mesh. To ensure pressure equilibrium in the initial conditions, we adopt temperature fluctuations of the form $nk_\mathrm{B}\delta T = -\delta\boldsymbol{B}^2/(8\pi)$. We then relax our mesh to obtain a computationally more efficient non-degenerate tessellation structure for AREPO. However, this setup does not balance the magnetic tension. The resulting turbulent motions initiate the decay of magnetic power. To

---

[1] We define the virial cluster radius as the radius at which the mean interior density equals 200 times the critical density of the universe today.

[2] Note that the cells in the AGN lobe have a super-Lagrangian resolution with typical grid-size $V^{1/3} = \Delta x = 188$ pc in our highest resolution simulations.

reinitialize the prescribed magnetic-to-thermal pressure ratio, we rescale the temperature as well as the magnetic field to the desired initial magnetic-to-thermal pressure ratio $X_{B,\mathrm{ICM}}$ while maintaining hydrostatic equilibrium.

The described procedure generates our initial conditions for simulations with a turbulent magnetic field. The initiated turbulence during the relaxation of the mesh initiates bulk velocities, which remain part of the initial conditions. For our comparison simulations without a magnetic field, we proceed as before, but set $\boldsymbol{B} = \mathbf{0}$. Thus, the atmosphere remains turbulent through the presence of initial flows and pressure irregularities. However, these runs show a lower degree of turbulence than the runs with finite magnetic field as the magnetic tension can drive and sustain turbulence on longer time scales.

As explained above, the stresses of the tangled magnetic field induce turbulent gas motions. In the absence of a driver of turbulence (as in our simulations) the turbulence gradually dissipates and the magnetic field strength and gas velocities decrease as a function of time.

3.3.2 Jet model

To study the influence of a SMBH-driven and CR-filled jet in a turbulent cluster environment, we employ the jet model of Weinberger et al. (2017). Here, we provide a brief summary of the implementation and describe modifications related to CR acceleration, CR cooling and the magnetic isolation of the injection region.

The jet becomes active at time t after the last injection event at t_{inj} when the available energy to the jet, $\dot{E}_{\mathrm{jet}}(t - t_{\mathrm{inj}})$, exceeds the required energy to redistribute the gas considering adiabatic changes and inject a predefined amount of energy (thermal and non-thermal). When the jet is active, the model identifies two opposing jet regions close to the black hole. A low density state ($\rho_{\mathrm{jet}}/\rho_{\mathrm{ICM}} \sim 10^{-4}$) is set up in pressure equilibrium with the surrounding medium. Mass and thermal energy are redistributed to and from neighbouring cells to ensure mass conservation. If desired, a magnetic field is included in a purely toroidal configuration. Due to gas flows in the bubble, the magnetic field is reshaped, but maintains its helical morphology. After accounting for adiabatic losses, the remaining jet energy is injected as kinetic energy to launch a bipolar outflow. To identify the bubble, an advective scalar X_{jet} is used, which corresponds to the mass fraction of the jet material in the cell. In the remainder of this work we refer to X_{jet} as jet tracer. The tracer is initialised in the jet injection region with a value of $X_{\mathrm{jet}} = 1$. The strong density contrast between bubble and cluster is maintained through refinement criteria based on the density gradient and cell volume (for details, see Weinberger et al., 2017). Throughout this work, we define lobe material to exhibit a jet mass fraction $X_{\mathrm{jet}} > 10^{-3}$ and checked that the conclusions of this paper are invariant with respect to variations of this choice.

The discrepancy between the inferred pressure of observed bubbles (via minimum energy arguments of radio observations) and the ambient ICM pressure (as inferred from X-ray observations) argues for a significant pressure contribution of CR protons that cannot directly be inferred by any interaction process due to the very low bubble densities (Bîrzan et al., 2008; Croston et al., 2008; Laing and Bridle, 2014; Croston and Hardcastle, 2014; Heesen et al., 2018). CRs could be accelerated at internal shocks of jets (Perucho and Martí, 2007). The strong non-thermal emission in knots observed in jets supports this mechanism (Worrall, 2009; Laing and Bridle, 2013; Duran et al., 2016). As we do not resolve internal shocks explicitly, we treat CR injection in a subgrid model. As most of the injected kinetic energy would immediately be thermalized, we instead ensure a minimum CR-to-thermal energy fraction $X_{\mathrm{cr,acc}} = E_{\mathrm{cr}}/E_{\mathrm{th}} = 1$ in every computational cell inside the jet/lobe for a time $\tau_{\mathrm{acc}} = 2\tau_{\mathrm{jet}}$, where τ_{jet} is the jet lifetime. When varying τ_{acc} we find that the resulting dynamical effects of late-time accelerated CRs ($t > \tau_{\mathrm{jet}}$) are negligible. This is an important difference in comparison to Weinberger et al. (2017) where the bubble CR pressure is specified at jet launch and successive CR acceleration in the jet is not accounted for, which yields a sub-dominant CR population.

3.3.3 CR transport

CRs as charged particles are bound to stay on flux-frozen magnetic field lines. As the magnetic field is transported alongside the gas, so are CRs. In addition to advection, CRs scatter on magnetic fluctuations which leads to transport by diffusion and streaming relative to the rest frame of the gas, mainly along the direction of the local mean magnetic field, which coincides with the large-scale field (Pfrommer et al., 2017).

Anisotropically moving CRs in the frame of propagating Alfvén waves are unstable to the streaming instability (Kulsrud and Pearce, 1969). These CRs resonantly excite Alfvén waves, which in turn causes the CRs' pitch angles to scatter and eventually to isotropize in the Alfvén frame (that moves with speed v_A). Hence, in galaxy clusters, the streaming velocity v_s relative to the thermal plasma corresponds approximately to the Alfvén velocity, i.e., $v_\mathrm{s} - v_\mathrm{A} \sim c^2/(3\nu l_\mathrm{cr})$, where ν is the pitch angle scattering rate and $l_\mathrm{cr} = P_\mathrm{cr}/\nabla P_\mathrm{cr}$ is the CR gradient length scale (Kulsrud, 2005). In addition, CRs diffuse along field lines with a diffusion coefficient $\tilde{\kappa} \equiv c^2/(3\nu) \sim (v_\mathrm{s} - v_\mathrm{A}) l_\mathrm{cr}$, which makes diffusion negligible compared to streaming in the strong scattering limit. Consequently, we introduce an effective CR diffusion coefficient $\kappa_\mathrm{cr,A} \sim l_\mathrm{cr} v_\mathrm{A}$ that emulates the combined effects of streaming and spatial diffusion (Sharma et al., 2009; Wiener et al., 2017).

Different damping mechanisms dissipate Alfvén waves, causing the streaming CRs in steady state to continuously transfer part of their energy into heat via *Alfvén wave heating* with a rate

$$\mathcal{H}_\mathrm{cr} = |\boldsymbol{v}_\mathrm{A} \cdot \nabla P_\mathrm{cr}|. \tag{3.2}$$

Note the dependence of the Alfvén heating rate on the CR pressure gradient. This directly relates $\mathcal{H}_\mathrm{cr}$ to the CR diffusion coefficient $\kappa_\mathrm{cr,A}$ in our effective model.

Following this self-confined picture, CRs are treated as a secondary fluid with adiabatic index $\gamma_\mathrm{cr} = 4/3$ (Pfrommer et al., 2017). We emulate streaming through a combination of anisotropic diffusion and Alfvén losses (Wiener et al., 2017). Our CRs are advected with the gas and anisotropically diffuse with a constant diffusion coefficient $\kappa_\parallel = 10^{29}\ \mathrm{cm^2 s^{-1}}$ along $\boldsymbol{B}$ and $\kappa_\perp = 0$ perpendicular to it (Pakmor et al., 2016a). The particular value of $\kappa_\parallel$ has been choosen so that it produces self-consistent results in our simulations (as we will see later in Section 3.6.1).

The CR distribution in the lobes quickly becomes uniform as the magnetic field confines the CRs initially to stay within the lobes. This leads to a negligible CR pressure gradient and hence an insignificant Alfvén wave cooling rate inside lobes. In our simulations, insufficiently resolved steep gradients at the lobe interface would lead to artificially large (numerical) cooling rates. We prevent this by imposing a maximum jet tracer threshold $X_\mathrm{jet,cool} \leq 10^{-3}$ for Alfvén wave cooling to be active (for a discussion, see Appendix 3.9.3). Our simulations also include the cooling of CRs through Coulomb and hadronic interactions (Pfrommer et al., 2017), which are however much smaller here in comparison to Alfvénic losses.

Physically, the jet fluid is magnetically unconnected to the ICM. In order to study the evolution of the diffusing CR distribution accurately, the jet launching region needs to be magnetically isolated to prevent spurious diffusion at the resolution limit along field lines that connect the jet launch region to the exterior ICM. Many individual injection events are present in our simulation, which require accurate magnetic isolation before each individual event. To this end, we project out the radial magnetic field components:

$$\boldsymbol{B} \to [1 - g(r)\hat{\boldsymbol{r}}\hat{\boldsymbol{r}}]\boldsymbol{B}, \tag{3.3}$$

where $\hat{\boldsymbol{r}}$ is the radial unit vector measured from the centre of our spherical jet launching region and $g(r) = 1 - |\cos(0.5\pi(x + \Delta x - 1)/\Delta x)|$ for $1 - \Delta x < x < 1 + \Delta x$, where $x = r/r_\mathrm{jet}$, $\Delta x = 0.25$, and r_jet is the radius of the jet launching region. Jets are launched from two regions on opposite sides of the centre. During the first injection event of a jet, the two bimodal jet regions are isotropically isolated, i.e., across the entire spherical surface (see equation 3.3). At all subsequent injection events while the jet is active, only the bubble hemisphere closer to the SMBH is isolated in order to retain the velocity structure in the direction of motion of the jet.

$P_{\rm jet}$ $[{\rm erg\,s^{-1}}]$	$X_{B,\rm ICM}$	$X_{B,\rm jet}$	$\tau_{\rm jet}$ [Myr]	$\kappa_{\|}$ $[{\rm cm^2\,s^{-1}}]$	$E_{\rm jet}$ $[10^{59}\,{\rm erg}]$
simulations with CRs					
4×10^{43}	0.05	0.1	10	10^{29}	0.13
4×10^{43}	0.05	0.1	25	10^{29}	0.31
4×10^{43}	0.05	0.1	50	10^{29}	0.63
1×10^{44}	0.05	0.1	10	10^{29}	0.32
1×10^{44}	0.05	0.1	25	10^{29}	0.79
1×10^{44}	0.05	0.1	50	10^{29}	1.58
2×10^{44}	0.05	0.1	10	10^{29}	0.63
$\mathbf{2\times10^{44}}$	**0.05**	**0.1**	**25**	$\mathbf{10^{29}}$	**1.58**
2×10^{44}	0.05	0.1	50	10^{29}	3.15
4×10^{44}	0.05	0.1	10	10^{29}	1.26
4×10^{44}	0.05	0.1	25	10^{29}	3.15
4×10^{44}	0.05	0.1	50	10^{29}	6.31
1×10^{45}	0.05	0.1	10	10^{29}	3.15
1×10^{45}	0.05	0.1	25	10^{29}	7.88
1×10^{45}	0.05	0.1	50	10^{29}	15.77
simulations without CRs					
2×10^{44}	0.05	0.1	25	0	1.58
2×10^{44}	0	0.1	25	0	1.58
2×10^{44}	0.05	0	25	0	1.58
2×10^{44}	0	0	25	0	1.58

Table 3.1: Jet parameters of the different models with combined jet power $P_{\rm jet}$ of the bipolar outflow, external magnetic-to-thermal pressure ratio $X_{B,\rm ICM}$, jet magnetic-to-thermal pressure ratio $X_{B,\rm jet}$, time of activity of the jet $\tau_{\rm jet}$, CR diffusion coefficient along the magnetic field $\kappa_{\|}$ and jet energy $E_{\rm jet} = P_{\rm jet}\tau_{\rm jet}$. The lower part of the table corresponds to our control runs without CRs, which are used for the analysis of the bubble stability. The fiducial run is marked in boldface.

3.3.4 Simulation models

Our MHD simulations are performed with the moving-mesh code AREPO (Springel, 2010), using an improved second-order hydrodynamic scheme with least-squares-fit gradient estimates and a Runge-Kutta time integration (Pakmor et al., 2016b). The MHD fluxes across cell interfaces are computed with an HLLD Riemann solver (Pakmor et al., 2011; Pakmor and Springel, 2013) adopting the Powell scheme for divergence control (Powell et al., 1999).

The bubble evolution is studied in a set of simulations listed in Table 3.1. The jets are active for a prescribed time $\tau_{\rm jet}$ with a certain jet power $P_{\rm jet}$. Our fiducial model corresponds to $P_{\rm jet} = 2\times10^{44}$ erg s^{-1}, $\tau_{\rm jet} = 25$ Myr, $X_{B,\rm ICM} = 0.05$, $X_{B,\rm jet} = 0.1$ and $\kappa_{\|} = 10^{29}$ cm^2 s^{-1}. We use this model in the analysis unless stated otherwise.

Sub-grid parameters and those responsible for the resolution of our simulation are given in Table 3.2. In Weinberger et al. (2017), we showed that the distance travelled by bubbles depends on the numerical resolution of the jet. Here, we focus on the previously dubbed high-resolution simulation. The numerical convergence of our results in comparison to lower resolution simulations is discussed in Appendix 3.9.2. When we compare several simulation models with varying parameters, we use the lower resolution simulations as this recovers qualitatively the same evolution of the jet at a significantly lower computational cost.

If included in the lobes ($X_{\rm jet} > 10^{-3}$), CRs are generally accelerated for time $\tau_{\rm acc} = 2\tau_{\rm jet}$ and we use a conversion fraction from thermal-to-CR energy of $X_{\rm cr,acc} = 1$. Reducing the fraction $X_{\rm cr,acc}$ only changes the normalisation of our CRs but has no significant impact on the studied features. Also, a much larger fraction of CRs is disfavoured as FRI jets are slowed down through the entrainment of ambient material. A remaining population of shocks seems unlikely to accelerate significant portions

Jet parameters		
Jet density	$\rho_{\rm target}$	10^{-28} g cm^{-3}
Jet launching region	$r_{\rm j}$	5 kpc
CR acceleration	$X_{\rm cr,acc}$	1
Magnetic field parameters		
Injection scale	$k_{\rm inj}$	37.5^{-1} kpc^{-1}
Resolution		
Target mass	$m_{\rm target,0}$	lower res.: 1.5×10^6 M$_\odot$ high res.: 1.5×10^5 M$_\odot$
Target volume	$V_{\rm target}^{1/3}$	lower res.: 405 pc high res.: 188 pc
Minimum volume	$V_{\rm min}$	$V_{\rm target}/2$

Table 3.2: A summary of our adopted parameters of the simulation.

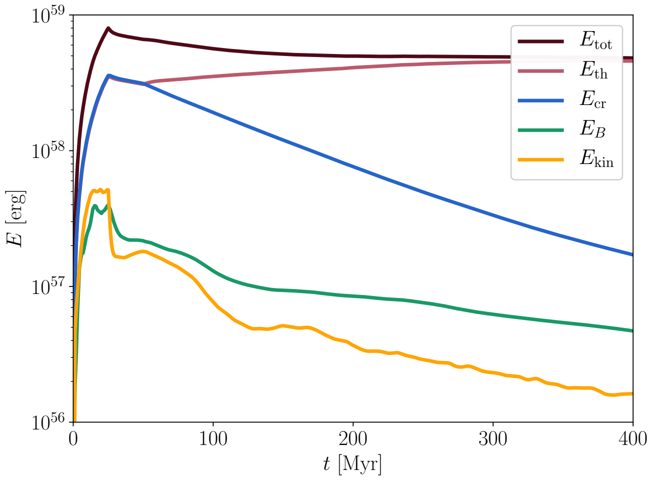

Figure 3.2: The time evolution of the energy components of the lobe. The lobe is defined as cells with jet mass fraction $X_{\rm jet} > 10^{-3}$. The thermal and CR energy are initially in equipartition. Later, CRs diffuse out of the lobe and thermal gas is entrained, which leads to an overall increase in thermal energy after the jet becomes inactive.

of the entrained protons. The conclusions of this paper also remain robust against variations of $\tau_{\rm acc}$ as long as $\tau_{\rm acc} \geq \tau_{\rm jet}$.

While magnetic tension initially generate significant levels of turbulence, this decays over the run time of our simulation since we do not model large scale flows due to substructure (Bourne and Sijacki, 2017) and neglect gas cooling, which also induces motions. In reality, the cooling gas accretes onto the central SMBH, powering jets in this process, leading to highly variable jet powers and lifetimes. Here, we instead decided to impose predefined jet energies to gain insight into the parametric dependencies of mixing, morphologies and CR distributions more easily. We postpone modelling of self-consistent jet injection through accreted cooling gas, which will enable us to study the long-term stability of the CC cluster due to CR heating.

3.4 Jet and bubble evolution

First, we discuss the evolution of our jets and bubbles in terms of global quantities and with detailed maps of thermodynamical quantities.

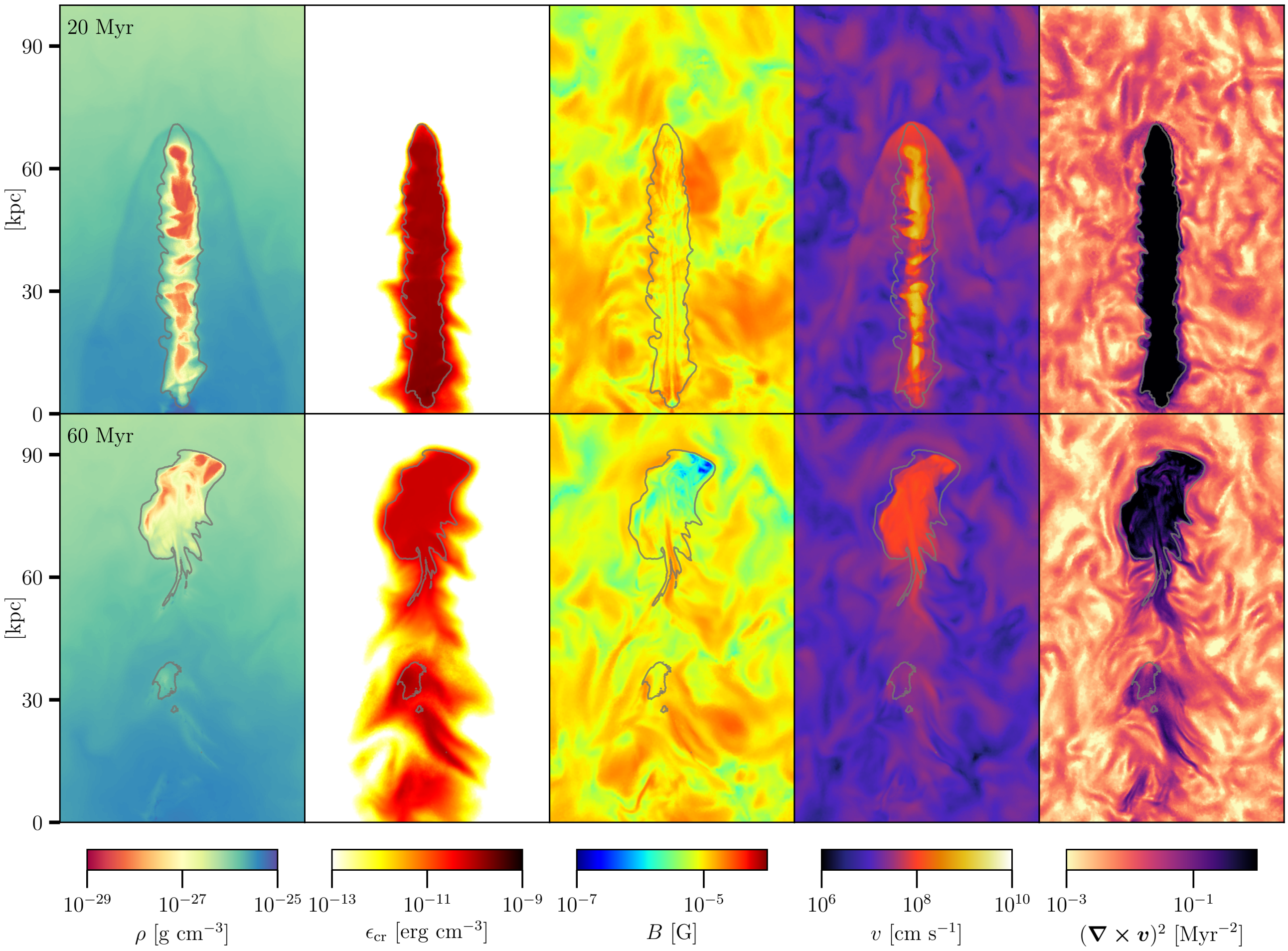

Figure 3.3: The mass density ρ, CR energy density $\epsilon_{\rm cr}$, magnetic field strength B, velocity v and vorticity squared $(\nabla\times v)^2$ of the fiducial run are portrayed at times 20 Myr and 60 Myr. The images correspond to projections of thin layers (100 kpc × 60 kpc × 4 kpc) centred at (50, 0, 0) and weighted by cell volume except for the velocity, which is weighted by the density. The grey contour corresponds to the jet tracer value $X_{\rm jet} = 10^{-3}$. The characteristic transition from jet to lobe becomes evident.

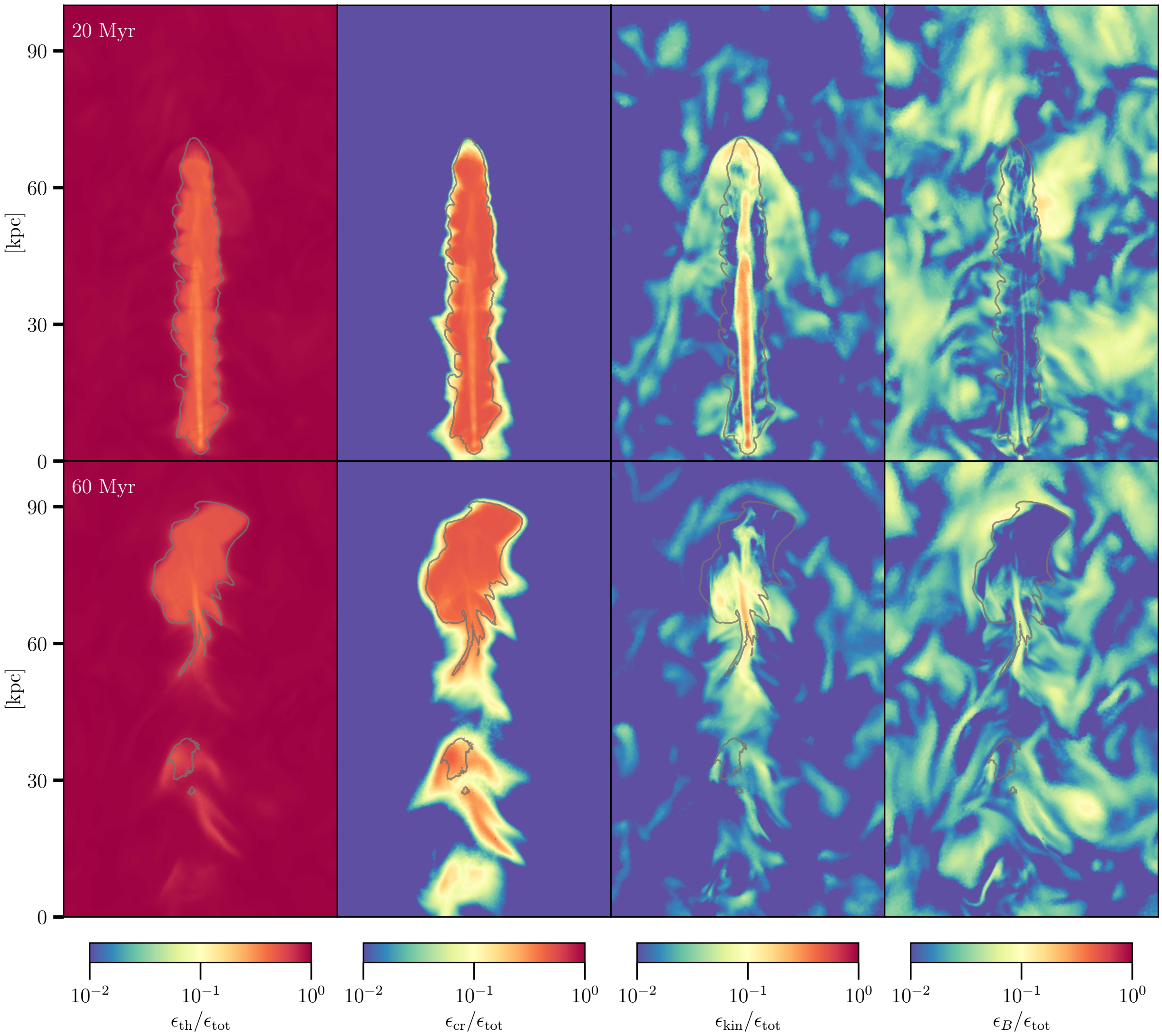

Figure 3.4: The thermal $\epsilon_{\rm th}$, CR $\epsilon_{\rm cr}$, kinetic $\epsilon_{\rm kin}$ and magnetic ϵ_B energy density, which are normalised to the total energy density $\epsilon_{\rm tot} = \epsilon_{\rm th} + \epsilon_{\rm cr} + \epsilon_{\rm kin} + \epsilon_B$ of the fiducial run, are portrayed at times 20 Myr and 60 Myr. The images correspond to projections of thin layers (100 kpc × 60 kpc × 4 kpc), which are volume weighted and centred at $(50, 0, 0)$. The grey contour corresponds to the jet tracer value $X_{\rm jet} = 10^{-3}$.

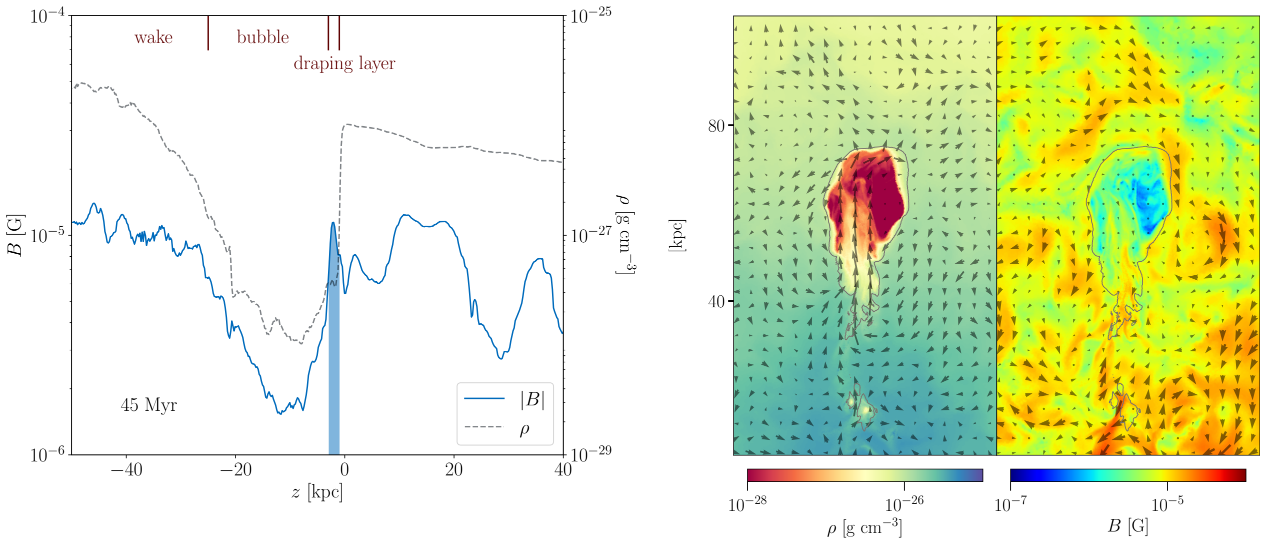

Figure 3.5: On the left, we show the mean magnetic field strength (blue) along a thin radially-aligned cylinder ($r = 1$ kpc) through the bubble as a function of distance z to the stagnation point at 45 Myr. We mark the thin magnetic draping layer with a filled blue contour and locate the extent of the bubble and its wake. To identify the extent of the bubble, the density is overlaid (black dashed). On the right, we show the density and magnetic field strength. The arrows correspond to the kinetic energy flux and the magnetic field directions, respectively, and the arrow length encodes the magnitude of these variables. The images correspond to projections of thin layers (100 kpc × 60 kpc × 4 kpc) centred on the wake of the bubble. The grey contour corresponds to the jet tracer value $X_{\mathrm{jet}} = 10^{-3}$. It becomes apparent that the magnetic field amplification at the bubble surface is not due to the compression of gas but rather due to draping in the direction of movement. The width of the draping layer corresponds to the theoretically predicted value of ≈ 2 kpc.

3.4.1 Global evolution

The jets are initialised with a dominant kinetic energy component. Through dissipation much of this kinetic energy is quickly thermalized. This would lead to thermally dominated lobes, in conflict with X-ray observations. The subgrid acceleration scheme employed for CR maintains them in equipartition with thermal energy until $2\tau_{\mathrm{acc}}$. Thus, CRs share a significant fraction of the energy and pressure in these simulations as shown in Fig. 3.2 which shows the time evolution of different energy components in the lobes. The strong dissipation of the kinetic energy of the jets effectively transfers kinetic energy into CR and thermal energy. Compared to the initial magnetic-to-thermal pressure ratio in the jet $X_{B,\mathrm{jet}} = 0.1$, the ratio drops by more than an order of magnitude due to the strong increase of thermal energy.

The thermal energy increases at later times whereas the CR energy decreases in Fig. 3.2. We adopt a morphology-based definition of lobes with a jet mass fraction exceeding 10^{-3}, which includes by definition heavily mixed cells. Thereby, mixing leads to an increase of mass and thermal energy in the lobes at later times. On the other hand, CRs continuously diffuse out of the bubbles, lowering their total energy. Note that CR energy losses due to cooling in the bubbles is solely restricted to the (almost negligible) hadronic and Coulomb losses as we suppress Alfvénic cooling in the bubble region (see Section 3.3.3).

The evolution of the thermodynamic cluster profiles (Fig. 3.1) shows a decrease in density and an increase in temperature at early times, which corresponds to the high thermal energy of the propagating jet. Because this hot gas has such a low-density it remains invisible in X-ray maps, which is in agreement with observations (e.g., Leccardi and Molendi, 2008). After the jet terminates and the bubbles rise buoyantly, the mean thermodynamic profiles nearly recover the initial conditions.

3.4.2 Morphology

The jet driving phase and subsequent phase of buoyant rise of the bubble are portrayed in Figs. 3.3 and 3.4 at 20 Myr and 60 Myr for the fiducial run. Figure 3.3 shows various thermodynamic variables

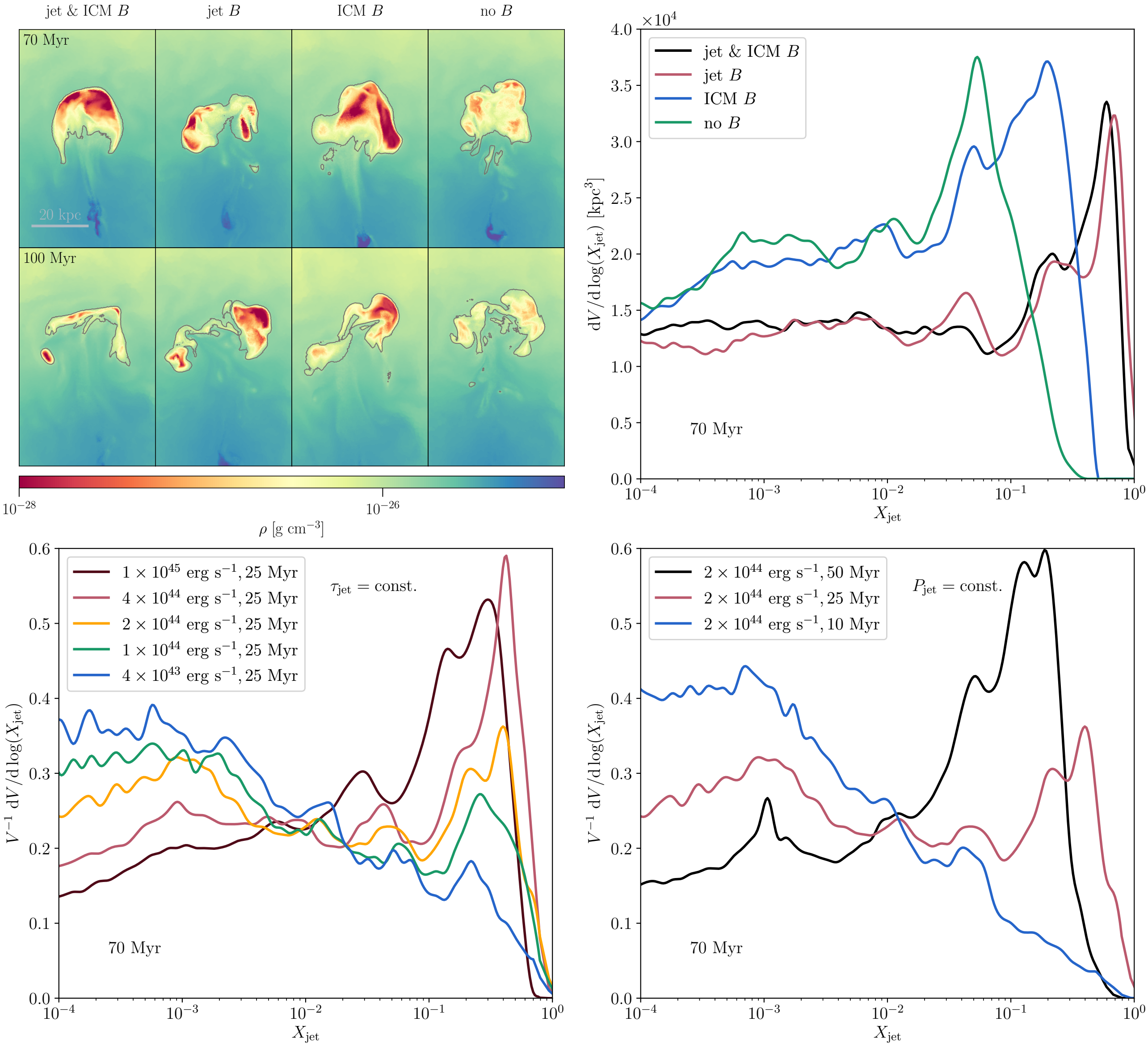

Figure 3.6: The mixing efficiency of the bubble for different magnetic field parameters of our lower resolution simulations. On the top left, we show lobe-centred projections of thin layers (80 kpc×50 kpc×4 kpc) of the density with jet mass fractions overlaid ($X_{\rm jet} = 10^{-3}$) for four simulations without CRs indicated above the panels. On the top right, the volume covered by gas, $dV/d\log(X_{\rm jet})$, with a given jet mass fraction $X_{\rm jet}$ is shown at 70 Myr for the same four simulations. The presence of magnetic fields significantly suppresses mixing in the bubble. The bottom panels portray the normalised volume covering fraction of a given jet mass fraction, $V^{-1}\ dV/d\log(X_{\rm jet})$. On the bottom left, we vary the jet power at constant time of jet activity $\tau_{\rm jet} = 25$ Myr. On the bottom right, we show bubbles inflated by jets of constant power $P_{\rm jet} = 2 \times 10^{44}$ erg/s. The peak of the volume fraction moves to the left for less energetic jets (decreased $P_{\rm jet}$ or $\tau_{\rm jet}$) indicating increased mixing efficiencies for these jets. The lines are smoothed for clarity.

projected in thin slices and Fig. 3.4 displays various energy densities, normalised to the total energy density. This enables direct comparisons of the dynamical impact of the different components.

Initially, the jet penetrates into the ambient medium forming a bow shock at its tip. The shock is visible in the first row of Fig. 3.3 as a discontinuity with increased density and velocity. The continuous mass flux is deflected at the tangential discontinuity between the jet and shock. The strong inflow expands horizontally and mixes with the shocked ICM gas streaming around the jet. This leads to the creation of an extended, highly turbulent region with high vorticity, see Fig. 3.3.

After the jet is switched off at 25 Myr, the remaining directed kinetic energy flux thermalises and catches up with the previously injected material forming a bubble, whose evolution is now solely driven by buoyancy. The high contrast in density between the lobes and the ambient medium makes the setup susceptible to the Rayleigh-Taylor instability. Thus, strong inflows develop in the wake of the bubble. In the second row of Fig. 3.3, the developing strong vorticity and high velocities are visible in the wake. They cause strong mixing of the bubble material with the ambient medium, which is accompanied by an increase in density.

The low magnetic field strength renders it dynamically irrelevant in the bulk of the ICM (Fig. 3.4). However, there are two cases where the dynamics amplifies the magnetic field to the point that it plays a significant role for the evolution of the system: first, there is significant magnetic field amplification in the wake of the bubble (Figs. 3.3 and 3.4). This is due to bubble-scale eddies that converge in the wake and adiabatically compress the field and stretch it by the strong shear flows that become evident in the vorticity map.

Second, the upwards motion of the bubbles in the ICM causes magnetic field lines of the IGM to accumulate at the leading surface of the rising bubble, which is a tangential discontinuity (Pfrommer and Dursi, 2010). These *draped* magnetic field lines lead to the suppression of Kelvin-Helmholtz and Rayleigh-Taylor instabilities (see also Section 3.5.1, for a detailed discussion). The bubble is eventually disrupted by strong uplifts of wake material, which are able to penetrate through the centre of the bubble. If turbulence is absent the resulting torus structure remains stable on timescales of > 100 Myr (Weinberger et al., 2017). In our simulations, the onset of a developing (deformed) toroidal structure is visible after $\sim 70 - 100$ Myr (see Fig. 3.6). However, the turbulent asymmetrical flow pattern of the uplift causes the break up of the lobe into two main pieces. If enough low density material remains, the two cavities can continue to rise as two independent bubbles until the uplift becomes too strong again and causes them to also break apart.

In addition to advection, CRs are allowed to anisotropically diffuse along magnetic field lines. However, the draped magnetic layer on top of the bubble confines the CRs inside and prevents escape ahead of the bubble. Instead, CRs are able to diffuse out of the lower part of the bubble along the strongly amplified magnetic filaments, which are bent by the strong uplift and align with the jet axis (see Fig. 3.3). The jet evolution and subsequent creation of the bubble is in excellent agreement with previous work (e.g., Lind et al., 1989; Reynolds et al., 2002), suggesting that the addition of internal and external magnetic fields as well as CRs does not change the overall evolution of the system.

3.5 Magnetic field evolution

In this section, we study the effect of magnetic draping at the bubble interface, amplification of magnetic fields in the bubble's wake, and the effect of magnetic fields on the mixing efficiency of the bubble fluid with the ICM.

3.5.1 Magnetic draping and amplification

Objects moving at super-Alfvénic speed through a magnetised medium accumulate magnetic field lines at their interface. This magnetic draping effect occurs only if the magnetic coherence scale is sufficiently large, i.e., $\lambda_B \gtrsim R/\mathcal{M}_\mathrm{A}$ where R is the curvature radius at the stagnation point and $\mathcal{M}_\mathrm{A}$ is the Alfvénic Mach number (Pfrommer and Dursi, 2010). In a steady state, the rate at which new magnetic field lines enter this strongly magnetised sheath balances the rate at which magnetic field lines are advected over the bubble's surface to eventually leave the draping layer. The magnetic tension exerted by this draping layer slows down the object as the magnetic field is anchored in the ICM in ideal MHD and thus acquires a large inertia (Dursi and Pfrommer, 2008). Moreover, draping makes the object more resilient against interface instabilities of the Kelvin-Helmholtz or Rayleigh-Taylor type (Dursi, 2007). This draping layer inhibits any particle transport across the bubble surface such as CR diffusion (Ruszkowski et al., 2008), heat conduction by thermal electrons and momentum transport or viscosity by thermal protons, which stabilises sharp temperature and density transitions observed in the ICM (i.e., cold fronts) against disruption (Vikhlinin et al., 2001; Lyutikov, 2006; Asai et al., 2007). Previous simulations acknowledge the stabilising effect of magnetic fields (Jones and De Young, 2005; O'Neill et al., 2009; Bambic et al., 2018a). Here, for the first time, we present results for the case of self-consistently inflated bubbles in a realistic turbulent magnetised environment.

Magnetic draping creates a layer of thickness l that is smaller than the curvature radius R of the bubble at the stagnation point by (Dursi and Pfrommer, 2008):

$$\frac{l}{R} = \frac{1}{6\alpha\mathcal{M}_\mathrm{A}^2} = \frac{1}{3\alpha\beta\gamma\mathcal{M}^2} = \frac{1}{3}\frac{B_\mathrm{ICM}^2}{B_\mathrm{max}^2}, \tag{3.4}$$

where α describes the magnetic-to-ram pressure ratio at the stagnation point ($B_\mathrm{max}^2/8\pi = \alpha\rho v^2$), $\mathcal{M}_\mathrm{A}$ corresponds to the Alfvénic Mach number $\mathcal{M}_\mathrm{A} = v/v_\mathrm{A}$, $\mathcal{M}$ is the sonic Mach number, $\gamma = 5/3$ is the adiabatic index and $X_{B,\mathrm{ICM}} = \beta^{-1}$ is the thermal-to-magnetic pressure ratio in the upstream ICM. In our simulations, $X_{B,\mathrm{ICM}} = 0.05$, we determine $\mathcal{M} \approx 0.2$ and take $\alpha \approx 2$ from Dursi and Pfrommer (2008). Thus, we expect draping layer thickness $l \approx 2$ kpc for a curvature radius $R = 20$ kpc at our simulated bubble. This implies that we are able to numerically resolve the draping layer due to our refinement prescriptions.

Figure 3.5 (left-hand panel) shows the magnetic field strength (blue line) along the stagnation line of the bubble. At the bubble edge, which is clearly identified by the sharp increase in density (black dashed), the magnetic field shows a pronounced narrow peak with width $l \approx 2$ kpc. In agreement with our theoretical predictions, the magnetic field rises from its mean value of $B_\mathrm{ICM} \approx 5\ \mu$G to $B_\mathrm{max} \approx 10\ \mu$G in the draping layer (see equation 3.4). In the magnetic field map (right-hand panel in Fig. 3.5), a thin enhanced magnetic field layer is also visible that corresponds to the draping layer surrounding the bubble. Consequently, we confirm that magnetic draping is an active process in bubble dynamics in agreement with previous studies (Ruszkowski et al., 2007; Dursi and Pfrommer, 2008).

In the wake of the jet, magnetic field lines are stretched by differential motions and compressed by converging downdrafts that compensate the upwards motion of the bubble. This process amplifies magnetic fields in the wake and aligns field lines with the jet axis (Fig. 3.5), in agreement with previous findings (O'Neill and Jones, 2010; Mendygral et al., 2012). This has important consequences for the CRs, which are confined in the bubble by the draped magnetic field at the leading interface. Hence, escape from the bubble only becomes possible in its wake as the converging eddies connect the bubble interior magnetically with the ICM via the amplified magnetic filaments (see Figs. 3.3 and 3.5). As a result, CRs are conducted diffusively along the magnetic filaments towards the cluster centre in the opposite direction to the CR pressure gradient (Fig. 3.3).

3.5.2 Mixing

In order to analyse the mixing efficiency for different magnetic field configurations, we use a suite of simulations without CRs (bottom in Table 3.1) to solely focus on magnetic effects. As discussed in the previous section, the effect of draping stabilises the bubble against early disruption from interface instabilities. However, the draping layer only suppresses the growth of wave modes along the direction of the mean field but not perpendicular to it. As the bubble rises in the cluster potential, its surface is constantly warped and twisted by the turbulence, which causes incomplete alignments of the external turbulent magnetic field with respect to the bubble surface. Possibly, magnetic fields also cancel out through numerical magnetic reconnection. These effects likely compromise the effects

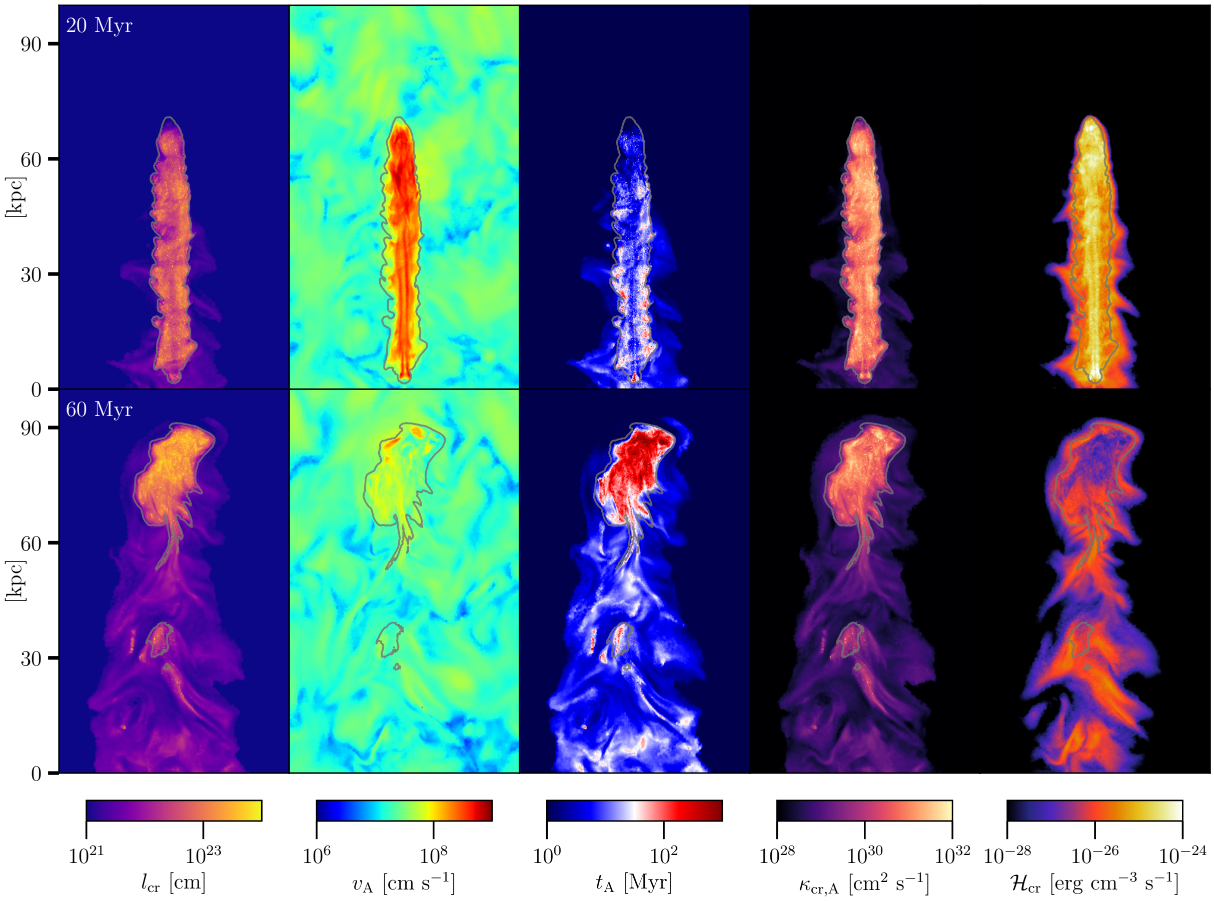

Figure 3.7: Quantities related to CR transport in jet and lobe. We show the CR gradient length scale $l_{\rm cr} = P_{\rm cr}/\boldsymbol{\nabla}P_{\rm cr}$, the Alfvén velocity $v_{\rm A}$, the Alfvén cooling time scale of CRs, $t_{\rm A} = l_{\rm cr}/v_{\rm A}$, the instantaneous CR diffusion coefficient $\kappa_{\rm cr,A} = v_{\rm A} l_{\rm cr}$ and the Alfvén heating rate $\mathcal{H}_{\rm cr} = |\boldsymbol{v}_{\rm A} \cdot \boldsymbol{\nabla}P_{\rm cr}|$ of the fiducial run at 20 Myr and 60 Myr. Here, we also display the measured heating rate inside the lobes to illustrate the strong increase of Alfvén heating at the lobe edges due to the large numerical CR pressure gradients there, which is for this reason suppressed in our simulations. The images correspond to projections of thin layers (100 kpc × 60 kpc × 4 kpc) weighted with the volume and centred at $(50, 0, 0)$. We only show $l_{\rm cr}$, $t_{\rm A}$, $\kappa_{\rm cr,A}$ and $\mathcal{H}_{\rm cr}$ in regions with $\epsilon_{\rm cr} > 10^{-14}$ erg cm^{-3} to exclude an energetically subdominant CR population, which has partially experienced numerical diffusion. The CR gradient is unavailable due to numerical reasons for individual saturated cells which are shown with yellow. The grey contour corresponds to the jet tracer value $X_{\rm jet} = 10^{-3}$.

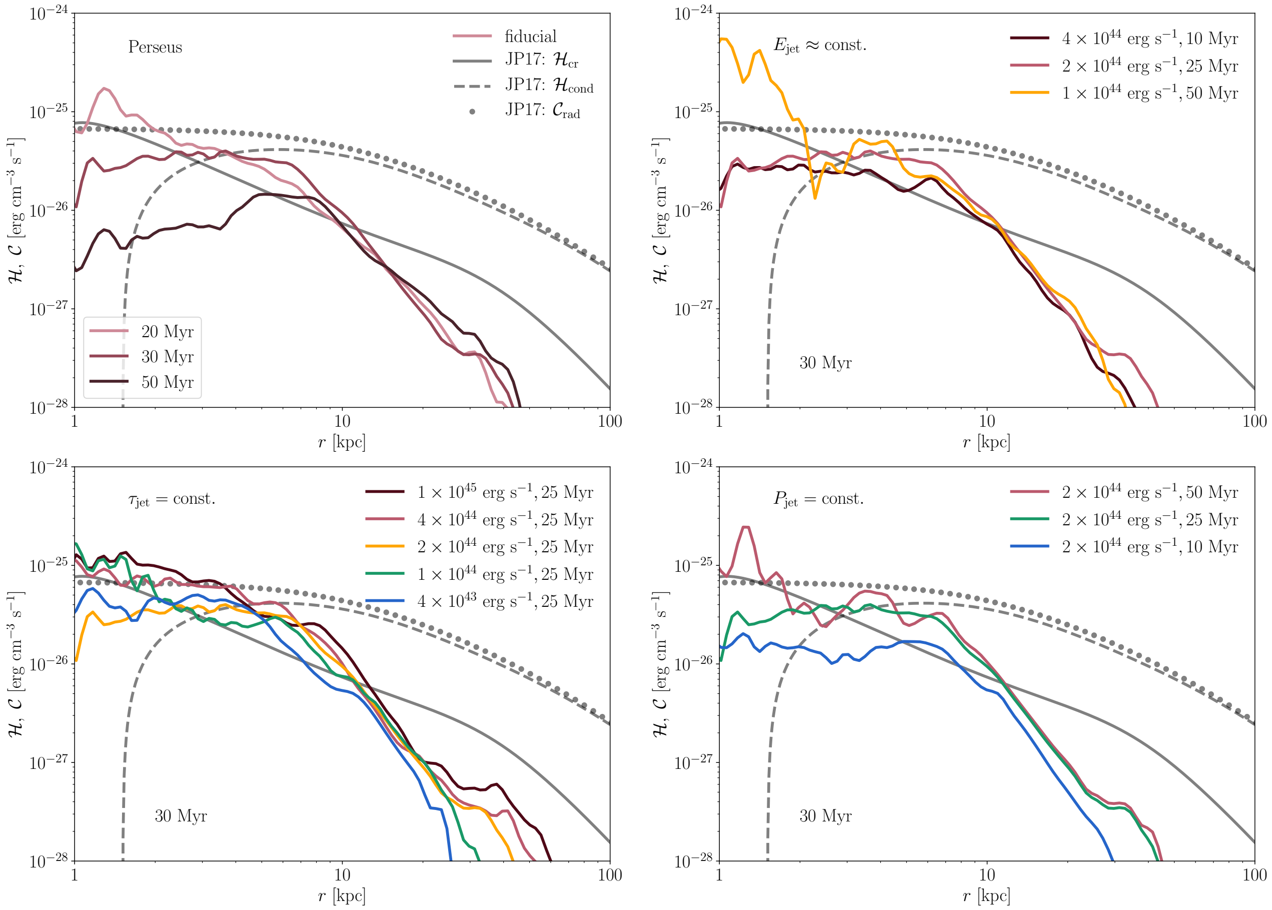

Figure 3.8: Radial profiles of the Alfvén heating rate in the ICM due to CR streaming, $\mathcal{H}_{\rm cr}$ (restricting ourselves to ICM simulation cells with $X_{\rm jet} < 10^{-3}$ and using our lower resolution simulations). We compare our simulation to a spherically symmetric, steady state solution in which CR heating (solid) and conductive heating ($\mathcal{H}_{\rm cond}$, dashed) balances radiative cooling ($\mathcal{C}_{\rm rad}$, dotted) in the Perseus cluster (Jacob and Pfrommer, 2017a). On the upper left, we show different radial profiles at times 20, 30 and 50 Myr for our fiducial model. On the upper right, we compare profiles of jets with similar energy ($E_{\rm jet} \approx 1.58 \times 10^{59}$ erg) but different $P_{\rm jet}$ and $\tau_{\rm jet}$: the heating rate profile is steeper for low-luminosity jets with longer activity times. On the bottom left, we compare jets with varying luminosity but constant duration $\tau_{\rm jet} = 25$: while the maximum heating radius scales with jet luminosity, there is no clear trend of $\mathcal{H}_{\rm cr}$ with luminosity at smaller radius. On the bottom right, we compare jets with constant jet power $P_{\rm jet} = 2 \times 10^{44}$ erg s^{-1} but varying jet activity time $\tau_{\rm jet}$: the prolonged CR production and ability to diffuse back to the centre for longer times compensates for the greater extent of the more energetic jets. The radial profiles generally correspond to volume-weighted averages.

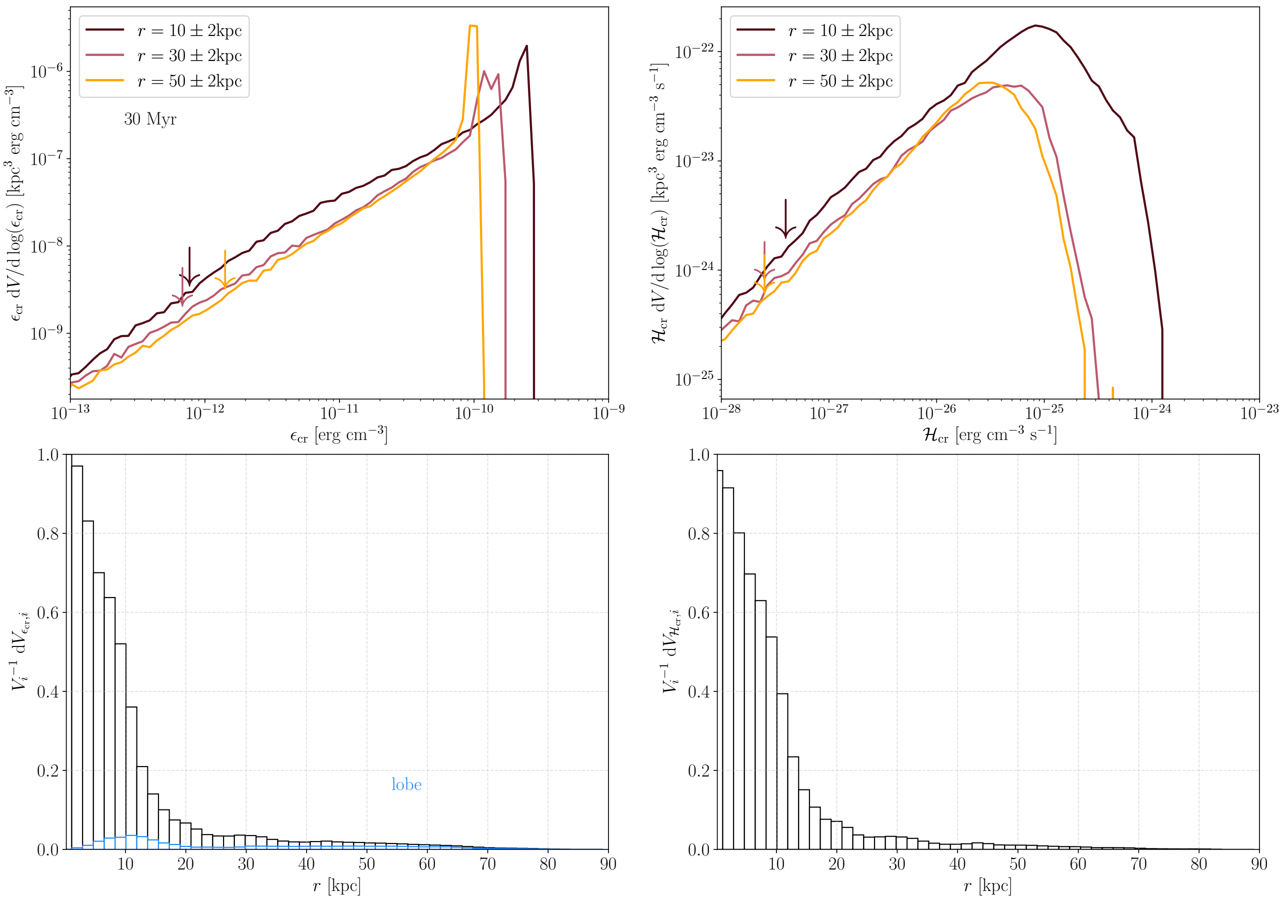

Figure 3.9: Weighted volume distributions and filling factors of the CR energy density $\epsilon_{\rm cr}$ and the Alfvén heating rate $\mathcal{H}_{\rm cr}$ of our fiducial simulation at 30 Myr. We show the weighted volume distribution of CR energy density $\epsilon_{\rm cr}{\rm d}V/{\rm d}\log(\epsilon_{\rm cr})$ (top left) and CR heating rate density $\mathcal{H}_{\rm cr}{\rm d}V/{\rm d}\log(\mathcal{H}_{\rm cr})$ (top right), which characterize the isotropy of our CR distribution. The arrows mark the minimum CR energy density and heating rate density necessary to cover 3σ (99.8%) of the CR energy and heating power at that radius, respectively. Due to their similarity, we adopt a common value for the floor values $\epsilon_{\rm cr,min} = 10^{-12}$ erg cm^{-3} and $\mathcal{H}_{\rm cr,min} = 3 \times 10^{28}$ erg cm^{-3} s^{-1} at all radii. In the bottom panels, we show the filling factor of $\epsilon_{\rm cr}$ and $\mathcal{H}_{\rm cr}$ for cells above these thresholds. Note that we suppress heating rates inside bubbles. The filling factor of the lobes ($X_{\rm jet} > 10^{-3}$) is overplotted in the bottom left panel. The small filling factor of the lobes highlights the importance of CR diffusion to isotropize CRs. The large volume filling factor of $\epsilon_{\rm cr}$ and $\mathcal{H}_{\rm cr}$ becomes evident for $r \lesssim 15$ kpc, suggesting that CR heating is isotropic at small radii.

of draping temporarily for our complex simulations in comparison to idealised setups. In addition, we model the effect of helical fields, which develop in the turbulent bubble from the initially toroidal fields in the jet and also show stabilising effects (Ruszkowski et al., 2007).

The simulations in the top left panel of Fig. 3.6 show a case with internal helical and external turbulent fields, two cases with either one of the two field configurations and one without any magnetic fields. Visually the morphology of the simulations including magnetic fields appear similar to the ones without (accounting for projection effects). However, the density contrast within the lobes is smaller in the simulation without magnetic fields, indicating that mixing is suppressed by either the helical lobe field and/or draped external fields. This can also be seen in the top right panel of Fig. 3.6, where we show the volume covered by a given jet mass fraction X_{jet}. Initially, the distribution peaks at $X_{\mathrm{jet}} = 1$ and if the bubble was perfectly insulated the distribution would stay there. The faster the distribution moves to lower values of X_{jet}, the more efficiently does the bubble material mix with the ICM. Conversely, a slow evolution indicates a significant suppression of mixing. Accounting for magnetic fields in the ICM, which enables magnetic draping, shifts the filling factor to higher values of X_{jet} indicating an insulating effect of draping and preventing fast mixing. In reality, this suppression of mixing should be even higher as the driven external turbulence is weaker in the case without magnetic fields in comparison to the case of ICM magnetic fields (see Section 3.3) since turbulence amplifies mixing (e.g., Ogiya et al., 2018).

Similarly, our simulation with purely internal helical magnetic fields suppresses mixing in comparison to the case without $\boldsymbol{B}$. This suggests that our case with internal and external fields should show an even smaller degree of mixing in comparison to either of the two individual cases with a single magnetic component. However, there is only a slightly smaller jet mass fraction retained in this double-magnetic case in comparison to the internal field case (Fig. 3.6). The loss of stability in the case of the additional draping layer can be explained with the increase in driven external turbulence for a magnetized ICM.

In the lower left panel of Fig. 3.6, we compare runs with constant jet lifetime (τ_{jet}) but varying jet power (P_{jet}). We find a decrease in the mixing efficiency for jets with higher power in agreement with Brüggen et al. (2002). Our normalisation ensures comparability across differently sized lobes. The high-power jets penetrate the inner region of the ICM as highly collimated outflows. Their disruption occurs further out in the cluster atmosphere where the magnetic fluctuations and thereby the level of turbulence is lower. This environment impedes mixing in comparison to low-power jets which get disrupted inside the highly turbulent cluster centre. In addition, Rayleigh Taylor instabilities should arise later for larger cavities (higher power jets at constant τ_{jet}) as the growth time scale of the instability increases for larger scales. This argument is confirmed when we compare simulations with varying τ_{jet}, but constant jet power (lower-right panel Fig. 3.6). Here, the larger cavities (larger τ_{jet}) remain more stable. We conclude that less energetic jets (decreased P_{jet} or τ_{jet}) show increased mixing efficiencies of lobes with the ICM.

3.6 Cosmic ray evolution

After discussing the magnetic structure at the rising bubbles, we now turn our attention to the distribution of CRs. First we examine the diffusive transport of CRs and then detail Alfvén wave heating by CRs.

3.6.1 CR diffusion and streaming

As discussed in Section 3.3.3, we model active CR transport via the anisotropic diffusion approximation to emulate CR streaming (see also Sharma et al., 2009). To this end, we include CR energy losses through Alfvén cooling and adopt a constant parallel diffusion coefficient ($\kappa_{\parallel} = 10^{29}\ \mathrm{cm}^2\ \mathrm{s}^{-1}$) so that it approximately matches the instantaneous CR diffusion coefficient $\kappa_{\mathrm{cr,A}} \equiv l_{\mathrm{cr}} \upsilon_{\mathrm{A}}$ in the ICM.

This choice for $\kappa_{\parallel}$ is examined in Fig. 3.7, which shows projections of thin layers of different quantities related to CR transport. As expected, the CR population has a large CR gradient length

l_{cr} in the bubble (except for the boundary) as the CR population quickly reaches a homogeneous distribution for our choice of $\kappa_{\|}$. Outside the bubble, l_{cr} drops quickly. The behaviour is echoed by the Alfvén velocity v_{A}: inside the jet (and bubble) it attains values up to 10^4 km s^{-1} owing to the low density and comparably large magnetic field whereas it fluctuates around a value of 10^2 km s^{-1} in the ICM. The distribution of Alfvén cooling times, $t_{\mathrm{A}} = l_{\mathrm{cr}}/v_{\mathrm{A}}$, is a direct consequence of this: t_{A} drops from values of ≈ 1 Gyr inside the bubbles to values ranging from 10–30 Myrs, comparable to typical jet duty time scales (e.g., Vantyghem et al., 2014; Turner, 2018).

The combination of high v_{A} and l_{cr} inside the bubble leads to a large value of the instantaneous CR diffusion coefficient $\kappa_{\mathrm{cr,A}} \approx 10^{32}$ cm^{2}s^{-1}. While this is much larger than our adopted constant diffusion coefficient of 10^{29} cm^{2}s^{-1}, the CR distribution in the bubble is already homogeneous as can be seen in the CR energy density in Fig. 3.3; increasing $\kappa_{\|}$ further would not alter our results. Outside the bubble, the diffusion coefficient drops by three orders of magnitude to $\kappa_{\mathrm{cr,A}} \approx 10^{29}$ cm^{2}s^{-1}. There, the CRs are magnetically unconfined and the value of the diffusion coefficient becomes crucial for accurately capturing the dynamics, justifying our choice of $\kappa_{\|}$.

The small CR length scale l_{cr} at the bubble interface combined with a high Alfvén velocity decreases the Alfvén cooling time t_{A} significantly to values of order 1 Myr. This would increase the Alfvén heating rate at the edges and drain a significant amount of CR energy from the bubble. In reality, the CR gradient would instead be smoothed out on the short Alfvénic crossing time across the jet and stay flat during inflation of the bubble and its evolution thereafter. This explains our initial choice of limiting Alfvén cooling to regions outside the bubble ($X_{\mathrm{jet}} < 10^{-3}$) as a numerical safeguard to prevent numerically-induced CR cooling.

We discuss in Section 3.5 that CRs can only escape through the lower part of the bubble. As they are conducted out of the bubble they remain confined to the magnetic field. Consequently, the vertically oriented, magnified magnetic field lines are traced by the Alfvén heating rate. This demonstrates the importance of simulating the exact structure of the magnetic field in the vicinity of the bubble. It will be interesting to see how substructure induced motions and radiative cooling influence this result.

3.6.2 CR distribution and Alfvén wave heating

In Fig. 3.8 (upper left panel) we show the radial profile of the Alfvén heating rate ($\mathcal{H}_{\mathrm{cr}}$) of our fiducial model at different times during and after the jet lifetime $\tau_{\mathrm{jet}} = 25$ Myr. In agreement with our subgrid model of CR Alfvén cooling in bubbles and in order to focus solely on the heating of the ICM, we impose a jet tracer threshold of $X_{\mathrm{jet}} < 10^{-3}$ to exclude artificially high cooling rates within the bubble. The result is robust up to factors of two when we vary the jet tracer threshold by an order of magnitude. We compare our simulated Alfvén heating rates to theoretical predictions by Jacob and Pfrommer (2017a) for the Perseus cluster who found steady-state solutions in which the heating rates due to Alfvén heating (at small radii) and thermal conduction (at larger radii) balance radiative cooling. Our simulated Alfvén heating rates are in good agreement with the theoretical predictions up to 30 Myr after jet launch with details depending on parameter choices as we will now discuss. At later times, newly launched jets are expected to replenish the CR energy reservoir, which has then significantly cooled via Alfvén wave losses.

The overall shape of the radial profile of $\mathcal{H}_{\mathrm{cr}}$ is determined by the jet energy, power and lifetime. For efficient CR heating in the centre of clusters, the exact value of the jet energy E_{jet} proves to be crucial: if it is too small there is not enough CR energy injected and the induced heating rate cannot balance radiative losses of the gas. On the other hand, if the jets are too energetic they pierce out of the cluster centre and reach the outskirts of the core, which makes it difficult for CRs to diffuse back to the origin and to maintain a large heating rate.

For jets with $E_{\mathrm{jet}} =$ const. but varying luminosity and lifetime, the profiles differ slightly (Fig. 3.8, top right panel). The heating rate profile is steeper for low-luminosity jets with longer activity times. This is because low-luminosity jets are more quickly decelerated by the inertia of the ambient ICM and CRs have more time to diffuse back towards the cluster centre where they sustain a larger central heating rate.

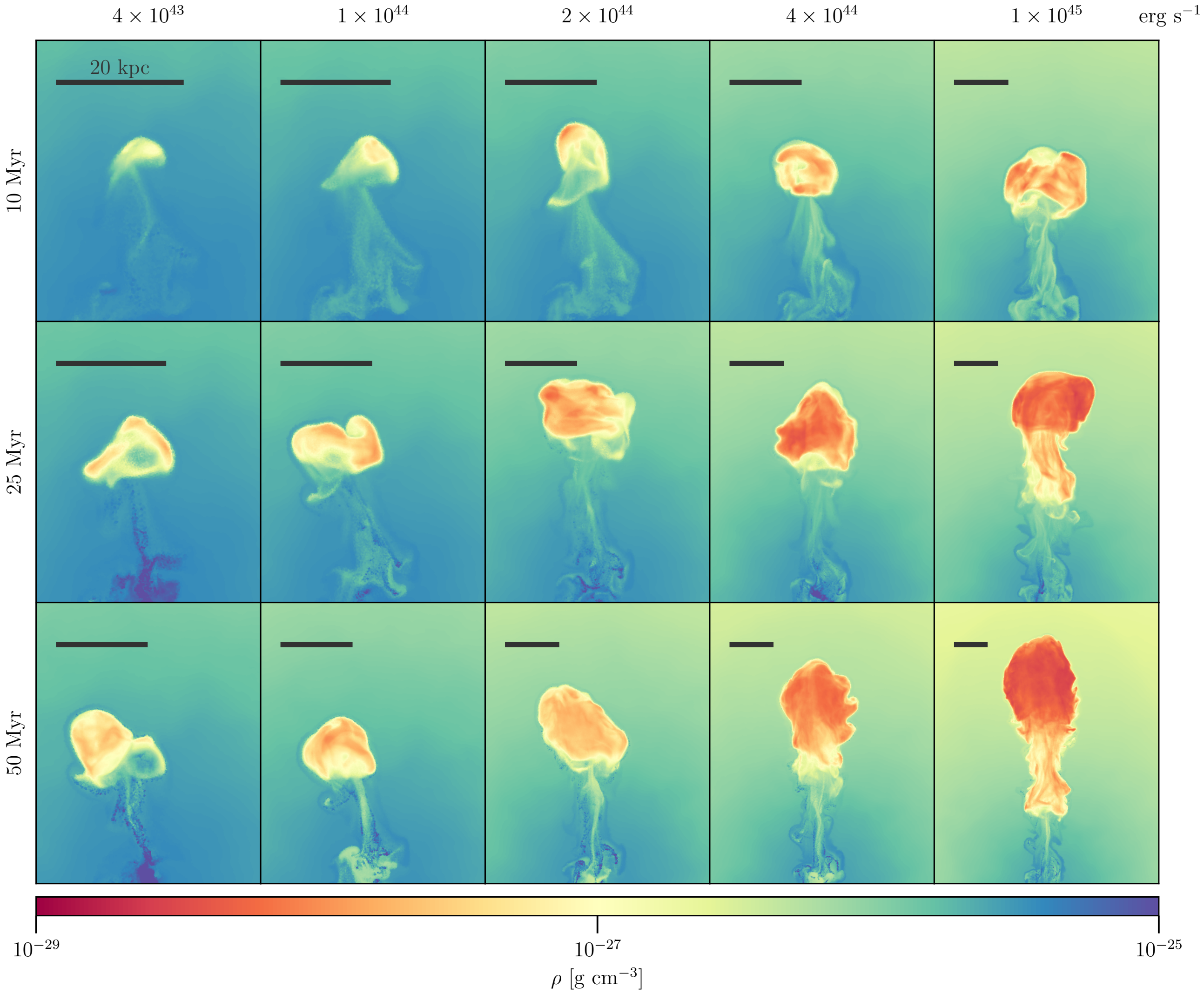

Figure 3.10: Density projections for our lower resolution simulations with varying jet parameters. We show a full projection of the jet tracer-weighted density at 70 Myr. The jet activity time increases from top to bottom and the jet power increases from left to right as indicated. Jets with similar energy are ordered along diagonals from the bottom left to the top right. The scale bar corresponds to 20 kpc in all panels and decreases from left to right but stays constant along diagonals with $E_{\text{jet}} \approx$ const.

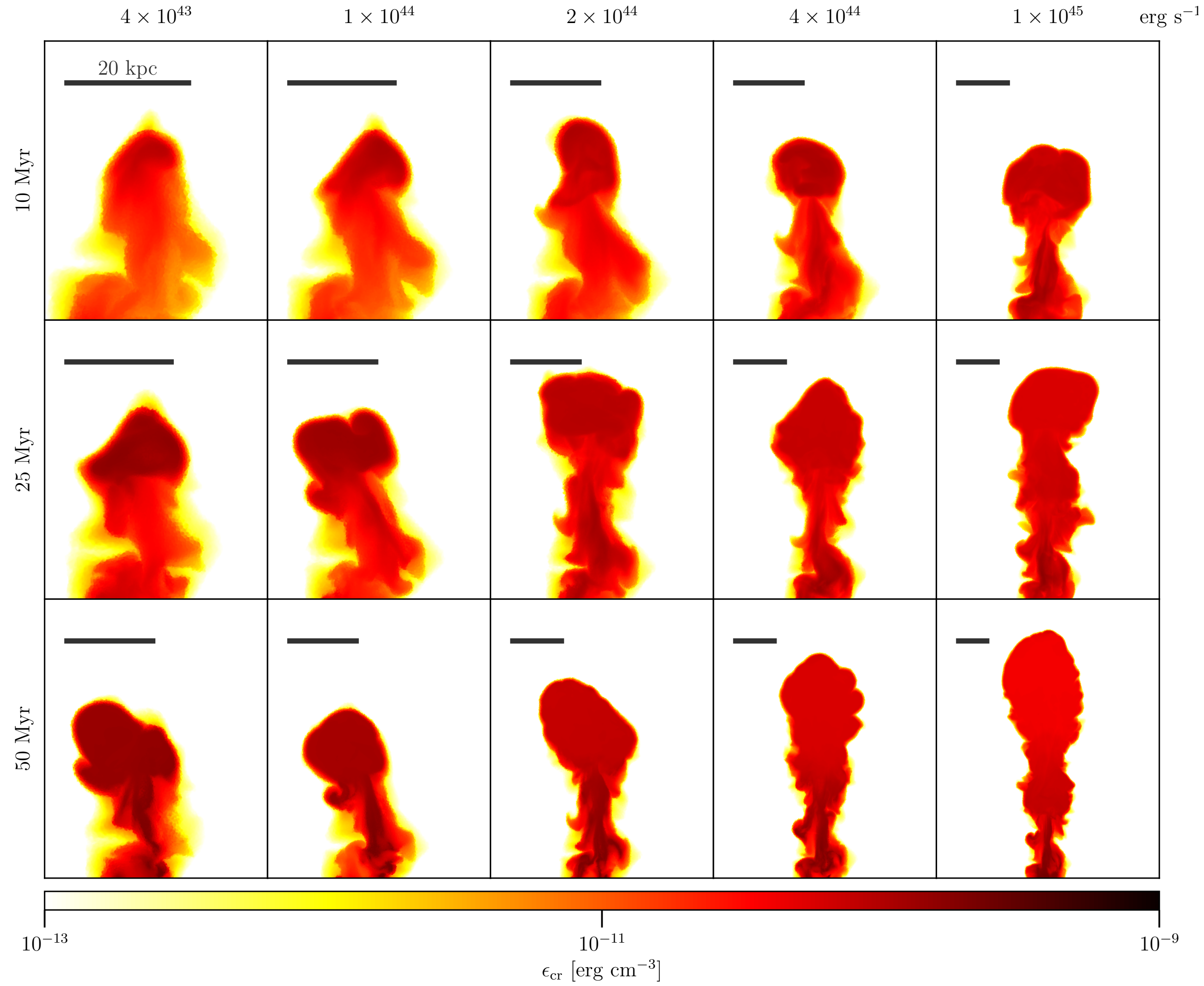

Figure 3.11: Same as in Fig. 3.10 but for the jet tracer-weighted CR energy density ϵ_{cr}. Even for bubbles with low density contrast (top left) there is significant CR energy density released into the ICM.

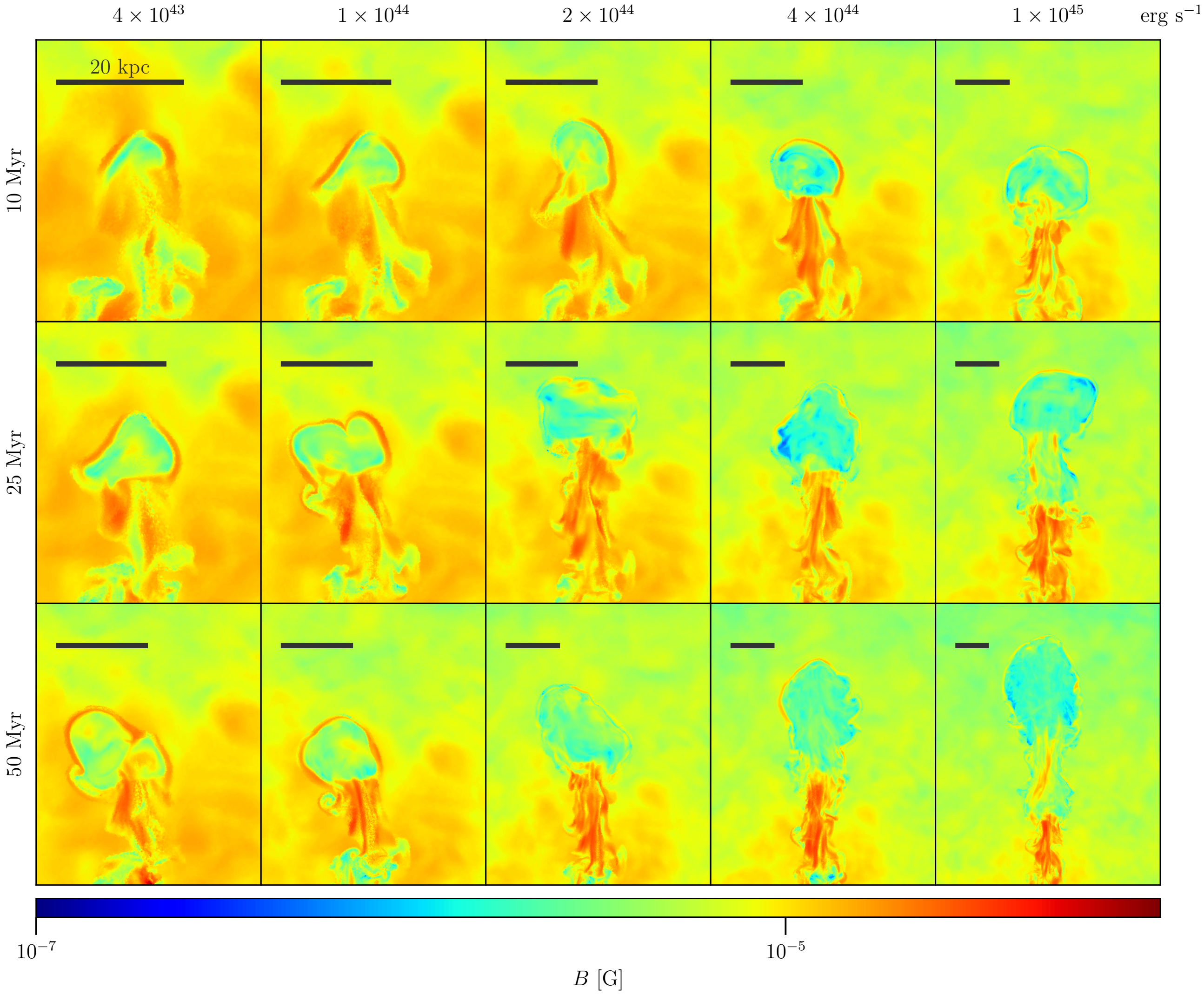

Figure 3.12: Same as in Fig. 3.10 but for the jet tracer-weighted magnetic field strength B. The red envelope surrounding the bubbles clearly show magnetic draping and magnetic fields in the wake of bubbles are strongly amplified. Note that the weighting procedure enhances the magnetic field in the wake of the bubble.

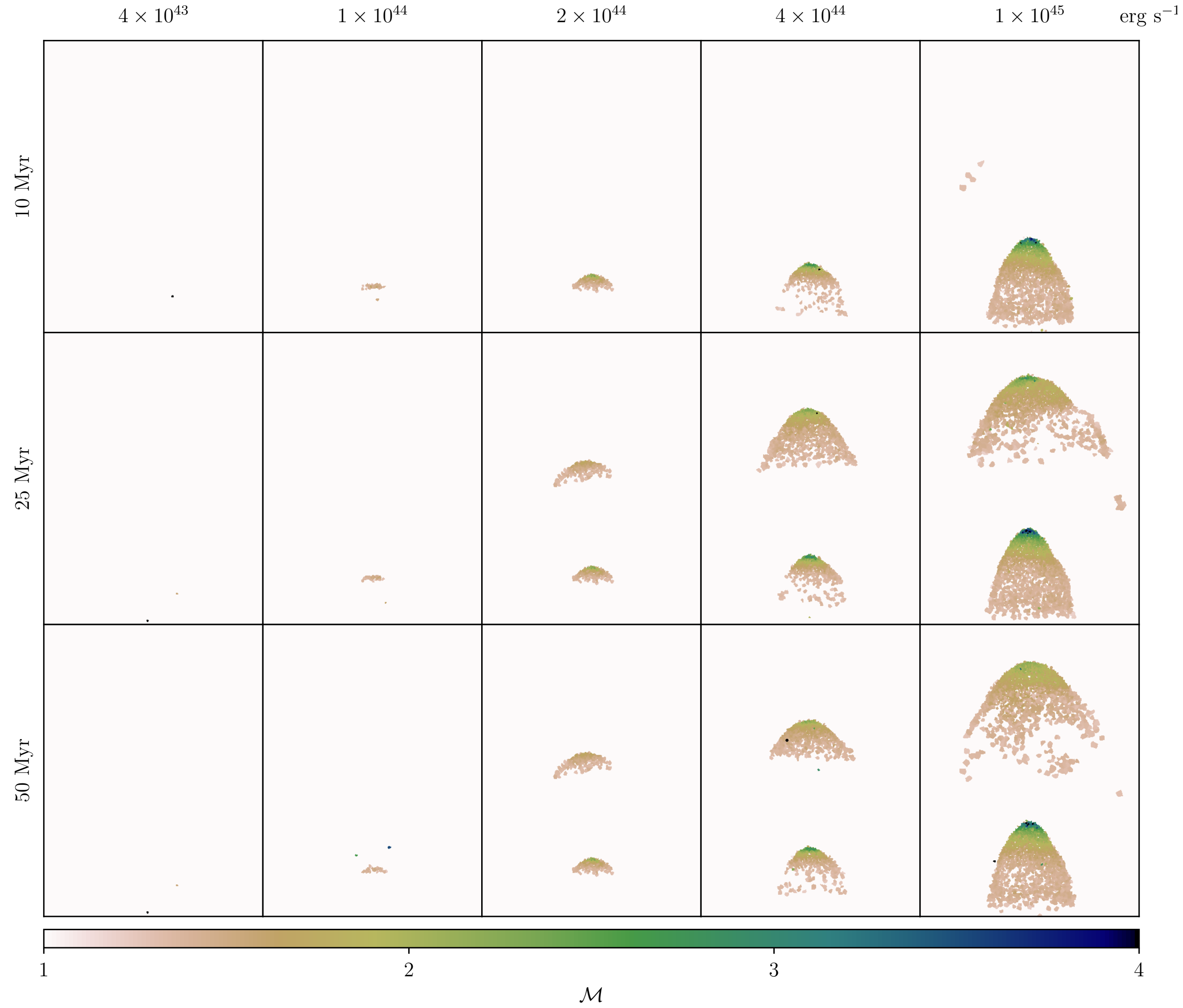

Figure 3.13: Same as in Fig. 3.10 but for the Mach number $\mathcal{M}$ that was weighted with the energy dissipation rate at the shocks. We overplot $\mathcal{M}$ projections of two snapshots, at 5 Myr and 20 Myr. Here, projections have constant dimensions of 80 kpc × 60 kpc × 60 kpc centred at (40-0-0). Low-power jets show at best small Mach numbers whereas the Mach numbers of high power-jets decrease quickly with time. These characteristics are in agreement with observations of FRI and FRII, respectively.

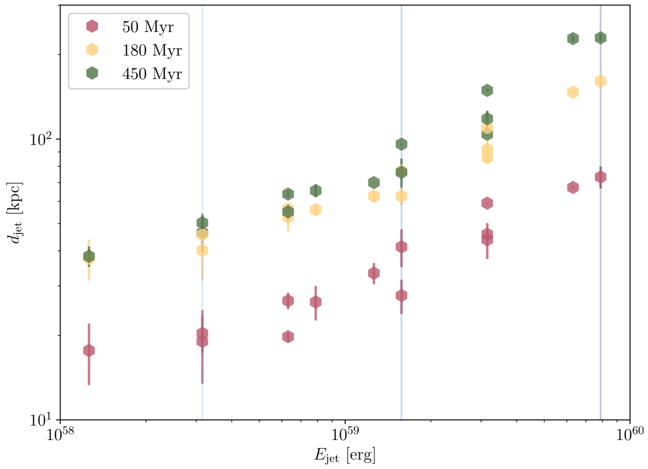

Figure 3.14: Distance of jet travel vs. jet energy of our lower resolution simulations. The jet distance d_{jet} for individual jets is defined as the distance from the SMBH to the point to which half the jet mass $X_{\text{jet}}m$ (of the upper hemisphere) has travelled (typically situated inside the lobe). We show the average distances of the upper and lower jets for every individual simulation (hexagons) and the error bar denotes the ranges for the two individual jets. There is a clear correlation of jet distance and energy at each of the three different simulation times (indicated by colour). The vertical (light blue) lines correspond to the three simulations shown in the left panel of Fig. 3.15.

Jets with constant τ_{jet} exhibit an increasing heating radius with increasing P_{jet} (Fig. 3.8, bottom left panel). A larger jet luminosity corresponds to enhanced CR production (at $\tau_{\text{jet}} = \text{const.}$) while the jet also pushes to larger radii. At small radii there is a larger variance of $\mathcal{H}_{\text{cr}}$ because of the fast CR transport to large radii in the jet which competes with the backwards CR diffusion and advection towards the dense cluster centre. Jets with $P_{\text{jet}} = \text{const.}$ produce almost self-similar $\mathcal{H}_{\text{cr}}$ profiles that scale with the amount of injected CR energy (Fig. 3.8, bottom right panel).

A successful heating mechanism in CC clusters is not required to act isotropically throughout the *entire* core region. However, as cooling material falls to the centre, eventually it should be heated at some inner radius (McNamara and Nulsen, 2012), which poses requirements for the isotropy of the proposed heating mechanism at *small* radii. To examine the volume-filling of CR heating in our simulations, we first show the volume distributions of CR energy density and Alfvén-heating rate in the top panels of Fig. 3.9. Diffusion leads to a shallow CR floor in the cluster centre and beyond at later times. To quantify the degree of CR isotropy, we define a minimum amount of the CR energy density and Alfvén heating rate by requiring that 3σ (99.8%) of CR energy and Alfvén heating power are above these floor values, respectively.

For each concentric shell of radius r, we display the volume fraction covered by cells with ϵ_{cr} (or $\mathcal{H}_{\text{A}}$) above these floor values and normalise it to the volume of the shell at this radius (bottom panels of Fig. 3.9). While the bipolar jets transport CRs mainly along the jet axes, subsonic CR advection and diffusion strongly limit lateral transport of CRs within a CR cooling time at large radii ($r \gtrsim 15$ kpc), precluding isotropic heating there. In contrast, Alfvén-wave heating is almost isotropic at small radii ($r < 15$ kpc).

In fact, observations favour a smooth heating process with only minimal temporal over-heating or -cooling (Fabian, 2012). Our simulations reproduce this property as we deduce from the evolution of the pressure and temperature profiles in Fig. 3.1. The profiles show little variance after the initial perturbation in temperature and density due to the propagating jet at 10 Myr.

The match of $\mathcal{H}_{\text{cr}}$ in our simulations to the steady-state solutions (Jacob and Pfrommer, 2017a) validates that dynamically evolved jets with plausible parameters can distribute CRs sufficiently well to successfully balance the radiative cooling losses of the ICM via CR heating on timescales $t \lesssim 30$ Myr. Future simulations including gas cooling and jet injection coupled to accretion will scrutinise the feasibility of the model on long timescales and whether it is self-regulating.

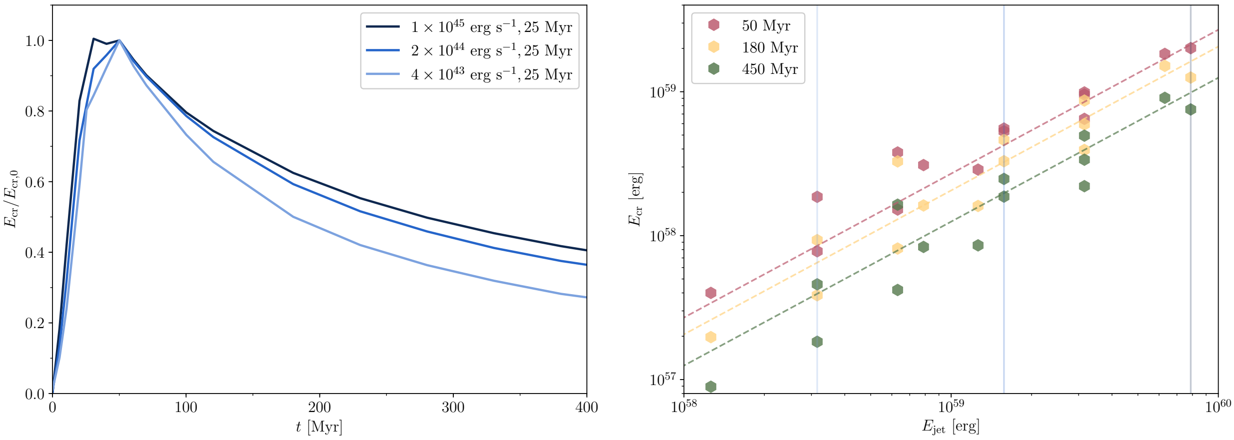

Figure 3.15: The evolution of the total CR energy as a function of jet energy for three different jet luminosities of our lower resolution simulations. On the left, we show the CR energy $E_{\rm cr}$ as a function of time normalised to its maximum value $E_{\rm cr,0}$. During the jet stage, the CR energy increases steadily until $\tau_{\rm acc}$ after which it decreases as a result of escaping CRs that suffer Alfvén wave losses in the ICM. On the right, we show the CR energy $E_{\rm cr}$ as a function of total jet energy $E_{\rm jet}$ for different simulations at three different times (colour coded). A linear fit to each of the three simulation times is shown with dashed lines and describes the simulations well. The significant scatter towards small jet energies corresponds to the increased mixing efficiency for these systems. The vertical (light blue) lines correspond to the simulations shown in the left panel.

3.7 Parameter study

The following parameter study focuses on jet power and lifetime. Here, we will show that instead of these two parameters, jet energy appears to be the most important parameter for determining jet morphology, CR distribution and magnetic field structure, whereas the jet power determines the maximum attainable Mach number.

3.7.1 Bubble morphology

In Fig. 3.10, we show how the bubble morphology changes with varying jet parameters at 70 Myr. While the jet acceleration of CRs in our subgrid model is still ongoing for jets in the bottom row, the resulting dynamical effects of this late-time acceleration ($t > \tau_{\rm jet}$) are negligible. Jet lifetime increases from top to bottom and jet power increases from left to right. Jets with similar energy are ordered along diagonals from the bottom left to the top right. In order to identify the highly anisotropic features of the bubble, Figs. 3.10, 3.11, and 3.12 show projections weighted with the jet tracer mass fraction $X_{\rm jet}$. Additionally, we show in Fig. 3.13 the Mach number $\mathcal{M}$ weighted with the energy dissipation rate at the shocks. Note that we assign a minimum value of $X_{\rm jet} = 10^{-10}$ to every cell to also display the background. The projection depth corresponds to the projection width.

We see that jet energy is responsible for setting the overall bubble morphology. Bubbles inflated with a low-power jet with a long activity time resemble bubbles originating from jets with high power but shorter lifetimes. In Fig. 3.14, we show the mean distance travelled by the jet as a function of the jet energy at three different times. We find a power-law relation $d_{\rm jet} \propto E_{\rm jet}^{\alpha}$ with $\alpha \approx 0.4$. Jets with the same energy reach similar heights, confirming the correlation. Because different jets with $E_{\rm jet} =$ const. produce bubbles of similar sizes, this implies comparable Rayleigh-Taylor lifetimes (see Section 3.5.2).

Low-energy jets inflate smaller lobes (Fig. 3.10, to the upper left), which terminate at lesser heights. They are deflected from their original jet trajectories and show clear signs of ongoing mixing (as indicated by the low density contrast with the ICM). These are the signatures of FRI-type jets according to the Fanaroff-Riley (FR) classification (Fanaroff and Riley, 1974). Increasing jet energy (top left to bottom right) results in jets that penetrate the ICM to larger distances from the cluster centre. They propagate mostly along the original jet direction and can sustain high-density contrasts for longer times. These properties resemble jets of the FRII-type category.

Producing realistic FRI jets in simulations requires resolving the radius of the jet with ≈ 10 cells (Anjiri et al., 2014), which is difficult to achieve in our large-scale simulations for our low-power jet models. In these idealised jet simulations the occurrence of low-power FRI-type jets is then attributed to the development of a turbulent structure rather then terminal shocks as in the case of high-power FRII jets. The jet power that marks a threshold between these jet categories is given by $P_{\mathrm{jet}} \sim 10^{43}$ erg s^{-1} according to simulations (Massaglia et al., 2016). Here, we can confirm that FRI-like jets are obtained in our simulations, albeit at a somewhat higher threshold luminosity. We address this point in Appendix 3.9.2 and find that while this threshold luminosity decreases with increasing numerical resolution, general properties regarding distribution of magnetic fields, CRs and heating rates remain qualitatively similar. Most importantly, we find that jet energy appears to be the leading variable to distinguish between the main FR jet features. Alternative scenarios for the origin of FRI jets include de-focusing due to a magnetic kink instability in the jet (Tchekhovskoy and Bromberg, 2016), mixing due to Kelvin-Helmholtz instabilities in sheared relativistic flows (e.g., Perucho et al., 2010) and mass entrainment from stellar winds (e.g., Wykes et al., 2015).

We leave detailed morphological studies of bubbles in cooling clusters that are generated through the interplay of accretion and jet launch for future studies. Additionally, the interaction of subsequent generations of bubbles may play a key role as they may merge and form large outflowing cavities (Cielo et al., 2018). Finally, the jet lifetime cannot be arbitrarily increased to form ever larger bubbles as these will inevitably fragment, generating multiple disconnected bubbles in a turbulent environment (Morsony et al., 2010).

3.7.2 CR distribution

Looking at the distribution of CR energy density, ϵ_{cr}, in Fig. 3.11, it becomes apparent that ϵ_{cr} is more homogeneous than the density across our models. This means that even if there is no visible cavity due to low contrast in X-rays, there may still be a substantial CR population that is responsible for efficient Alfvén wave heating.

The previously described trend that low-energy jets form bubbles that are easily deflected and dispersed early-on translates to a very centrally localised CR distribution with a high degree of isotropy (Fig. 3.11). Conversely, high-energy jets develop bubbles that stay intact out to large distances. CRs continuously diffuse out of the bubble but the majority of the CR energy is transported to large radii. This makes low-energy jets more efficient in heating the fast-cooling cluster centres. These low-energy systems have a larger mixing efficiency and their bubbles remain in the central regions of the cluster (Mukherjee et al., 2016).

The sequence of CR acceleration, bubble disruption, diffusive CR escape, and successive Alfvén cooling is expected to reflect on the available CR energy for individual jets (Fig. 3.15). Interestingly, we observe a linear correlation between CR energy and the total jet energy. When considering a sample of jets with the same energy, the jet with the longest lifetime τ_{jet} will accelerate CRs for longer periods of time. As CRs cool over time, the low-power (high-lifetime) jet is expected to maintain a larger CR energy, which explains the scatter at constant energy in Fig. 3.15.

Another source of scatter in the linear relation is due to the difference in mixing efficiency for jets with variable jet power. The left panel of Fig. 3.15 exemplifies this point as it shows the normalised CR energy for jets with constant lifetime but varying jet power. During the jet stage, the CR energy increases as kinetic energy is dissipated and transferred to CR energy until τ_{acc}. Afterwards, CR energy decreases as a result of escaping CRs that suffer Alfvén wave losses in the ICM. A decrease in jet power implies a decrease of CR energy in the entire cluster. As discussed in Section 3.5.2, low-power jets mix more efficiently, which results in earlier disruption times of the lobe and thereby an earlier onset of CR cooling.

3.7.3 Magnetic field structure

The magnetic field structure shows the draping layer wrapped around the bubbles in most of the different jet simulations (Fig. 3.12). Even though the draping layer lies outside the bubble interface with the ambient ICM, the numerically diffused advective jet tracers still highlight this feature. Consequently, the jet tracer-weighted projection leads to apparent amplification ratios of > 2. However, the actual ratios are on the order of ~ 2 as discussed in Section 3.5.1. In some exceptional cases, the draping layer remains absent. This is due to the turbulent nature of the ICM that causes perturbations in the trajectory of the bubble and generates a corrugated bubble interface as the bubble expands into a region of lower ambient pressure. The local change of propagation direction forces the bubble to accumulate a new draping layer. In addition, numerical reconnection of magnetic field lines in the turbulent environment may temporarily erase the draping layer as fields of different polarity accumulate in the layer.

We observe strongly amplified magnetic filaments in the wakes of every bubble, which reach field strengths up to 30 μG. These elongated filaments align approximately along the jet axis and point back to the cluster centre to which they conduct the diffusing CRs. These strongly magnetised magnetic structures resemble observed Hα filaments in CC clusters.

As we have seen, a large fraction of the jet tracers is mixed with the ICM in the wake of the jet. This causes the magnetic field in the region to be significantly enhanced compared to the surrounding magnetic field. Due to this effect the contrast in magnetic field strength between wake region and ICM increases for larger projection box sizes (bottom right of Fig. 3.12).

3.7.4 Shocks and Mach numbers

Most observed Mach numbers of expanding lobes that reside in CC clusters are observed to be at the order of $\mathcal{M} \sim 1$ (McNamara and Nulsen, 2007). Using a shock finder in AREPO (Schaal and Springel, 2015), we detect and characterise the bow shock that is driven into the ICM by the propagating lobes. In Fig. 3.13, we show projections of the Mach numbers of this bow shock, weighted with the energy dissipation rate at two different times, at 5 Myr and 20 Myr.

The shock strength scales with the jet power as expected. At 5 Myr, the lobes of low-power jets ($\leq 2 \times 10^{44}$ erg s^{-1}) predominantly exhibit Mach numbers $\mathcal{M} \lesssim 1.5$, similar to observations. In contrast, the lobes of high-power jets ($> 2 \times 10^{44}$ erg s^{-1}) exhibit strong Mach numbers $\mathcal{M} > 4$. However after 20 Myr those have already decreased to values of $\mathcal{M} \sim 2 - 3$. After the jet is switched off, only individual cells exhibit Mach numbers $\mathcal{M} > 1$. Thus, even our lobes from high-power jets only exhibit high Mach numbers for a short period of time and low-to-intermediate Mach numbers for most of the time the jet is active. We conclude that our simulations successfully reproduce the observed low Mach numbers for the lobes of low-power jets.

3.8 Conclusions

Using 3D MHD simulations with the moving-mesh code AREPO, we study the evolution of magnetised and CR-filled jets in an idealised Perseus galaxy cluster. Following the jet-driven inflation of underdense bubbles, we study their buoyant rise in the cluster atmosphere and how they interact with a turbulent cluster magnetic field. The bubbles are exposed to interface instabilities which finally disrupt the bubbles and enable initially confined CRs to diffusively escape and to heat the ambient ICM. Here we summarise our main findings:

- The accumulation of magnetic fields at the bubble interface as a result of buoyant bubble motion relative to the ambient ICM stabilises the bubble against the turbulent environment, suppresses Kelvin-Helmholtz instabilities, and reduces the mixing efficiency. Internal helical magnetic fields show a similar effect.

- We find that a decrease in jet power and/or in total jet energy increases the mixing efficiency of the jet.

- CRs inside the bubbles are confined by the draped magnetic field that inhibits diffusion across the bubble surface.

- In the wake of the bubble, the magnetic field is strongly amplified and adiabatically compressed by converging inflows that are compensating the upwards motion of the bubble. Differential motions stretch the magnetic field so that it becomes filamentary and aligned along the jet axis. These strongly magnetised filaments acquire strengths of 30 μG and resemble observed Hα filaments in clusters. We postpone a detailed study to future work.

- These radial magnetic filaments connect the bubble interior to the ambient ICM, and allow CRs to diffusively escape into the ICM and heat the surrounding medium. Our simulated radial profiles of the CR-induced Alfvén wave heating rate match CR heating rates predicted by steady-state models of CC clusters extremely well (Jacob and Pfrommer, 2017a). Inside a radius $r \lesssim 15$ kpc, we find a volume-filling CR distribution that generates isotropic Alfvén wave heating, which is necessary for solving the cooling flow problem at the centres of clusters. The temporal evolution varies significantly such that time-dependent modeling becomes crucial.

- A parameter study of different jet simulations with varying jet lifetime and jet power reveals that the jet energy is the critical parameter for determining the overall bubble morphology and CR distribution. Magnetic draping as well as the strong filamentary magnetic field amplification in the wakes is ubiquitous in our sample.

- We find a high degree of coherence and decreasing mixing efficiency with increasing jet energies. This finding and the observed low Mach numbers show that we can reproduce the main features of both, FRI and FRII-like jets: FRII jets exhibit bipolar, lobe-brightened morphologies with high density contrasts that power high Mach numbers $\mathcal{M} \sim 4$ in the ICM at early times. On the other hand, FRI jets are characterized by lower density contrasts, show more deflected and corrugated bubbles that generate a laterally more expanded CR distribution at the centre, and do not drive detectable shocks into the ICM.

These results encourage further studies of the impact of CR-filled AGN bubbles on radiatively cooling CC cluster atmospheres. Accounting for accretion onto SMBHs and successive jet formation will enable us to find out whether we can obtain a self-regulated CR heating-radiative cooling cycle.

Acknowledgements

We thank the anonymous referee for helpful suggestions and comments. This work has been supported by the European Research Council under ERC-CoG grant CRAGSMAN-646955, ERC-StG grant EXAGAL-308037 and by the Klaus Tschira Foundation.

3.9 Appendix

3.9.1 Magnetic Field Generation

The external turbulent magnetic field follows a Kolmogorov spectrum in agreement with observations (Bonafede et al., 2010; Kuchar and Enßlin, 2011). The generation of the initial conditions for the magnetic field follows largely Appendix A in Ruszkowski et al. (2007). The Gaussian-distributed random magnetic field with vanishing mean ($\langle \boldsymbol{B} \rangle = \boldsymbol{0}$ but $\sqrt{\langle \boldsymbol{B}^2 \rangle} \neq 0$) is set up with a Kolmogorov power spectrum in Fourier space. The magnetic field is scaled to ensure a shell-averaged constant magnetic-to-thermal pressure ratio $X_{B,\mathrm{ICM}} = P_B/P_{\mathrm{th}}$ throughout the cluster. The three components of the magnetic field B_i ($i \in \{1, 2, 3\}$) are treated independently to ensure that the final distribution of $\boldsymbol{B}(\boldsymbol{x})$ has a random phase. The large discrepancy between minimum cell size and computational box size necessitates the interpolation of fields from multiple nested Cartesian grids with increasing resolution onto our initial setup.

First, we compute Gaussian-distributed field components that obey a one-dimensional power spectrum $P_i(k)$, given by $P_i(k) \propto k^2|\tilde{B}_i(k)|^2$, with

$$|\tilde{B}_i(k)|^2 = \begin{cases} A, & k < k_{\mathrm{inj}}, \\ A\left(\dfrac{k}{k_{\mathrm{inj}}}\right)^{-11/3}, & k_{\mathrm{inj}} \leq k, \end{cases} \tag{3.5}$$

where A is a normalisation constant, $k = |\boldsymbol{k}|$, and k_{inj} is the injection scale of the field. Modes on large scales ($k < k_{\mathrm{inj}}$) follow a random white-noise distribution while modes in the inertial range ($k > k_{\mathrm{inj}}$) obey a Kolmogorov power spectrum. For each magnetic field component, we set up a complex field such that

$$[\mathfrak{Re}(\tilde{B}_i(\boldsymbol{k})), \mathfrak{Im}(\tilde{B}_i(\boldsymbol{k}))] = [G_1(\Lambda_1, \Lambda_2, \sigma_k), G_2(\Lambda_1, \Lambda_2, \sigma_k)], \tag{3.6}$$

where Λ_1 and Λ_2 are uniform random deviates so that the function $G_i(\Lambda_1, \Lambda_2, \sigma_k)$ ($i \in \{1, 2\}$) returns Gaussian-distributed values with standard deviation $\sigma_k = \tilde{B}_i$ for every value of k. We then normalise the spectrum to the desired variance of the magnetic field components in real space, σ_B using Parseval's theorem,

$$\sigma_B^2 = \frac{1}{N^2} \sum_i \sum_{k_j} |\tilde{B}_i(k_j)|^2. \tag{3.7}$$

To eliminate overlapping magnetic field lines between different nested meshes, we (i) reorient radial field lines in the overlap region and (ii) remove the inner part of our coarser mesh via a spherical tapering function and replace it with the tapered high-resolution mesh. Since this process introduces divergences in the magnetic field, we iteratively perform divergence cleaning steps while accounting for the reorientation of radial magnetic field:

1. *Divergence cleaning in Fourier space.* We eliminate the field component in the direction of $\boldsymbol{k}$, via the projection operator:

   $$\tilde{\boldsymbol{B}} \rightarrow \tilde{\boldsymbol{B}} - \hat{\boldsymbol{k}}(\hat{\boldsymbol{k}} \cdot \tilde{\boldsymbol{B}}) \tag{3.8}$$

   in order to fulfil the constraint $\nabla \cdot \boldsymbol{B} = 0$.

2. *Field rescaling to constant $X_{B,\mathrm{ICM}}$.* We rescale the magnetic field to obtain a constant average value of $\langle X_{B,\mathrm{ICM}}(r) \rangle$ in thin concentric shells of radius r around the cluster centre.

3. *Cleaning and smoothing transition regions between meshes.* In order to prevent interconnecting field lines between meshes, we force the radial magnetic field lines to bend in the overlap regions of different meshes. To this end, we remove the radial component of the magnetic field in real space via

   $$\boldsymbol{B} \rightarrow [1 - g(r)\hat{\boldsymbol{r}}\hat{\boldsymbol{r}}]\boldsymbol{B} \tag{3.9}$$

   where $\hat{\boldsymbol{r}}$ is the unit radial vector and

   $$g(r) = 1 - \left|\cos\left(\frac{\pi}{2}\frac{x + \Delta x - 1}{\Delta x}\right)\right| \tag{3.10}$$

   for $1 - \Delta x < x < 1 + \Delta x$ with $x = r/r_{\mathrm{m}}$ and $\Delta x = 0.05$. The overlap radius of the two meshes is given by r_{m}.

   Afterwards, we taper the field strength in the overlapping regions of one mesh with a spline $f_S(x) = 0.5\cos(\pi(r - r_m)/d_m)$, where the taper width d_m is set to the larger (outer) cell size of the two adjacent meshes. Its neighbouring mesh uses the spline $f_C(x) = 1 - f_S(x)$.

   Steps (i)-(iii) are repeated until the divergence of the magnetic field has sufficiently decreased. The resulting field is interpolated on our adaptive, smoothly varying mesh in the initial conditions, which are setup in hydrostatic equilibrium. To maintain this equilibrium, the temperature is varied according to

   $$n k_{\mathrm{B}} \delta T = -\frac{\delta \boldsymbol{B}^2}{8\pi}. \tag{3.11}$$

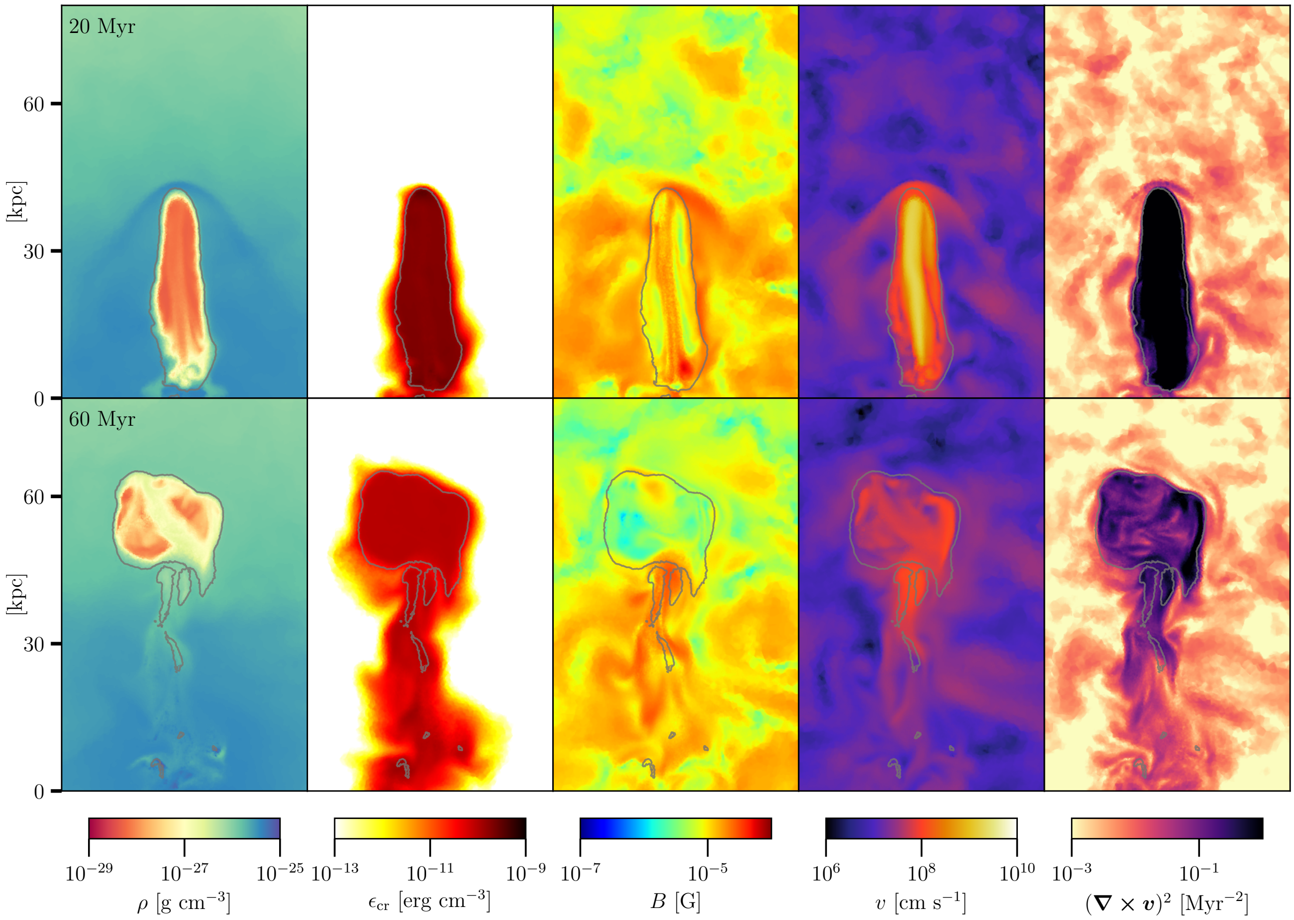

Figure 3.16: Same model as in Fig. 3.3 at lower resolution with projection dimensions 80 kpc × 50 kpc × 4 kpc. Because magnetic tension is less well resolved and more affected by numerical diffusion, the external magnetic field strength and turbulent motions are smaller in amplitude. Moreover, at lower numerical resolution the velocity gradient at the jet foot is not sufficiently resolved, which implies that the jet does not travel as far as for the high-resolution simulation. Thus, momentum transport is less efficient here.

Finally, we relax the mesh with AREPO so that a remaining (small) divergence is cleaned with the Powell algorithm. To reverse the decrease of the magnetic field strength due to the conversion from magnetic to turbulent energy, we rescale the magnetic field with a constant factor and obtain $X_{B,\rm ICM}$.

3.9.2 Resolution study

To test numerical convergence, we compare simulation runs with the fiducial jet parameters at high and lower resolution (cf. Table 3.2). The overall evolution (Fig. 3.16) of the jet remains qualitatively similar. However there are (smaller) quantitative differences such as the emergence of Kelvin-Helmholtz instabilities on the jet surface in our high-resolution simulation. That instability remain dynamically subdominant as the more dominant Rayleigh-Taylor instability starts to develop. However, the magnetic field strengths in the ICM remain larger for longer time scales in comparison to the run at fiducial resolution since we better resolve magnetic tension due to the lower level of numerical diffusion. This increased level of magnetic turbulence causes the bubble to change direction more often at late times.

As discussed in Weinberger et al. (2017), the distance travelled by the jet is resolution dependent. For this, resolving the velocity structure of the jet proves crucial. The jet expands more laterally at lower resolution as the prescribed jet width used for all simulations is insufficient to resolve the velocity gradient of the jet. The jet compensates by broadening. This spreads the area of the effective momentum leading to a decrease of the jet velocity and thus a smaller distance travelled at lower

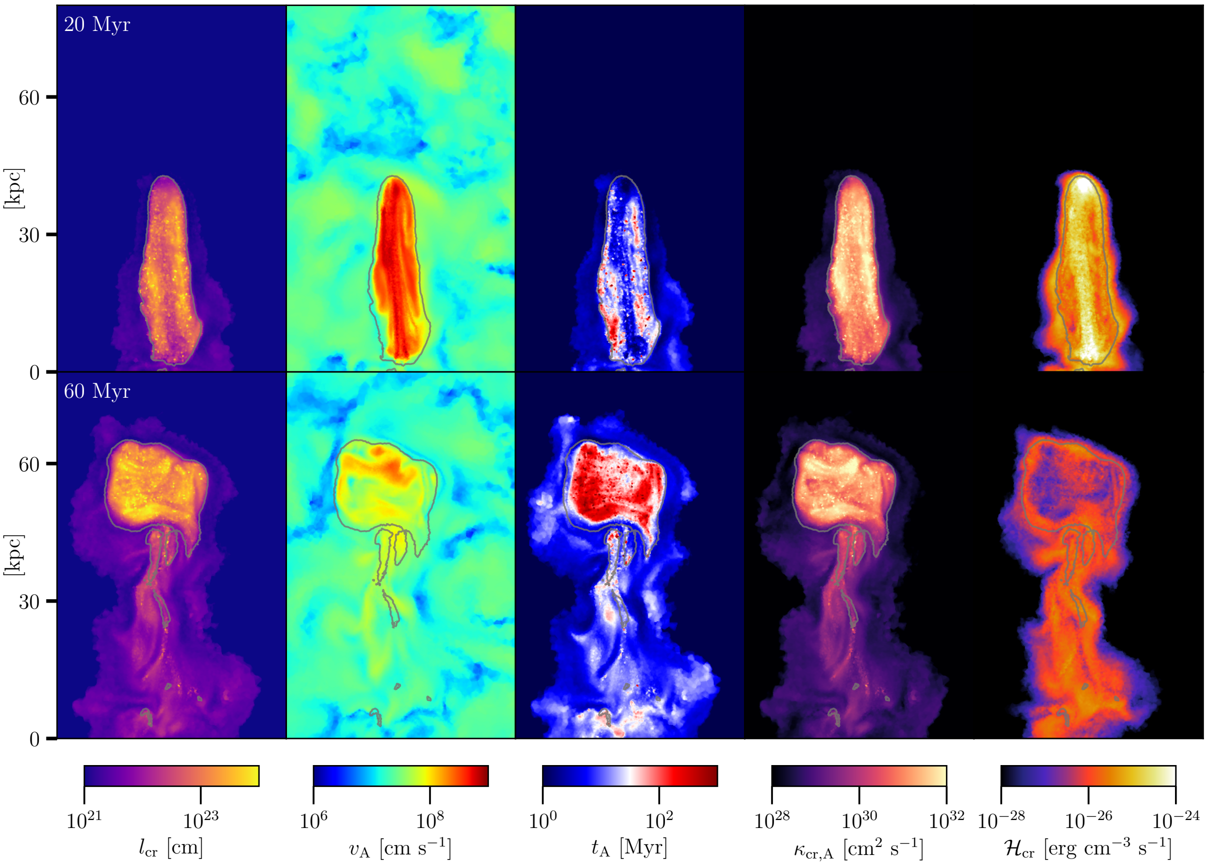

Figure 3.17: Same model as in Fig. 3.7 at lower resolution with projection dimensions 80 kpc × 50kpc × 4 kpc. The exact distribution of CRs depends somewhat on resolution because jet the distance of jet travel increases with numerical resolution. However, the quantities related to CR transport ($\kappa_{\rm cr,A}$ and $\mathcal{H}_{\rm cr}$) show general agreement with our high-resolution simulation.

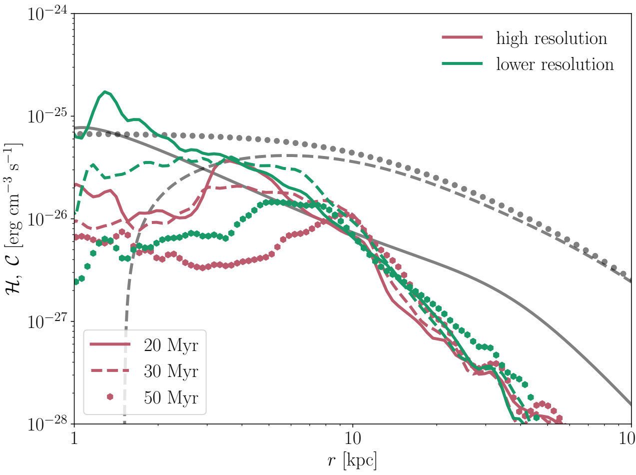

Figure 3.18: Comparing the Alfvén-wave heating rate due to streaming CRs for our low- and high-resolution simulations at t = 20, 30 and 50 Myr (see also Fig. 3.8). While the jet in the high-resolution simulation propagates further, the CR heating rate drops slightly in the cluster centre by a factor of less than two.

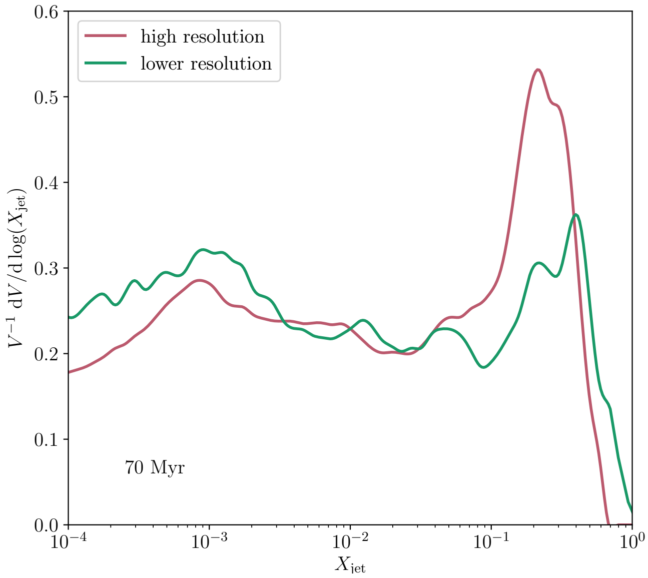

Figure 3.19: Comparing the mixing efficiency of the bubble for CR simulations at different numerical resolutions (cf. Fig. 3.6). To ensure an unbiased comparison we show the normalised filling factor of a given jet mass fraction $V^{-1}\ \mathrm{d}V/\mathrm{d}\log(X_\mathrm{jet})$. Mixing is suppressed at higher resolutions due to the more compact jet that propagates to larger distances. The lines are smoothed for clarity.

resolution. However, the properties of CRs remain robust against changes in resolution (Fig. 3.17 vs. Fig. 3.7).

Figure 3.18 compares radial profiles of the Alfvén heating rate for our fiducial and high-resolution simulations. Because better resolved jets travel further, the Alfvén heating rate is somewhat increased at larger distances for the high resolution run. This faster transport to larger distance comes at the price of a somewhat reduced heating rate at smaller radii. However, these differences stay below a factor of two, reinforcing the robustness of our result on CR heating with respect to numerical resolution.

Even though the increased level of turbulence should be able to amplify the mixing efficiency, the high-resolution run shows a significantly lower degree of mixing in comparison to the fiducial (see Fig. 3.19). Possible causes of this are (i) faster transport of CRs to larger distance which delays the onset of the Rayleigh-Taylor instability and the successive disruption of the bubble and (ii) better resolved magnetic field structures in the jet as well as in the draping layer. Additionally, (iii) increased numerical diffusivity at lower resolution facilitates mixing.

In conclusion, all discussed results are qualitatively robust to changes in resolution. However, quantitative findings may be subject to (minor) revision. This is in particular the case for the transition energy of FRI- and FRII-like jets, which moves to lower values with increasing resolution, thus, resolving the discrepancy of our runs with idealised jet simulations (Massaglia et al., 2016). Here, we choose fiducial (moderate) resolution since we run a comprehensive parameter study to address the impact of CRs and turbulent magnetic fields on a large variety of jet luminosities and activity times. Moreover, this papers also serves as a first step towards studying self-regulated CR-AGN feedback in cosmological cluster simulations in which we have resolution requirements not too dissimilar from the adopted resolution.

3.9.3 Bubble cooling

To remain consistent with our definition of the lobe, i.e., $X_\mathrm{jet} < 10^{-3}$, we set the jet tracer threshold for CR acceleration and cooling to $X_\mathrm{jet,acc} = X_\mathrm{jet,cool} = 10^{-3}$. To test the robustness of our choice, Fig. 3.20 shows radial profiles of the CR-induced Alfvén wave heating rate if we vary $X_\mathrm{jet,acc}$ and $X_\mathrm{jet,cool}$ each by one order of magnitude. In the inner 10 kpc, the CR distributions agree within a factor of a few. Further out in the vicinity of the bubbles, the radial profiles agree well. We generally

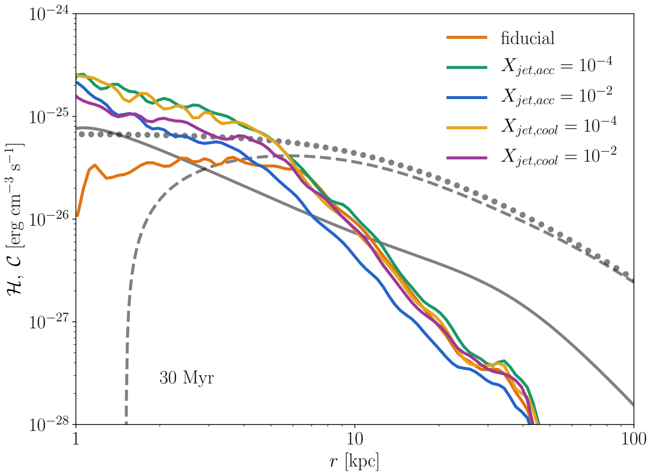

Figure 3.20: Same as in Fig. 3.8, here showing profiles of lower resolution simulations with varying jet tracer thresholds for subgrid CR acceleration $X_{\mathrm{jet,acc}}$ and CR Alfvén cooling $X_{\mathrm{jet,cool}}$ at 30 Myr. Varying the thresholds by an order of magnitude in both directions, the resulting heating rate differs at most by a factor of a few at small radii and converges at large radii.

find that changing the cooling threshold $X_{\mathrm{jet,cool}}$ has a smaller impact than varying the acceleration threshold $X_{\mathrm{jet,acc}}$.

The Sunyaev-Zel’dovich effect of simulated jet-inflated bubbles in clusters

4

This chapter is an adapted version of the paper *The Sunyaev-Zel’dovich effect of simulated jet-inflated bubbles in clusters* published as Ehlert et al. (2019).

4.1 Abstract

Feedback by active galactic nuclei (AGNs) is essential for regulating the fast radiative cooling of low-entropy gas at the centers of galaxy clusters and for reducing star formation rates of central ellipticals. The details of self-regulation depend critically on the unknown contents of AGN-inflated bubbles. Observations of the Sunyaev-Zel’dovich (SZ) signal of AGN bubbles provide us with the ability to directly measure the lobe electron pressure given a bubble morphology. Here we compute the SZ signal of jet-inflated bubbles in three-dimensional magnetohydrodynamical simulations of the galaxy cluster MS0735.6+7421 with the Arepo code, and compare our synthetic SZ results to inferences obtained with popular modelling approaches. We find that cutting out ellipsoidal bubbles from a double-beta pressure profile only matches the inner bubble edges in the simulations and fails to account for the emission of the shock-enhanced pressure cocoon outside the bubbles. This additional contribution significantly worsens the accuracy of the cut-out method for jets with small inclinations with respect to the line of sight. Also, the kinetic SZ effect of the bubbles, a previously neglected contribution, becomes relevant at these smaller inclinations due to entrainment and mixing of the intracluster medium with low-density jet material. Fortunately, the different signs of the kinetic SZ signal in opposite lobes allow modelling this effect. We present an approximate method to determine the jet inclination, which combines jet power and lifetime estimates, the stand-off distance between jet head and bow shock, and the kinetic SZ effect, thereby helping to correctly infer the bubble contents.

4.2 Introduction

The radiative cooling time of the intra-cluster medium (ICM) in the center of cool core clusters is less than 1 Gyr. The central AGN provides a powerful heating source that offsets cooling and reduces star formation (McNamara and Nulsen, 2012). AGN jets power lobes, which detach and buoyantly rise in the cluster atmosphere. However, the detailed lobe content and thus, the heating mechanism remains uncertain. While X-ray observations can only provide lower limits to the temperature of lobes (Worrall, 2009), the SZ signal (Sunyaev and Zeldovich, 1972) is directly sensitive to the thermal and non-thermal heat contents. Hence, SZ observations of bubbles have been suggested (Pfrommer et al., 2005) and simulated (Prokhorov et al., 2012; Yang et al., 2018) to understand the physics of the heating mechanism. Recently, Abdulla et al. (2019) observed the cavities of the cluster MS 0735.6+7421 (hereafter MS0735) and found that they have very little SZ-contributing material. This suggests a lobe pressure support of diffuse thermal plasma with temperature in excess of hundreds of keV, or non-thermal relativistic particle populations.

Assuming energy equipartition between relativistic electrons and magnetic fields, radio synchrotron observations also necessitate an additional pressure component (Bîrzan et al., 2008), suggesting relativistic protons as a likely candidate that matches jet morphologies (Croston et al., 2018). As these cosmic ray (CR) protons escape into the ICM, they resonantly excite Alfvén waves. Damping of those waves provides a promising heating scenario (Guo and Oh, 2008; Enßlin et al., 2011; Fujita and Ohira, 2012; Pfrommer, 2013; Jacob and Pfrommer, 2017a,b). Jet-driven bubble simulations in a galaxy cluster (Ruszkowski et al., 2017; Ehlert et al., 2018) demonstrate that streaming CRs from the bubbles provide a sufficient heating rate to halt the cooling catastrophe. Alternative AGN heating mechanisms include mixing of hot-bubble gas with the ICM (Soker, 2016), dissipation of sound waves (Fabian et al., 2017), weak shocks (Li et al., 2017), turbulence (Zhuravleva et al., 2014; Bambic et al., 2018b) and/or gravity waves (Bambic et al., 2018a).

Early simulations of AGN bubbles reproduce the main features of observed X-ray cavities (Churazov et al., 2001; Brüggen et al., 2009). Simulations including magnetic fields (Robinson et al., 2004; Ruszkowski et al., 2007) and/or viscosity (Reynolds et al., 2005; Sijacki and Springel, 2006) stabilize the bubble against developing fluid instabilities. Turbulence and substructure show a significant impact on bubble dynamics (Heinz et al., 2006; O'Neill and Jones, 2010; Mendygral et al., 2012). The addition of CRs in bubbles leads to more elongated bubbles that reside closer to the cluster center, which is favoured by observations (Sijacki et al., 2008; Guo and Mathews, 2011). Recent simulations gained higher resilience against numerical mixing due to sophisticated refinement criteria (Weinberger et al., 2017; Bourne and Sijacki, 2017). This allows for more realistic (higher) density contrasts between simulated bubbles and ICM on long time scales.

For the first time, we use MHD jet simulations to study how the thermal and kinetic SZ signal of dynamical jet-blown bubble simulations compare to the simplified modelling of bubbles as ellipsoids. To facilitate observational comparison, we simulate CR-filled bubbles in a turbulent and magnetized cluster. We pick the observationally favoured, largest observed AGN outbreak in MS0735 to exemplify our analysis (McNamara et al., 2005; Colafrancesco, 2005).

We describe our simulation methods and setup in Section 4.3. In Section 4.4, we summarize the characteristics of jet evolution and the details of our SZ modelling. We show the expected signal of simulated bubbles with different fillings in Section 4.5 and compare the SZ signal from a simulated bubble to a modelled ellipsoidal bubble. In Section 4.6, we discuss our findings regarding the kinetic SZ effect from our simulated bubbles and the influence of jet inclination on the SZ signal. We propose a method of combining simulations and observations to constrain jet inclination enabling more stringent limits on bubble content. We conclude in Section 4.7.

4.3 Simulations

To study the SZ signal from an AGN bubble, we simulate a jet, which self-consistently inflates an MS0735-like bubble in a turbulently magnetized cluster atmosphere. We use the same simulation techniques as for the fiducial run in Ehlert et al. (2018) with parameters adopted to the outburst and ICM in MS0735.

The dark matter profile is modelled after MS0735 as a static Navarro-Frenk-White (NFW) profile with $M_{200,\mathrm{c}} = 1.5 \times 10^{15}\ \mathrm{M}_\odot$, $R_{200,\mathrm{c}} = 2.43$ Mpc and concentration parameter $c_{\mathrm{NFW}} = 3.8$ (Gitti et al., 2007). The electron number density follows a double-beta profile fit to MS0735 (Vantyghem et al., 2014) modified to obtain a gas fraction of 16% at $R_{200,\mathrm{c}}$:

$$\begin{aligned} n_\mathrm{e} = 0.05 &\left[1 + \left(\frac{r}{100\ \mathrm{kpc}}\right)^2\right]^{-4.9} \mathrm{cm}^{-3} \\ + 0.01 &\left[1 + \left(\frac{r}{400\ \mathrm{kpc}}\right)^2\right]^{-1.6} \mathrm{cm}^{-3}. \end{aligned} \tag{4.1}$$

The Gaussian-distributed, turbulent magnetic field is generated in Fourier space and exhibits a Kolmogorov power spectrum on scales larger than the injection scale $k_{\mathrm{inj}} = 37.5^{-1}\ \mathrm{kpc}^{-1}$. On scales $k < k_{\mathrm{inj}}$ the spectrum follows a white noise distribution. The magnetic field is scaled in concentric spherical shells to obtain a predefined average magnetic-to-thermal pressure ratio of $X_{B,\mathrm{ICM}} = 0.05$. Multiple nested meshes of magnetic fields with decreasing resolution from the central AGN, respectively, are required for the large range in spatial resolution within the box. Overlapping regions of neighbouring meshes are iteratively smoothed and cleaned off magnetic divergence. The initial Cartesian mesh is relaxed to obtain a honeycomb-like structure, which is more efficient for the unstructured, moving mesh code AREPO. When evolved, the magnetic field drives turbulence through tension forces, which gradually decrease the magnetic field strength. Thus, we rescale the magnetic field to the desired $X_{B,\mathrm{ICM}}$ to obtain our initial conditions (see Ehlert et al., 2018, for further details).

We model the jets by injecting kinetic energy in two spherical regions with radius $r_j = 1.65$ kpc on opposite sides of the centrally placed supermassive black hole (BH) particle. Mass is removed from these injection regions and thermal energy is added from the surroundings to obtain low-density jets ($\rho_{\mathrm{jet}} = 10^{-28}$ g cm^{-3}, $\rho_{\mathrm{jet}}/\rho_{\mathrm{ICM}} \sim 10^{-4}$) in pressure equilibrium with the ICM (for more details, see Weinberger et al., 2017). Our fiducial run features a jet with power $P_{\mathrm{jet}} = 2\times10^{46}$ erg s^{-1} and lifetime $\tau_{\mathrm{jet}} = 150$ Myr, amounting to an injected energy $E_{\mathrm{jet}} = P_{\mathrm{jet}}\tau_{\mathrm{jet}} \approx 10^{62}$ erg in MS0735 (Vantyghem et al., 2014). In addition, we inject a helical magnetic field in the jet region with magnetic-to-thermal pressure ratio $X_{B,\mathrm{jet}} = 0.1$. Our lobes are defined via an advective scalar X_{jet}, which is set to unity in the jet injection region. We define our lobes as the union of all cells with $X_{\mathrm{jet}} > 10^{-3}$. During jet activity CRs are accelerated in the lobes by converting thermal energy to CR energy whenever the CR-to-thermal pressure X_{cr} ratio falls below a predefined value $X_{\mathrm{cr}} < X_{\mathrm{cr,acc}} = 1$. We explicitly isolate our jet injection region magnetically to inhibit unphysical CR diffusion.

In addition to advection, CRs are expected to scatter on self-excited Alfvén waves in galaxy clusters (Kulsrud and Pearce, 1969; Enßlin et al., 2011). The low efficiency of Alfvén wave damping in the ICM limits the CRs to *stream* down their pressure gradient ∇P_{cr} along magnetic field lines at the Alfvén speed $\boldsymbol{v}_{\mathrm{A}}$ (Wiener et al., 2013). The damping of Alfvén waves effectively transfers CR to thermal energy, giving rise to the so-called Alfvén heating with a power $\mathcal{H}_{\mathrm{cr}} = |\boldsymbol{v}_{\mathrm{A}} \cdot \nabla P_{\mathrm{cr}}|$.

The equations of MHD are discretized on a moving-mesh and evolved with second-order accuracy using the massively parallel AREPO code (Springel, 2010; Pakmor et al., 2016b). Cosmic rays are treated as a second fluid including hadronic and Coulomb losses (Pfrommer et al., 2017). These losses are small in comparison to Alfvénic losses, which we include here. In combination with anisotropic diffusion (Pakmor et al., 2016a) (with a parallel diffusion coefficient $\kappa_{\parallel} = 10^{29}$ cm^2 s^{-1}) this is used to emulate CR streaming. We employ mass-based refinement with target mass $m_{\mathrm{target}} = 1.5\times10^6\ M_{\odot}$. In addition, we impose a refinement criterion based on the density gradient, jet scalar and cell volume difference as in Weinberger et al. (2017) to maintain the large density contrast at the jet-ICM interface with target volume V_{target} ($V_{\mathrm{target}}^{1/3} = 405$ pc).

4.4 Evolving SZ signal from simulated bubbles

Free electrons in the ICM Compton up-scatter cosmic microwave background (CMB) photons. We follow the procedure described in Pfrommer et al. (2005) to compute the resulting SZ signal of our ICM and bubbles. The relative change $\delta i(x)$ in the flux density as a function of dimensionless frequency $x = h\nu/(kT_{\mathrm{CMB}})$ is given by

$$\begin{aligned}\delta i(x) =& g(x) y_{\mathrm{gas}}[1+\delta(x,T_e)] - h(x) w_{\mathrm{gas}} \\ &+ [j(x) - i(x)]\tau_{\mathrm{rel}}.\end{aligned} \tag{4.2}$$

with the Planckian distribution of the CMB given by

$$I(x) = i_0 i(x) = i_0 \frac{x^3}{\exp(x)-1}, \tag{4.3}$$

where $i_0 = 2(kT_{\mathrm{CMB}})^3/(hc)^2$ and $T_{\mathrm{CMB}} = 2.725$ K. The first term in Equation (4.2) describes the thermal SZ effect that is proportional to the integrated thermal pressure of the ICM along the line of sight $y_{\mathrm{gas}} \propto \int dl\ n_{\mathrm{e,gas}} kT_{\mathrm{e}}$. Relativistic corrections $\delta(x, T_{\mathrm{e}})$ become relevant at high temperatures $kT_e \gtrsim 5$ keV (Mroczkowski et al., 2018). Throughout the analysis, we include relativistic corrections from Itoh et al. (1998). The second term corresponds to the kinetic SZ effect due to gas motion relative to the Hubble flow $w_{\mathrm{gas}} \propto \int dl\ n_{\mathrm{e,gas}} v_{\mathrm{gas}}$, where $v_{\mathrm{gas}} < 0$ if the gas is approaching the observer. The last

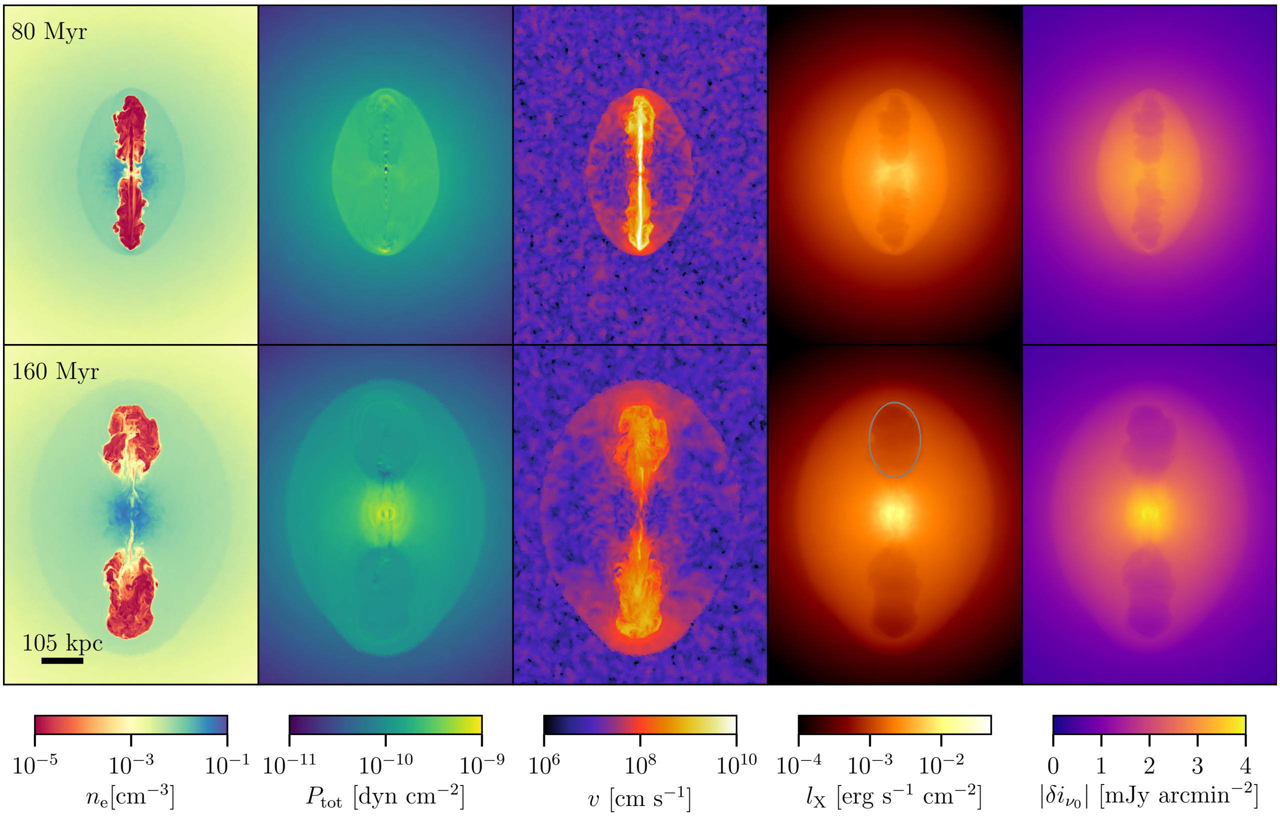

Figure 4.1: We show the electron density n_e, total pressure P_{tot} ($P_{\mathrm{tot}} = P_{\mathrm{th}} + P_{\mathrm{cr}} + P_B$), velocity v, X-ray emissivity integrated along the line-of-sight l_X and the SZ signal $|\delta i_{\nu_o}|$ of the fiducial run at times 80 Myr and 160 Myr (top and bottom row, respectively). For the SZ effect, we assume a bubble filled with relativistic electrons and an observing frequency ν_0 = 30 GHz. The images correspond to projections of thin layers (1000 kpc × 750 kpc × 4 kpc) centred on the BH and weighted by cell volume except for the density-weighted velocity. The jet terminates at 150 Myrs after which buoyantly rising bubbles form that can be observed as cavities in X-ray and SZ images. The grey contour exemplifies our ellipsoidal bubble model.

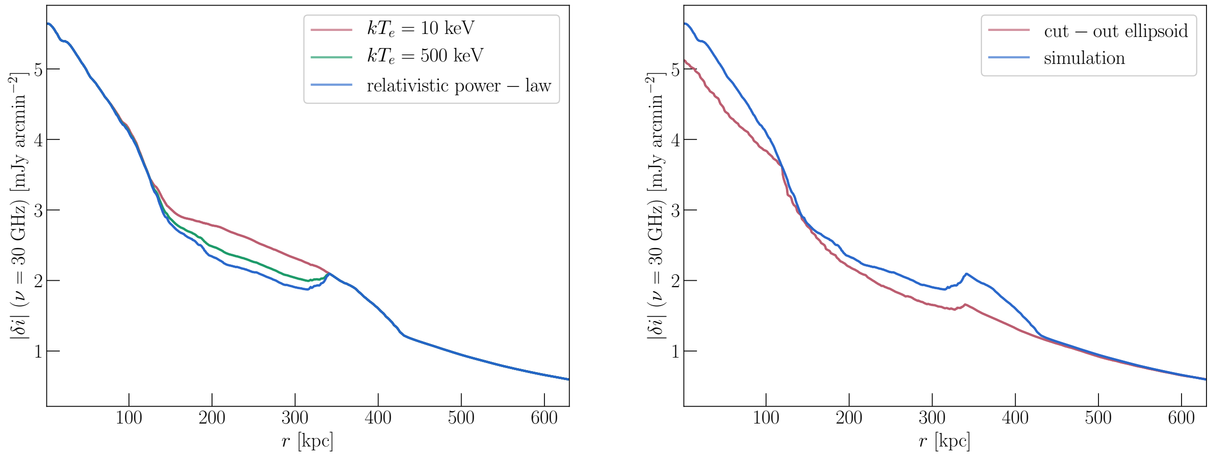

Figure 4.2: On the left-hand side, we show profiles of the SZ signal along the jet axis at 180 Myr. We vary the filling from thermal (kT_e = 10 keV) electrons to relativistic electrons that either follow a thermal distribution (kT_e = 500 keV) or a power-law distribution. Relativistically filled bubbles show a significantly larger SZ contrast, which is used to constrain the bubbles' content. On the right-hand side, we contrast the profiles of our simulated bubble to an ellipsoidal cut-out from our initial conditions, in which the jet outburst is viewed perpendicular to the line of sight. The cut-out approximation mimics the signal of the simulated bubble well at the inner rim and starts to deviate towards the bubble edges due to the increased pressure of the shocked cocoon that surrounds the bubble in the simulation.

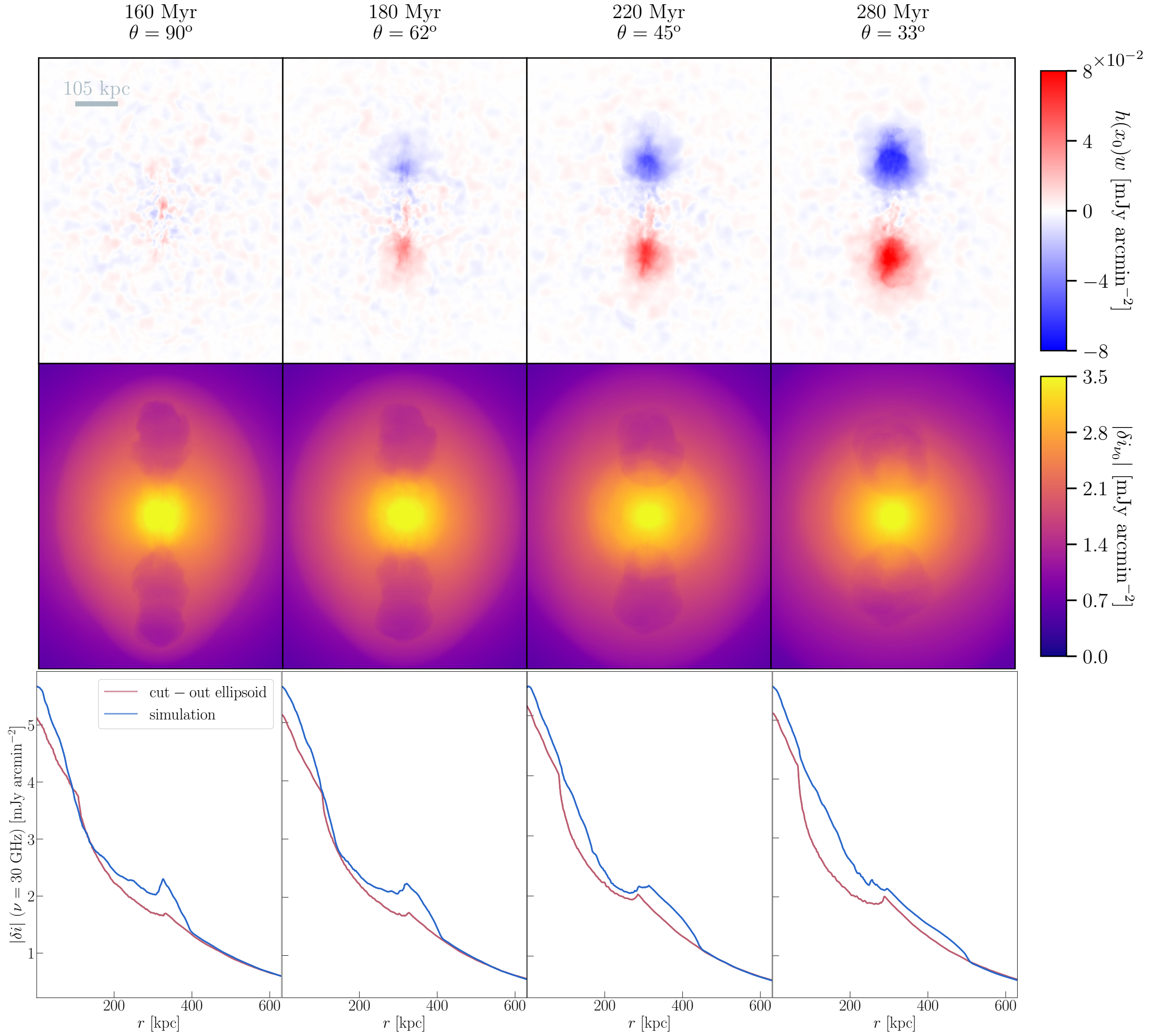

Figure 4.3: The top row shows the integrated kinetic SZ effect $h(x_0)w$ at frequency $\nu_0 = 30$ GHz. The panels in the middle row show the thermal SZ signal for bubbles, which are filled with a relativistic power-law electron distribution. The angle of inclination θ between jet axis and line of sight is decreased from left to right. The images have dimensions 1000 kpc × 750 kpc and are centred on the BH. At low angles, i.e., $\theta = 33°$, the kinetic SZ signal can reach values of up to 10% of the total SZ signal. The lower panel shows profiles of the SZ signal along the jet axis of the simulated bubbles (blue) and the cut-out model (red). While the model matches the simulations at the inner bubble edge for high values of inclinations, it differs significantly for lower inclinations as CMB photons intersect a larger portion of the ellipsoidal shocked cocoon including the central dense cool core region.

term describes the relativistic SZ effect. For fully relativistic fillings the distribution function of the electrons determines the form of $j(x)$ and $\tau_{\rm rel} \propto \int dl\ n_{\rm e,rel}$. Only the terms $g(x)$, $h(x)$ and $i(x)$ depend on observing frequency.

Throughout the Letter, we focus on three different bubble fillings: 1.) a thermal electron distribution with $kT_{\rm e} = 10$ keV, 2.) a single-temperature, relativistic Maxwellian with $kT_{\rm e} = 500$ keV and 3.) a single-temperature, relativistic electron population that follows a power-law in normalized momentum-space $p = \gamma_{\rm e}\beta_{\rm e}$ defined by

$$f_{\rm CRe}(p, \alpha, p_1, p_2) = \frac{(\alpha - 1)p^{-\alpha}}{p_1^{1-\alpha} - p_2^{1-\alpha}}, \tag{4.4}$$

where $\alpha = 2$, $p_1 = 1$ and $p_2 = 10^3$. For all three models, we recompute the electron density of lobe cells while keeping the total (simulated) pressure $P_{\rm tot}$.

In Fig. 4.1, the initial jet inflates lobes which, after jet shut-down, rise buoyantly in the cluster atmosphere. The high jet power leads to jet velocities approaching the speed of light, where our non-relativistic treatment degrades in accuracy. While this influences the details of the kinematics and shock dissipation (Perucho et al., 2017), our results on bubble morphology and SZ signal are expected to be robust. The jet initially drives a shock wave into the ICM. Generally, the Mach number in the jet direction exceeds that perpendicular to the jet, thereby creating an ellipsoidal shock. The trailing contact discontinuity is clearly visible in the electron number density n_e and temperature T maps. The dimensions of the bubbles and the morphology of the contact discontinuity in the X-ray brightness $l_{\rm X}$ are in good agreement with observations of MS0735 (Vantyghem et al., 2014).

Assuming a relativistic power-law distribution of electrons in the bubbles implies a larger contrast of the SZ signal δi_{ν_0}. Note, a hypothetical thermal filling of the under-dense bubble with densities as shown in Fig. 4.1 implies relativistic temperatures. The high density contrast between bubble and ICM makes the bubble susceptible to the Rayleigh-Taylor instability. Dense gas streams into the lower part of the bubble, generates turbulence and mixes with the bubble gas. This process progressively dilutes the bubble material and transports it into the ICM until complete disruption.

4.5 Probing relativistic bubble fillings

The observed decrement in the SZ signal due to different bubble fillings can help to unravel its constituents. In the left panel of Fig. 4.2, we show the SZ signal along the jet axis for bubbles filled with thermal gas ($kT_e = 10$ keV) or relativistic gas, which either follows a thermal distribution ($kT_e =$ 500 keV) or a power-law distribution ("relativistic power-law"). The larger SZ contrast for relativistic fillings becomes apparent.

Abdulla et al. (2019) compared cut-out ellipsoids from a fitted, smooth background cluster with their SZ observations to constrain the bubble filling. Rather than reproducing their analysis, we focus on the consequences for the SZ signal of modelling bubbles as ideal ellipsoids including variations in inclination.

On the right-hand panel in Fig. 4.2, we contrast the expected SZ signal from our simulated bubble to an ellipsoidal cut-out in our simulation, assuming the unperturbed initial profile. Throughout this Letter, we determine the dimensions of the cut-out ellipsoid and its position from unsharped masked X-ray maps of our simulated bubbles. We assume that the depth of the modelled bubble corresponds to its width. On the right-hand panel in Fig. 4.2, both bubbles are viewed perpendicular to the jet axis and contain a relativistic power-law filling. The profiles show good agreement at the inner rim of the bubble and start to deviate towards the bubble edges, where we see an enhanced SZ signal in the simulations out to the ellipsoidal shock. This feature corresponds to the increased pressure in the shocked cocoon powered by the outburst and is neglected in the simple cut-out model. This highlights the importance of including the bow shock in the model.

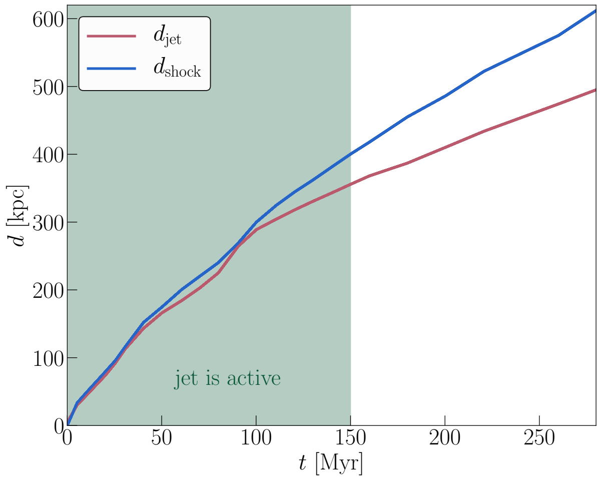

Figure 4.4: Cluster-centric distance of the shock (blue) and head of the jet and bubble, respectively (red) as a function of time. After two thirds of the jet lifetime, the shock detaches and propagates with almost constant velocity $v \approx 1670\,\mathrm{km\,s^{-1}}$ while the bubble rises with the slower buoyancy velocity $v \approx 1110\,\mathrm{km\,s^{-1}}$, which causes an increasing stand-off distance with time.

4.6 Degeneracies with jet inclination

In Fig. 4.3, we study the influence of inclination on the SZ signal. An angle of $\theta = 90$ corresponds to a jet axis that is perpendicular to the line of sight. We compare the amplitude of the kinetic SZ effect w (top row of Fig. 4.3) to the thermal SZ effect y (middle row of Fig. 4.3). From left to right, we use later times for larger inclinations to keep the projected distance from the BH to the lower bubble edge approximately constant. We see a strong increase in signal strength of the kinetic SZ effect for larger inclinations. In the wake of the bubble, highly turbulent, dense gas pushes into the region previously occupied by the bubble. This bipolar structure develops significant velocities at high densities that contribute up to 10% of the thermal effect to the total SZ signal at $\theta = 33°$. Future high sensitivity observations of inclined jets should be able to measure this effect. The expected opposite sign of the signal in the two bubbles aids in modelling this effect.

The bottom panels of Fig. 4.3 show the expected SZ signal at 30 GHz for the differently tilted simulations and the cut-out model, for which we always assume an inclination of $\theta = 90°$ to mimic the SZ modeling in observations, which currently have no access to the intrinsic inclination. In both models, we adopt a power-law distribution of relativistic electrons in the bubbles. The model reproduces the SZ signal at the inner bubble edges well for large inclinations while the agreement becomes worse for smaller inclinations. When viewed face-on ($\theta = 90°$), the inclusion of the bow shock in the model is critical to correctly reproduce the SZ signal from the simulation. The bow shock loses its momentum and covers a larger volume as a function of time such that the signal from the shocked region flattens for later times (panels towards the right).

In addition, the SZ contrast due to the relativistically filled bubbles disappears almost entirely for smaller inclinations. Here, lines of sight pass through significantly larger portions of the shocked gas region. This is especially true for the inner part of the bubble where lines of sight intersect the dense central cool core. The effect is amplified for older bubbles through the advanced state of entrainment and mixing of ICM material with the relativistic bubble contents due to the Rayleigh-Taylor instability (see Section 4.4).

Contamination by the signal from the cluster core appears like a significant source of uncertainty for the analysis of observations as θ is unconstrained a priori. However, X-ray observations can inform simulations about jet power and bubble/shock ages (e.g., Diehl et al., 2008). Our simulation shows that the stand-off distance between bow shock and jet/bubble head is increasing with time. In particular, entraining the ambient ICM towards the end of the jet lifetime slows the jet down, see Fig. 4.4. Varying the viewing angle of the jet axis then helps to disentangle projection effects and potentially constrain inclination.

For large inclinations, the projected stand-off distance decreases for decreasing inclinations. However, at small inclinations the outer edge of the ellipsoidally shocked region enlarges the projected bow shock region beyond the projected distance of the upper tip of the bow shock. The ellipticity of the bow shock itself may aid in providing a coarse estimate of the inclination. Even though the details may depend on the concentration of the NFW potential, a spheroidal bow shock should generally favour small angles of inclination. Note that these features have a weak resolution dependence in our simulations, which is studied in Weinberger et al. (2017) and Ehlert et al. (2018). With high-sensitivity observations the kinetic SZ effect can be identified through its bimodality and used as an additional constraint for the suggested method.

4.7 Conclusion

We show that three-dimensional MHD simulations are instrumental to carefully model the SZ signal of jet-inflated bubbles and conclude:

- Relativistic bubble fillings imply a large SZ contrast, which is observable in high-resolution SZ observations.
- The SZ profiles of simulations and the cut-out model show good agreement at the inner rim of the bubble and start to deviate towards the bubble edge because the simplified model fails to account for the shock-enhanced pressure cocoon outside the bubbles.
- The match between simulations and model becomes worse when considering small inclinations between line-of-sight and jet axis ($\theta \lesssim 45°$). This geometry probes a larger fraction of the shocked ICM, which leads to an increase of thermal SZ signal also towards the inner bubble rim region. Additionally, the light material of the bubble is progressively mixed with denser ICM due to the Rayleigh-Taylor instability, making the bubble indistinguishable from the surrounding ICM. Thus, the SZ signal from older bubbles is reduced in comparison to modelling them with cut-out ellipsoids.
- At small inclinations, the kinetic SZ effect reaches up to 10% of the thermal SZ effect. The wake of the bubble causes dense ICM to enter the bubble from below, causing a comparably large kinetic SZ signal. The opposing signs of the signal of inclined bipolar outflows are a smoking-gun signature for identifying this kinetic SZ signal.
- We propose to constrain the inclination with the stand-off distance between shock and jet/bubble, the elliptical appearance of the bow shock, and (if available) the amplitude of the kinetic SZ effect. To this end, a combination of high-resolution X-ray and SZ observations and full MHD simulations are crucial to break degeneracies due to projection effects.

This Letter opens up the possibility to understand biases associated with simplified SZ modeling of AGN bubbles and to finally constrain their contents so that we can observationally identify the physical processes underlying AGN feedback.

Acknowledgements

We acknowledge support by the European Research Council under ERC-CoG grant CRAGSMAN-646955.

Connecting turbulent velocities and magnetic fields in galaxy cluster simulations with active galactic nuclei jets

5

This chapter is an adapted version of the paper *Connecting turbulent velocities and magnetic fields in galaxy cluster simulations with active galactic nuclei jets* published as Ehlert et al. (2021).

5.1 Abstract

The study of velocity fields of the hot gas in galaxy clusters can help to unravel details of microphysics on small-scales and to decipher the nature of feedback by active galactic nuclei (AGN). Likewise, magnetic fields as traced by Faraday rotation measurements (RMs) inform about their impact on gas dynamics as well as on cosmic ray production and transport. We investigate the inherent relationship between large-scale gas kinematics and magnetic fields through non-radiative magnetohydrodynamical simulations of the creation, evolution and disruption of AGN jet-inflated lobes in an isolated Perseus-like galaxy cluster, with and without pre-existing turbulence. In particular, we connect cluster velocity measurements with mock RM maps to highlight their underlying physical connection, which opens up the possibility of comparing turbulence levels in two different observables. For single jet outbursts, we find only a local impact on the velocity field, i.e. the associated increase in velocity dispersion is not volume-filling. Furthermore, in a setup with pre-existing turbulence, this increase in velocity dispersion is largely hidden. We use mock X-ray observations to show that at arcmin resolution, the velocity dispersion is therefore dominated by existing large-scale turbulence and is only minimally altered by the presence of a jet. For the velocity structure of central gas uplifted by buoyantly rising lobes, we find fast, coherent outflows with low velocity dispersion. Our results highlight that projected velocity distributions show complex structures which pose challenges for the interpretation of observations.

5.2 Introduction

Roughly half of all known galaxy clusters show cooling times $\lesssim 1\,\mathrm{Gyr}$ but lack the expected high star formation and cooling rates (Fabian, 2012). Active galactic nuclei (AGN) powered by supermassive black holes (SMBH) in the center of these cool-core (CC) clusters inflate buoyantly rising bubbles of hot gas, which are believed to heat the intra-cluster medium (ICM) (Gitti et al., 2012; McNamara and Nulsen, 2012). The details of the heating process are unknown. Possible mechanisms include mixing of hot bubble gas with the ICM (Yang and Reynolds, 2016; Hillel and Soker, 2017a, 2018), possibly facilitated by external cluster turbulence (Bourne et al., 2019, 2021), the decay of turbulence (Zhuravleva et al., 2014, 2018; Fujita et al., 2020; Mohapatra and Sharma, 2019), the uplift of cold gas in the wake of bubbles (Guo et al., 2018; Chen et al., 2019), the dissipation of sound waves (Fabian et al., 2017; Tang and Churazov, 2017; Bambic and Reynolds, 2019), the dissipation of weak shocks (Li et al., 2017; Martizzi et al., 2019b) or the damping of cosmic ray (CR) induced Alfvén waves (Loewenstein et al., 1991; Guo and Oh, 2008; Enßlin et al., 2011; Pfrommer, 2013; Jacob and Pfrommer, 2017a,b; Ruszkowski et al., 2017). The structure of the velocity field in the ICM contains important information about the relevance of many of these processes: the amplitude and scale of the ICM turbulence can be used to infer a turbulent dissipation rate (Zhuravleva et al., 2014), turbulent velocities combined with the cooling time set an effective range for turbulent transport (Fabian et al., 2017) and the morphology of the magnetic and velocity field impacts the transport of CRs (Ehlert et al., 2018).

Observationally, many details of the velocity structure of the hot gas in the ICM remain open questions (Simionescu et al., 2019). Early results of the *Suzaku* satellite found no velocity gradient within their calibration uncertainty, which provided upper limits of a few thousand km s^{-1} for cluster bulk velocities (e.g., Ota et al., 2007; Ota and Yoshida, 2016; Sugawara et al., 2009; Tamura et al., 2011, 2014). Spectral analysis of *XMM-Newton* data put first direct constraints on the turbulent motions in the ICM, finding large scale velocities on the order of hundreds of km s^{-1} (Sanders et al., 2010; Bulbul et al., 2012; Sanders and Fabian, 2013; Pinto et al., 2015). Resonant scattering of lines in the core of clusters causes an apparent suppression of some lines compared to others. Thus, turbulent velocities can be constrained due to their influence on the optical depth (see Gu et al., 2018, for a review).

Recent more refined analysis of resonant scattering with *XMM-Newton* RGS spectra found turbulent velocities in the center of clusters on scales $\lesssim 10\,\mathrm{kpc}$ of hundreds of km s^{-1} (e.g., Xu et al., 2002; Werner et al., 2009; De Plaa et al., 2012; Ogorzalek et al., 2017). A different inference method relies on X-ray fluctuations in the smooth cluster potential that correlate with the velocity fluctuations (Schuecker et al., 2004; Churazov et al., 2012; Gaspari and Churazov, 2013). The method allows the computation of the velocity power spectrum, which provides constraints on the kinematic viscosity in clusters. In agreement with discussed alternative methods, recovered velocities of gas motions in the center of analyzed clusters reach a few hundred km s^{-1} (Walker et al., 2015; Zhuravleva et al., 2018). Most recently, the significant increase in spectral resolution and high broadband spectral resolution allowed the X-ray satellite *Hitomi* to directly determine the bulk velocities of Perseus to be $|v_\mathrm{bulk}| \lesssim 100\ \mathrm{km\,s^{-1}}$ and turbulent velocities of $\sigma_\mathrm{los} \approx 100-200\,\mathrm{km\,s^{-1}}$ on spatial scales of $\approx 20\,\mathrm{kpc}$ (Hitomi Collaboration, 2016, 2018). However, detailed high-resolution velocity maps of clusters are not available and the impact of the AGN on the velocity remain unclear, which is crucial for identifying relevant heating mechanisms.

However, we can make progress by realizing that magnetic fields are tightly coupled to fluid velocities which can amplify seed magnetic fields that can themselves back-react to the flow velocities provided they are sufficiently strong. This coupling may potentially allow velocities to be deduced from magnetic fields and vice versa. In the framework of numerical ideal MHD, a turbulent velocity field leads to the amplification of the magnetic field $\boldsymbol{B}$, with the rate of change given by the induction equation,

$$\frac{\partial \boldsymbol{B}}{\partial t} = -\boldsymbol{v}\cdot\nabla\boldsymbol{B} + \boldsymbol{B}\cdot\nabla\boldsymbol{v} - \boldsymbol{B}\nabla\cdot\boldsymbol{v} + \eta\nabla^2\boldsymbol{B}, \tag{5.1}$$

which relates magnetic field evolution to the velocity field $\boldsymbol{v}$ and the magnetic diffusivity η. The evolution is governed by advection, stretching, compression and (numerical) dissipation of the field, respectively. Here and elsewhere in the paper we adopt the Gaussian cgs system of units.

The induction equation provides the theoretical basis for a turbulent dynamo that amplifies a seed magnetic field (e.g., Kazantsev, 1968; Subramanian, 1999; Schober et al., 2015; Beresnyak and Miniati, 2016; Schekochihin and Cowley, 2006). Numerical simulations support this picture (Dolag et al., 2005; Ryu et al., 2008; Beresnyak, 2012; Cho, 2014; Roh et al., 2019). The dynamo reaches magnetic-to-thermal pressure ratios of a few percent (Schober et al., 2015; Vazza et al., 2018). Additional amplification is expected via compression, shocks and CRs (see review by Donnert et al., 2018). AGN feedback may cause advection of galactic magnetic fields to the ICM (Dubois et al., 2009; Xu et al., 2009; Donnert et al., 2009).

The evolution of the velocity field, in turn, is given by

$$\frac{\partial \boldsymbol{v}}{\partial t} = -\boldsymbol{v}\cdot\nabla\boldsymbol{v} - \frac{\nabla p}{\rho} - \nabla\Phi + \frac{1}{4\pi\rho}\left[\boldsymbol{B}\cdot\nabla\boldsymbol{B} - \frac{1}{2}\nabla\cdot\left(\boldsymbol{B}^2\right)\right], \tag{5.2}$$

where p denotes the thermal pressure, ρ is the gas mass density, and Φ is the (external) gravitational potential. The terms on the right describe advection, pressure force, gravity, magnetic tension and magnetic pressure, respectively. These equations, combined with the fact that the dynamical timescale is smaller than the lifetime of galaxy clusters, imply that intra-cluster medium turbulence is expected to show both, turbulent velocities as well as magnetic fields of corresponding specific energy. For reference, equipartition of kinetic and magnetic energy density implies

$$\frac{\rho}{10^{-25}\,\mathrm{g\ cm^{-3}}}\left(\frac{|v|}{100\,\mathrm{km\ s^{-1}}}\right)^2 \approx \left(\frac{|B|}{11.2\,\mu\mathrm{G}}\right)^2. \tag{5.3}$$

Indeed, observations of large-scale diffuse radio structures on up to Mpc scale in galaxy clusters, i.e. radio halos, support the notion that the ICM is magnetized (see review by van Weeren et al., 2019). Faraday RMs uncover the strength and scale of magnetic turbulence in clusters (Clarke, 2004). Assuming that the magnetic field scales as a power-law with density, the expected RM from simulated fields can be compared to observations to measure its strength and injection scale. Applying this method to radio galaxies in the Coma cluster, Bonafede et al. (2010) determine a central magnetic field strength of 5 μG. Additionally, Kuchar and Enßlin (2011) analyzed the magnetic field of Hydra A and found a central magnetic field strength of 36 μG. Generally, hotter, more massive clusters show larger dispersion in RM distributions (Govoni et al., 2010) and magnetic power spectra are consistent with a Kolmogorov slope (e.g., Vogt and Enßlin, 2005b; Guidetti et al., 2008; Vacca et al., 2012; Govoni et al., 2017).

This paper aims to shed light on the connection between large-scale magnetic and velocity fields and their observables, i.e. Faraday RM and X-ray emission-line broadening, by studying simulations of decaying cluster turbulence. By simulating an AGN outburst in a Perseus-like cluster, we demonstrate that jet driven turbulence is mostly limited to the near vicinity of the jet, more specifically to the wake of the bubbles. We also relate the kinetic to the Faraday RM powerspectra and detail the velocity fields of dragged up material by the jet.

For this, we describe our initial conditions and simulation setup in Section 5.3. In Section 5.4, we analyze our simulations of the ICM without jets. In Section 5.5, we then study the effects of AGN driven turbulence in simulations with and without pre-existing turbulence and connect them to X-ray and RM maps. Subsequently, in Section 5.6, we focus on AGN jet induced uplifts and conclude in Section 5.7.

5.3 Methods

We use simulations of isolated galaxy clusters to study the impact of AGN driven jets on the magnetized ICM. The equations of ideal magnetohydrodynamics (MHD) are solved on a moving mesh using the AREPO code (Springel, 2010; Pakmor et al., 2016b). CRs created in the jets are treated as a second fluid including advection, Alfvénic, hadronic and leptonic losses (Pfrommer et al., 2017) and anisotropic diffusion along magnetic field lines (Pakmor et al., 2016a). The simulation setup closely resembles the one in previous work (Ehlert et al., 2018), with some minor changes.

5.3.1 Initial conditions

We model our simulated cluster after the Perseus cluster: the dark matter profile follows a Navarro-Frenk-White (NFW) profile (Navarro et al., 1996, 1997) with virial radius[1] $R_{200,\mathrm{c}} = 2.12\,\mathrm{Mpc}$, virial mass $M_{200,\mathrm{c}} = 8\times10^{14}\,\mathrm{M}_\odot$ (Reiprich and Bohringer, 2002), and concentration parameter $c_{\mathrm{NFW}} = 5$. We adopt the electron number density profile from Churazov et al. (2003) rescaled to a cosmology with $h = 0.67$:

$$\begin{aligned} n_\mathrm{e} = {} & 46\times10^{-3}\left[1+\left(\frac{r}{60\,\mathrm{kpc}}\right)^2\right]^{-1.8}\mathrm{cm^{-3}} \\ & + 4.7\times10^{-3}\left[1+\left(\frac{r}{210\,\mathrm{kpc}}\right)^2\right]^{-0.87}\mathrm{cm^{-3}}. \end{aligned} \tag{5.4}$$

---

[1] We define the cluster virial radius as the radius at which the mean enclosed density equals 200 times the critical density of the universe today.

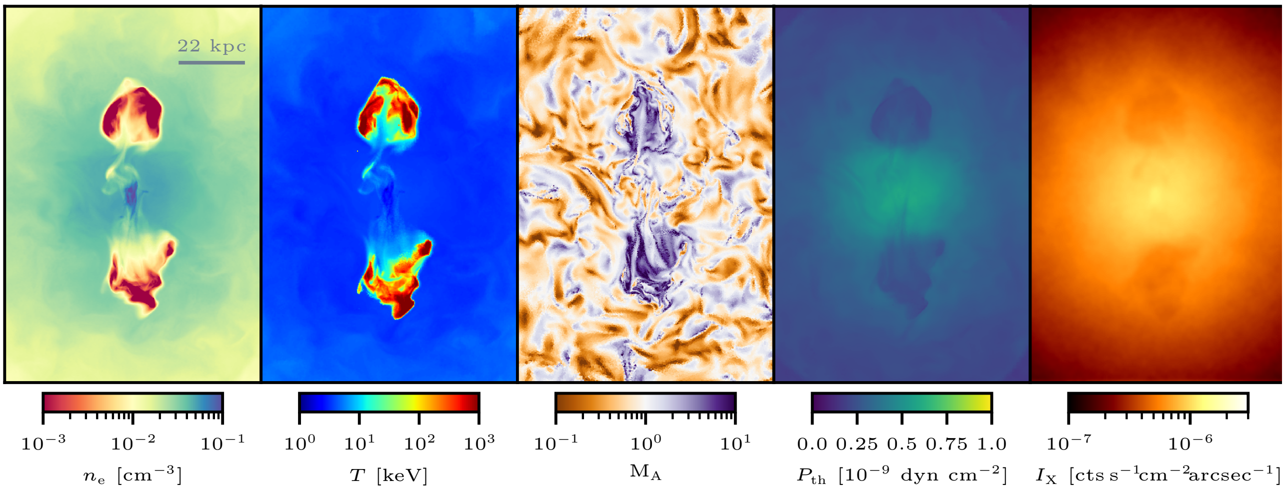

Figure 5.1: We show thin projections (132 kpc × 90 kpc × 4 kpc) of density ρ, temperature T, Alfvénic Machnumber $\mathrm{M_A} = \sqrt{\epsilon_{\mathrm{kin}}/\epsilon_B}$, thermal pressure P_{th} and 2 – 12 keV X-ray surface brightness I_X centred on the BH at 50 Myr. To reduce photon noise, the simulated X-ray exposure is 2.5 Ms and the map has been smoothed with a Gaussian kernel of 2 arcsec width. The bubbles are in the process of disruption by dense central gas that is accelerated upwards in the wake of the bubbles.

We include a turbulent magnetic field in the ICM. In Fourier space the magnetic field follows a Kolmogorov spectrum on scales smaller than the injection scale $k_{\mathrm{inj}}^{-1} = 37.5\,\mathrm{kpc}$ and white noise on larger scales. Our choice of k_{inj} is motivated by observations of RMs of CC clusters, which find magnetic fields fluctuating on scales from a few to tens of kpc (Vacca et al., 2018). Motivated by Bonafede et al. (2010), who find their large sample of RMs for Coma to be consistent with a constant magnetic-to-thermal pressure ratio, we scale the concentric shell averaged magnetic field strength to a magnetic-to-thermal pressure ratio of $X_{B,\mathrm{ICM}} = 0.05$, independent of radius. The strength of the magnetic field is motivated by radio synchrotron (de Gasperin et al., 2012) and RMs (Kuchar and Enßlin, 2011) by scaling magnetic field strength to the density of the Perseus cluster (see Section 3.1 in Pfrommer, 2013). We refer to our previous work (Ehlert et al., 2018) for the precise procedure to set up this divergence-free field.

5.3.2 Jet modeling

The launching of the jet follows previous work (Weinberger et al., 2017; Ehlert et al., 2018), with some minor modifications: we set up two spherical *injection regions* with radius $r_{\mathrm{jet}} = 1.65\,\mathrm{kpc}$ at a distance of 3.3 kpc on opposite sides of a central SMBH. These regions serve as inflow boundary regions, in which the jet density $\rho_{\mathrm{jet}} = 10^{-28}\,\mathrm{g\,cm^{-3}}$ is kept constant throughout the injection and the thermal energy, as well as a weak toroidal magnetic field with relative energy density $X_{B,\mathrm{jet}} = 0.1$ are adjusted to be in pressure equilibrium with the surrounding medium. To ensure overall mass conservation, the mass that was taken out of (or put into) the injection region is added (or removed) from the SMBH surroundings that is not within these injection regions. After accounting for the (comparably small amount of) energy required for the preparation of this state, the remaining energy is added in the form of kinetic energy creating bipolar outflows from the jet regions. We inject a passive (mass-weighted) tracer X_{jet} with the jet fluid and initialize it with $X_{\mathrm{jet}} = 1$. This allows us to define our jet/lobe as all cells where $X_{\mathrm{jet}} > 10^{-3}$.

In our previous work, we assumed a jet opening angle of zero. We showed that a low-density jet does not necessarily suffer from the drilling though the ICM reported in previous works of this kind (Weinberger et al., 2017). Yet, when matching the Perseus lobes in energy, the resulting simulated lobes still come out too elongated in radial direction and at too large radii. To overcome this problem, we choose to increase the working surface of the jet by introducing an opening angle, leading to a termination at lower radii and more horizontally extended lobes. Empirically, we found a 30-degree half opening angle to reproduce the Perseus lobe dimensions adequately (discussed in Section 5.5.1). Note that the kernel-weighted injection favors the components close to the jet axis, de facto leading

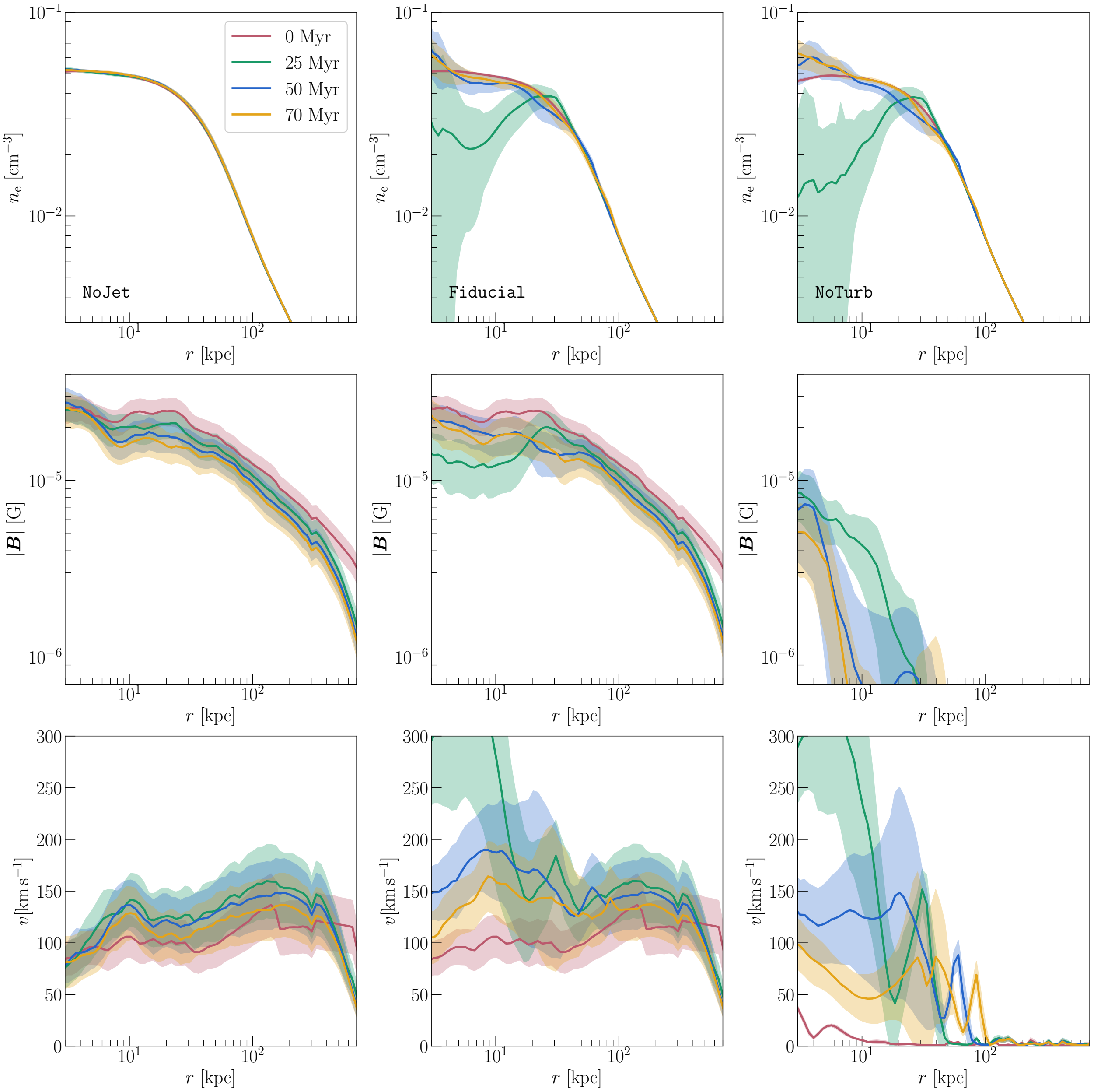

Figure 5.2: From top to bottom we show radial profiles of volume-weighted density, square root of volume-weighted magnetic field strength and square root of mass-weighted velocities for models `NoJet`, `Fiducial` and `NoTurb` (from left to right) at stated times. The bubbles are visible as depressions at $r < 20$ kpc at 25 Myr. The turbulent magnetic field decays as a function of time. AGN-induced velocities are limited to the vicinity of the bubble.

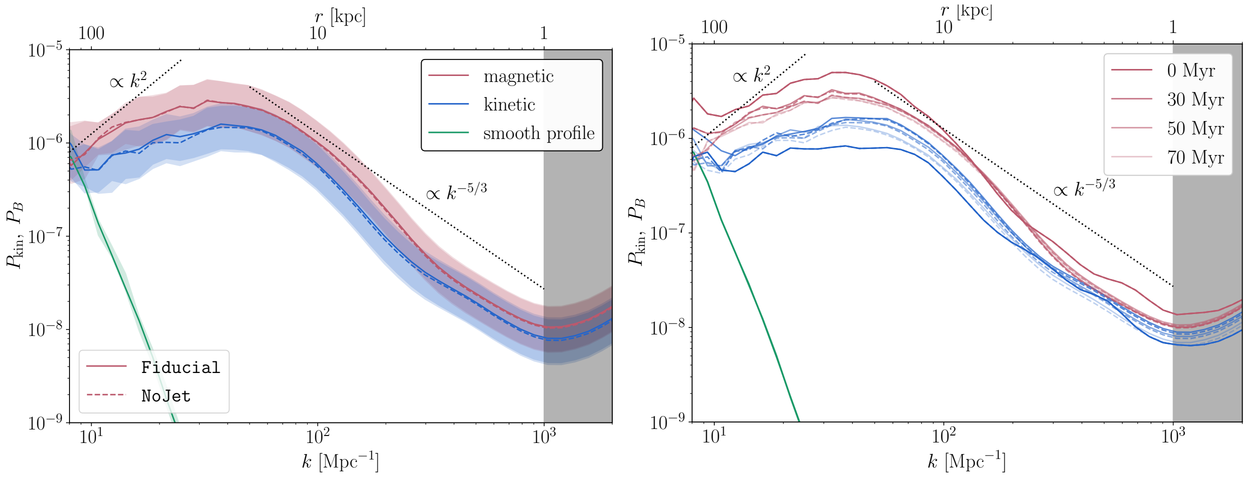

Figure 5.3: We show one-dimensional power spectra of kinetic energy density, magnetic energy density (left panel) and its evolution at 0, 30, 50, 70 Myr (right panel) of a BH-centred box with $L = 400\,\text{kpc}$ of `Fiducial` (lines) and `NoJet` (dashed). Additionally, power spectra assuming a smooth magnetic profile are plotted ('smooth profile') to quantify the contributions from the cluster profile, which only become relevant on large scales (> 200 kpc). Shaded regions show an artificial increase in power due to leaking from higher scales which is caused by the inherent (and incorrect) assumption of periodicity. The influence of the AGN on the power spectrum is minuscule. Magnetic tension initially leads to an increase of kinetic power. After 30 Myr the driving by the progressively more relaxed magnetic field (as evident by decaying magnetic power) cannot keep up with the competing decay of kinetic turbulence. This leads to an overall decrease of kinetic power.

to half the injected momentum being injected at an angle of less than 10 degree. The necessity for this opening angle hints towards more complex small-scale jet physics below the resolution limit of our simulation[2], yet we caution to not over-interpret its precise value, since the jet propagation still suffers from substantial numerical uncertainties in our setup (Appendix 5.8.2 and Weinberger et al., in prep.). Figure 5.1 shows a snapshot of a simulation including thin density and temperature slices at 50 Myr, i.e. 35 Myr after the jet became inactive.

Since we cannot resolve the acceleration of CR protons at internal shocks self-consistently within this model, we adopt a subgrid-scale model that dissipates the initial kinetic energy into CR and thermal energy. In practice, we convert thermal energy to CR energy in the lobes ($X_{\rm jet} > 10^{-3}$) such that a minimum CR-to-thermal energy ratio $X_{\rm cr,acc} = 1$ is obtained while the jet is active. Our (conservative) choice of the CR contribution follows from a systematic comparison of the plasma conditions in Fanaroff & Riley class I and II radio galaxies that suggest that their internal composition is systematically different: the different radio morphologies and jet-power/radio-luminosity relationship are best explained by the presence of an energetically dominant proton population in the FRI, but not the FRII radio galaxies (Croston et al., 2018). We magnetically isolate the injection region to inhibit unphysical diffusion of CRs. In the ICM, CRs are expected to scatter on self-generated Alfvén waves (Kulsrud, 2005). Due to inefficient Alfvén wave damping CRs are confined to stream down their pressure gradient $\nabla P_{\rm cr}$ close to the Alfvén speed $v_{\rm A}$ (Zweibel, 2013; Thomas and Pfrommer, 2019; Thomas et al., 2020). CRs that stream faster than the local Alfvén speed excite the streaming instability that continuously generates Alfvén waves, which experience damping processes. Thereby, CR energy is effectively transformed into thermal energy via *Alfvén heating* with power $H_{\rm cr} = |\boldsymbol{v}_{\rm A} \cdot \nabla P_{\rm cr}|$. In line with Sharma et al. (2009) and Wiener et al. (2017), we introduce an effective CR diffusion coefficient $\kappa_{\rm cr,A} = 10^{29}\,\text{cm}^2\,\text{s}^{-1}$ and emulate CR streaming by including CR advection, anisotropic diffusion and account for Alfvénic losses (see Ehlert et al., 2018, for more details).

For the high resolution runs, to focus the computational resources on the region of interest, we chose the target mass to be dependent on distance from the centre r,

$$m_{\rm target} = m_{\rm target,0}\, \exp(r/100\,\text{kpc}), \tag{5.5}$$

---

[2] Possible effects could include the interaction with a clumpy interstellar medium (Mukherjee et al., 2016), jet instabilities such as the magnetic kink instability (Tchekhovskoy and Bromberg, 2016; Mukherjee et al., 2020) or an actual, wider opening angle wind component (Yuan et al., 2015).

Jet parameters		
Jet power	$P_{\rm jet}$	$10^{45}\,{\rm erg\,s^{-1}}$
Jet life time	$\tau_{\rm jet}$	$15\,{\rm Myr}$
Jet density	$\rho_{\rm jet}$	$10^{-28}\,{\rm g\,cm^{-3}}$
Jet launching region	$r_{\rm jet}$	$1.65\,{\rm kpc}$
CR acceleration	$X_{\rm cr,acc}$	1
Jet magnetization	$X_{B,\rm jet}$	0.1
Magnetic field parameters		
Injection scale	$k_{\rm inj}$	$37.5^{-1}\,{\rm kpc}^{-1}$
Resolution		
Target mass	$m_{\rm target,0}$	low res.: $1.5\times10^{7}\,{\rm M}_\odot$ interm. res.: $1.5\times10^{6}\,{\rm M}_\odot$ high res.: $4.5\times10^{4}\,{\rm M}_\odot$
Jet target volume	$V_{\rm target}^{1/3}$	lower res.: 873 pc interm. res.: 405 pc high res.: 188 pc
Minimum volume	$V_{\rm min}$	$V_{\rm target}/2$

Table 5.1: Parameters for jet, the magnetic field and refinement.

Label	Jet active	$X_{B,\rm ICM}$	Resolution
`Fiducial`	True	0.05	High
`NoTurb`	True	0	High
`NoJet`	False	0.05	High
`X25`	True	0.25	Interm.
`X5`	True	0.05	Interm.
`X1`	True	0.01	Interm.

Table 5.2: List of simulations and magnetic parameter variations. Note, run `NoTurb` is setup without magnetic fields in a hydrostatic atmosphere.

with cells at the outskirts limited to a maximum volume. We summarize adopted parameters for our simulations in Table 5.1, where target mass refers to the maximum mass per cell in the inner region of the ICM and the jet target volume is the volume resolution in our lobes ($X_{\rm jet} > 10^{-3}$). Note that the cells are (de-)refined if the mass deviates more than a factor of two from the target mass (and similarly for the jet volume). We list our main simulations in Table 5.2. Target mass and target volume represent the two resolution parameters of the simulation, each for a different part of the simulation (ICM and jet/lobe, respectively). In this study, we only present runs where both are varied by the same factor, allowing for a single definition of resolution. In the following we focus our analysis on our high resolution simulations unless stated otherwise.

5.3.3 Analysis

X-ray emission

To create velocity dispersion maps, we create synthetic X-ray observations of the simulation snapshots and fit the line profile of the mock spectrum. In particular, we employ the PYXSIM code (ZuHone and Hallman, 2016) using the specific internal energy and density of each gas cell, assuming a metallicity of the gas to be 0.7 solar metallicity and Asplund et al. (2009) element abundance ratios. The code makes use of the APEC library (Smith et al., 2001, version 3.0.9) to calculate emission spectra in the energy range 2 – 12 keV. The spectra are sampled with photon packages, taking into account thermal and Doppler broadening. The photon packages are then projected onto the detector plane, taking into account ISM absorption using the Tuebingen-Boulder absorption model (Wilms et al., 2000) assuming a column density of $4 \times 10^{-20}\,\mathrm{cm}^{-2}$, and astrophysical backgrounds are added. We put the galaxy cluster at a redshift of $z = 0.017284$, with 1 arcmin corresponding to 21 kpc using the cosmological parameters $h = 0.67$, $\Omega_m = 0.3$, $\Omega_\Lambda = 0.7$. We then convolve the photons with instrumental effects of XRISM Resolve using the Soxs library, including an Auxiliary Response File (ARF), point spread function (PSF) effects as well as energy scattering is introduced using a Redistribution Matrix File (RMF)[3], and perform the synthetic observation with exposure time 250 ks.

We then use the mock spectrum and fit a multi-Gaussian to the FeXXV He-α complex. Similar to Hitomi Collaboration (2016), we use a single width for all but the strongest line, as well as a single offset, but variable amplitudes, thus ending up with 12 fit-parameters. Note however that we omit the fitting of the weaker lines for simplicity. We obtain the bulk velocity and line width from the fit parameters. Subtracting the square of the expected thermal broadening (assuming a single-temperature gas at 4 keV) from the squared line width, we obtain the squared velocity dispersion.

To assess the effect of the different steps in this pipeline, we also produce (2 – 12 keV) emission weighted velocity dispersion maps as well as maps of 'ideal' observations (omitting instrumental effects). We discuss these effects in Appendix 5.8.3. Note, however, that due to the idealized nature of the simulations, uncertainties resulting from temperature and metallicity variations are not captured in this setup.

Faraday rotation measure

The rotation measure RM is given by

$$\mathrm{RM} = \frac{e^3}{2\pi m_\mathrm{e}^2 c^4} \int_0^{s_\mathrm{e}} \mathrm{d}s\; n_\mathrm{e} B, \tag{5.6}$$

where the magnetic field is integrated along the line of sight from the source at s_e to the observer at $s = 0$.

This is done by sampling the magnetic and electron density field with a finely spaced ($\Delta x = 90\,\mathrm{pc}$) 3D cartesian grid of dimensions 110 kpc – 70 kpc – 1.5 Mpc, and numerically integrating along the third axis for each pixel.

Kinematics of uplifted gas

In order to study the motions of the central ICM induced by the AGN, we initialize a passive scalar within 5 kpc of the SMBH to unity. This scalar is only advected with the flow and prone to dilution. To determine the velocity dispersion and mean velocity in individual pixels in the projected map we compute scalar mass weighted histograms. For this, we only consider cells with mass fractions of $> 10^{-3}$. Velocity dispersion and mean velocity correspond to the variance and mean of a Gaussian that we fit to the highest peak in the velocity distribution. If fitting errors exceed 50%, we double the bin size in the corresponding pixel, refit the velocity distribution, and check new fitting errors. The later applies to a few cells in the outskirts of the lobes. We confirmed that our results remain invariant under variations of detailed parameters (bin size, mass fraction, etc.). All individual fits contain of order 10^4 unique data points. Thereby, sufficient sampling is ensured by enforcing high resolution in the ICM.

5.4 Large-scale turbulence

To study the impact of AGN driven jets on ICM turbulence, we first discuss the evolution of the ICM in absence of jets. Subsequently, we discuss the lobe properties as well as the impact of jets in both,

---

[3] We use the ARF and PSF file version 20170818.

a quiescent and a turbulent ICM environment in Section 5.5.

First, we focus on the inherent link between equations (5.1) and (5.2) which allows us to resort to the case of decaying MHD turbulence. Since the ICM is in hydrostatic equilibrium, i.e. the total pressure gradient is balanced by gravity, magnetic tension forces convert magnetic energy to kinetic energy as described in equation (5.2). Note that in this setup the magnetic field initially dominates over the kinetic turbulence. This implies that the magnetic field is not substantially replenished by dynamo processes and thus magnetic energy decreases over time, while the kinetic energy increases initially. This can be seen in the radial profiles of electron number density n_e, magnetic field strength $|\boldsymbol{B}|$ and absolute velocity v at different times as shown in Figure 5.2. The magnetic field strength decreases independently of radius by ≈ 0.2 dex over 70 Myr. After ≈ 30 Myr, stirring by magnetic tension forces becomes subdominant compared to turbulent dissipation, leading to a decrease in kinetic energy.

To study the scale-dependence of magnetic and kinetic energy density, we show the respective one-dimensional power spectra in Figure 5.3. The magnetic power decays on most scales as shown in the right panel. To quantify the modulation of the spectrum by the profile of the cluster, we plot the power spectrum of a smooth magnetic field with magnetic-to-thermal pressure ratio $X_{B,\mathrm{ICM}}$. Magnetic tension stirs the medium and thereby increases the kinetic power. After 30 Myr, the kinetic turbulence decreases on all scales. The modulation due to the profile of the cluster dominates the large scales of the power spectra ($k \lesssim (100\,\mathrm{kpc})^{-1}$). On scales $(100\,\mathrm{kpc})^{-1} \gtrsim k \gtrsim (40\,\mathrm{kpc})^{-1}$, the magnetic field roughly follows a white noise distribution. On smaller scales a Kolmogorov slope is observed.

Having established the overall behaviour, we now show synthetic observables of our simulations after 50 Myr when both magnetic and kinetic fields decay globally. In Figure 5.4, we show (from top to bottom) slices of the velocity, the velocity dispersion along the line of sight, slices of the magnetic field and the RM of `NoJet`, `Fiducial` and `NoTurb` (from left to right).

We find Faraday RMs that are an order of magnitude above observed values. This is somewhat surprising as magnetic field parameters were directly taken from observations. The magnetic field of the jet has negligible effect on the overall RM (see Section 5.8.1). However, we note that RM measurements are well known to be inherently sensitive to fine details of topological magnetic field structures, especially in complex environments like clusters so that the magnetic field strength in clusters can only be estimated within a factor of a few (Newman et al., 2002; Johnson et al., 2020). In addition, we identify four effects that could be responsible for the discrepancy. (i) Possibly our adopted coherence scale is too large and we therefore underpredict depolarization. To test this hypothesis, we ran an additional simulation with an injection scale of $k_\mathrm{inj} = 15^{-1}\,\mathrm{kpc}^{-1}$, which decreases RM by 30 % (see Figure 5.5). (ii) Observed RMs are limited to few small patches in clusters that are provided by the angular extends of radio lobes. Especially the bright central radio sources in CC clusters imply a large dynamic range that challenges high-frequency polarized observations of lobes, which are negligibly affected by Faraday depolarisation. (iii) Beam smoothing artificially lowers the dispersion of observed RMs. We neglect this effect here. (iv) Vazza et al. (2018) find their simulated magnetic fields to depart from a Gaussian distribution that is usually assumed when modeling Faraday RMs. Consequently, observations of RM possibly overestimate cluster magnetic field strengths. This highlights the relevance of cosmological MHD simulations that are able to self-consistently drive and sustain large scale magnetic fields. Moreover, this calls for a dedicated synthetic modeling of observations to take into account all possible observational effects.

The velocity dispersion σ_los corresponds to the variance of a Gaussian fit to X-ray weighted velocities along the line of sight. Gas velocities $|\boldsymbol{v}|$ in the ICM reach a few hundred km/s throughout the cluster in simulations with initial turbulent magnetic field (`Fiducial` and `NoJet`). These translate to a velocity dispersion of $\sigma_\mathrm{los} \sim 100\,\mathrm{km\,s^{-1}}$ (second row; left and central panel), which corresponds to the observed levels by *Hitomi*. This gives us another indication that our assumed field strengths are too high as this magnitude of velocity dispersion would hardly be able to sustain our initial field strengths. Varying magnetic field strengths, we find that velocity dispersion induced by fields with weaker field strengths (`X1`) yield a velocity dispersion of $\approx 30 - 60\,\mathrm{km\,s^{-1}}$ (Figure 5.10). Higher field strengths (`X25`) yield a velocity dispersion of $\approx 130-180\,\mathrm{km\,s^{-1}}$ (see Appendix 5.8.1). We confirmed the numerical convergence of these results (Figure 5.11).

We conclude that the magnetic field strength in combination with the turbulent injection scale directly corresponds to the observed levels of ICM velocity dispersion. Detailed simulations of cluster evolution therefore provide a direct link between magnetic field strength and tracers of velocity. Fundamentally, this demonstrates that RM and line broadening in X-ray spectra are just two sides of the same coin with their physical origin in cluster turbulence. The presence of magnetic turbulence implies velocity dispersion and vice versa. Our simulations of decaying turbulence are meant as a proof of concept to explore the relationship between velocity fields and magnetic fields. In reality, perturbations to the cluster potential induced by merger or accretion induce velocity fluctuations that excite a small-scale dynamo, which leads to exponential amplification of the magnetic field on the dissipation scale. After equilibrating with the kinetic energy at this scale the magnetic field might inverse cascade and is expected to saturate at a fraction of the kinetic energy (e.g., Schober et al., 2015; Dominguez-Fernandez et al., 2019), unlike what we have adopted in the initial conditions. Our results highlight the necessity for a self-consistent turbulent dynamo to amplify the magnetic field to equilibrium levels to reliably determine the normalization in the relationship between RM and ICM velocity dispersion. We conclude that one can predict levels of turbulence and magnetic field strengths by observing the other, provided the turbulent injection scale and the growth history is correctly simulated.

5.5 Impact of jets on the ICM

5.5.1 Lobe properties

In Figure 5.1, we show the bubble after 50 Myr, i.e. 35 Myr after the jet became inactive. From left to right, we show density, temperature, Alfvénic Mach number, thermal pressure and X-ray emissivity. The bubbles appear as cavities in the integrated X-ray emissivity. The Alfvénic Mach number corresponds to the ratio of kinetic and magnetic energy density, which, in parts of the ICM reaches $M_\mathrm{A} < 1$. Thus the magnetic pressure is dominant and stirs the medium. The jet inflated lobes rise buoyantly in the cluster atmosphere. At this time, the Rayleigh-Taylor instability starts to markedly disrupt the bubbles. In the wake of the bubbles dense gas is pulled upwards from below. The core of both bubbles is already filled with denser ICM and the southern bubble is in the process of splitting (see density and temperature map). The thermalization of kinetic energy during jet propagation and lobe formation drastically lowers the magnetic-to-thermal pressure ratio compared to the initial value in the jet, $X_{B,\mathrm{jet}}$. Consequently, the magnetic field becomes subdominant in the lobes (see Alfvénic Mach number $\mathrm{M_A} > 1$). In the thermal pressure map the bubbles appear as cavities due to the significant pressure support by CRs, as is evident from the large CR-to-thermal pressure ratio $X_\mathrm{cr} \geq 0.5$.

The total work required to inflate the lobes can be quantified as the sum of $p_\mathrm{tot} V$ of all cells with a jet scalar contribution $X > 10^{-3}$ (assuming that the bubbles are in pressure equilibrium with the ambient ICM). Here $p_{\mathrm{tot},i}$ is the total pressure of cell i, taking into account thermal, CR and magnetic pressure and V its volume. In the present snapshot the energy determined this way is $\sum_i p_{\mathrm{tot},i} V_i = 9.9 \times 10^{58}$ erg for both lobes combined. The energy estimate changes by roughly 30% if the threshold for X is changed by an order of magnitude, highlighting the robustness of this result.

The thermal, CR and magnetic energies in the lobe are 1.1×10^{59} erg, 7.6×10^{58} erg and 7.2×10^{56} erg, respectively, constituting a total lobe enthalpy of $2.8 \times 10^{59}\,\mathrm{erg} = 2.87 \sum_i p_{\mathrm{tot},i} V_i$ (the total injected energy is 4.7×10^{59}). We note that CR and thermal energy in the active jet are brought to equipartition by construction, implying an enthalpy of $3 \sum_i p_{\mathrm{tot},i} V_i$ at these times. The subsequent dominance of the thermal component is due to CRs diffusing out of the lobe during the 35 Myr since the termination of the jet. Adiabatic expansion of the lobe drives the lobe towards being more CR dominated (since the adiabatic index of the CR fluid is lower). However, this effect is evidently smaller than diffusive CR losses. We can also infer that about 60 per cent of the injected jet energy is

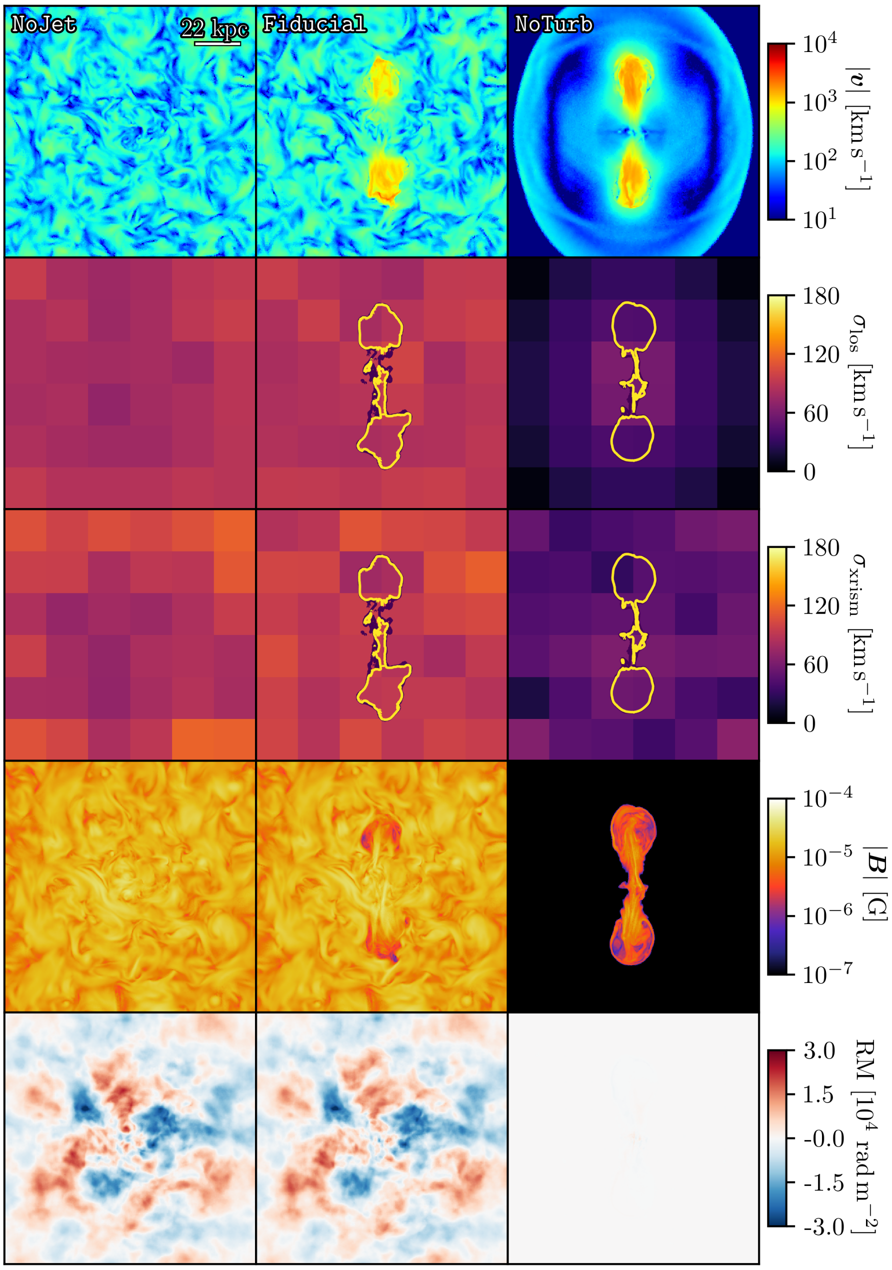

Figure 5.4: From left to right, we display simulations `NoJet`, `Fiducial` and `NoTurb` at 50 Myr. In the first row we show thin projections (4 kpc) of velocity $|v|$ weighted with density. The second row shows velocity dispersion estimates along the line of sight $\sigma_{\rm los}$ directly computed from the velocity distribution in the simulation. The third row depicts the velocity dispersion obtained from fits to mock spectra $\sigma_{\rm xrism}$ including instrumental effects of XRISM. The fourth row shows thin projections (4 kpc) of the magnetic field $|B|$ centred on the BH weighted with the volume. Finally, we show Faraday RM maps. Displayed images have dimensions 132 kpc × 132 kpc. Calculated velocity dispersion and RM encompass the full depth of the box (1.5 Mpc). Our initial turbulent magnetic field induces velocity dispersion at the observed level as seen for `NoJet` and `Fiducial`. The AGN affects turbulence (velocity dispersion) only in its near vicinity. Secondly, the contribution of the jet to RM is negligible.

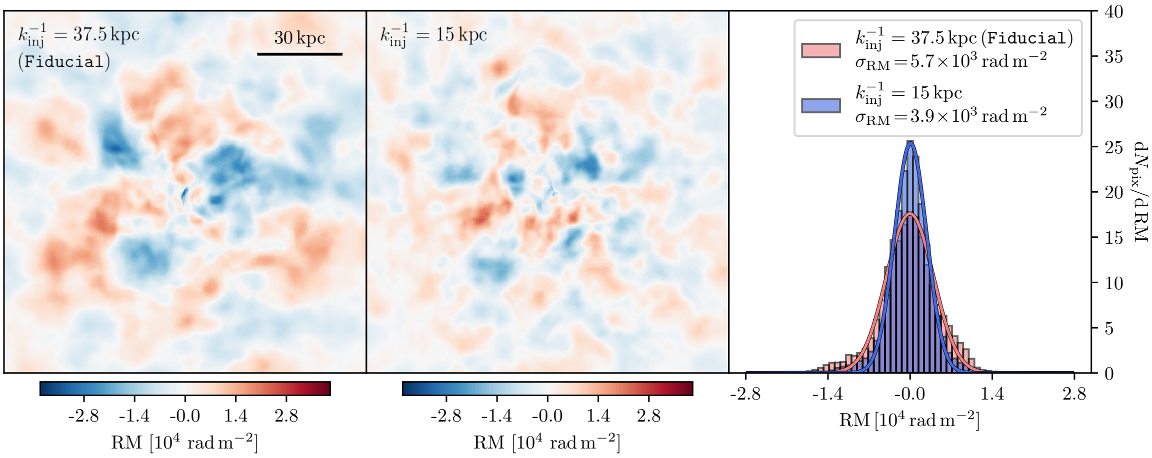

Figure 5.5: Maps of Faraday RM of our simulations with a magnetic injection scale $k_{\rm inj}^{-1} = 37.5\,$kpc (`Fiducial` model, left) and $k_{\rm inj}^{-1} = 15\,$kpc (centre). Histograms of RM distribution with corresponding dispersion $\sigma_{\rm RM}$ are shown on the right. A decreasing injection scale implies a smaller RM dispersion.

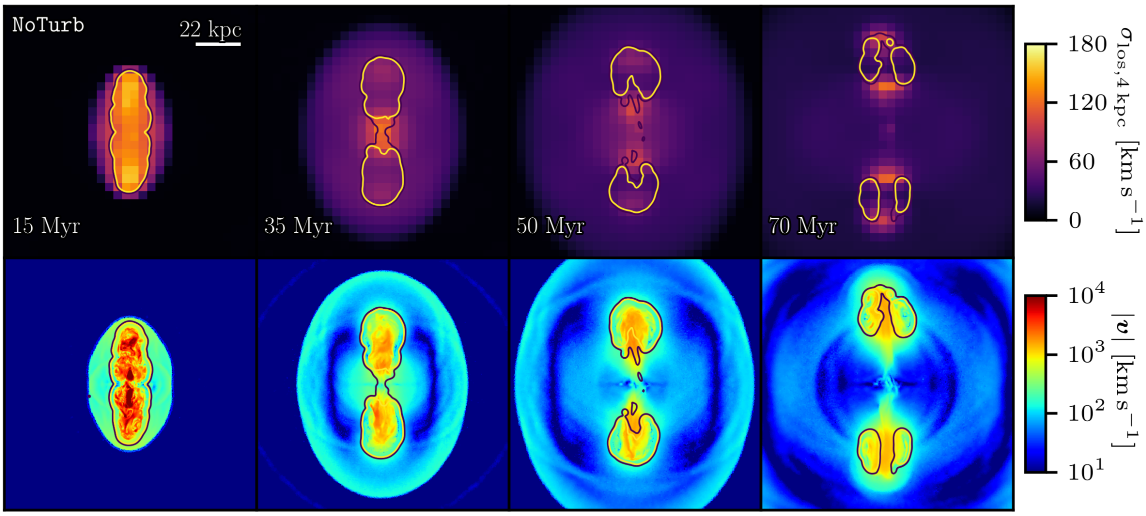

Figure 5.6: We show the velocity dispersion of the ICM (top) and slices of the velocity (bottom) at different times (left to right) of the model `Noturb`. We overlay contours of slices of the jet tracers $X_{\rm jet} = \left\{10^{-3}, 10^{-2}\right\}$ (purple and yellow) to highlight the location of the lobes. Displayed images have dimensions $132\,{\rm kpc} \times 132\,{\rm kpc}$. After passing of the initial shock wave, the rising bubbles only causes an increased velocity field in the immendiate wake of the bubbles.

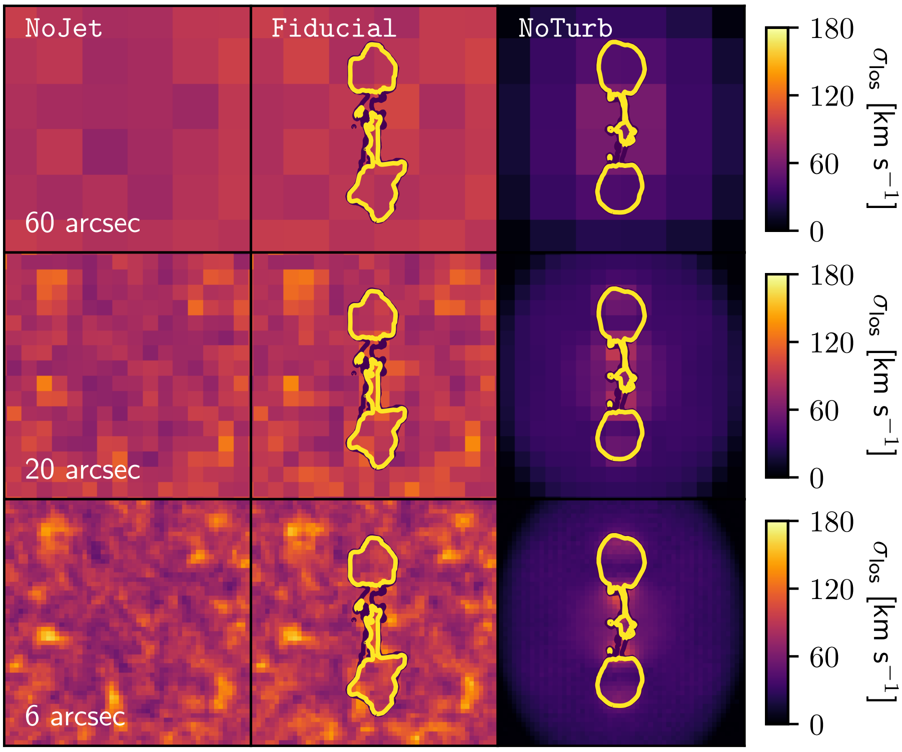

Figure 5.7: Emission weighted velocity dispersion maps with different spatial resolution at 50 Myr.

no longer associated with the lobes. This energy has been (i) dissipated in the bow shock during jet propagation, (ii) invested in pdV work on the ambient ICM during the formation and expansion of the lobes, and (iii) lost by diffusing CRs that have escaped the lobes as well as hydrodynamic mixing of lobe material with the surroundings.

The extent and shape of the lobes can be evaluated from the X-ray emissivity image, with a lobe diameter of about 20 kpc at a distance of 25 kpc from the center. These values can be compared to literature values of the lobes in the Perseus Cluster, e.g. Bîrzan et al. (2004); Rafferty et al. (2006); Diehl et al. (2008), which have similar dimensions and positions. We are therefore confident that the behaviour of these lobes is similar enough to meaningfully compare their effect in the simulated ICM to observational data.

5.5.2 Dynamical impact of jets

Having presented the properties of the ICM and the lobes, we move on to focus on the effect of a single jet outburst on observable ICM properties.

The inflation of the bubble is visible as a drop in both density and magnetic field strength within the inner 10 kpc at 25 Myr in Figure 5.2. The compression of the upstream gas due to the shock front is also evident in the profile shown in Figure 5.2. From the magnetic field and particularly the absolute velocity profiles, it becomes evident that the jet does have some impact on the kinematic structure of the gas within the range of the lobe itself, however not beyond this radius. The simulations without initial turbulence clearly show the limited range of the turbulent driving of the AGN lobes.

Turning to the spatial distribution of the turbulence using line of sight velocity and velocity dispersion in Figure 5.4, it becomes evident that the arcmin spatial resolution mostly reveals large-scale turbulence which in our simulations originates from the initial conditions, rather than the jet. However, a small, but subdominant effect from the jet is observable, yet only differentially. In the case of a quiescent ICM it becomes particularly clear that the impact on the ICM turbulence is only present at the location of the lobes and in their past trajectory, disfavoring the idea that the lobes can sustain ICM turbulence throughout the entire cluster core and on scales up to several tens of kpc. This also suggests that the observations probing these spatial scales might not directly probe AGN induced turbulence, but rather turbulence induced by other processes such as fluctuations of the cluster potential as a result of mergers or accretion, substructure infall, or thermal instability (all of which are not included in these simulations). We discuss the required spatial resolution to detect the lobe-induced turbulence in the next subsection.

Although our analysis is limited to a single jet outburst, Figure 5.6 illustrates that jet-driven turbulence is spatially constrained to the wake of the rising bubbles. We focus on our model `NoTurb` and show the velocity dispersion of the ICM (top) and slices of the absolute velocity (bottom panels). The initial AGN outburst drives a shock wave into the ICM, which induces small-amplitude vorticity, which quickly decays. Significant turbulence is therefore limited to the wake region of the jet/bubbles, which is then advected upwards as those buoyantly rise. Our jet parameters are modelled after detected bubbles in Perseus. While more powerful AGN events are expected to possess larger wake regions, they are not observed in Perseus. In addition, duty cycles in Perseus are not observed to be short enough for a concatenation of small outbursts to be able to sustain turbulence in the entire core region. Nevertheless, the uncertain degree of jet precession may potentially increase the level of isotropy of the jet driven turbulence somewhat.

Zhuravleva et al. (2014) infer the ICM heating rate due to dissipation of turbulence from X-ray observations of CC clusters. They conclude that the turbulent heating rate is sufficient to halt cooling in these clusters and suggest it as the main heating mechanism (Zhuravleva et al., 2016). In contrast, Mohapatra and Sharma (2019) find the required level of turbulence for turbulent dissipation to be the dominant heating mechanism to be inconsistent with *Hitomi* measurements. Our results indicate that lobes of the size of the ones in Perseus cannot be the sole driver for this level of turbulence. This is in agreement with findings of other simulations in the literature (Reynolds et al., 2015; Bourne and Sijacki, 2017; Bambic et al., 2018a; Bambic and Reynolds, 2019). Interestingly, simulations in self-regulated setups (e.g. Lau et al., 2017; Li et al., 2017) show slightly higher levels of turbulence.

5.5.3 Observational effects

In Figure 5.4 we show emission weighted velocity dispersion maps (second row) and velocity dispersion maps determined by fitting spectra of synthetic XRISM observations (third row). Overall, the two maps show agreement, highlighting the robustness of the method, however with a noteworthy systematically higher velocity dispersion in the outer regions of the synthetic observations. To understand this discrepancy, it is important to realize that the fitted line broadening is a superposition of thermal and Doppler broadening. Thus, to infer the velocity dispersion, we subtract the effect of thermal broadening, for which we assume a temperature of 4 keV. Since the cluster is set up as a cool-core cluster, its real temperature in the center is slightly lower in comparison to the edges of the projection, which leads to an incomplete subtraction of thermal broadening at the edges and thus an overestimate of the velocity dispersion in these regions. Note that the temperature differences in our simplified setup are likely lower than in reality since we do not include cooling or cosmological environment in our setup. In Appendix 5.8.3 we disentangle the instrumental effects from the effect of fitting the spectra on the inferred map.

In addition, we show emission weighted velocity dispersion maps at different spatial resolutions in Figure 5.7. While the 60 arcsec resolution map shows the overall level of velocity dispersion, the 20 arcsec resolution map already resolves the largest modes of the turbulence. Most strikingly on display at the highest resolution map (6 arcsec) is the fact that the `Fiducial` map seems to be a superposition of the external turbulence of the `NoJet` and the jet driven turbulence of the `NoTurb` runs. This indicates that the degree of ICM turbulence into which the jets are launched does not impact the extent to which they drive more turbulence. We speculate that this breaks down once the shape and position of the jet inflated lobes is substantially altered by existing ICM turbulence.

In summary, we find that the kinematic impact of the lobes is very localized, which is only identifiable at high resolution, when the lobes are spatially resolved. This is particularly true when considering the bulk velocities with superimposed lobe velocities seen at an inclination (not shown here). We note that we did not create full synthetic observations (in Figure 5.7) and ignored the effect of photon noise in this example. However, Figure 5.7 illustrates the wealth of additional information higher resolution velocity dispersion maps contain about the state of turbulence in the ICM and its origins.

We conclude that AGNs only drive turbulence locally. This is in line with previous work, which find AGNs to be very inefficient drivers of kinetic energy (Reynolds et al., 2015; Yang and Reynolds, 2016; Bourne and Sijacki, 2017; Hillel and Soker, 2017b; Prasad et al., 2018). Consequently, cluster turbulence seen by Hitomi Collaboration (2016) appears rather related to sloshing motions initiated by mergers (ZuHone et al., 2018; Walker et al., 2018; Ichinohe et al., 2019) and/or cosmological flows (e.g., Vazza et al., 2012). Having shown that the main impact on gas flows from jets is in the wake of inflated lobes, we focus on this region in the following.

5.6 Jet-induced uplift of the ICM

Cold gas is observed as disks and/or filamentary structures in the center of galaxy clusters (e.g., Koekemoer et al., 1999; Salomé et al., 2006; Russell et al., 2019). Submillimeter to optical observations reveal the complex velocity structures of cold gas. While disks show circular motions, filaments often surround bubbles or are found in the downstream regions. Predominantly smooth velocity gradients in filaments provide additional evidence that AGNs have a strong influence on their velocity structures (e.g., Werner et al., 2014; Tremblay et al., 2018; Gendron-Marsolais et al., 2018b). Its origin is under debate. One idea is that cold gas condenses out of the hot phase when the ratio of cooling time t_{cool} and free-fall time t_{ff} fall below a critical value $t_{\mathrm{cool}}/t_{\mathrm{ff}} < 10$. This cold gas is then uplifted by an AGN (Gaspari et al., 2012; Voit et al., 2017). Alternatively, the thermal instability may be triggered by the turbulent uplift by an AGN (McNamara et al., 2016; Olivares et al., 2019; Martz et al., 2020) or possibly a sloshing galaxy (Vantyghem et al., 2019). Simulations by Beckmann et al. (2019) find evidence for the former two.

In the following, we focus on the flow patterns of gas that is dragged up by the jet from the vicinity of the SMBH. We employ our idealized, non-radiative MHD setup to separate motions induced by cooling from motions caused primarily by the AGN. Motions induced by condensating material that is collected in the so-called cloud-growth regime (Gronke and Oh, 2018; Li et al., 2020; Sparre et al., 2020) require higher resolutions and are usually studied in dedicated simulations of cooling clouds submerged in hot winds. Consequently, this effect is not present in our setup.

Our analysis is focused on the `Fiducial` run at 50 Myr. In Figure 5.8, we portray the column density, velocity dispersion and mean velocity component along the line-of-sight of the traced gas in each row, respectively. The jet is rotated around the SMBH towards the observer (θ) and anti-clockwise in the plane (ϕ) at the same angle of $\theta = \phi = 0°, 22°, 45°, 68°$ in panels from left to right, respectively. At 50 Myr, lobes are inflated, which rise buoyantly as bubbles in the cluster. Their powerful wake causes magnetic field amplification and drags up gas from the center (Jones and De Young, 2005; O'Neill et al., 2009). The later process is visible as filamentous structures of enhanced column densities that extend from the centre of the cluster to the bubbles.

Induced mean velocities are highest in the filamentous structures and exceed values of $1000\,\mathrm{km\,s^{-1}}$. They are best visible when looking into the jet (high values of θ). Furthermore, the transverse component reaches velocities exceeding $\gtrsim 500\,\mathrm{km\,s^{-1}}$. The inner material is dragged along with the jet while downwards motions towards the SMBH are more common in the outer parts of the cocoon. The dragged up material even penetrates the center of the bubble and the bubble morphs into a torus. High vorticity and turbulence is generated throughout the bubble and wake. However, the velocity dispersion of the dragged up material remains surprisingly low with velocities in the range $10 - 40\,\mathrm{km\,s^{-1}}$.

Figure 5.9 shows a sample of four histograms that provide an overview of diversity seen in the velocity structure in individual pixels, corresponding to individual line-of-sight projections. Pixels show single Gaussian peaks with subdominant secondary flows (upper panels). At least two Gaussian components can be identified in the lower left panel. But we also find very heterogeneous velocity distributions in a significant fraction of pixels (lower right panel). Here, we see a clear peak in ad-

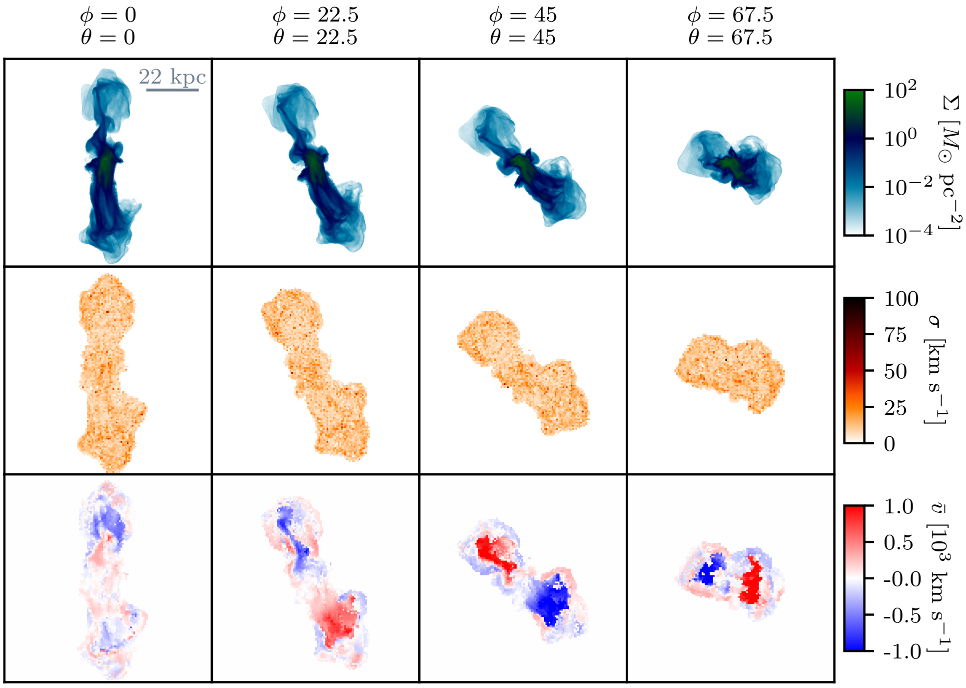

Figure 5.8: From top to bottom, we show surface density Σ of tracer material lifted from the center, tracer mass-weighted velocity dispersion σ and mean velocity $\bar{v}$ along the line of sight through the simulation box. Variables are binned in pixels of 0.7 kpc × 0.7 kpc. Images have dimensions 90 kpc × 90 kpc. We show results for `Fiducial` at 50 Myr. From left to right, the jet is rotated towards the observer at angle θ and counter-clockwise in the plane at angle ϕ. The wake accelerates the tracers up to 1000 km s^{-1} along the jet axis (high θ). The main velocity component shows low dispersion. Our high resolution allows us good sampling of the velocity distribution.

dition to many additional components moving in opposite directions. Thereby, a single Gaussian fit and its velocity dispersion cannot accurately account for the intermittent velocity structures of multiple velocity components in the flow patterns of the dragged-up material. Note that the turbulent ICM also influences the motion of the scalar. However, our comparison of induced velocities in `Fiducial` and `NoTurb` showed that the ICM contribution is secondary.

In summary, we are left with a remarkably coherent outflow in the wake of the bubble, at or exceeding the buoyant rising velocity of the jet-inflated bubble, reaching Mach numbers of almost unity (see Figure 5.6, bottom panel, sound speed around 10^3 km s^{-1}), and fairly insensitive to pre-existing turbulence. Since the bubble velocity is mostly set by cluster properties and bubble size (Churazov et al., 2001), we expect it to be fairly insensitive to details of the jet other than the total injected energy (which determines the bubble size, as shown in Ehlert et al., 2018). In the outflow reference frame, the local velocity dispersions constitute Mach numbers of only around 0.01-0.05. This has important implications for future studies of the thermodynamics of these outflows since it allows to study thermal instability in local simulations of outward moving patches of gas, without the need for a global, cluster wide simulation. While we only investigate one specific case, there is no reason to assume this changes qualitatively with changed jet parameters, though it is plausible to assume that the range of turbulent Mach numbers in the outflow frame across varying jet parameters is larger than presented here.

5.7 Conclusions

We run MHD simulations of jet-inflated bubbles in a Perseus-like CC cluster with a turbulent magnetic field. The equations of MHD directly relate large-scale magnetic and velocity fields via the momentum and induction equation, which we connect to two observables: line of sight velocity dispersion as measured by high spectral resolution X-ray spectroscopy and RM. Furthermore, we study the influence of the AGN on the velocity field, its detectability and the effect of spatial resolution.

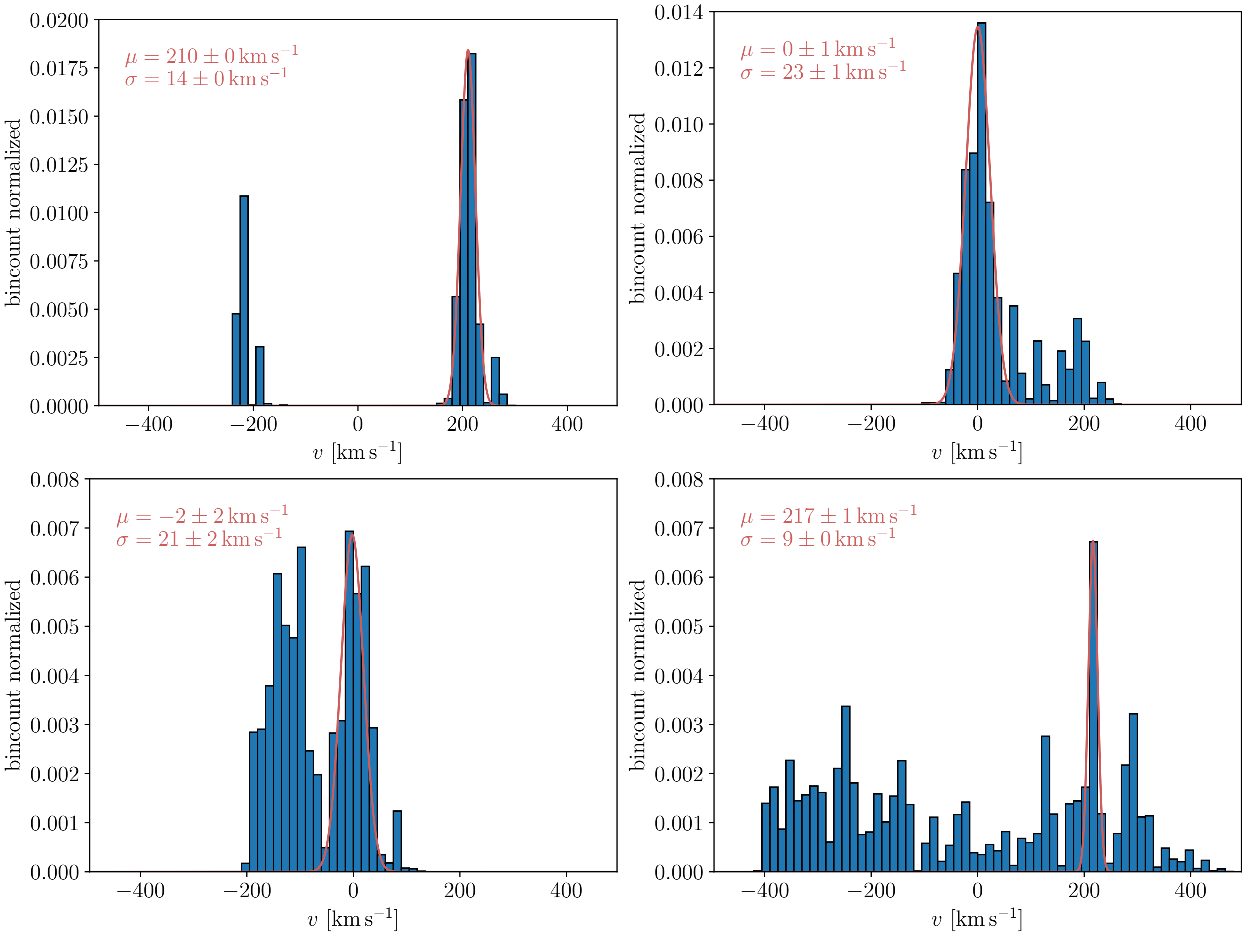

Figure 5.9: Histograms of the velocity of uplifted tracers by the AGN. Panels correspond to the line-of-sight velocity distribution in a single pixel weighted with tracer mass. We also overplot Gaussian fits that are used to determine mean velocity and velocity dispersion of the main velocity component (see Figure 5.8). The velocity distribution is dominated by a single Gaussian in the upper panels. However, the velocity distribution in the lower panels shows two distinct peaks or a predominantly flat distribution, respectively. The induced turbulent velocities show diverse and very complex distributions. Assuming a single velocity component is clearly insufficient to represent the complex flow structure.

Finally, we analyze the velocity structure of uplifted central gas in the wake of the buoyantly rising radio-lobes. We summarize our findings as follows.

- Measurements of large scale magnetic fields and velocities in galaxy clusters are inherently coupled. The strength, radial scaling and injection scale of our magnetic fields are motivated by observations. Interestingly, they yield RM values that are an order of magnitude higher than observed. While uncertainties of order a few are unavoidable when determining magnetic field strengths from RM measurements, observationally obtained magnetic field strengths may additionally suffer from Faraday depolarization and only probe a very limited spatial window. Assuming too large magnetic coherence scales may also bias the inferred magnetic field strengths high. Finally, beam smoothing and possible departures from Gaussianity may further alleviate this discrepancy (see discussion in Section 5.4). This highlights the relevance of cosmological MHD simulations that are able to self-consistently drive and sustain large scale magnetic fields. Moreover, this calls for a dedicated synthetic modeling of observations to take into account all possible observational effects.
- The influence of the AGN driven jet on the velocity fields is limited to the lobe's proximity. Gas flows on scales larger than the characteristic size of the lobes are not AGN driven.
- Given the arcmin resolution of the analysis of the *Hitomi* data of Perseus, we conclude that the measured cluster turbulence is likely not directly driven by rising radio lobes.
- Central gas is dragged up in filament-like structures by the AGN. A complex multi-component velocity structure is induced in the lifted material. While the bulk velocity of the lifted material exceeds 1000 km s^{-1}, the line of sight velocity dispersion is remarkably low with only about 50 km s^{-1}. The previously central gas remains constrained to the wake and near proximity of the rising bubbles.

The connection of line of sight velocity dispersion and RM studied in this work highlights the multi-facetted nature of intra-cluster turbulence, and the role numerical simulations can play to connect the different observables. We restricted this study to non-radiative simulations in order to quantify the role of 'stirring' by rising radio lobes without the additional effects of an (AGN moderated) cooling flow, as well as to an individual outburst. In the future, we plan to study the influence of cooling on the local AGN-induced velocity fields. This will allow us to compare our model to observed filaments in CC clusters.

Acknowledgements

KE and RW would like to thank John ZuHone for the insightful discussions and for making the PYXSIM code publicly available. We thank the anonymous referee for helpful suggestions and comments. KE and CP acknowledge support by the European Research Council under ERC-CoG grant CRAGSMAN-646955.

Data availability

The data underlying this article will be shared upon request to the corresponding author.

5.8 Appendix

5.8.1 Varying magnetic field parameters

We varied the initial magnetic field strength in our simulations and depict the resulting velocity dispersion in Figure 5.10. The magnetic-to-thermal pressure ratio in the ICM $X_{B,\mathrm{ICM}}$ decreases as

$X_{B,\mathrm{ICM}} = 0.25, 0.05, 0.01$ from left to right. Consequently, the velocity dispersion decreases as $\gtrsim 150\,\mathrm{km\,s^{-1}}$, $\sim 100\,\mathrm{km\,s^{-1}}$ and $\lesssim 60\,\mathrm{km\,s^{-1}}$, respectively. The lowest magnetic field run `X1` cannot stir the ICM sufficiently, to reach the velocity dispersion observed by *Hitomi*. Both `X25` and `X5` produce a velocity dispersion that is consistent with *Hitomi* measurements. However, we emphasize that cosmological simulations are necessary to follow the evolution of the magnetic dynamo and obtain self-consistent velocity fields.

In addition, we show simulations at decreasing resolution from left to right in Figure 5.11. The velocity dispersion decreases slightly with resolution. This is likely due to the increased numerical diffusivity in the lower resolution runs, which decrease the effectiveness of the stirring on longer timescales. The RMs show higher maxima in the low resolution run. Intermittent magnetic field strengths are less resolved so that the cancelling of RM is reduced.

Turning our attention now to the influence of jet magnetic fields on the overall RM, we see that RM is dominated by the contributions from the ICM. In Figure 5.12 we compare the total RM from ICM and jet (left) with the RM from the jet only (right). Some rims of the bubble and sparse filaments show relatively high signal. Here, only a few cells exceed the threshold in X_{jet} and thereby suffer from minimal depolarization. Comparing magnitudes, we see that the lobes contribute at least two orders of magnitude less signal compared to the ICM. This is consistent with observations, that would otherwise generally suffer from considerable beam polarization (e.g., Han, 2017). Note however, that some sources show evidence for a dominating contribution from locally compressed ICM close to the lobes (Rudnick and Blundell, 2003; Guidetti et al., 2012).

5.8.2 Jet resolution study

To improve the numerical convergence with respect to the distance traveled of our jets, we introduce an opening angle δ_j to the model. As discussed in Section 5.3.2, half of the momentum is injected with an angle smaller than 10 degree from the jet axis, while the maximum angle is 30 degree. While the jet initially fans out, it is almost immediately collimated by the pressure of the ambient ICM. This leads to an overall broadening of the jet where better resolved jets are affected more. Thereby better convergence of jet distance is obtained. In Figure 5.13, we contrast the bubble distance with and without opening angle as a function of time for simulations at three different resolutions. Simulations with an opening angle of $\delta_j = 30^\circ$ converge more to similar distances than those without opening angle ($\delta_j = 0^\circ$).

5.8.3 Synthetic X-ray observations

Figure 5.14 shows velocity dispersion maps using different methods from a full synthetic observation (top row), a fit to photon spectrum, i.e. synthetic observation without instrument response (middle row), and a $2-12$ keV emission weighted velocity dispersion. While there is a systematic increase in velocity dispersion originating from a higher temperatures at the outskirts of the projection, the instrumental effect mainly introduces scatter on a pixel by pixel basis.

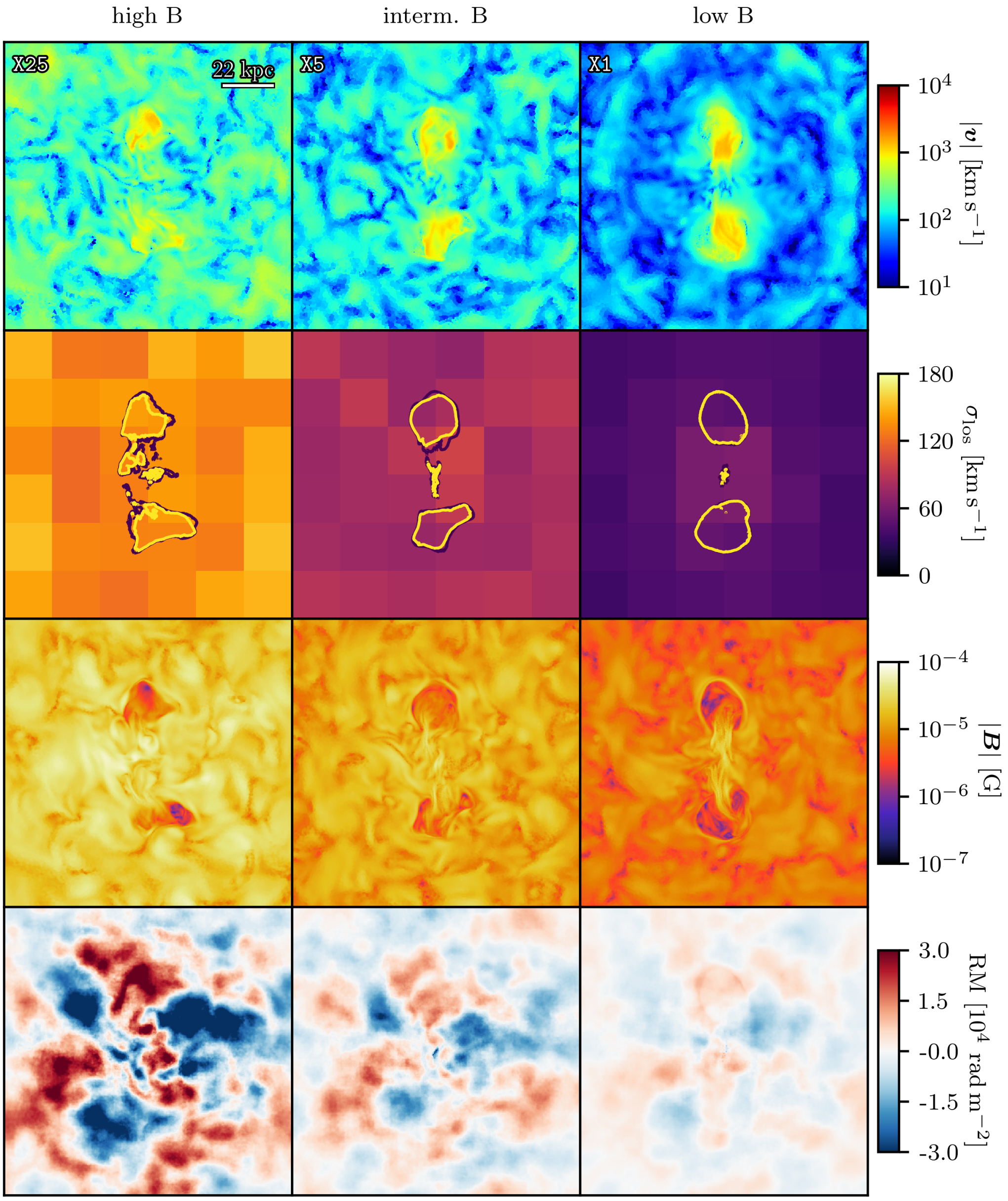

Figure 5.10: From left to right, we compare runs `X25`, `X5`, `X1` with varying magnetic field strengths $X_B = 0.25, 0.05, 0.01$, respectively. A higher magnetic fields strength provides a stronger tension force that induces higher velocities and velocity dispersion in the ICM. Both `X25` and `X5` induce a velocity dispersion consistent with *Hitomi* measurements, `X25` is at the upper end and `X5` thereby preferred. See Figure 5.4 for details on shown quantities.

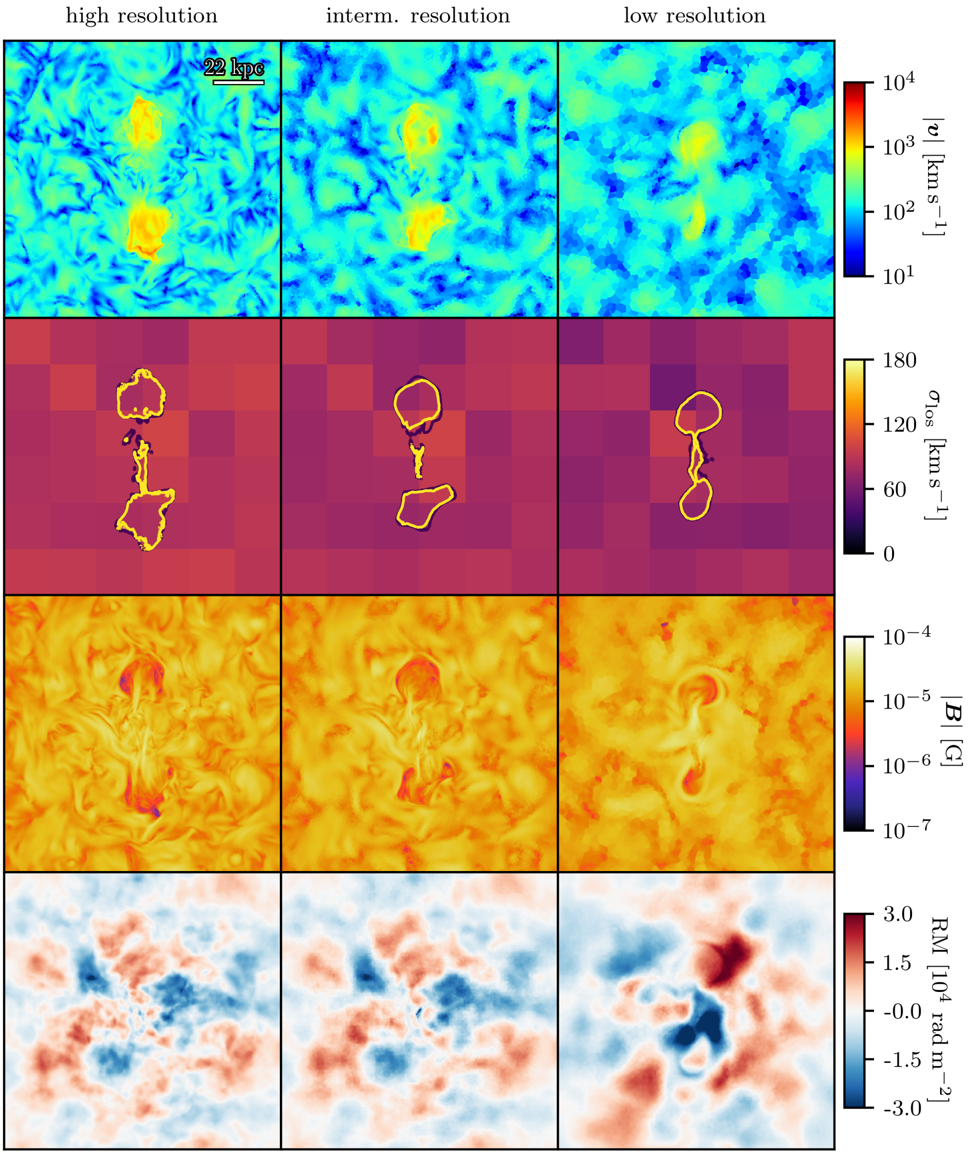

Figure 5.11: From left to right, we compare simulations at high, intermediate and low resolution, respectively. The loss of small scale structures leads to an increase in RM for the low resolution run as depolarization is reduced. However, overall features in runs at high and intermediate resolution show convergence. See Figure 5.4 for details on shown quantities.

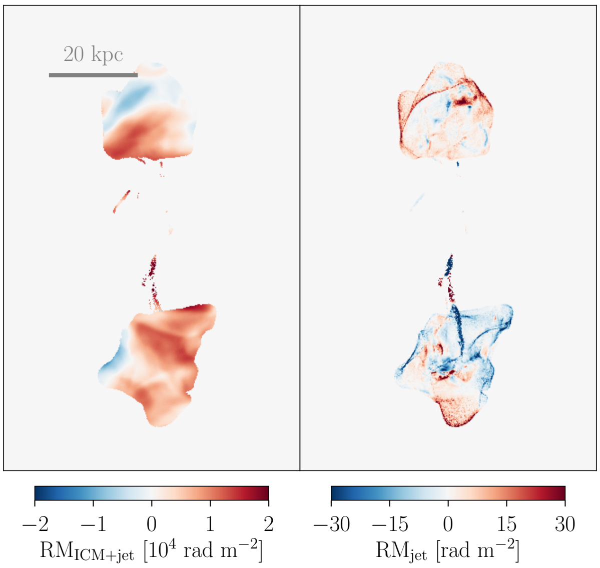

Figure 5.12: We show the RM of the fiducial run at 50 Myr for varying sources of emission. On the left, we include both the ICM and AGN as the source. On the right, we show the contribution from jet only ($X_{\mathrm{jet}} > 10^{-3}$). The ICM contribution dominates the RM signal by at least two orders of magnitude. The enhancement in parts of the bubbles' rim and some filaments is an artifact of the tagging process of the lobes.

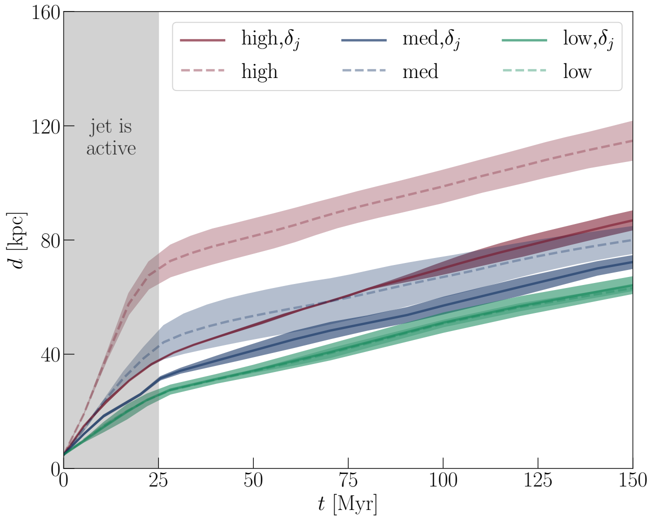

Figure 5.13: Average distance of the jets at low, intermediate and high resolution (shown with different colours) as a function of time. We compare our new model that includes an opening angle of $\delta_j = 30°$ (solid lines) to simulations with our previous model ($\delta_j = 0°$, dashed lines). The errorbars indicate the distance of the individual jets. Including an opening angle leads to improved numerical convergence of the jet distance travelled, especially for jets at high resolution.

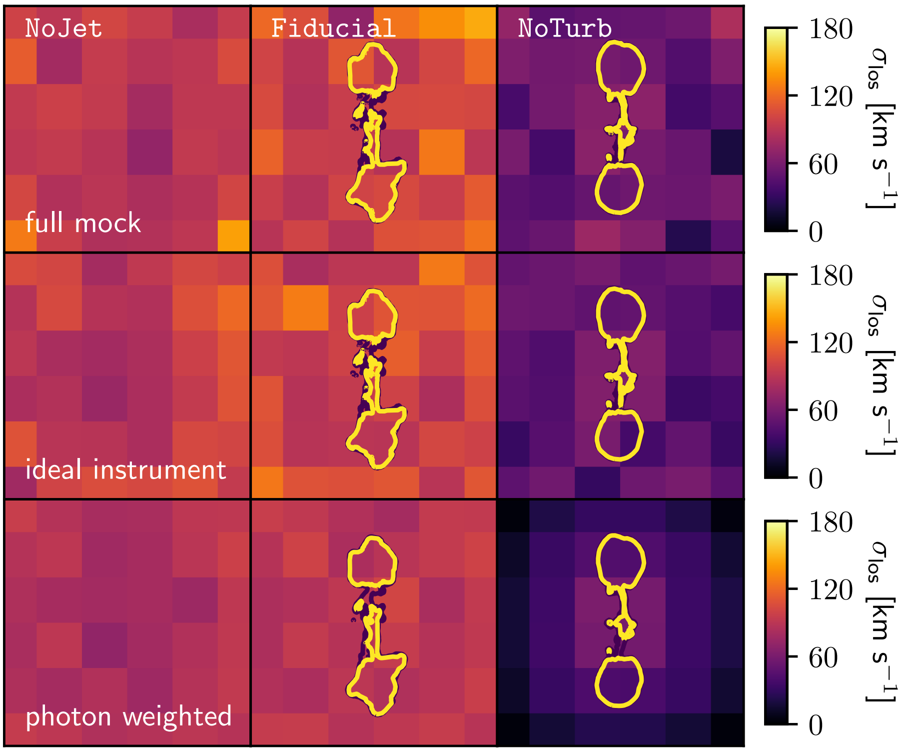

Figure 5.14: Velocity dispersion maps from mock Xrism observations (top), fits to the emitted photon spectrum (center) and the emission weighted velocity dispersion (bottom).

Self-regulated AGN feedback of light jets in cool-core clusters

6

This chapter is an adapted version of the paper *Self-regulated AGN feedback of light jets in cool-core clusters* submitted to MNRS and posted on arXiv as Ehlert et al. (2022).

6.1 Abstract

Heating from active galactic nuclei (AGN) is thought to stabilize cool-core clusters, limiting star formation and cooling flows. We employ radiative magneto-hydrodynamic (MHD) simulations to model light AGN jet feedback with different accretion modes (Bondi-Hoyle-Lyttleton and cold accretion) in an idealised Perseus-like cluster. Independent of the probed accretion model, accretion efficiency, jet density and resolution, the cluster self-regulates with central entropies and cooling times consistent with observed cool-core clusters in this non-cosmological setting. We find that increased jet efficiencies lead to more intermittent jet powers and enhanced star formation rates. Our fiducial low-density jets can easily be deflected by orbiting cold gaseous filaments, which redistributes angular momentum and leads to more extended cold gas distributions and isotropic bubble distributions. In comparison to our fiducial low momentum-density jets, high momentum-density jet heats less efficiently and enables the formation of a persistent cold-gas disc perpendicular to the jet that is centrally confined. Cavity luminosities measured from our simulations generally reflect the cooling luminosities of the intracluster medium (ICM) and correspond to averaged jet powers that are relatively insensitive to short periods of low-luminosity jet injection. Cold gas structures in our MHD simulations with low momentum-density jets generally show a variety of morphologies ranging from discy to very extended filamentary structures. In particular, magnetic fields are crucial to inhibit the formation of unrealistically massive cold gas discs by redistributing angular momentum between the hot and cold phases and by fostering the formation of elongated cold filaments that are supported by magnetic pressure.

6.2 Introduction

Cool-core (CC) clusters with central cooling times smaller than 1 Gyr form a subclass of galaxy clusters. However, the expected cooling flows are absent. Instead these clusters posses low star formation rates and low central entropies (Peterson and Fabian, 2006). Jets driven by the central AGNs inflate buoyantly rising bubbles that are observed as X-ray cavities. The mechanical luminosity of AGNs estimated from cavity enthalpy appears to be tightly linked to the cooling luminosity (e.g., Bîrzan et al., 2004; Rafferty et al., 2006; Diehl et al., 2008), leaving sufficient heating energy to offset the energy losses by the cooling ICM and establishing feedback from AGNs as the main heating source (McNamara and Nulsen, 2012; Fabian, 2012) in CC clusters.

The AGN is fueled by cooling gas accreted by the central super massive black hole (SMBH). The exact accretion mechanism remains uncertain. In many numerical simulations, Bondi-Hoyle-Lyttleton accretion (Bondi, 1952; Hoyle and Lyttleton, 1941) is employed due to its simplicity. However, observations find that Bondi accretion provides insufficient power to fuel active jets in clusters (e.g., Cavagnolo et al., 2011; McNamara et al., 2011; Russell et al., 2015; Fujita et al., 2016; Russell et al., 2018). The ICM is prone to the thermal instability, which acts when the cooling time t_{cool} is of order or shorter than the free fall time t_{ff} (Mccourt et al., 2012). Cold gas may condense in the galaxy or can become thermally unstable as it is dragged up by the AGN (e.g., McNamara et al. 2016; Russell et al. 2017; Tremblay et al. 2018, but see, Jones et al. 2017). The condensing cold gas is then predicted to rain on the central SMBH as *cold accretion* (Pizzolato and Soker, 2005; Sharma et al., 2012; Gaspari et al., 2017). Tremblay et al. (2016) report observational evidence of such a cold clumpy accretion flow towards a SMBH. In many CC clusters, cold gas takes a filamentary shape (e.g., Russell et al., 2019; Olivares et al., 2019) where clusters with low values of $t_{\mathrm{cool}}/t_{\mathrm{ff}}$ show more massive filaments (e.g., Cavagnolo et al. 2008; Voit and Donahue 2015; Lakhchaura et al. 2018 but see Martz et al. 2020).

Hydrodynamic simulations of galaxy clusters are able to produce a self-regulated feedback loop using a cold gas triggered SMBH accretion model which is coupled to the AGN feedback injection (e.g., Gaspari et al., 2012; Li and Bryan, 2014; Prasad et al., 2015). However, there are various AGN jet models proposed in the literature that range from high-momentum density jets (with or without precession, Sternberg and Soker, 2008a; Hillel and Soker, 2014, which heat mainly via mixing the cold and hot phases) to low-momentum density jets of various ICM-to-jet density ratios (Yang and Reynolds, 2016; Weinberger et al., 2017; Beckmann and Dubois, 2022), which can be more easily deflected by dense gas clouds in the path of propagation or by coherent and/or turbulent motions of the ambient ICM (Heinz et al., 2006).

When including star formation, Li et al. (2015) find a substantial suppression of the star formation rate compared to the expectation from an unmediated cooling flow for large enough efficiencies. A too low feedback efficiency, however, leads to high star formation rates $\gg 100\,\mathrm{M}_\odot\,\mathrm{yr}^{-1}$, inconsistent with observations (e.g., Fogarty et al., 2015). Cold gas properties are highly interconnected with the heating-cooling cycle: AGN-induced uplift is key in shaping the spatial distribution of cold gas (Yang et al., 2016), producing a wide range of cold gas cloud morphologies. Jets tend to shatter these structures (Beckmann et al., 2019). The addition of magnetic fields in simulations leads to a suppression of unrealistically massive cold gas discs that tend to appear in purely hydrodynamic simulations (Wang et al., 2021).

We simulate hot, low-density jets in an idealised magnetized CC cluster. In a companion paper (Weinberger et al., in prep.), we compare our low-density jet implementation to other AGN feedback implementations and study uncertainties arising due to resolution, parameter and model choices in detail. Here, we focus on (i) self-regulated feedback in CC clusters, and its dependence on the accretion prescription and jet properties, (ii) studying how mechanical X-ray cavity powers are related to the cooling luminosities and (simulated) jet luminosities, (iii) addressing the relevance of magnetic fields in redistributing the AGN feedback energy and in shaping the cold gas kinematics, and (iv) exploring how sensitive these results are to jet and accretion parameter choices.

The outline of our work is as follows. In Section 6.3, we describe our initial conditions and simulation setup. In Section 6.4 we demonstrate that independent of model choices, i.e. the adopted accretion model, probed jet efficiency and jet density, we obtain a self-regulated CC cluster. We analyse mechanical luminosities derived from X-ray cavities of our runs in Section 6.5 and study magnetic fields and the emerging cold gas in Section 6.6. We discuss our results in Section 6.7 and conclude in Section 6.8.

6.3 Methods and simulation models

We compute three-dimensional MHD simulations of AGN feedback in an idealised Perseus-like cluster with the moving-mesh code AREPO (Springel, 2010; Pakmor et al., 2016b). We use an HLLD Riemann solver (Pakmor et al., 2011; Pakmor and Springel, 2013) with the Powell 8-wave scheme for magnetic divergence control (Powell et al., 1999). In the following we describe the initial conditions, our ISM modeling, and further details of our jet/accretion models and simulation runs.

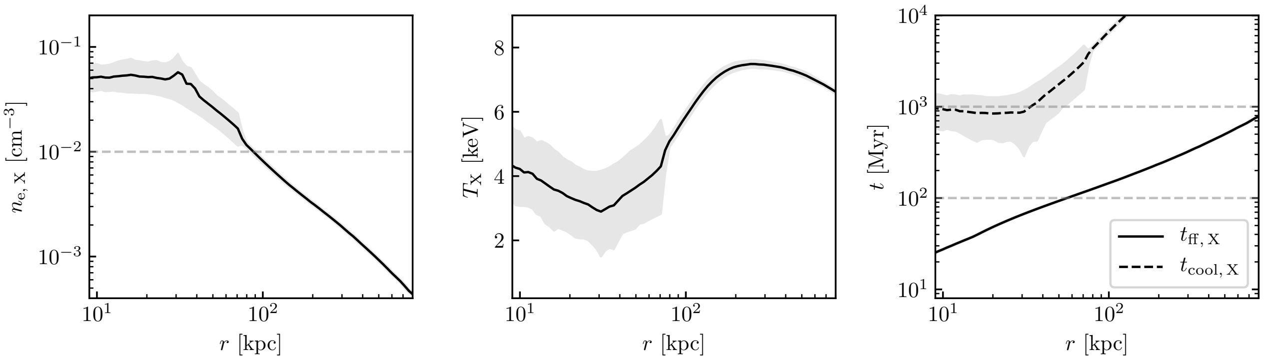

Figure 6.1: Radial profiles of the X-ray luminosity weighted electron number density (left), temperature (center), cooling time t_{cool} and free fall time t_{ff} (right) in our initial conditions. The shaded regions indicate the 10th and 90th percentiles. Only gas cells with $0.2\,\mathrm{keV} < k_{\mathrm{B}}T < 10\,\mathrm{keV}$ are considered.

6.3.1 Initial conditions

We adopt the radial electron density profile from Churazov et al. (2003) rescaled to a cosmology with $h = 0.67$:

$$\begin{aligned} n_{\mathrm{e}} = 46 \times 10^{-3} &\left[1 + \left(\frac{r}{60\ \mathrm{kpc}}\right)^2\right]^{-1.8} \mathrm{cm}^{-3} \\ + 4.7 \times 10^{-3} &\left[1 + \left(\frac{r}{210\ \mathrm{kpc}}\right)^2\right]^{-0.87} \mathrm{cm}^{-3}, \end{aligned} \tag{6.1}$$

which is set up in hydrostatic equilibrium with the gravitational potential comprised of an NFW cluster potential with virial radius $R_{200,\mathrm{NFW}} = 2\,\mathrm{Mpc}$, mass $M_{200,\mathrm{NFW}} = 8\times10^{14}\,\mathrm{M}_\odot$ and concentration parameter 5. On top of this cluster potential, we add a central galaxy potential approximated as an isothermal sphere with $M_{200,\mathrm{ISO}} = 2.4 \times 10^{11}\,\mathrm{M}_\odot$ with $R_{200,\mathrm{ISO}} = 15\,\mathrm{kpc}$ (Mathews et al., 2006). We only account for the gravity that results from a static background potential, neglecting effects of self-gravity. We confirmed that it has negligible effect in comparison runs.

The turbulent magnetic field is introduced as a Gaussian random field with a Kolmogorov slope on scales smaller than $k_{\mathrm{inj}} = 37.5^{-1}\,\mathrm{kpc}^{-1}$ and white noise on larger scales. The chosen scale is consistent with observations (Vacca et al., 2018). We use a constant thermal-to-magnetic pressure ratio of $X_{B,\mathrm{ICM}} = P_B/P_{\mathrm{th}} = 0.0125$, lower than in previous work to reduce rather large resulting values of Faraday rotation measure (Ehlert et al., 2021). The initial mesh consists of three nested meshes, with increasing resolution towards the center. We used an iterative procedure to provide an initial magnetic field that obeys the magnetic divergence constraint, $\nabla \cdot \boldsymbol{B} = 0$. Details of the divergence-free field setup can be found in Ehlert et al. (2018).

We introduce temperature fluctuations in the initial condition, seeding thermal instabilities at various stages to prevent the sudden emergence of a large amount of cold gas. We multiply the hydrostatic temperatures by values drawn from a Gaussian random field for $\delta T/T$ with dispersion $\sigma = 2$ and mean $\mu = 1$. The power spectrum of temperature fluctuations follows the Kolmogorov slope on scales smaller than $k_{\mathrm{inj}} = 37.5^{-1}\,\mathrm{kpc}^{-1}$ and corresponds to white noise on larger scales, consistent with the power spectrum of the fluctuations in the magnetic field strength.

In addition, we seed velocity fluctuations in the central 800 kpc of the initial conditions to mimic orbiting substructures and random gas motions that result from gravitational potential rearrangements in the virialisation process. We initialize individual field components as a Gaussian random field with standard deviation $\sigma = 70\,\mathrm{km\,s}^{-1}$. Powers on other scales are set to zero. The history of the initial velocity field is quickly erased as the jet significantly perturbs the velocity field within the crucial inner 200 kpc. Note, we use the same velocity fluctuations for all simulations analysed to simplify comparison across the different simulations.

In order to ease comparison to X-ray observations, we weight some quantities with the cooling luminosity of the X-ray emitting gas cells. Here, we only include cells with temperatures $0.2\,\mathrm{keV} < k_\mathrm{B}T < 10\,\mathrm{keV}$. The cooling luminosity is directly taken from the simulation. We refer to this weighting scheme as "X-ray luminosity weighted" in the following. In Fig. 6.1, we show radial profiles of the X-ray luminosity weighted electron number density, temperature, cooling time t_cool and free fall time t_ff.

The free-fall time t_ff (Sharma et al., 2012) (or *local dynamical time*, Mccourt et al. 2012) is given by

$$t_\mathrm{ff} = \sqrt{2r/g} \tag{6.2}$$

where $g = \mathrm{d}\Phi/\mathrm{d}r$ corresponds to the local acceleration due to gravity. The cooling time is defined via

$$t_\mathrm{cool} = \frac{\varepsilon_\mathrm{th}}{\dot{\varepsilon}_\mathrm{cool}}, \tag{6.3}$$

where ε_th is the thermal energy density and $\dot{\varepsilon}_\mathrm{cool}$ is the cooling luminosity for X-ray emitting gas (with $0.2\,\mathrm{keV} < k_\mathrm{B}T < 10\,\mathrm{keV}$) in our simulations. Figure 6.1 shows that the Gaussian temperature fluctuations introduce cells that start condensing soon after the start of the simulations while more than 90 per cent of the gas has cooling times exceeding 300 Myrs.

6.3.2 Cooling and star formation

The modeling of cooling, star formation and stellar feedback follows Vogelsberger et al. (2013) with updates and parameter choices consistent with the IllustrisTNG model (Pillepich et al., 2018). Cooling is modeled down to temperatures of 10^4 K using primordial and metal-line cooling assuming a constant metallicity of 0.3 times the solar value, which is motivated by an observed uniform ICM iron abundance $Z_\mathrm{Fe} \approx 0.3$ in solar units (Werner et al., 2013) for $r \lesssim 1.5\,\mathrm{Mpc}$. Treatment of star formation and supernova feedback are part of the ISM model described in Springel and Hernquist (2003). The model implements star formation as a stochastic process, where the star formation probability is tied to the free fall time of the gasÂ and calibrated to follow the observed Kennicutt relation (Kennicutt, 1998). Supernovae feedback heats the hot ICM and evaporates cold clouds. This leads to a tightly regulated regime for star formation. In the model this translates to an ISM that is pressurized by star formation feedback such that cold and hot phase coexist in pressure equilibrium, with the pressure given by a density dependent effective equation of state (eEOS). Above a density threshold of $n_\mathrm{e} = 0.13\,\mathrm{cm}^{-3}$, gas can exist either on this effective equation of state (see red line in Fig. 6.2) and form stars or as non star-forming phase with larger temperatures, but not below it. Gas on this eEOS is by definition star forming and, as mentioned in the previous subsection, also the main fuel for SMBH accretion. Stellar feedback beyond that implicitly accounted for by the eEOS is not modeled. At the chosen halo mass scale these stellar feedback effects are anyhow subdominant.

6.3.3 Jet

Provided the AGN cavities are in pressure equilibrium with the ambient ICM and supported by (entrained) thermal plasma (Croston and Hardcastle, 2014; Croston et al., 2018), the X-ray surface brightness maps imply a low cavity density and constrain this gas to be much hotter than the surrounding ICM. Because the bright X-ray emission of the ICM along the line of sight is projected onto the potentially faint emission from the cavities, X-ray spectroscopy alone is unable to probe the existence of very hot diffuse thermal plasma in excess of tens of keV filling the cavities. In fact, the high cavity-to-ICM density contrast was used to constrain the temperature of thermal plasma potentially supporting the cavities to $k_\mathrm{B}T > 20$–50 keV (Nulsen et al., 2002; Blanton et al., 2003; Sanders and Fabian, 2007).

Instead, a thermally supported cavity provides a Sunyaev-Zel'dovich (SZ) signal that is distinguishable from the signal of a cavity supported by magnetic fields and non-thermal relativistic particles, which themselves contribute minimally to the SZ effect (Pfrommer et al., 2005; Ehlert et al., 2019). Observations of the Sunyaev-Zel'dovich Effect in MS 0735.6+7421 show a clear deficit in signal consistent with temperatures of $\gtrsim 1000\,\mathrm{keV}$ in the case of thermal pressure supported bubbles (Abdulla et al., 2019). This corresponds to an ICM-to-jet density contrast of $\rho_\mathrm{ICM}/\rho_\mathrm{jet} > 10^2$ to 2×10^2 (and likely much larger). We therefore adopt $\rho_\mathrm{jet} = 10^{-28}\,\mathrm{g\,cm^{-3}}$ (i.e., $\rho_\mathrm{ICM}/\rho_\mathrm{jet} \sim 3\times10^3$–$10^4$) as our fiducial jet density. Jets are injected in a bi-directional fashion with zero opening angle from a spherical region with radius $r = r_\mathrm{acc}/3$ (Weinberger et al., in prep.). We inject a helical magnetic field in the jet fluid with a magnetic-to-thermal pressure ratio $X_{B,\mathrm{jet}}$.

Talbot et al. (2021) model accretion of geometrically thin discs and launch jets using the Blandford and Znajek (1977) model. They find that the jet direction varies mildly by 25° over 10 Myr for the most extreme case, when the jet is launched into the accretion disc, while it remains stable otherwise. Lower black hole-spin values lead to a more efficient reorientation of the spin (Beckmann et al., 2019), because only little accreted material (with a different spin) is needed to torque the SMBH spin while maximally spinning Kerr black holes require the accretion of at least the mass of the black hole itself to change the spin orientation by unity. Realistic accretion models require the modeling of a geometrically thick disc in the low-Eddington accretion regime as expected for jets. This implies turbulent discs in which the mageto-rotational instability can transport angular momentum to larger radii, thus limiting the accreted angular momentum and black-hole spin reorientation, which has a direct consequence on the jet launching direction. Importantly, chaotic cold accretion implies the feeding of the accretion disc with material of random angular momentum, such that the average angular momentum does not appreciably change over time scales of 1 Gyr, which justifies our choice of a steady jet direction. Similar theoretical arguments have been made by Nixon and King (2013), suggesting that rapidly reorienting jets would be an indication against a Blandford-Znajek jet launching mechanism.

To set up the jet state, we select gas cells within a spherical region with radius $r = r_\mathrm{acc}/3$ and set their density to the pre-defined value ρ_jet. Unlike in previous studies (Weinberger et al., 2017), this is done directly in the center and the mass that is removed from (or added to) this jet region is not redistributed to the surroundings, but added to the gravitating mass of the black hole, ensuring total mass conservation. This mass is treated as a reservoir for future accreted gas in the black hole accretion routine. The total energy in the system is reduced by $\Delta m\langle u\rangle$, where Δm is the mass change and $\langle u\rangle$ is the ambient specific thermal energy. The gas cells in the spherical shell outside the jet region but within a radius of r_acc are used to determine these ambient gas properties. In the jet region, we add internal energy to ensure that cells are at least in pressure equilibrium with the surroundings. Note that we do not allow for internal energy to be reduced at this step. From the jet energy available at a timestep, $L_\mathrm{jet}\mathrm{d}t$, we subtract the energy required to set up the jet state with its fixed density and in pressure equilibrium with its surroundings and inject the remaining energy in the form of kinetic energy bidirectionally without opening angle into the jet region. To trace the jet, we initialize a passive scalar $X_\mathrm{jet} = 1$ in the jet region and advect it with the fluid. Our target mass is based on distance from the centre as

$$m_\mathrm{target} = m_\mathrm{target,0}\exp(r/100\,\mathrm{kpc}), \tag{6.4}$$

with cells at the outskirts limited to a maximum volume with a cell radius $r_\mathrm{cell} = 370\,\mathrm{kpc}$. To sustain the strong density gradient between jet and ICM, we additionally refine cells with $X_\mathrm{jet} > 10^{-3}$ to a target volume $V_\mathrm{jet,target}$, where we limit the volume ratio between neighboring cells to 4 (see Weinberger et al., 2017, and Weinberger et al., in prep. for further details on the jet implementation). Table 6.1 shows the corresponding values for the discussed parameters in our runs.

6.3.4 Accretion

One focus of this study is to analyse the impact of the employed accretion model. Here, we use Bondi accretion and chaotic cold accretion with implementation details presented in the following. For the accretion rate estimate we use gas properties from cells within radius r_acc from the SMBH (excluding the jet region). We assume an initial black hole mass of $4\times10^9\,\mathrm{M}_\odot$, in rough agreement with expectations from black hole-halo scaling relations. This is an order of magnitude more massive than the SMBH in NGC1275 in the center of the Perseus cluster (Wilman et al., 2005; Scharwächter et al., 2013), which is an outlier in the black hole - host scaling relations (Sani et al., 2018).

Cold accretion

We parameterize the SMBH accretion rate $\dot{M}$ in the cold mode as

$$\dot{M}_{\mathrm{cold}} = \epsilon \frac{M_{\mathrm{cold}}}{t_{\mathrm{ff}}}, \tag{6.5}$$

where M_{cold} includes star forming gas and gas with a temperature below $2 \times 10^4\,\mathrm{K}$. Note, M_{cold} corresponds to the total gas mass of the cell. We do not explicitly compute the mass component of the cold phase in the ISM model. We then drain mass $\Delta M_{\mathrm{bh},i} = \dot{M}_{\mathrm{cold},i} \Delta t$ from all cold gas cells i during timestep Δt and increment the black hole mass by the total drained gas mass $\Sigma_i \Delta M_{\mathrm{bh},i}$. When calculating the free-fall time t_{ff}, we only consider gravitational acceleration due to the static galaxy and cluster potential.

Not all gas arrives at the BH within t_{ff} due to the angular momentum of the gas. Processes that lead to angular momentum cancellation, e.g. cloud collisions (Gaspari et al., 2017), are not necessarily efficient enough under all circumstances. In addition, unresolved small-scale feedback may evaporate a fractions of the cold gas. To take these effects into account, we introduce the parameter $\epsilon < 1$ which represents a simple parametrization of the importance of these effects. Due to the high pressure environment of a massive galaxy cluster, our temperature threshold is below the effective temperature of most cold gas given by the effective equation of state of the interstellar medium (ISM, Springel and Hernquist, 2003, see Fig. 6.2). Therefore the SMBH is de-facto mostly accreting gas from the star forming phase.

The jet power L_{jet} is proportional to a fraction η of the accreted rest-mass energy

$$L_{\mathrm{jet}} = \eta \dot{M}_{\mathrm{cold}} c^2 = \eta \epsilon \frac{M_{\mathrm{cold}}}{t_{\mathrm{ff}}} c^2, \tag{6.6}$$

where c denotes the speed of light.

Bondi accretion

We compare the cold gas based accretion model to the frequently used Bondi accretion estimate. The Bondi accretion rate is given by

$$\dot{M}_{\mathrm{bondi}} = \frac{4\pi G^2 M^2 \rho}{c_{\mathrm{s}}^3}, \tag{6.7}$$

where M is the SMBH mass, c_{s} is the speed of sound, ρ is the mass density of the accreting medium. Assuming spherical accretion, the accretion rate must be below the Eddington limit. In practice, this limit is never reached in our runs. Analogously to cold accretion, the jet power is given by

$$L_{\mathrm{jet}} = \eta \dot{M}_{\mathrm{bondi}} c^2. \tag{6.8}$$

Label	accretion	ϵ	η	$\rho_{\rm jet}$ [g cm^{-3}]	$m_{\rm target,0}$ [$10^5\,{\rm M}_\odot$]	$V_{\rm jet,target}^{1/3}$ [kpc]	$r_{\rm acc}$ [kpc]	radiative cooling	$X_{B,\rm ICM}$	$X_{B,\rm jet}$
`Fiducial`	cc	0.1	0.01	10^{-28}	15	0.65	2	✓	0.0125	0.1
`Dense`	cc	0.1	0.01	10^{-25}	15	0.65	2	✓	0.0125	0.1
`HD`	cc	0.1	0.01	10^{-28}	15	0.65	2	✓	0	0
`Bondi`	bo	-	0.01	10^{-28}	15	0.65	2	✓	0.0125	0.1
`NoBH`	-	-	-	-	15	-	-	✓	0.0125	-
`NoBHNoCool`	-	-	-	-	15	-	-	-	0.0125	-
`HR`	cc	0.1	0.01	10^{-28}	1.5	0.3	1	✓	0.0125	0.1
`HDHR`	cc	0.1	0.01	10^{-28}	1.5	0.3	1	✓	0	0
`BondiHR`	bo	-	0.01	10^{-28}	1.5	0.3	1	✓	0.0125	0.1
Varying accretion parameters										
	cc	0.1	0.1	10^{-28}	15	0.65	2	✓	0.0125	0.1
	cc	0.01	0.01	10^{-28}	15	0.65	2	✓	0.0125	0.1
	cc	0.01	0.001	10^{-28}	15	0.65	2	✓	0.0125	0.1
	cc	1	0.0001	10^{-28}	15	0.65	2	✓	0.0125	0.1
	bo	-	0.001	10^{-28}	15	0.65	2	✓	0.0125	0.1

Table 6.1: Simulation parameters with accretion model (bo for Bondi accretion, and cc for chaotic cold accretion), efficiency parameters ϵ and η, jet density $\rho_{\rm jet}$, target mass $m_{\rm target,0}$, jet target volume $V_{\rm jet,target}$, radius of accretion region $r_{\rm acc}$, thermal-to-magnetic pressure ratio in the ICM $X_{B,\rm ICM}$ and in the jet $X_{B,\rm jet}$.

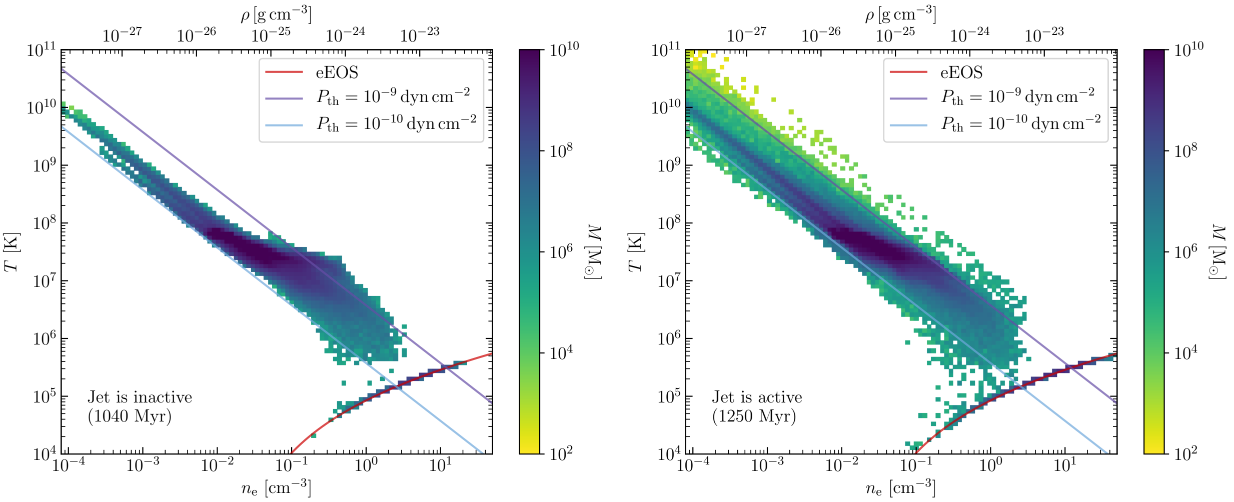

Figure 6.2: Phase diagram of the electron number density n_e and temperature in the central 100 kpc at 1040 Myr (where the jet is inactive) and at 1250 Myr (where the jet is active) in the run `Fiducial`. Color coding corresponds to total mass in respective bins. The effective model of the ISM inhibits cooling below the effective equation of state (red line). The plasma is near pressure equilibrium. Lines of constant pressure are shown in blue and purple.

6.3.5 Simulation runs

Simulations discussed in the following are summarized in Table 6.1. The `Fiducial` model uses cold accretion with our fiducial efficiency parameters $\epsilon = 0.1$ and $\eta = 0.01$. To study the impact of magnetic fields, we rerun `Fiducial` by excluding MHD, which we call `HD`. Our `Bondi` run with fiducial Bondi accretion allows comparisons with a different mode of accretion. We analyse effects of numerical resolution by rerunning `Fiducial`, `HD` and `Bondi` at 10 times higher mass resolution, reduced accretion radius $r_\mathrm{acc} = 1\,\mathrm{kpc}$ and a factor of 2 higher spatial resolution in the jet (see Table 6.1). We refer to the high resolution runs as `HR`, `HDHR` and `BondiHR`, respectively. We also vary the efficiency parameters ϵ and η of the cold accretion model and increase the jet density by 10^3 in our `Dense` model. To assess the effects of our jet feedback, we remove the SMBH and its associated feedback in run `NoBH`.

6.4 A self-regulated cool-core cluster

We first focus on the state of self-regulation seen in our simulations. The time evolutions of the different models are exemplified in Fig. 6.3, where we show density and entropy slices, the surface density of the gas with a cooling time below 30 Myr and the X-ray emissivity of gas with $0.2\,\mathrm{keV} < k_\mathrm{B}T < 10\,\mathrm{keV}$ of our `HR` model ($\epsilon = 0.1$, $\eta = 0.01$, cold accretion). Low density jets inflate cavities with density contrasts of $\sim 10^4$ that rise buoyantly in the cluster atmosphere.[1] Cluster weather resulting from turbulent intracluster motions deflects bubbles throughout the run. Additionally, central cold gas deflects the forming bubbles early which leads to more isotropised feedback. Deflection of bubbles by cluster weather and cold gas is seen in many simulations (e.g., Sijacki et al., 2008; Morsony et al., 2010; Mendygral et al., 2012; Bourne and Sijacki, 2017; Bourne et al., 2019). The gas in the wake of bubbles experiences a strong uplift, which advects low-entropy gas from the center to larger radii so that the upwards path leading to the high-entropy bubbles is traced by low-entropy gas that originates from the center (as discussed in Chen et al., 2019; Ehlert et al., 2021; Zhang et al., 2022). Gas with low cooling time accumulates in the center and forms filamentary structures and/or transient discs (e.g. at 1600 Myr). The bubbles are clearly discernible as high-contrast cavities in the

---

[1] While the central electron number density in the initial conditions is $5 \times 10^{-2}\ \mathrm{cm}^{-3}$ (Eq. 6.1), successive cooling and compression increases the central electron density so that it self-regulates around a new equilibrium profile with central densities of ~ 0.3–$1\ \mathrm{cm}^{-3}$ (see Fig. 6.4), which implies ICM-to-jet density contrasts of $\sim 3 \times 10^3$–10^4 in our fiducial low-density jets (and ~ 10 in our `Dense` model) at jet launching.

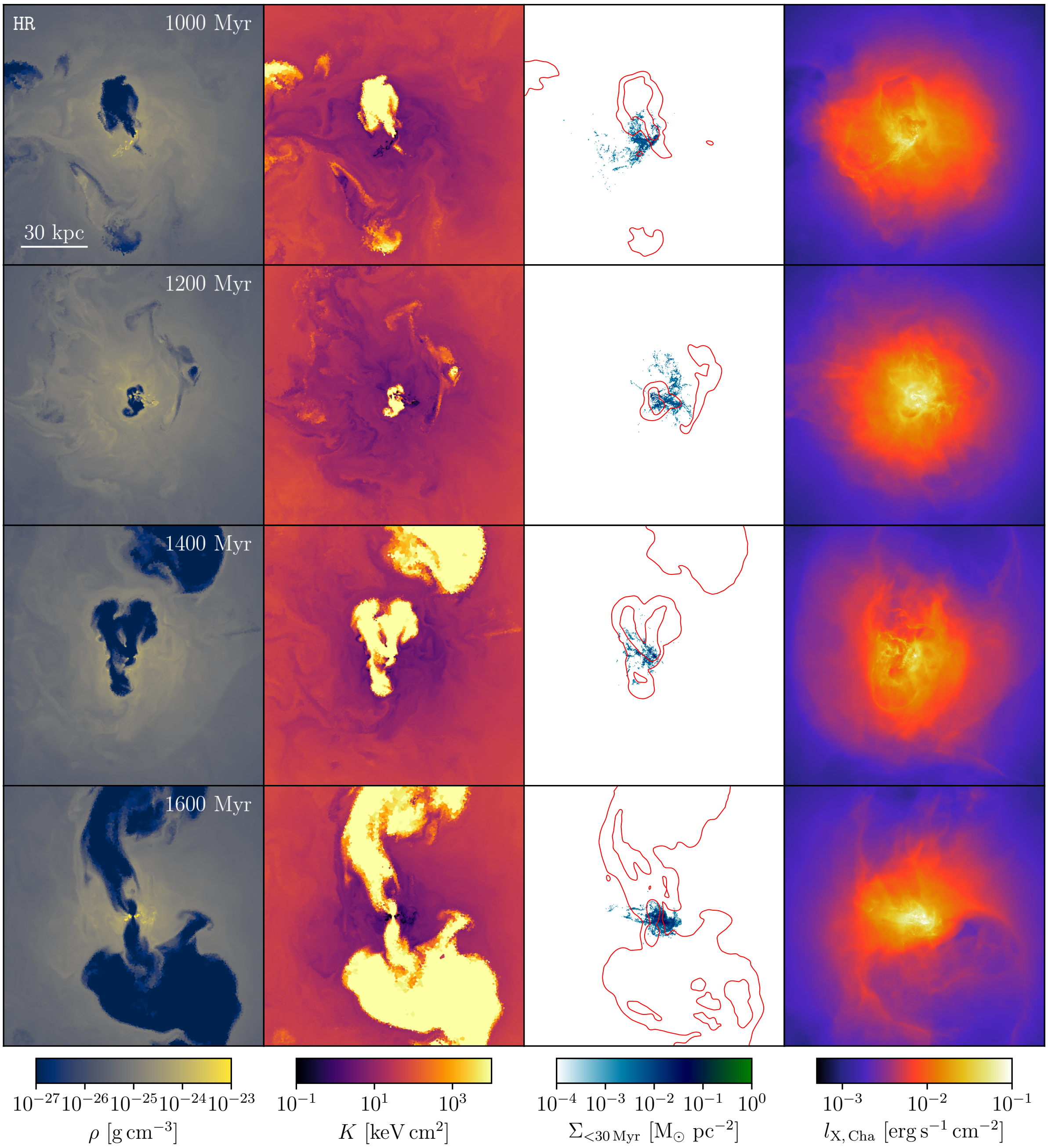

Figure 6.3: Overview of the fiducial high resolution cold accretion simulation **HR** (with accretion parameters $\epsilon = 0.1$ and $\eta = 0.01$). We show thin slices of side length 120 kpc of the mass density ρ, entropy $K = k_\mathrm{B} T n_\mathrm{e}^{-2/3}$, cold gas surface density $\Sigma_{<30\,\mathrm{Myr}}$ where $t_\mathrm{cool} < 30\,\mathrm{Myr}$ and the X-ray emissivity $l_{\mathrm{X,Cha}}$ is in the Chandra band (for which we adopt our simulated cooling luminosity that includes metal line cooling). Cold gas deflects the jet which allows it to heat the cooling ICM more isotropically. High entropy gas is only found in the bubbles, whereas the bulk of the ICM remains at low entropy typical for CC clusters.

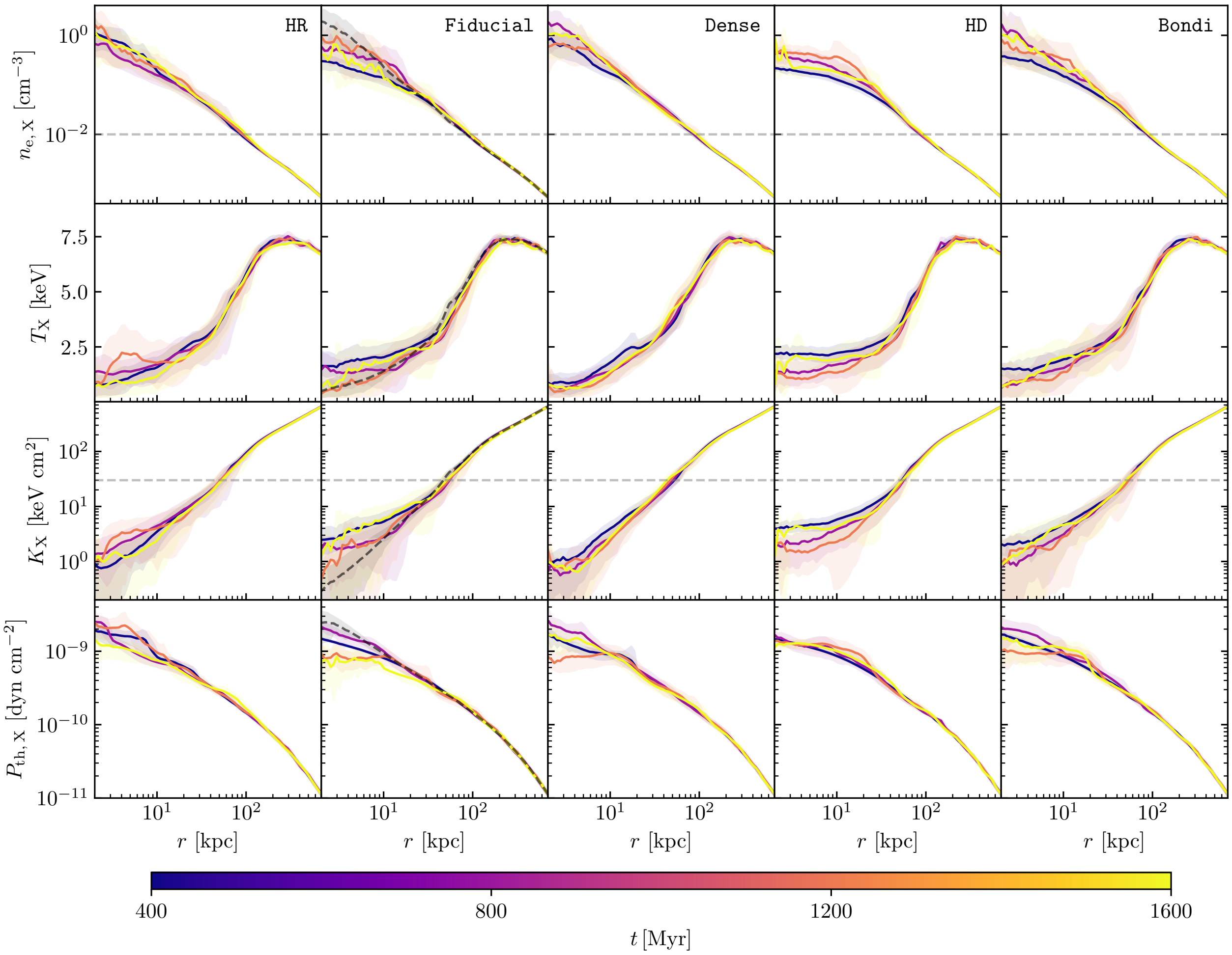

Figure 6.4: Radial profiles of the X-ray weighted density $n_{\rm e,X}$, temperature $T_{\rm X}$, entropy $K_{\rm X}$ and thermal pressure $P_{\rm th,X}$. The different colours correspond to simulation times as indicated on the colour bar. Profiles for model `NoBH` at 1200 Myr are shown in dashed in the second column. Shaded areas indicate the 10th to 90th percentiles and dashed lines represent popular choices for defining CC clusters (with central densities above 10^{-2} cm^{-3} and central entropies less than 30 keVcm^2). A self-regulated heating-cooling cycle leads to a dynamical attractor solution resembling that of observed CC clusters irrespective of the accretion mode and for all probed parameters.

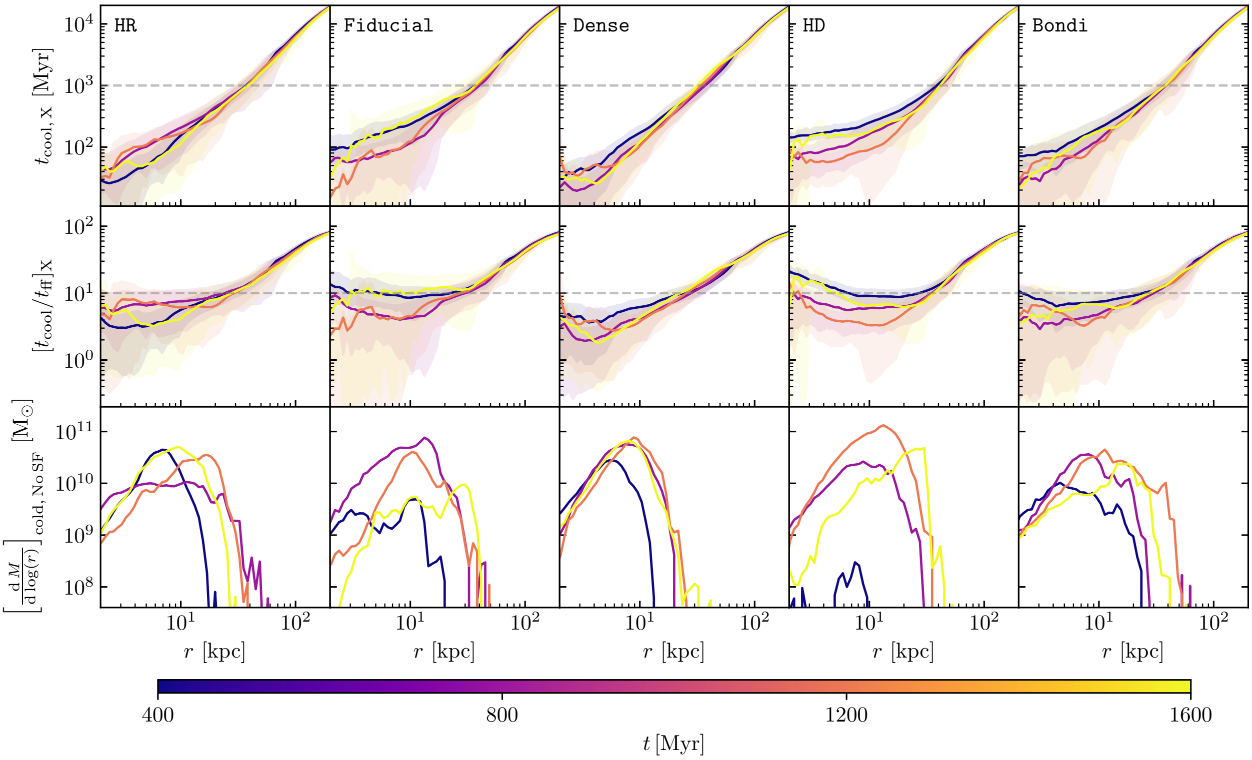

Figure 6.5: Radial profiles show the X-ray weighted cooling time t_{cool}, the ratio of cooling-to-free fall time $t_{\mathrm{cool}}/t_{\mathrm{ff}}$ and the total mass per bin normalized by the bin size for non-star forming gas with $t_{\mathrm{cool}} < 100$ Myr, i.e., $[\mathrm{d}M/\mathrm{d}\log(r)]_{\mathrm{cold,No\,SF}}$. The different colours correspond to simulation times as indicated on the colour bar. Shaded areas indicate the 10th to 90th percentiles. The ratio $t_{\mathrm{cool}}/t_{\mathrm{ff}}$ falls below 10 in the central region ($r \lesssim 50$ kpc), where cold gas forms stars. The minimum in $t_{\mathrm{cool}}/t_{\mathrm{ff}}$ roughly corresponds to the maximum amount of cooling gas mass.

X-ray emissivity.

In Fig. 6.2, we show a phase diagram of temperature T vs. electron number density n_{e} when the jet is inactive (left) and active (right) in the central 100 kpc of the cluster. As our low-density jets are set up in pressure equilibrium with the surrounding ICM, the jets are comprised of hot, low-density gas. Interestingly, the ICM pressure in the cluster center only varies by roughly an order of magnitude. This implies that jet feedback does not create any dramatically over-pressured gas in galaxy clusters, which, in turn, would cause strong shocks (see the parameter study in Ehlert et al., 2018). Cooling gas moves isobarically onto the effective equation of state (eEOS) where it forms stars. Further cooling to higher densities and lower temperatures is limited by the eEOS.

We study the long-term impact of AGN feedback on the ICM in Fig. 6.4, where we show radial profiles of the X-ray weighted ($0.2\,\mathrm{keV} < k_{\mathrm{B}}T < 10\,\mathrm{keV}$) density $n_{\mathrm{e,X}}$, temperature T_{X}, entropy K_{X} and thermal pressure $P_{\mathrm{th,X}}$ of various runs. Dashed lines separate strong CC clusters from moderate CC/non CC clusters as observationally determined (Cavagnolo et al., 2008; Hudson et al., 2010). Central densities remain high throughout time independent of accretion model, resolution and jet density, well above the CC limit. The initialization of denser jets in our `Dense` model lead to even higher densities in this run. Generally, the central entropy stays well below $10\,\mathrm{keV\,cm}^2$. As noted previously, radiative cooling of our initial conditions causes the central temperature to drop by a factor of ~ 3, the density to increase by a factor of a few and therefore the entropy to decrease by a factor ~ 10.

Interestingly, the cluster self-regulates at these new equilibrium profiles throughout the runtime of the simulation, implying that our AGN jet feedback stabilises the system but cannot substantially alter the thermodynamic profile of our CC galaxy cluster or even transform it into a non-CC cluster (in agreement with the statistics of observed AGN bubble enthalpies and central ICM entropies, Pfrommer et al., 2012). For comparison, we show profiles for model `NoBH` at 1200 Myr in the second column of Fig. 6.4, which enters a run-away cooling state with a dense cold core that causes SFRs

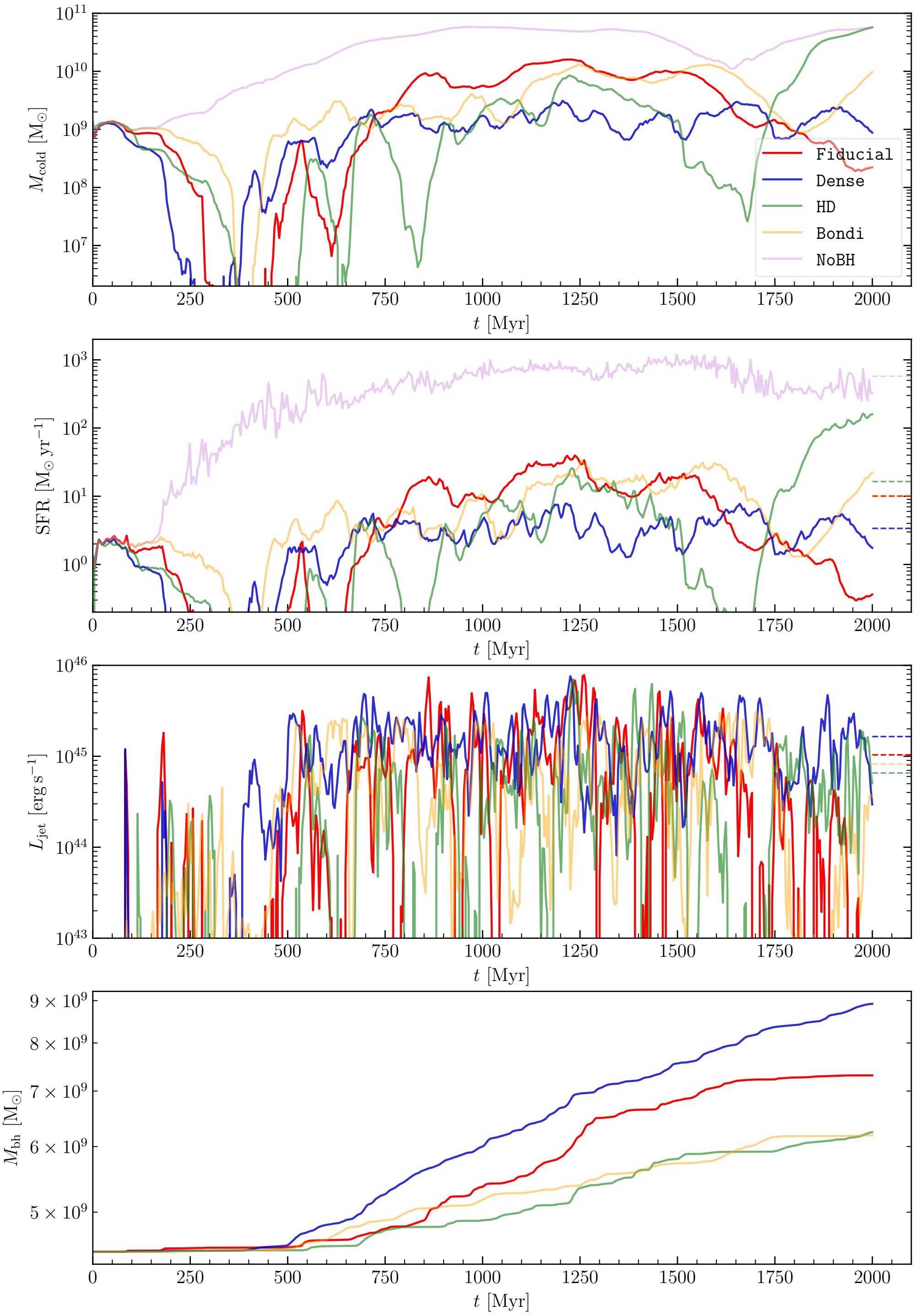

Figure 6.6: Time evolution of cold gas mass $M_{\rm cold}$ ($T < 10^6$ K), star formation rate SFR, jet power $L_{\rm jet}$ and SMBH mass $M_{\rm bh}$. Averages for times $t > 500$ Myr are shown with dashed horizontal lines on the right. If no feedback is included (`NoBH`) runaway cooling is observed and unobserved star formation rates of $> 100\,{\rm M}_\odot\,{\rm yr}^{-1}$. After 500 Myr all feedback models establish a self-regulated state with moderate star formation rates ($\sim 10\,{\rm M}_\odot\,{\rm yr}^{-1}$) and jet powers ($\sim 8 \times 10^{44}$ erg s). Dense jets have a larger momentum density and deposit their energy at larger radii so that the central gas cools more strongly and gives rise to larger SMBH masses in comparison to the other models. The hydrodynamical model forms an unobserved type of massive disc at 2 Gyr with extreme star formation rates ($\sim 100\,{\rm M}_\odot\,{\rm yr}^{-1}$). In Fig. 6.10 we show histograms of the jet power.

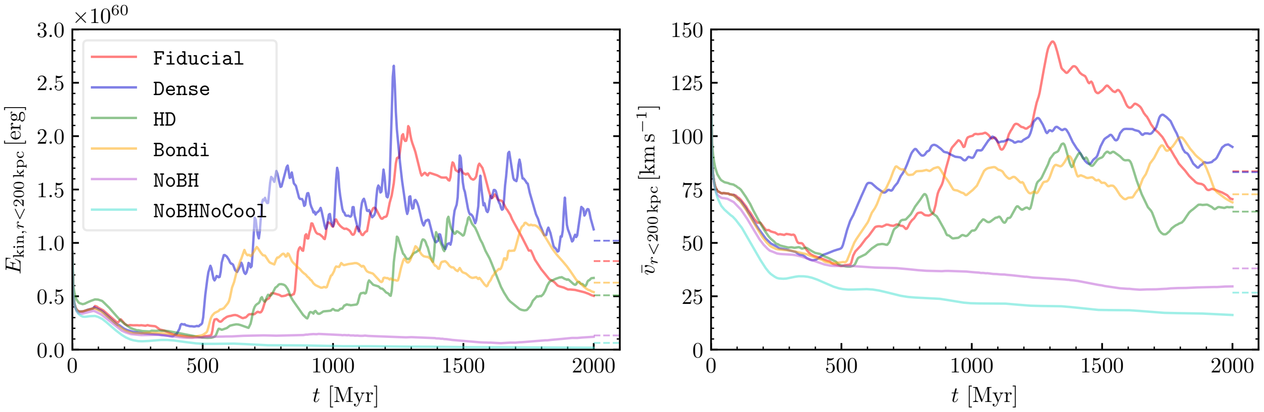

Figure 6.7: Time evolution of the total kinetic energy within 200 kpc ($E_{\mathrm{kin},r<200\,\mathrm{kpc}}$) and mass-weighted average velocity within 200 kpc ($\bar{v}_{r<200\,\mathrm{kpc}}$). Averages for all times are shown with a dashed horizontal lines on the right. Turbulent velocities that are present in the initial conditions decay as a function of time. The onset of jet feedback at $t > 500$ kpc in runs `Fiducial`, `Dense`, `HD` and `Bondi` injects substantial kinetic energy. On the other hand, runs excluding AGN feedback `NoBH` and `NoBHNoCool` (with and without radiative cooling, respectively) continue to lose kinetic energy.

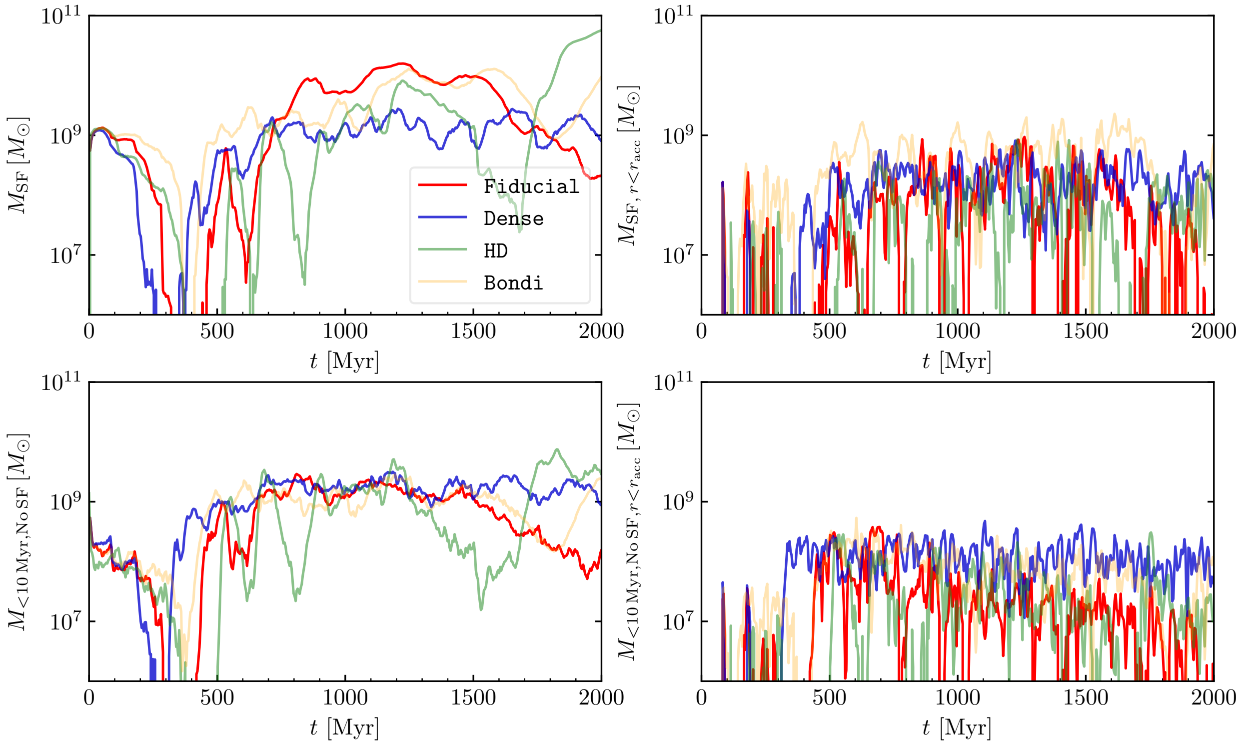

Figure 6.8: Mass in star forming gas (top) and gas with $t_{\mathrm{cool}} < 10$ Myr (bottom) within the entire simulation (left) and inside the accretion radius, $r < r_{\mathrm{acc}}$ (right). While cold and star forming gas is present throughout the simulation, its presence in the central accretion region is intermittent and varies with time. The gas is dragged up by the AGN and accelerated away from the center.

elevated by nearly two orders of magnitude over the other models. More work with different initial conditions and cosmological settings is needed to test the universality of this prediction. Increasing the initial density and introducing a more granulated density structure as seen in turbulent box simulations (e.g., Mohapatra et al., 2021) may lead to equilibrium densities at the observed levels (see Eq. (6.1), Churazov et al., 2003).

To explore the cooling gas, we show in Fig. 6.5 radial profiles of X-ray weighted ($0.2\,\mathrm{keV} < k_\mathrm{B}T < 10\,\mathrm{keV}$) cooling time $t_\mathrm{cool,X}$ and the cooling-to-free fall time ratio $[t_\mathrm{cool}/t_\mathrm{ff}]_\mathrm{X}$. In addition, we plot the total mass per logarithmic bin, $[\mathrm{d}M/\mathrm{d}\log(r)]_{<100\,\mathrm{Myr,No\,SF}}$, for non-star-forming gas with $t_\mathrm{cool} <$ 100 Myr. The cooling times stay below 1 Gyr within the inner 50 kpc independent of the accretion model, resolution and jet density. The cooling-to-free fall time ratio remains low within $r \lesssim 50\,\mathrm{kpc}$ at $[t_\mathrm{cool}/t_\mathrm{ff}]_\mathrm{X} < 10$. For $t > 400\,\mathrm{Myr}$ cold gas is present in the center at $r \lesssim 30\,\mathrm{kpc}$. This state of cooling appears to be a general feature of our simulations.

In Fig. 6.6, we show the time evolution of the cold gas mass (M_cold with $T < 10^6\,\mathrm{K}$), the star formation rate (SFR), the jet luminosity (L_jet) and the SMBH mass (M_bh). Due to the Gaussian temperature fluctuations in the initial conditions, cold gas collapses in multiple clumps at $r \sim 20\,\mathrm{kpc}$. The clumps fall towards the center but due to their angular momentum, they overshoot in their orbits. Initial SMBH accretion is thus limited to short bursts when the clumps pass near the SMBH. After $\sim 500\,\mathrm{Myr}$, our AGN jet feedback establishes a cycle of self-regulation on characteristic timescales throughout individual runs with similar jet powers and SFRs for each run. Therefore, we focus our analysis on times after 500 Myr. SFRs are closely tied to cold gas formation. Runs including AGN jet feedback show SFR $\sim 10\,\mathrm{M}_\odot\,\mathrm{yr}^{-1}$ while our `NoBH` model reaches SFR $> 400\,\mathrm{M}_\odot\,\mathrm{yr}^{-1}$. The `Dense` model shows systematically larger SMBH accretion rates. The increased accretion rates imply larger SMBH masses and AGN jet luminosities (by a factor of ~ 2, see dashed lines in Fig. 6.6) so that the SFR is more quenched in comparison to the other models. As we will show below, this model enables the formation of long-lived discs that continuously feed the SMBH.

For runs including jet feedback, the cold gas masses mostly stay in the range $10^9\,\mathrm{M}_\odot < M_\mathrm{cold} < 10^{10}\,\mathrm{M}_\odot$ after $t > 500\,\mathrm{yr}$. Only the model `NoBH` forms significantly more cold gas, which implies a substantially increased SFR. Towards the end of our `HD` simulation, we observe a large amount of cold gas, which results from a forming massive gas disc with radius $r > 5\,\mathrm{kpc}$ in the center. Cold gas is trapped on circular orbits and cannot be accreted by the SMBH to fuel the feedback cycle. Li and Bryan (2014) observe a similar disc in their hydrodynamical simulations.

After time $t > 500\,\mathrm{Myr}$, the jet power hovers between $10^{44}\,\mathrm{erg\,s^{-1}} < L_\mathrm{jet} < 10^{46}\,\mathrm{erg\,s^{-1}}$, in agreement with observational power estimates that are required to inflate X-ray cavities in a sample of CC clusters (e.g., Rafferty et al., 2006). While jets in `Bondi` and `Dense` remain active throughout the simulation time, `Fiducial` and `HD` show more intermittent jet behavior. The jet luminosities in the `Dense` model are on average twice as high as in the `Fiducial` model. In the `Fiducial` model, the low density jets are easily deflected by cold central clumps, yielding drastically varying jet directions. The jets with a much higher momentum density in the `Dense` model, however, keep their direction. Final SMBH masses reach $\mathrm{M}_\mathrm{bh} \sim 7-9 \times 10^9\,\mathrm{M}_\odot$. Consequently, SMBHs grow at most by a factor of 3 over 2 Gyr in line with expectations.

Figure 6.7 shows the time evolution of the total kinetic energy and mass-weighted average velocity within 200 kpc. The initial velocity fluctuations quickly decay as our non-cosmological set-up does not support continuous driving as a result of gravitational potential fluctuations owing to gas accretion and mergers. Once AGN feedback sets in (at $t > 500\,\mathrm{kpc}$), kinetic energy is injected into the central regions that self-regulates at a level of $E_{\mathrm{kin},r<200\,\mathrm{kpc}} \sim (0.5\text{–}1) \times 10^{60}$ erg. This generates mass-weighted average velocities at the level of around $\bar{v}_{r<200\,\mathrm{kpc}} \approx 75\,\mathrm{km\ s^{-1}}$, with fluctuations of a factor of two, which are qualitatively similar in our different AGN feedback models (`Fiducial`, `Dense`, `HD` and `Bondi`). Clearly, simulations without AGN feedback (`NoBH` and `NoBHNoCool`) continue to lose kinetic energy. Interestingly, the effect of radiative cooling (model `NoBH`) causes precipitation and thus injects kinetic energy, which partially compensates for the turbulent decay of kinetic energy and thus sustains larger velocities in comparison to our non-radiative model (`NoBHNoCool`).

In Fig. 6.8, we show the total mass in star forming gas (top) and non-star-forming gas with $t_\mathrm{cool} <$

10 Myr (bottom) while we compare the gas reservoirs in the entire simulation (panels on the left-hand side) and within the accretion radius (panels on the right-hand side). Whereas the amount of star formation and cold gas varies with time, the cluster remains in a state of constant cooling and star formation. However, if the presence of cold gas is intermittent in the accretion region, the SMBH accretion rate reflects this behaviour. Especially in the runs `HD` and `Fiducial`, cold gas and star forming gas are temporarily absent in the accretion region.

6.5 Connecting jet activity to observations of X-ray cavities

Jet activity on tens of Myr timescales in CC clusters can be constrained by measuring the energy contained in hot bubbles inflated by AGN driven jets and observed as X-ray cavities. Here, we want to compare the cavity luminosity with the instantaneous jet power and cooling luminosity obtained from the simulations.

6.5.1 Fitting X-rays cavities in the simulations

To efficiently identify cavities in our simulations with similar constrains as imposed by observations, we first compute the X-ray emissivity I_X within a SMBH-centered image with dimension 150 kpc × 150 kpc and depth 150 kpc (left and right panels Fig. 6.9). Defining the azimuthally averaged X-ray profile $\bar{I}_\mathrm{X}$, we construct the X-ray fluctuation image via $(I_\mathrm{X} - \bar{I}_\mathrm{X})/\bar{I}_\mathrm{X}$. To simplify our fitting procedure, we use a coarse grained X-ray image with a bin size of 10 kpc and fit ellipses to contour lines with $\delta I_\mathrm{X}/\bar{I}_\mathrm{X} = -0.15$. This enables us to compute cavity energies $E_\mathrm{cav} = P_\mathrm{th} V$, where the thermal pressure P_th is the average value at the radius of the bubble center and V is the ellipsoid volume by assuming the depth of the ellipsoid to be equal to the minor axis of the fitted ellipse. We reject any fitted cavities with centers outside a cube of side length of 150 kpc. The cavity luminosity L_cav is then given by

$$L_\mathrm{cav} = \frac{E_\mathrm{cav}}{t_\mathrm{rise}} = \frac{P_\mathrm{th} V}{t_\mathrm{rise}}, \tag{6.9}$$

where t_rise is the bubble rise time, which we assume to be equal to the sound crossing time t_sc;

$$t_\mathrm{rise} = t_\mathrm{sc} = R\sqrt{\frac{\mu m_\mathrm{p}}{\gamma_\mathrm{a} k_\mathrm{B} T}} \approx 40\,\mathrm{Myr}\left(\frac{R}{40\,\mathrm{kpc}}\right)\left(\frac{k_\mathrm{B} T}{3\,\mathrm{keV}}\right)^{-1/2}, \tag{6.10}$$

where $\gamma_\mathrm{a} = 5/3$ for the ambient ICM.

The method is able to recover the most relevant cavities. Bubbles can disrupt into smaller cavities during their late-time evolution as a result of Kelvin-Helmholtz instabilities, which are suppressed by magnetic draping (Dursi, 2007; Dursi and Pfrommer, 2008; Ehlert et al., 2018). An example of such a splitting of an AGN lobe into two smaller bubbles can be observed in the bottom-left corner of the top panel of Fig. 6.9. Note that our algorithm with the detection threshold is tuned to bubbles inflated by our low-density (fiducial) jets. Therefore, denser bubbles inflated in our model `Dense` may therefore not be fully recovered, especially if they are small.

6.5.2 Comparing cavity powers to jet powers and cooling luminosities

Figure 6.10 shows from left to right probability distribution functions (PDFs) of jet power, cavity powers and ICM cooling luminosities within the central 30 kpc for models indicated in the legends. Jet powers encompass a range between 10^{43}–$10^{46}\,\mathrm{erg\,s^{-1}}$, where the exact distribution is somewhat model dependent. The jet powers of model `Dense` show a lower scatter with an increased median (dashed lines) compared to the `Fiducial` model, which in turn shows a slightly higher median value than the models `HD` and `Bondi`. Interestingly, median cavity powers are much more similar at ~ 6–$7 \times 10^{44}\,\mathrm{erg\,s^{-1}}$ for all models. ICM luminosities also show a smaller scatter around median values of ~ 7–$10 \times 10^{44}\,\mathrm{erg\,s^{-1}}$.

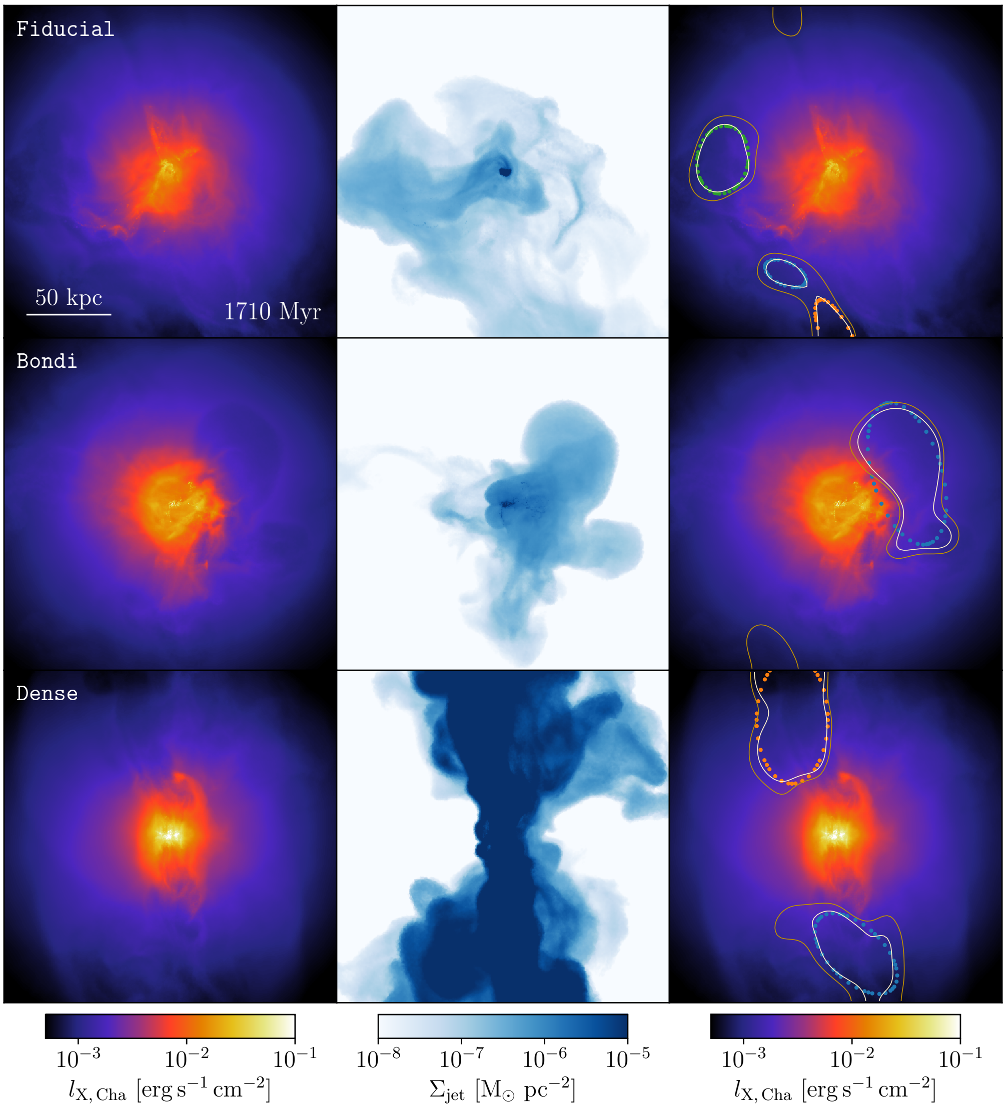

Figure 6.9: X-ray emissivity in the Chandra band (left and right) and integrated jet mass surface density (central). The size of the images is 200 kpc and we show a simulation time of 1560 Myr. We devise an automated algorithm for finding cavities in the X-ray images by (i) subtracting an azimuthally symmetric profile I_s of the X-ray emissivity and normalizing it with the mean profile, $\delta I_X/\bar{I}_X$, and (ii) fitting ellipses to cavities with a contrast of 15 per cent in the residual maps. Cavities in the resulting image at 10 per cent (red) and 15 per cent (gray) are marked with contours and the fitted ellipses are shown with dots. The ellipse volume (where depth is assumed equal to the minor axis) and average pressure at its center are used to determine the cavity power L_{cav} (see Fig. 6.10).

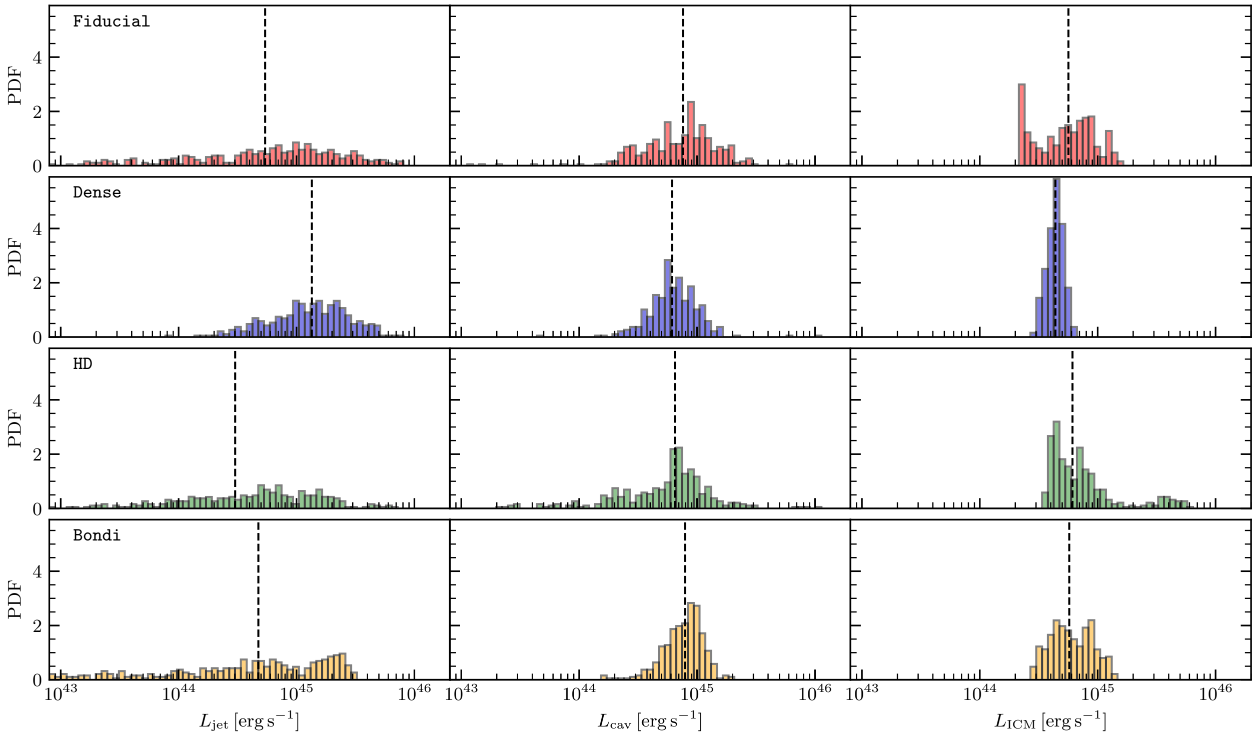

Figure 6.10: Normalized histograms of the jet power, cavity power, and cooling power within 30 kpc (left to right) of the `Fiducial`, `Dense`, `HD`, and `Bondi` run after 500 Myr. Dashed lines indicate median values. Low-power jet events ($L_{\rm jet} \lesssim 10^{44}\,{\rm erg\,s^{-1}}$) inflate cavities that are systematically missed by our cavity detection algorithm. While the distributions of cooling power and cavity power are very similar, we observe a broader distribution of jet powers with a tail towards low-luminosity events that are triggered by individual cooling filaments.

The main reason that these highly variable jet powers do not result in similar variances of the cavity powers is the high-frequency time variability of these powers. Because cavities are inflated over timescales of ~ 10s Myr, the cavity powers correspond to average values over at least these timescales. Our algorithm is able to detect old cavities (with a start of the inflation > 100 Myr) out to scales of > 50 kpc, rising in the atmosphere. The continuous inflation of new bubbles with only short times of quiescence of ~ 50 Myr (cf. the evolution of $L_{\rm jet}$ in Fig. 6.6) causes bubbles to always exist in the cluster and to encompass a combined jet cavity power ($L_{\rm cav}$) that reaches similar values in our different models. In Fig. 6.11, we show jet power vs. cavity power on the right, which echoes these results. Jets with $L_{\rm jet} \lesssim 10^{44}\,{\rm erg\,s^{-1}}$ do not result in separate cavities but instead are contributing to inflating larger, higher luminous cavities. Note that our simulated cavity powers reflect observational estimates of cavity luminosities (Bîrzan et al., 2004; Rafferty et al., 2006; Diehl et al., 2008).

While the jet power evolutions in Figs. 6.6 and 6.15 show periods of jet inactivity in some models, we find that cavities are always present throughout the runtime. This is consistent with observations of 55 cluster of which 60–100 per cent show cavities (Bîrzan et al., 2012). Interestingly, we find that the jet powers $L_{\rm jet}$ exceed the central cooling luminosities $L_{\rm ICM}$ at most by an order of magnitude. However, jet powers that are up to 2 orders of magnitude lower than cooling luminosities are relatively common. Consequently, AGN feedback keeps the cluster in a state of moderate cooling with low but persistent star formation (e.g., Voit and Donahue, 2005; Cavagnolo et al., 2009).

6.6 Magnetic coupling of cold and hot gas

In this section, we study the morphology and kinematics of the cold gas and how magnetic fields influence it. We also address the relevance of magnetic fields in redistributing the AGN feedback energy and how it is related to the hot-phase observables, such as the velocity distribution of the X-ray emitting gas and the Faraday rotation measure.

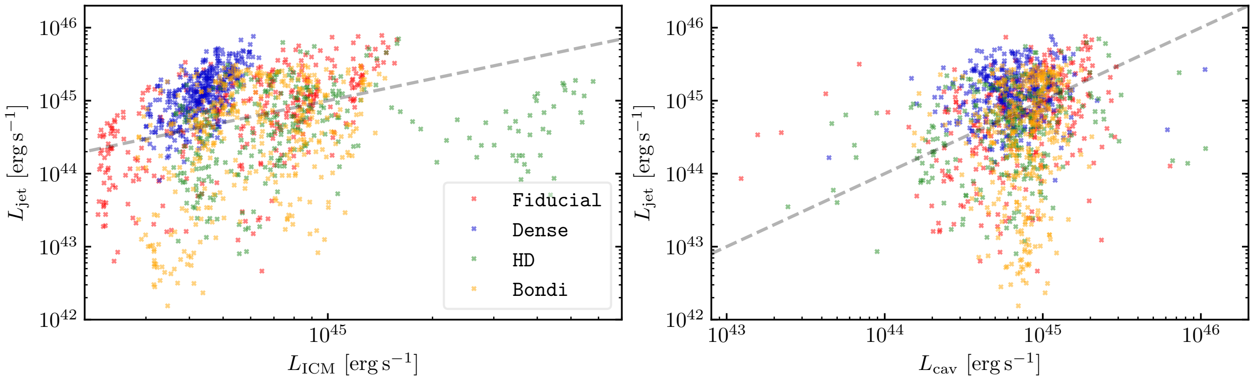

Figure 6.11: Jet power L_jet vs. ICM cooling luminosity L_ICM (left) and jet power vs. cavity power (right) after 500 Myr. Jet powers do not necessarily correspond to the current cooling luminosity. Self-regulation is achieved in an average sense on longer timescales. The hydrodynamical run shows an excursion of a phase of stronger cooling, especially at later times when a disc is formed. We note that our cavity powers span two orders in magnitude while the corresponding jet powers span four orders of magnitude.

6.6.1 Impact of magnetic fields on cold gas morphology and kinematics

The dynamics in the cluster center is dominated by the jet and its interaction with cold gas (especially for low-density jets). Consequently, a clear connection between cold gas and bubbles is expected. To this end, we analyse the cold gas morphology and kinematics by looking at internal alignment of the cold gas angular momentum. In the following we only consider cold cells with $T < 2 \times 10^4\,\mathrm{K}$ or SFR > 0 which constitute the filamentary structures seen in our simulations. We define the angular momentum of those individual cells of cold gas, $\boldsymbol{l}_{\mathrm{fil},i} = m_i \boldsymbol{r}_i \times \boldsymbol{v}_i$ and calculate the total angular momentum of the cold gas via

$$\boldsymbol{L}_\mathrm{fil} = \sum_i m_i \boldsymbol{r}_i \times \boldsymbol{v}_i \tag{6.11}$$

where we measure all velocity and radius vectors with respect to the cluster center and only account for cold cells according to the criterion defined above. This enables us to compute the alignment statistics of individual cold cells with the total angular momentum by computing the vector product of the normalised cell's angular momentum $\hat{\boldsymbol{l}}_\mathrm{fil}$ with the unit total angular momentum $\hat{\boldsymbol{L}}_\mathrm{fil}$, i.e. $|\hat{\boldsymbol{L}}_\mathrm{fil} \cdot \hat{\boldsymbol{l}}_\mathrm{fil}|$. Figure 6.12 shows projections of this quantity and PDFs where colors in the lower left corner of each image label individual distributions in the respective PDFs. The formation and presence of individual filamentary structures are transient phenomena on timescales of a 100s of Myr so that sufficient time-sampling is required. PDFs of a single model for different times are compared in the bottom panels, while different models at individual times are shown on the right. Distributions that peak at low values of $|\hat{\boldsymbol{L}}_\mathrm{fil} \cdot \hat{\boldsymbol{l}}_\mathrm{fil}|$ are more random/filamentary than distributions peaking at higher values which are more discy.

In general, the models `Fiducial` and `Bondi` show very elongated filamentary structures extending out to $r \sim 30$–$50\,\mathrm{kpc}$. We see a coherent kinematic structure along the filaments with a slowly varying angular momentum distribution. While there are also filamentary cold structures in the `Dense` model, they are confined to smaller radii. Magnetic fields in combination with radiative gas cooling cause the formation of these filamentary structures while purely hydrodynamic simulations shatter cooling clouds into small cloudlets as a result of Kelvin-Helmholtz instabilities (Sparre et al., 2020; Müller et al., 2021), similar to the formation of long filamentary tails of jellyfish galaxies.

In the models `Fiducial` and `Bondi`, which enable extended filamentary structures, we only observe transient disc structures in the cold gas phase, which either foster star formation or get accreted onto the SMBH on short timescales of a few 100s of Myr. Importantly, in these models the disc is not continuously fed with gas of similar angular momentum, which is consistent with observations (Russell et al., 2019). By contrast, there are persistent and long-lived discy cold gas morphologies in the `Dense` and `HD` models. In particular, the `HD` model clearly shows a strong discy distribution

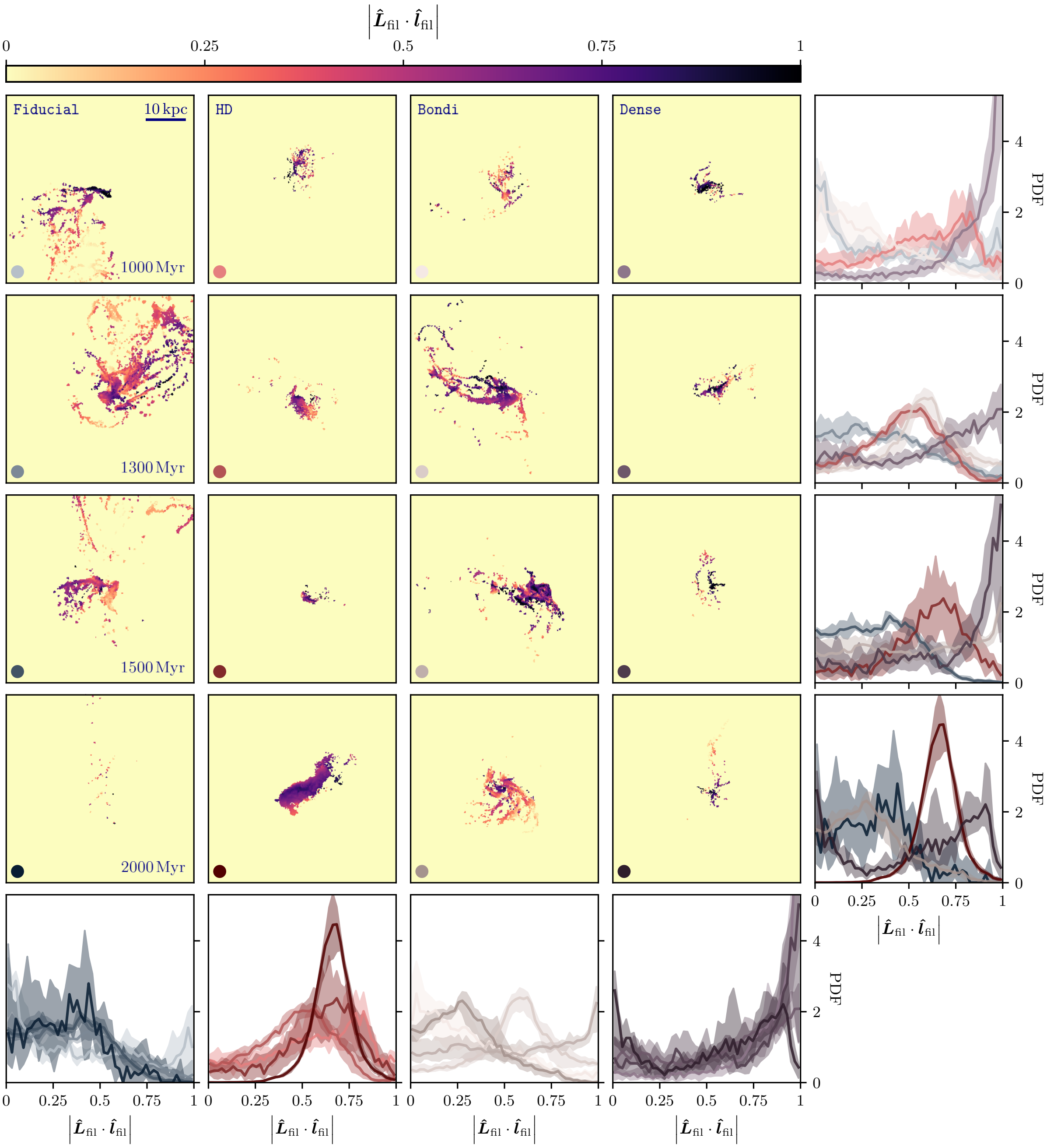

Figure 6.12: Projection of normalized angle between total angular momentum of the cold gas and that of the individual cells $|\hat{L}_{\mathrm{fil}} \cdot \hat{l}_{\mathrm{fil}}|$ at 1000, 1300, 1500 and 2000 Myr (top to bottom) for different runs indicated in the legends (left to right). The bottom (right-most) panels show the PDF of $|\hat{L}_{\mathrm{fil}} \cdot \hat{l}_{\mathrm{fil}}|$ of the different panels in the respective columns (rows) with colors in the lower left corners of the panels identifying the corresponding PDFs. A discy distribution implies values of $|\hat{L}_{\mathrm{fil}} \cdot \hat{l}_{\mathrm{fil}}| \approx 1$ while a random distribution is flat in this quantity. We see a large variety of gas kinematics over time for the different models while the `HD` and – to some extent – the `Dense` models are significantly discier than our MHD models with light jets.

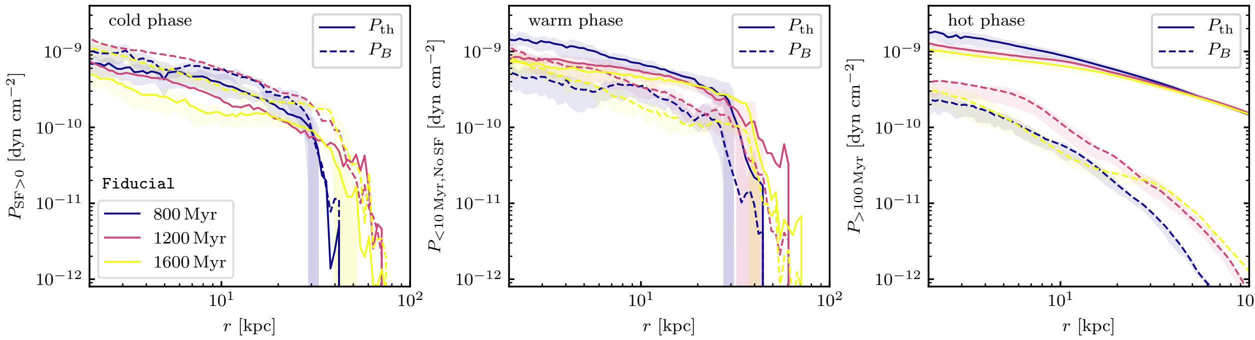

Figure 6.13: Radial profiles of the thermal pressure (solid) and magnetic pressure (dashed). From left to right, we show the star forming cold gas ($P_{\rm SF>0}$), non-star forming, warm gas with $t_{\rm cool} < 10\,{\rm Myr}$ ($P_{<10\,{\rm Myr,No\,SF}}$) and hot gas with $t_{\rm cool} > 100\,{\rm Myr}$ ($P_{>100\,{\rm Myr}}$). Radial profiles correspond to average profiles within 160 Myr and shaded areas denote the 10th to 90th percentiles. In the cold phase, the magnetic field becomes dynamically relevant because of a loss of thermal support as a result of radiative cooling.

of the cold gas phase throughout. In model `Dense`, there is a long-lived coherent discy structure at the cluster center, while at radii $r \gtrsim 10\,{\rm kpc}$ we observe a more random distribution of filamentary structures. We see that in the presence of a cold-gas disc, the cold gas is much more confined to the center and less volume filling.

Magnetic fields allow for a more efficient coupling of cold and hot phases, by efficiently sharing momentum between these two phases through the magnetic pressure and tension forces (Wang et al., 2021). In addition, the increased magnetic field strength in the cooling gas leads to magnetic breaking, reducing angular momentum, which may limit disc formation (Wang et al., 2020). Here, magnetic fields appear to be necessary to transfer jet-induced angular momentum from the hot phase onto the cooling gaseous phase so that later accreting filaments condense into a central configuration with a different angular momentum distribution, thus precluding the formation of a sustained and massive disc. In general, jets induce turbulence in the central region of the cluster, which interferes with condensing gas. This in combination with the turbulence from the initial conditions affects the dynamics of the cold gas. While we do not follow the evolution of the cold gas to the Hα and carbon-oxygen (CO) emitting phases, we speculate that the steady injection of momentum in the same direction of the high density jets appears to facilitate the formation of more discy structures that seem to be inconsistent with observed extended filamentary structures surrounding cD galaxies in clusters (Russell et al., 2019). On the other hand, the deflected low-density jets can lift up cold gas in their wakes and stir the cold gas in more isotropic directions.

6.6.2 Influence of the magnetic field on AGN feedback

In Fig. 6.13, we show radial profiles of the thermal (solid) and magnetic (dashed) pressure in the model `Fiducial` at different times. From left to right, we show profiles in the cold phase (SFR > 0), warm phase ($t_{\rm cool}$ < 10 Myr, SFR = 0) and hot phase ($t_{\rm cool}$ > 100 Myr). Magnetic fields become progressively more dynamically relevant for colder phases to the point where the cold phase is dominated by magnetic pressure (Wang et al., 2021). Consequently, magnetic fields will play a significant role in the dynamics of filaments. Note, as our ISM model prevents cooling to observed temperatures that are orders of magnitudes lower than in our model, we expect thermal pressure losses due to additional cooling to increase the magnetic fields even further. Consequently, the implications for stability and dynamics are expected to be even more severe.

As discussed in Ehlert et al. (2021), magnetic fields and velocity fields are inherently coupled via the induction equation and the equation of motion. It may therefore be instructive to look at the velocity field here. In Fig. 6.14, we show slices of the absolute velocity $|\boldsymbol{v}|$, line-of-sight velocity dispersion $\sigma_{\rm los}$ of the X-ray emitting gas ($k_{\rm B}T < 15\,{\rm keV}$) with contours of a jet tracers on a cut-plane through the cluster center, slices of the absolute magnetic field $|\boldsymbol{B}|$, the magnetic-to-thermal pressure

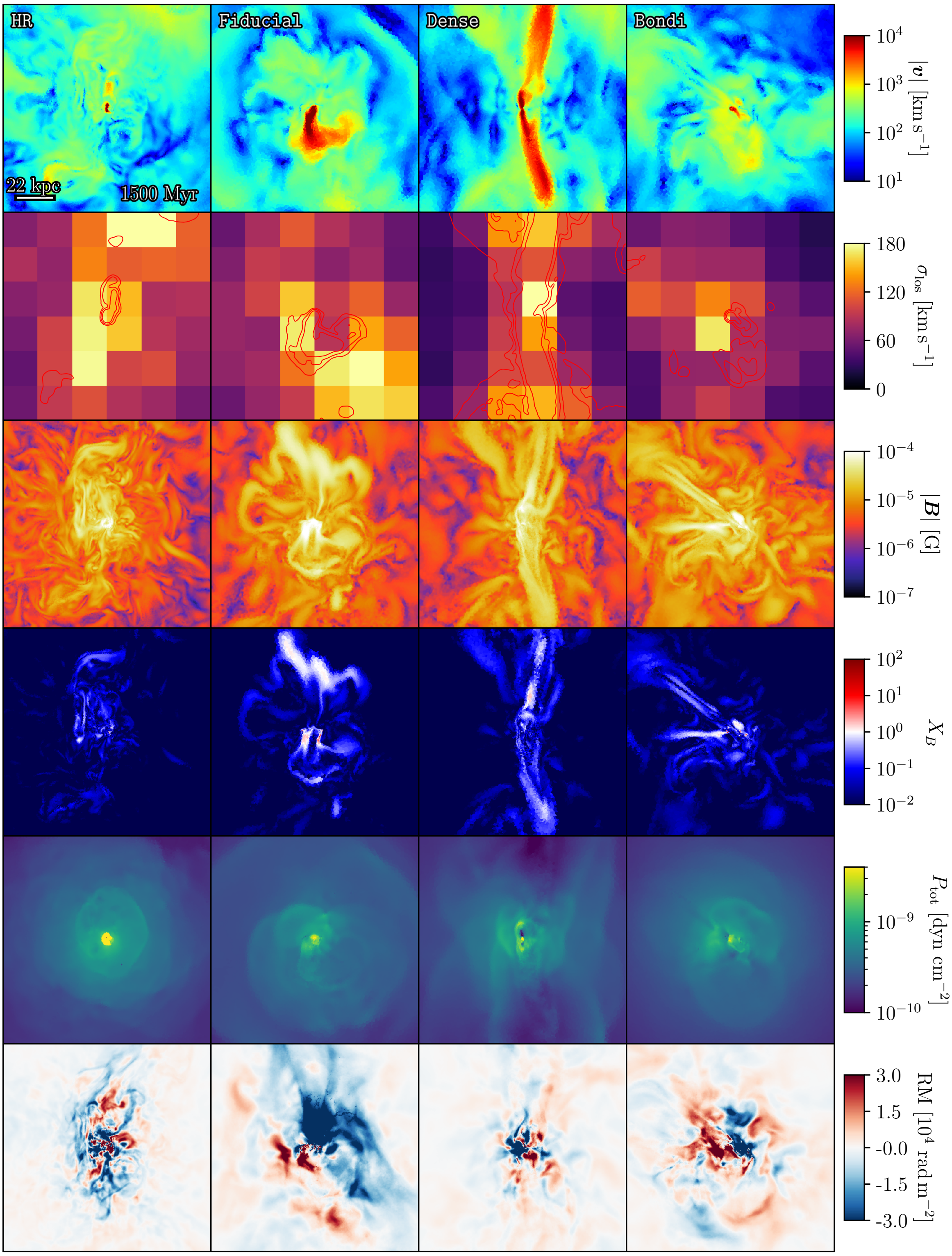

Figure 6.14: From top to bottom, we show slices of the velocity $|v|$, X-ray weighted mean line-of-sight velocity dispersion, slices of the magnetic field, magnetic-to-thermal pressure ratio X_B, total pressure $P_{\rm tot}$ and Faraday rotation measure at 1500 Myr. Contours correspond to jet tracer values of 10^{-4}, 10^{-3} and 10^{-2} in a midplane slice. Jet induced turbulence is visible as increased velocity dispersion. In our model `Dense`, high momentum-density jets propagate nearly unperturbed and cause conically enhanced velocities and velocity dispersion while low-momentum density jets in the three other models are more easily deflected, which results in more isotropic velocity fields. The magnetic field is strongly amplified in the wake of the jets due to increased cooling rates that are triggered by converging gas flows giving rise to substantial rotation measure values.

ratio X_B, the total pressure $P_{\rm tot}$, and the Faraday rotation measure:

$$\mathrm{RM} = \frac{e^3}{2\pi m_{\rm e}^2 c^4} \int_0^L n_{\rm e}\, \boldsymbol{B} \cdot \mathrm{d}\boldsymbol{s}, \tag{6.12}$$

where the integral extends along the line of sight from the source to the observer, e is the elementary charge and $m_{\rm e}$ is the electron rest mass. The magnetic field and thermal electron density are results of our simulations. For gas that is not forming stars, we directly use the thermal electron density as calculated in the cooling module of the code. For star-forming gas, we need to account for the subgrid-scale model of the ISM (Springel and Hernquist, 2003) used in our simulations. This model implicitly assumes an unresolved multi-phase ISM consisting of a volume-filling warm phase and a neutral cold phase at 10^4 K that dominates the gas mass. Hence, in order to calculate the contribution to the Faraday rotation measure of star-forming gas, we self-consistently calculate gas that our subgrid model assigns to the volume-filling warm phase as laid out in Springel and Hernquist (2003) and assume that it is fully ionised. Note that we may still overestimate the electron number density as the AGN outflow may contain a molecular gas component that we do not account for here.

In Fig. 6.14, the high-velocity jet is discernible especially in the `Dense` model, where the jet faces minimal deflection. However, corresponding line-of-sight velocities are small $\sigma_{\rm los} \sim 120\,\mathrm{km\,s^{-1}}$. In contrast, the `HR` and `Fiducial` models show multiple pixels with $\sigma_{\rm los} \gtrsim 180\,\mathrm{km\,s^{-1}}$ at this time. Here, larger fractions of the velocity are diverted into the line of sight. Due to the persistent jet directions in model `Dense`, the enhancement of the ICM velocity dispersion is limited to a cone region in jet direction. On the other hand, low-density jets induce more isotropic turbulence, which is reflected in the velocity dispersion maps where increased values coincide with the jet location. Propagating jets induce shocks in the ICM that are clearly discernible as regions of increased $P_{\rm tot}$ in Fig. 6.14. While shocks in runs with low density jets appear spherical, the shocks in simulation `Dense` are more ellipsoidal and therefore mostly interact in the direction perpendicular to the direction of jet injection.

In our simulations, jets amplify the magnetic field in the wake to values of order 100 μG, as a result of converging gas flows that compress the gas (Ehlert et al., 2021). This increases the cooling rate so that the thermal gas quickly loses pressure support to the point where the magnetic pressure dominates over the thermal pressure, i.e., $X_B \gtrsim 1$. In these regions, the magnetic tension force withstands the turbulent motions in the ICM, giving rise to comparably straight filaments (see Fig. 6.14). Note that fluctuations in the total pressure appear due to jet-induced shocks. There is no obvious correlation between total pressure and the magnetic field structure, implying that these highly magnetized filaments are in approximate pressure equilibrium with the surrounding ICM.

By construction, our initial magnetic field strength $X_{B,\rm ICM} = 0.0125$ yields bulk rotation measures that are in agreement with observations (Clarke, 2004; Murgia, 2011). However, in the regions of strong magnetic field, the rotation measure reaches values in excess of $\mathrm{RM} > 3 \times 10^4$ rad m^{-2}, which is an order of magnitude above observed values. However, the rotation measure morphology is a strong function of numerical resolution (bottom two panels of Fig. 6.14). We see alternating regions with differing signs of the Faraday rotation measure on small angular scales, suggesting that beam smoothing effects and other observational uncertainties may bring our simulations closer to the observed results (e.g., Newman et al., 2002; Johnson et al., 2020). Most importantly, the amplified magnetic field stays generally confined to the path of the bubble on simulated timescales. Thereby, low-density jets amplify magnetic field more isotropically compared to the unidirectional jets in our `Dense` model.

6.7 Discussion

In this paper, we examined simulations of isolated CC galaxy clusters including radiative cooling, star formation and black-hole accretion-regulated feedback from AGN driven jets. We explore variations of different aspects of the simulations including the presence of magnetic fields, the SMBH accretion rate model, the density of the AGN driven jet as well as efficiency parameters. In all our simulations, radiative cooling is on average well-balanced by heating from AGN-driven jets, with at most a factor of a few higher instantaneous jet luminosities (compared to the halo cooling losses), but at times also orders of magnitude lower luminosities (Fig. 6.11).

6.7.1 Self-regulated CC clusters

In all explored model variations that include jets, the SFR in the cluster is suppressed by at least one order of magnitude compared to the no-feedback case (Fig. 6.6), yet the thermodynamic profiles remain characteristic for CC galaxy clusters, i.e. with high central densities at or exceeding $0.3\,\mathrm{cm}^{-3}$, central temperatures below 2.5 keV, and entropies well below $10\,\mathrm{keV\,cm}^2$ (Fig. 6.4). A *gentle* mode of AGN feedback has also been demonstrated in simulations by Yang and Reynolds (2016); Li et al. (2017); Meece et al. (2017); Bourne et al. (2021), which they attribute to jet-induced shock heating and mixing. Furthermore, our jet feedback is unable to convert CC to non-CC clusters as also seen by Hahn et al. (2017); Chadayammuri et al. (2021). In line with the resulting CC characteristics, a substantial amount of the central ICM gas remains in a state where cooling times are low compared to the free-fall time (Fig. 6.5), cold gas is constantly present in the cluster (Fig. 6.8), yet only a small, highly time-variable fraction of it directly feeds the SMBH in the center, causing the instantaneous jet luminosities to fluctuate substantially (Fig. 6.10). While the presence of cold gas is universal, we find its properties to be highly dependent on different modeling choices: our fiducial model of a magnetized ICM heated by light jets tends to create transient gas filaments with low circularity parameters (i.e. either on predominantly radial or uncorrelated orbits) extending several tens of kpc from the center, while two model variations create cold gas structures with large circularity parameter, i.e. coherent, disc-like rotation (Fig. 6.12). This includes the simulation without magnetic fields, indicating that continuous feeding of gas with the same angular momentum is precluded by magnetic fields interconnecting the hot and cold phases. Even in the presence of magnetic fields, the model employing a dense jet produces coherently rotating cold gas discs, however, significantly more compact ones than the ones in the `HD` case. A plausible reason for this is the directionality of the jet that clearly constrains the direction of resulting lobe structures (a proxy for the large-scale gas flow patterns) in the case of dense jets, but not in the case of light jets (Fig. 6.9). This implies that in the case of low-density jets, centrally forming cold gas is dragged around by large-scale turbulent motions in the central region of the cluster, while dense jets facilitate a more coherent flow pattern that facilitates the buildup of a rotating disc. The resulting continuous presence of cold gas near the SMBH for dense jets leads to increased accretion rates as seen in Figure 6.6.

We fitted ellipses to X-ray images of our simulations to more easily connect our simulations to observations of X-ray cavities. Our cavity luminosities are in the range $10^{44}\,\mathrm{erg\,s}^{-1} \lesssim L_\mathrm{cav} \lesssim 3\times10^{45}\,\mathrm{erg\,s}^{-1}$ across simulations, which is in general agreement with the observed total bubble luminosity in Perseus (Bîrzan et al., 2004; Rafferty et al., 2006; Diehl et al., 2008). The corresponding spread in cavity luminosities of four orders of magnitude agrees with the variance observed when looking at cluster samples at similar ICM luminosities (see Fig. 6 in Rafferty et al., 2006).

We found a successful solution for self-regulation in a Perseus-like cluster based on physical principles. However, the shallower potential of groups and smaller clusters is expected to show a different coupling efficiency of the AGN and the ICM as suggested by Prasad et al. (2020). On the other hand, in the Phoenix cluster, one of the most massive clusters observed, AGN feedback appears to be too inefficient to halt cooling (McDonald et al., 2019). Therefore more simulations across the cluster mass range in a cosmological setting are required to demonstrate that the presented models are able to successfully self-regulate CC clusters. Nevertheless, our work opens up an avenue to simulate realistic CC clusters in cosmological zoom-in simulations and to finally answer the question about the origin of the bimodality of CC and non-CC systems.

6.7.2 Accretion models and jet propagation direction

For our simulated scales the exact accretion model has limited relevance. Both Bondi and chaotic cold accretion are very sensitive to dense, cold gas, which makes up the majority of gas accreted in our runs (see Fig. 6.8). The additional continuous accretion in the Bondi model leads to small outbursts with limited influence on the cluster. In agreement with simulations by Meece et al. (2017), we find that the exact triggering mechanism is secondary for runs with sufficiently high resolution. For the cold accretion model, CCs stay intact independent of probed choices for ϵ and η. However, our run with $\epsilon = 1$, $\eta = 0.0001$ grows the SMBH to $M > 10^{11}\,\mathrm{M}_{\odot}$ within 2 Gyr (see Fig. 6.15), while observed most massive SMBHs have smaller masses: $6.6 \times 10^{10}\,\mathrm{M}_{\odot}$ (TON 618; Shemmer et al., 2004), $5.1 \times 10^{10}\,\mathrm{M}_{\odot}$ (MS0735-BCG; Dullo, 2019), $4 \times 10^{10}\,\mathrm{M}_{\odot}$ (Holmberg 15A; Mehrgan et al., 2019). Observational biases should favor more massive SMBHs rather than smaller ones. In addition, King (2016) shows that active SMBHs can grow to a maximum mass $M_{\mathrm{max}} \simeq 5 \times 10^{10}\,\mathrm{M}_{\odot}$ for typical parameters and only reach $2 \times 10^{11}\,\mathrm{M}_{\odot}$ in rather extreme cases over a Hubble time. Hence, we conclude that this parameter combination is unlikely to be realised in nature.

We parametrise our accretion models by two variables, the accretion efficiency ϵ in the cold accretion model and the accretion-to-jet power conversion efficiency, η. We find that the total jet efficiency, i.e. the product of the two, $\epsilon\eta$ is most important for describing the properties of the ICM rather than varying both parameters individually (see Fig. 6.15 and Appendix 6.9.1 for the detailed analysis). In particular, we find that the jet efficiency $\epsilon\eta$ determines the level of intermittency in our runs. More efficient jets (higher $\epsilon\eta$) are able to temporarily push and/or drag cold gas out from the central regions. Lower efficiencies force the jet to be active at all times, limiting jet powers to the maximum while extra cooling is converted into star formation. On the other hand, more energetic outbursts from high-power jets can increase cooling times on larger scales, which can possibly reduce the amount of newly collapsing gas and stabilize the atmosphere more efficiently. However, we note that generally cooling gas with $t_{\mathrm{cool}} < 10\,\mathrm{Myr}$ and star formation are always present in all simulations. The large variety of efficiency parameters (with $\eta = 1$) of self-regulated feedback models used by other research groups generally confirm our findings, which range from $\epsilon = 6 \times 10^{-5}$ (Prasad et al., 2015), $\epsilon = 10^{-4}$ (Prasad et al., 2020), $\epsilon = 5 \times 10^{-4}$ (Prasad et al., 2018), $\epsilon = 10^{-3}$ (Li and Bryan, 2014; Meece et al., 2017), $\epsilon = 5 \times 10^{-3}$ (Wang et al., 2019) to $\epsilon = 10^{-2}$ (Li et al., 2015). While these models vary in exact jet powers and SFRs, we consider the similarities of the self-regulated state reassuring considering the vast spectrum of codes, jet models, ISM implementations and resolutions used. More detailed analysis is required to constrain specific parameters.

Our clusters are in a state of condensation with minimum cooling-to-free fall time ratios $\min(t_{\mathrm{cool}}/t_{\mathrm{ff}}) < 10$, with some a fraction of the ICM reaching $\min(t_{\mathrm{cool}}/t_{\mathrm{ff}}) < 1$ (see Fig. 6.5 middle panel). Previous simulations generally report instability for gas with $t_{\mathrm{cool}}/t_{\mathrm{ff}} < 10$ (Sharma et al., 2012; Gaspari et al., 2012, 2015; Choudhury et al., 2019). Observations of cold filaments in clusters find similar values (Voit and Donahue, 2015) but also somewhat larger values in the range $10 \lesssim t_{\mathrm{cool}}/t_{\mathrm{ff}} \lesssim 25$ (Pulido et al., 2018; Olivares et al., 2019). The low end of the entropy distribution at a certain radius may explain high values in clearly thermally unstable clusters (Voit, 2021).

As discussed in Section 6.3.3, the random nature of (chaotic cold) accretion limits the expected jet precesssion considerably. However, we find that the exact jet direction is extremely important for heavy jets because their high-momentum density implies a fast transport to larger radii and minimizes the lateral heating rate so that the gas quickly becomes thermally unstable and feeds the SMBH perpendicular to the jet direction. Varying the jet direction should have a smaller impact on the self-regulation in the light-jet models because their propagation direction is determined by deflection events off of cold gas filaments and clouds, leading to more isotropic heating in the central regions owing to the increased lateral momentum deposition.

6.7.3 Hα and CO filaments and the role of non-thermal components

While observed filaments reach down to smaller temperatures than simulated here, we argue that comparing our results to observations is nevertheless instructive. Observed filaments in Hα and CO show a large distribution of morphologies, ranging from disc-dominated to filamentary structures that can extend over several kpc in length (e.g., Russell et al., 2016; Gendron-Marsolais et al., 2018b). Most cold gas and filaments are located below or near bubbles (see Fig. 6.3). In addition, smooth velocity gradients along the filaments support the idea that buoyantly rising bubbles lift central cold gas and/or lifted gas becomes thermally unstable and cools (Russell et al., 2019). This agrees with our results on the kinematics and morphology of cold phase filaments (see Fig. 6.12). Beckmann et al. (2019) analyse cold gas in their hydrodynamical simulations and find that filaments are easily shattered by the jet leading to overly clumpy morphologies compared to observations. While we defer a detailed analysis to future work, we also notice clumps in our simulations that are not directly connected in filaments.

In general, the exact details of the feedback loop sensitively depend on the cooling processes via the thermal instability which is in turn sensitive to resolution effects (Martizzi et al., 2019a), limiting the scope of detailed quantitative predictions from our simulations. However, our higher resolution runs confirm the findings discussed throughout the paper (see Appendix 6.9.2 for details). In addition, a detailed analysis of resolution dependencies for the jet can be found in Weinberger et al., in prep.

Magnetic fields lead to a strong coupling between cold and hot gas phases (Wang et al., 2021), by sharing momentum between these two phases through the magnetic pressure and tension forces. As a result, the cold phase adopts a more filamentary morphology (Sparre et al., 2020) as magnetic draping suppresses Kelvin-Helmholtz instabilities (Ruszkowski et al., 2007; Dursi, 2007; Dursi and Pfrommer, 2008; Ehlert et al., 2018). As such, magnetic fields preclude the formation of long-lived cold discs in the first place and do not have to disrupt an already formed disc. In addition, magnetic fields provide substantial pressure support to the cold gas.

Analogously, cosmic ray protons prone to the streaming instability can potentially provide stability to Hα filaments and provide heating to power the emission (Ruszkowski et al., 2018). In addition, Alfvén heating from streaming cosmic ray protons may be the dominant heating mechanism in CC clusters with profound implications on the dynamics of the cluster and the resulting feedback cycle (e.g., Guo and Oh, 2008; Pfrommer, 2013; Jacob and Pfrommer, 2017b; Ruszkowski et al., 2017; Ehlert et al., 2018; Wang et al., 2020). We defer their inclusion to future work.

6.8 Conclusions

Jet feedback is able to stabilize CC galaxy clusters against thermal collapse. We employ MHD simulations to study AGN feedback in an idealised turbulent Perseus-like cluster. Our findings can be summarized as follows:

- Independent of the accretion model (Bondi vs. chaotic cold accretion), probed accretion efficiency, magnetisation of the cluster and jet density, the cluster settles into a state of self-regulation after $\sim 500\,\mathrm{Myr}$ (see Figs. 6.6 and 6.15) with density, entropy and cooling time consistent with observed CC clusters (see Fig. 6.4).

- More efficient jet feedback leads to more intermittent jet power and star formation (see Figs. 6.6 and 6.15).

- Our fiducial low-density jets are easily deflected by cold gas, which leads to more isotropic turbulence injection and bubble distributions (see Fig. 6.3). The dense jets form bubble distributions almost exclusively in the jet direction (see Fig. 6.9). Here, cooling gas is continuously funneled onto the SMBH perpendicular to the jet direction, which leads to quick accretion from a discy distribution that is much more confined to the cluster center ($r \lesssim 10\,\mathrm{Myr}$, see Fig. 6.12).

- Our purely hydrodynamic run forms a massive disc ($r \gtrsim 10\,\mathrm{kpc}$) for $t \gtrsim 200\,\mathrm{Myr}$ (see Fig. 6.12) which leads to unrealistically high SFRs (see Fig. 6.6). Transient disc formation that is not long-lived in our MHD runs supports the idea that magnetic fields anchored in the hot phase redistribute angular momentum with the cooling gaseous phase so that filaments accreting later settle into a central configuration with a different angular momentum distribution, thus precluding the formation of a sustained and massive disc.

- In broad agreement with observations, a plethora of cold gas morphologies ranging from discy to very extended filamentary structures is observed across our MHD runs but morphology and extent ($r < 40\,\mathrm{kpc}$) varies significantly with time in individual runs (see Fig. 6.12).

- Our inferred luminosities from cavity size measurements correspond to averaged jet powers that are therefore insensitive to periods of short and low-luminosity jet injection. Our imposed temperature threshold for cold accretion leads to $\sim 50\,\mathrm{Myr}$ long breaks in jet injection in comparison to the continuous accretion condition prescribed in the Bondi model. However, the long life-time of cavities of $> 100\,\mathrm{Myr}$ since injection leads to a comparable presence of cavities for both models (see Fig. 6.11).

- The magnetic field is strongly amplified in the wake of the jets due to the increased cooling rates that are triggered by converging gas flows, giving rise to substantial rotation measure values (see Fig. 6.14).

AGN feedback has been established as the main heating source that allows CCs to reach a state of self-regulation at the observed levels. In order to rule out any specific accretion and jet models, secondary observables such as bubble and cold gas morphologies are needed.

In a next step, accounting for the cosmological assembly of a galaxy cluster is crucial for obtaining a more realistic environment and evolution. We find that light AGN jets are required to obtain the observed extended filaments with an averaged isotropic distribution of the kinematics of filaments. Numerically converged heating rates in the light-jet model imply a minimum resolution of 0.6 kpc in the jet launching region (Weinberger et al., in prep.). We caution that further zooming into the acretion region could reveal distinct smal-scale differences for the accretion model (Bondi vs. chaotic cold accretion). In addition, future work will model the cold gas more accurately so that we may disentangle different AGN models by means of the observed distributions of Hα and CO filaments.

Acknowledgements

KE and CP acknowledge support by the European Research Council under ERC-CoG grant CRAGSMAN-646955 and ERC-AdG grant PICOGAL-101019746. This work was supported by the Natural Sciences and Engineering Research Council of Canada (NSERC), funding reference #CITA 490888-16. The authors gratefully acknowledge the Gauss Centre for Supercomputing e.V. (www.gauss-centre.eu) for funding this project by providing computing time on the GCS Supercomputer SuperMUC-NG at Leibniz Supercomputing Centre (www.lrz.de).

Data availability

The data underlying this article will be shared on reasonable request to the corresponding author.

6.9 Appendix

6.9.1 Model parameters

To assess the relevance of parameter choices governing jet efficiency, we varied both ϵ and η independently. However, we find that only their product $\epsilon \times \eta$, which we refer to as *jet efficiency*, gives significant differences in the cluster evolution. In Fig. 6.15, we report on the evolution of the cold gas mass (with $T < 10^6\,\mathrm{K}$), SFR, jet luminosity L_{jet} and SMBH mass M_{bh} for runs with $\epsilon \times \eta = 0.001$ (red) and $\epsilon \times \eta = 0.0001$ (blue).

Runs with increased jet efficiency (reddish colours) in general show greater intermittency in star formation and jet power. More efficient jets pump more energy into the surrounding medium and halt cooling on longer timescales. Therefore, lower SFRs are observed. In addition, an increased

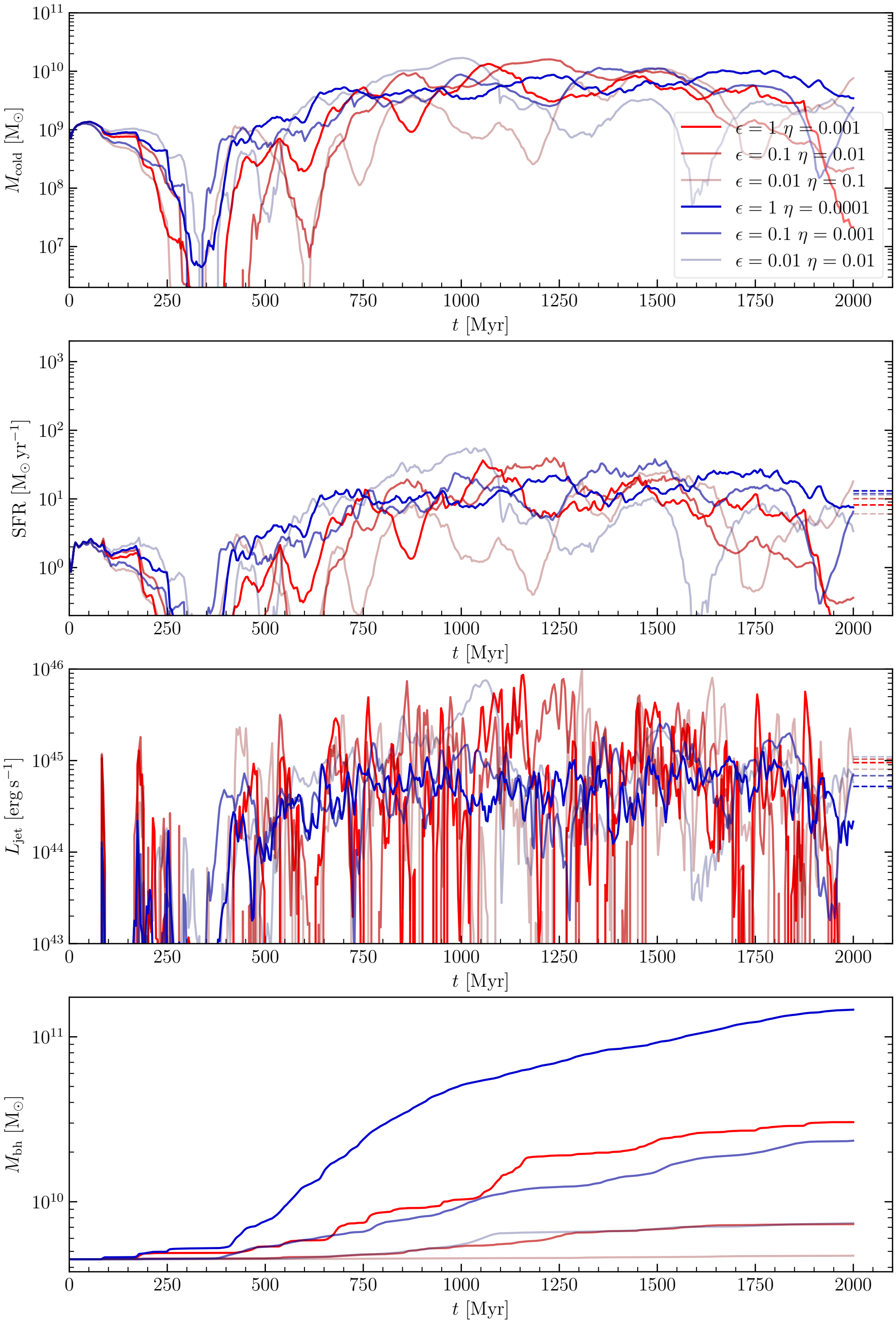

Figure 6.15: Same as in Fig. 6.6 for runs with varying parameters of the cold accretion model. Analogously, all models attain to a state of self-regulation with very similar average SFRs (SFR $\sim 10\,\mathrm{M_\odot\,yr^{-1}}$) and jet powers ($L_{\rm jet} \sim 10^{45}\,\mathrm{erg\,s^{-1}}$). Red and blue color shadings correspond to runs with $\epsilon \times \eta = 0.001$ and $\epsilon \times \eta = 0.0001$, respectively. Runs with lower coupling efficiencies show almost constant jet powers and SFRs while higher efficiencies cause star formation and jet powers to become more intermittent.

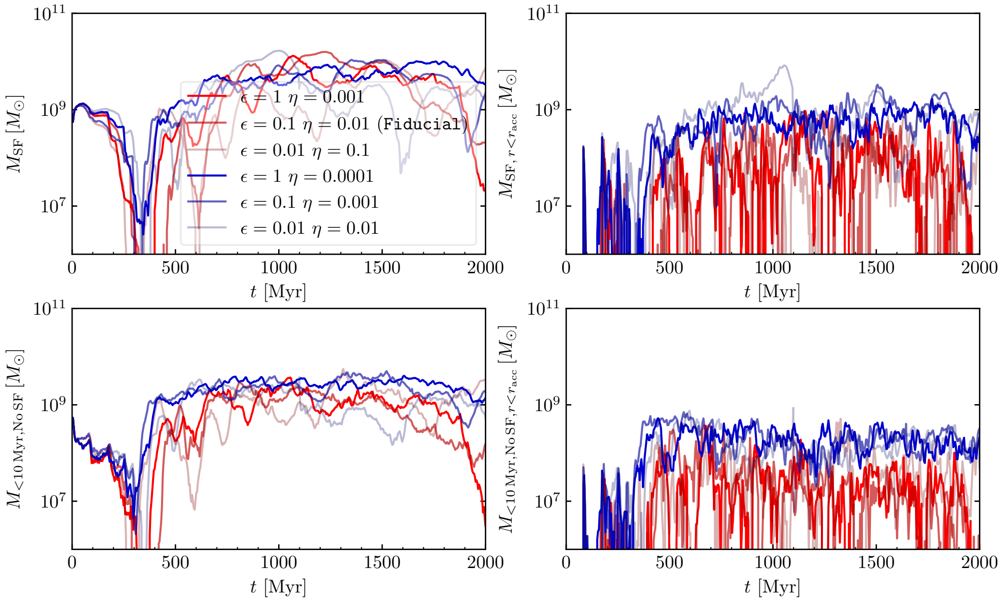

Figure 6.16: Same as in Fig. 6.8 for runs with varying parameters of the cold accretion model. Red and blue color shadings correspond to runs with $\epsilon \times \eta = 0.001$ and $\epsilon \times \eta = 0.0001$, respectively. Runs with lower efficiencies have a constant supply of cold gas that keeps powering the jets. More intermittent fluctuations are seen in the high efficiency runs. However, total cold and star forming gas masses stay within an order of magnitude.

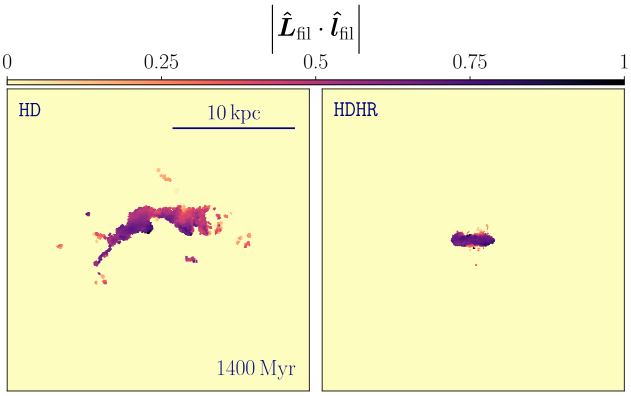

Figure 6.17: Same as in Fig. 6.12 for **HD** and **HDHR** at 1400 Myr. Both hydrodynamical runs form a strong disc at the end of the run. In **HDHR** the disc is funneled into the SMBH completely depleting the entire cold gas reservoir in the cluster.

injection of momentum forces cold gas on larger orbits around the center so that the accretion region is temporarily devoid of cold gas even though it remains present in the cluster (see Fig. 6.16).

On the other hand, lower jet efficiencies (bluish colours) lead to the formation of cold gas that is more closely tied to the center and is depleted at a constant *maximum* rate. Jet feedback is more continuous and less time-variable, while the high efficiency runs show higher burst powers and intermittent states of inactivity. Only the run with $\epsilon = 0.01$, $\eta = 0.01$, shows any significant variance after $t > 500\,$Myr as a massive disc forms at $t \sim 1\,$Gyr that is funneled into the accretion region on short timescales. Cooling is more significantly halted in the overheated cluster compared to its analogues at the same jet efficiency.

6.9.2 Resolution

In agreement with our findings for the **HD** model, the high resolution analogue **HDHR** also forms a massive disc at $t \sim 1000\,$Myr, which is accreted within $\Delta t \sim 800\,$Myr (see Fig. 6.17). Hence, this demonstrates numerical convergence of the main properties of our hydrodynamic simulations. Throughout the simulation **HDHR**, the jet injects energy with $L_{\rm jet} > 10^{45}$ erg s^{-1}, which is significantly more than in

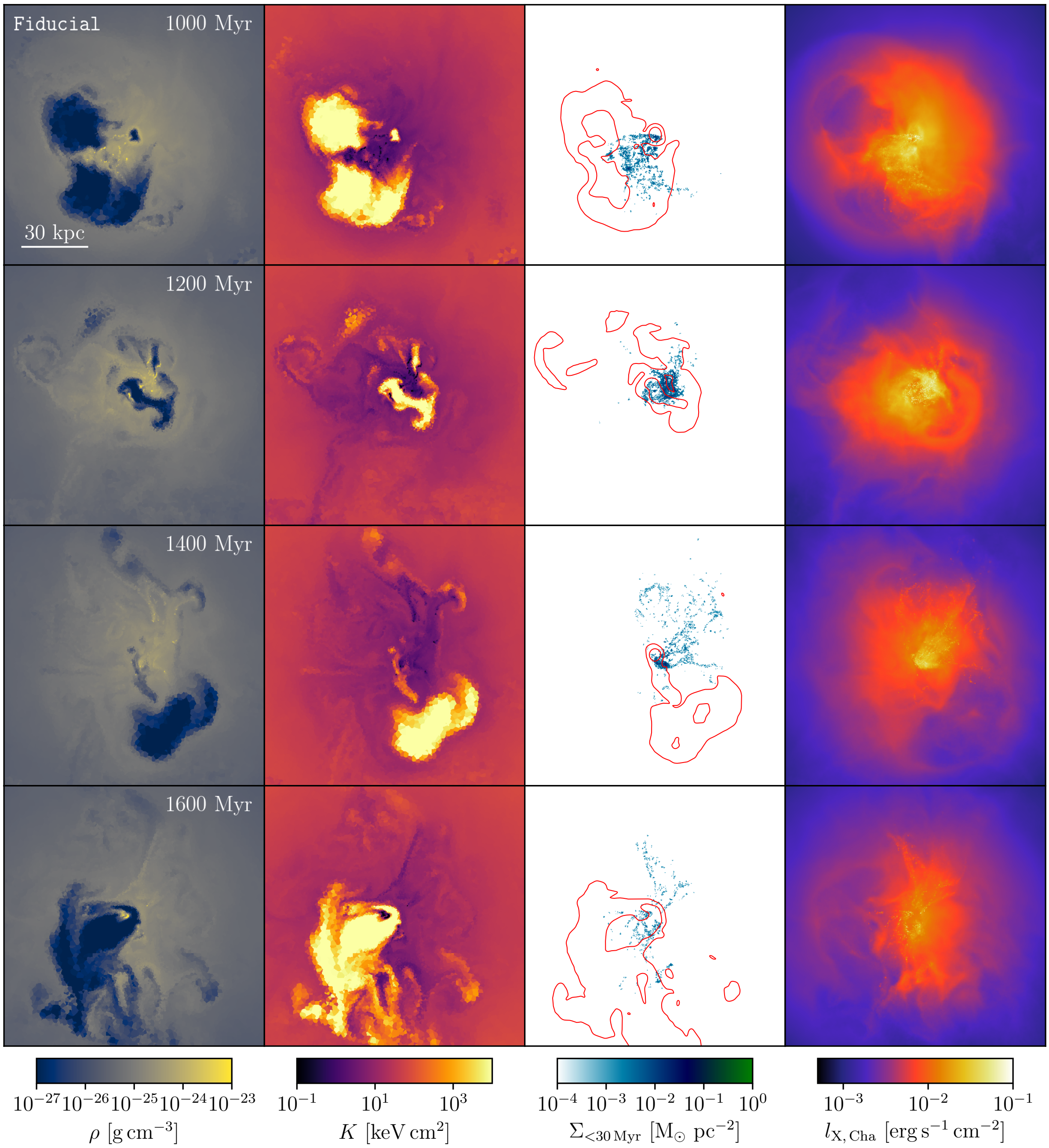

Figure 6.18: Same as in Fig. 6.3 for the same run at fiducial resolution `Fiducial`. The main features are independent of resolution.

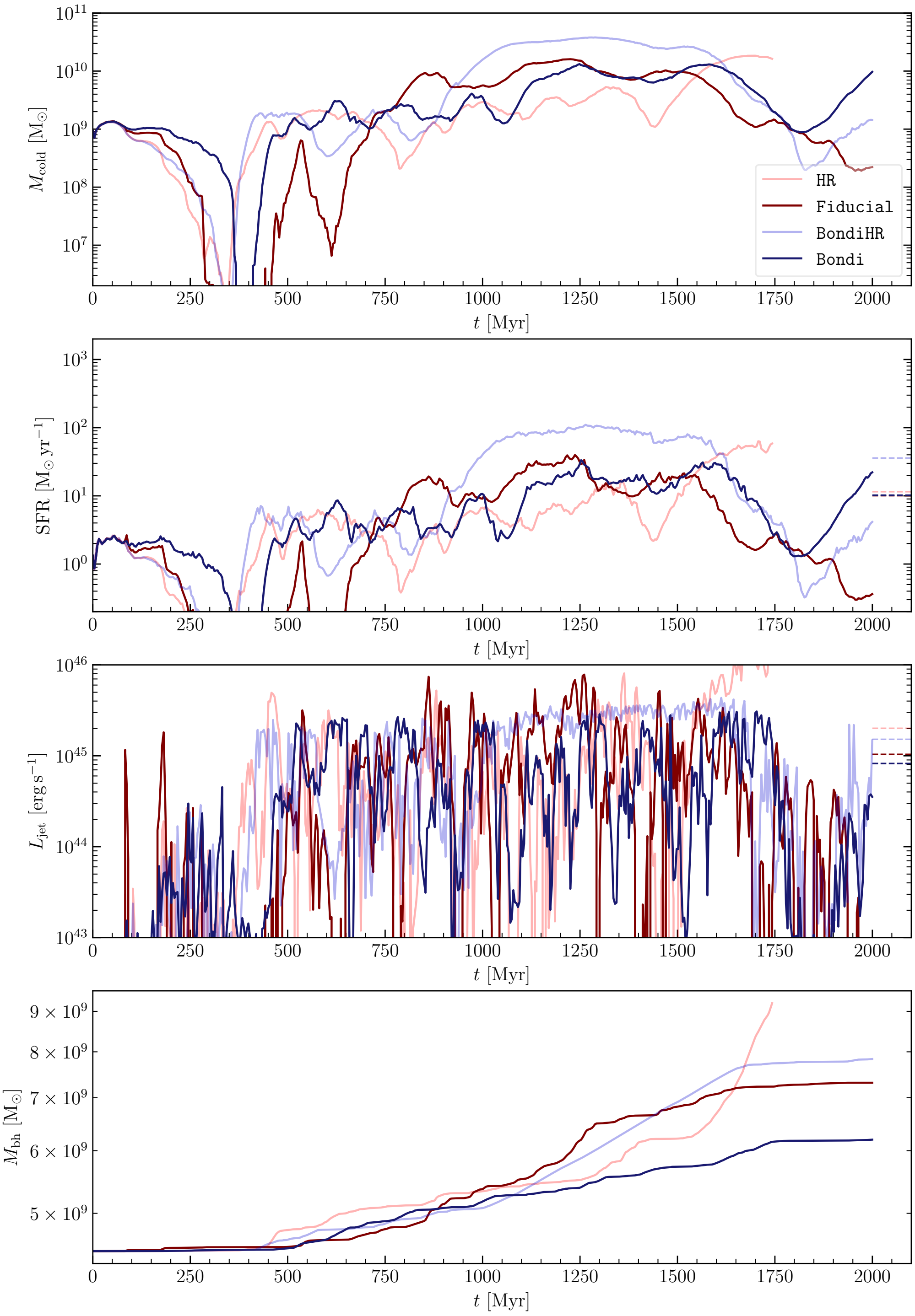

Figure 6.19: Same as in Fig. 6.6 for fiducial cold accretion and Bondi runs at varying numerical resolution. The cold accretion run gives very similar results at both resolutions. During the high resolution Bondi run a transient disc is formed with high SFRs (SFR $\sim 100\,\mathrm{M}_\odot\,\mathrm{yr}^{-1}$). The reason for its formation should probably be attributed to a chance event rather than the difference in resolution as varying parameters may also lead to the formation of transient discs.

any other run. This leads to an overheated core so that no further cooling is triggered until $t = 2\,\mathrm{Gyr}$. We attribute this behavior to incomplete coupling with the hot and cold phases. As established earlier, magnetic fields are required to inhibit uncontrolled disc formation, we therefore omit the run from the following analysis.

In Fig. 6.18, we show our `Fiducial` model at the fiducial resolution. Compared to the high resolution analogue shown in Fig. 6.18, the general features are retained. Low-density bubbles rise that are deflected by cold gas in the ICM. Cavities are clearly discernible in X-ray emissivity.

In Fig. 6.19, we show the cold gas mass (M_{cold} with $T < 10^6\,\mathrm{K}$), SFR, jet luminosity (L_{jet}) and SMBH mass (M_{bh}). The evolution of the cold gas mass, star formation and jet power at high resolution are in general agreement with the low resolution counterparts. However, `BondiHR` forms a disc at $t \sim 1,\mathrm{Gyr}$, which has vanished 500 Myr later. The related increased star formation and elevated jet power due to constant feeding leads to a somewhat distinct development. However, continued cooling quickly restores its earlier state of intermittent jet power and star formation as observed in `Bondi`. Similarly, the model `HR` shows a sudden increase in jet power at $t \sim 1750\,\mathrm{Myr}$ probably due to accumulation of cold gas in the accretion region, which leads to a sudden spike in SMBH growth. We conclude that simulation-to-simulation variance appears more significant than resolution effects.

7

Discussion, conclusion and outlook

7.1 Discussion and conclusion

While the classical cooling flow problem in CC clusters has been "solved" by heating from AGN jets in cluster centers, many details regarding the heating mechanism remain unclear, which is the focus of this thesis. In particular, this thesis considers light jets filled with CRs in a turbulent magnetic field in the context of a Perseus-like CC cluster. While these crucial ingredients of CC clusters have mostly been studied individually, we aim to include the interplay between these components. In addition, the advent of ALMA and high resolution kinematic studies of cold gas filaments in clusters opened the door to deepening our understanding of ICM cooling with the help of simulations. This provides an exciting field for future numerical studies, that will be alluded to afterwards. In the following, we summarize our findings and embed them within the literature of CC clusters.

Details of heating depend crucially on bubble composition, which is poorly constrained. Observations of the SZ signal from AGN bubbles provide unique information on their electron population. To model the signal in observations as proposed in Pfrommer et al. (2005), the emission volume is approximated as an ellipsoid by the first observation of its kind (Abdulla et al., 2019). We scrutinize their approximation regarding bubble morphology by simulating a jet outburst with matching energy of the observed bubbles. The SZ signal of our self-consistently inflated bubbles shows little deviation from the ones of an ellipsoid. However, for small inclinations between line-of-sight and jet axis, $\theta < 45°$, large portions of shocked material are probed, which dilutes the signal. As θ is unconstrained a priori and degenerate with bubble age, we propose new methods to measure θ based on (1) the stand-off distance between bow shock and jet/bubble head, (2) the ellipticity of the bow shock or (3) future observations of the kinetic SZ effect of the bubble's wake. We therefore for the first time demonstrated the inherent degeneracy between jet angle and bubble age in the context of these crucial observations, which can have a profound impact on modeling results.

Generally, the study by Abdulla et al. (2019) provides very strong evidence for low-density jets with density contrast $\rho_{\mathrm{ICM}}/\rho_{\mathrm{jet}} > 10^2$ and likely much higher. While magnetic fields rather than CRs could provide the required non-thermal pressure, modeling results of jet emission and energy evolution by Croston and Hardcastle (2014) clearly prefer a scenario where entrained gas rather than magnetic fields dominate jet energetics. For this reason, we employ the jet model presented in Weinberger et al. (2017) implemented in the moving-mesh code AREPO. The model allows us to set a fixed density (when the ICM density stays constant, e.g. during adiabatic runs) and/or density contrast at observed values. This approach requires non-trivial management of the jet injection region. The Lagrangian properties of AREPO allow us to efficiently incorporate refinement criteria to sustain the density contrast as well as reducing numerical mixing and truncation errors, while upholding the presence of physical fluid instabilities (see discussion of numerical methods in this context by Ogiya et al., 2018). Alternative studies mostly either use (i) wide, high density jets (Gilkis and Soker, 2012), (ii) jets with variable density with density contrasts that are usually lower than observed (Prasad et al., 2015; Yang and Reynolds, 2016), (iii) magnetically dominated jets (Gan et al., 2017) or (iv) simply insert a bubble by hand (Dong and Stone, 2009). This provides our studies with a unique vantage point, that is expected to make bubble dynamics more realistic in comparison to previous work. We apply our jet model in a realistic cluster environment including magnetic fields and turbulent motions to relate simulations to observations.

The success of steady state solutions for a large sample of CC clusters where CR heating balances cooling by Jacob and Pfrommer (2017a,b) motivated the first part of this thesis (Ehlert et al., 2018). Here, we simulated the injection of CRs by jet-inflated bubbles in a magnetized ICM. We find that magnetic fields drape around the head of the bubble, which enhances bubble stability and inhibits CR transport in front of the bubble. In the wake of the bubble converging flows compress and stretch magnetic fields. CRs are then able to escape along these enhanced field lines. Recovered CR heating rates for single injection events are sufficient to stabilize expected cooling rates and heat cluster centers isotropically. Global studies looking for steady state solutions where CR heating balances cooling need to assume very approximate injection functions instead (Guo and Oh, 2008; Fujita and Ohira, 2011; Jacob and Pfrommer, 2017a,b). Our results justify their approach qualitatively.

In addition, our work extends previous studies of hydrodynamical CR-filled jets (Guo and Mathews, 2011) by including magnetic fields at unprecedented resolution and studying the inflation of our bubbles. We identify the additional effect of magnetic draping and its impact on CR transport and bubble stability. While this effect has been studied before for bubbles that are setup by hand (Ruszkowski et al., 2007; Dursi and Pfrommer, 2008) or at lower resolution (Yang et al., 2012), we quantify its role in stabilizing jet-inflated bubbles at high resolution.

As noted above, magnetic fields are crucial for CR transport. They stabilize bubbles and couple the cold and hot gas phases via pressure and tension forces. The magnetic field also becomes progressively more dynamically relevant for colder gas phases such that cold gas can be dominated by magnetic pressure (Wang et al., 2021). A turbulent velocity field on the other hand degrades bubble stability. The magnitude of the velocity affects the efficiency of turbulent heating and the transport of gravity and sound waves in the ICM. However, the most detailed observations of magnetic fields are based on Faraday measurements with observations covering limited volumes due to their dependence on scarce background sources. Similarly, X-ray spectroscopy studies that constrain velocity fields at high spectral resolution are so far limited to the Perseus cluster (Hitomi Collaboration, 2016). Fundamentally, magnetic and velocity fields are dynamically coupled. However, measurements of magnetic fields via Faraday rotation measure (Govoni et al., 2010; Böhringer et al., 2016) do not include information provided by measurements of turbulent velocities and vice-versa (Tamura et al., 2014; Hitomi Collaboration, 2018). By demonstrating their clear inherent link in our third study, we would like to inspire future simulations to link these observables, which provides observers with "free" additional information to constrain magnetic and velocity field strengths collectively, which appears rather underappreciated in the field.

Finally, we implement a model of cold accretion in AREPO and include radiative cooling in our simulations to study self-regulated jet feedback in an idealized Perseus-like cluster. Gaspari et al. (2011, 2012) demonstrated that bipolar jets fueled by cold accretion can balance cooling in numerical simulations. Here, we focus on varying accretion models, jet efficiency and accretion efficiencies and jet density. Most authors vary jet efficiency as its impact to a certain degree depends on model and code (see comparison between Prasad et al., 2020; Wang et al., 2019, as discussed in the former). While most authors assume an accretion efficiency of unity, incomplete momentum cancellation as well as unresolved small scale feedback that evaporates cold gas can reduce accretion rates. By varying the accretion efficiency in our model, we account for a likely smaller but currently unknown value. We retain thermodynamic profiles and star formation rates consistent with observed profiles independent of these modeling choices, which is in line with previous studies (Prasad et al., 2015; Yang et al., 2016; Wang et al., 2019). In addition, we find that Bondi and cold accretion give very similar results, which confirms findings by Meece et al. (2017) but for a different code and jet model.

Furthermore, we suggest to further scrutinize feedback models by looking at additional features not captured by thermodynamic profiles or star formation rates. In Ehlert et al. (2022), we identify cold gas morphology as a promising feature, which appears sensitive to jet density. Dense jets pierce through the ICM and in the absence of precession lead to a stable configuration of jet injection. Consequently, cold gas is preferentially accreted perpendicular to the jet axis. This leads to a more disky distribution of cold gas with a more limited extent. Whereas reduced ram pressure in low-density jets makes them more vulnerable to deflection by cold gas and turbulent motions. Here, turbulence is injected more isotropically, which leads to more extended filamentary cold gas distributions. Therefore, we propose to use cold gas morphology as a new method to constrain free parameters of numerical models. In addition, our low density jets inflate bubbles reminiscent of observed X-ray cavities. This allows us for the first time to directly relate the observable bubble power pV/t_{age} (see Section 2.3.2) to the instantaneous physical jet power, which is hard to compute from observational data.

Alternatively, Talbot et al. (2022) and Bourne et al. (2021) study accretion at higher resolution and include a more physical accretion model based on BH spin or a cosmological environment, respectively. In contrast, our approximations in these areas reduce computational costs such that we are able to run our model on Gyr timescales, while previously mentioned model run times are limited to $\sim 10\,\mathrm{Myr}$ and $\sim 100\,\mathrm{Myr}$, respectively. Consequently, we can follow the evolution of the heating and cooling cycle on the cooling timescale of the ICM.

In conclusion, our work provided us with a sustainable AGN jet model, which enables future CC clusters cosmological simulations of realistic low-momentum density jets including CRs and magnetic fields at high resolution.

7.2 Outlook

We showed that the dynamics and stability of AGN bubbles are significantly affected by turbulence in the ICM and magnetic fields. Throughout our studies, we initialize turbulent magnetic fields in our simulations based on observed strengths and power spectra in nearby clusters. Stresses of the tangled magnetic field induce turbulent gas motions. In the absence of sustained driving of turbulence or when neglecting precipitation of cold clouds and filaments, as in our simulations, turbulence dissipates over time and velocity and magnetic field decay gradually (Ehlert et al., 2018). In reality, cluster mergers amplify seed fields in the ICM. Therefore, cosmological simulations are required to obtain self-consistently generated large scale velocity fields and turbulence as well as magnetic field structures and strengths (Donnert et al., 2018). The advent of X-ray telescope XRISM is expected to provide detailed velocity measurements of the ICM that will help constrain CC cluster models.

In addition, the origin of the dichotomy in galaxy clusters between CC and non-CC clusters remains uncertain even though it appears related to mergers (Sanderson et al., 2006; Rossetti et al., 2011). While recent simulations investigate the conversion of CC to non-CC clusters in isolated halos (Nobels et al., 2022), cosmological simulations (similar to Chadayammuri et al., 2021) comprising a large sample of clusters at a variety of masses are required. For this, techniques of AGN jet feedback employed throughout our studies may have to be adopted for expensive cosmological simulations which have so far struggled to obtain CC clusters (Barnes et al., 2018). Successes in this area will likely deepen our understanding of AGN feedback on smaller scales as well and help characterize a universal model for AGN jets in simulations.

Currently simulations are unable to capture details of multiphase gas that is observed to condense out of the ICM (Martizzi et al., 2019a). For example, the evolution of dense clouds have been shown to disrupt and/or grow depending on cloud size (Sparre et al., 2020), which is not captured by current cluster simulations but may have profound impact on the cooling and heating cycle. While constraints on resolution especially in the cosmological context may make direct simulations unfeasible, one can treat different phases separately, which may overcome some of the current restrictions of effective models on small scales. Physically motivated source and sink terms will be required to bridge unresolved scales as alluded to in Weinberger and Hernquist (2022). Progress in this area will substantially ease comparisons with observations in the respective bands of probed emission.

Further progress on identifying relevant heating mechanisms is possible by developing new energy tracking methods, possibly starting with ideas developed in Martizzi et al. (2019b). Turning to CR induced Alfvén wave heating, a more complete description of CR streaming (e.g., Thomas et al., 2021) should be added in the future. Generally, our understanding of CR transport and the weakly collisional ICM are still evolving (Zweibel, 2020; Drake et al., 2021). Further insights into the transport of CRs and sound waves will be crucial to estimate the relevance of CR heating and widening our understanding of ICM physics.

Publication list

In the following, I list my publications that comprise the accompanying thesis. My contributions are detailed in Section 2.6. In addition, I list publications that are not directly part of this thesis.

Publications presented in this thesis

- Ehlert, K.; Weinberger, R.; Pfrommer, C.; Pakmor, R.; Springel, V. *Simulations of the dynamics of magnetized jets and cosmic rays in galaxy clusters*, Monthly Notices of the Royal Astronomical Society, Volume 481, Issue 3, p.2878-2900 (2018). (Ehlert et al., 2018)

- Ehlert, K.; Pfrommer, C.; Weinberger, R.; Pakmor, R.; Springel, V. *The Sunyaev-Zel?dovich Effect of Simulated Jet-inflated Bubbles in Clusters*, The Astrophysical Journal Letters, Volume 872, Issue 1, article id. L8, 6 pp. (2019). (Ehlert et al., 2019)

- Ehlert, K.; Weinberger, R.; Pfrommer, C.; Springel, V. *Connecting turbulent velocities and magnetic fields in galaxy cluster simulations with active galactic nuclei jets*, Monthly Notices of the Royal Astronomical Society, Volume 503, Issue 1, pp.1327-1344 (2021). (Ehlert et al., 2021)

- Ehlert, K.; Weinberger, R.; Pfrommer, C.; Pakmor, R.; Springel, V. *Self-regulated AGN feedback of light jets in cool-core galaxy clusters* , eprint arXiv:2204.01765 (2022), submitted to MNRS. (Ehlert et al., 2022)

Additional publications

- Weinberger, R.; Ehlert, K.; Pfrommer, C.; Pakmor, R.; Springel, V. *Simulating the interaction of jets with the intracluster medium*, Monthly Notices of the Royal Astronomical Society, Volume 470, Issue 4, p.4530-4546 (2017) (Weinberger et al., 2017)

- Pais, M.; Pfrommer, C.; Ehlert, K.; Pakmor, R. *The effect of cosmic ray acceleration on supernova blast wave dynamics*, Monthly Notices of the Royal Astronomical Society, Volume 478, Issue 4, p.5278-5295 (2018) (Pais et al., 2018)

- Pais, M.; Pfrommer, C.; Ehlert, K.; Werhahn, M.; Winner, G. *Constraining the coherence scale of the interstellar magnetic field using TeV gamma-ray observations of supernova remnants*, Monthly Notices of the Royal Astronomical Society, Volume 496, Issue 2, pp.2448-2461 (2020) (Pais et al., 2020)

- Sparre, M.; Pfrommer, C.; Ehlert, K. *Interaction of a cold cloud with a hot wind: the regimes of cloud growth and destruction and the impact of magnetic fields*, Monthly Notices of the Royal Astronomical Society, Volume 499, Issue 3, pp.4261-4281 (2020) (Sparre et al., 2020)

- ZuHone, J.; Markevitch, M.; Weinberger, R.; Nulsen, P.; Ehlert, K. *How Merger-driven Gas Motions in Galaxy Clusters Can Turn AGN Bubbles into Radio Relics*, The Astrophysical Journal, Volume 914, Issue 1, id.73, 14 pp. (2021) (ZuHone et al., 2021b)

- ZuHone, J.; Ehlert, K.; Weinberger, R.; Pfrommer, C. *Turning AGN Bubbles into Radio Relics with Sloshing: Modeling CR Transport with Realistic Physics*, Galaxies, Volume 9, Issue 4, p. 91 (2021) (ZuHone et al., 2021a)

Bibliography

Abdulla, Z. et al: 2019, *Astrophys. J.* **871(2)**, 195

Ackermann, M. et al: 2014, *Astrophys. J.* 787(1)

Ahnen, M.L. et al: 2016, *Astron. Astrophys.* **595**, 1

Anjiri, M. et al: 2014, *Mon. Not. R. Astron. Soc.* **442(3)**, 2228

Asai, N., Fukuda, N. and Matsumoto, R.: 2007, *Astrophys. J.* **663**(2), 816

Asplund, M. et al: 2009, *Annu. Rev. Astron. Astrophys.* **47**, 481

Balbus, S.A. and Hawley, J.F.: 1998, *Rev. Mod. Phys.* **70(1)**, 1

Bambic, C.J., Morsony, B.J. and Reynolds, C.S.: 2018a, *Astrophys. J.* **857**, 84

Bambic, C.J. et al: 2018b, *Mon. Not. R. Astron. Soc. Lett.* **478(1)**, L44

Bambic, C.J. and Reynolds, C.S.: 2019, *Astrophys. J.* **886**(2), 78

Barnes, D.J. et al: 2018, *Mon. Not. R. Astron. Soc.* **481**(2), 1809

Beck, R. and Krause, M.: 2005, *Astron. Nachrichten* **326(6)**, 414

Beckmann, R.S. and Dubois, Y.: 2022, *preprint(arXiv:2204.03629)*

Beckmann, R.S. et al: 2019, *Astron. Astrophys.* **631**, A60

Beresnyak, A.: 2012, *Phys. Scr.* **86**, 058201

Beresnyak, A. and Miniati, F.: 2016, *Astrophys. J.* **817**(2), 127

Bîrzan, L. et al: 2008, *Astrophys. J.* **686**(2), 859

Bîrzan, L. et al: 2004, *Astrophys. J.* **607**(2), 800

Bîrzan, L. et al: 2012, *Mon. Not. R. Astron. Soc.* **427**(4), 3468

Blandford, R., Meier, D. and Readhead, A.: 2019, *Relativ. Jets from Act. Galact. Nucl.* **57**, 467

Blandford, R.D. and Znajek, R.L.: 1977, *Mon. Not. R. astr. Soc* **179**, 433

Blanton, E.L. et al: 2011, *Astrophys. J.* **737**(2), 99

Blanton, E.L., Sarazin, C.L. and McNamara, B.R.: 2003, *Astrophys. J.* **585(1)**, 227

Böhringer, H., Chon, G. and Kronberg, P.P.: 2016, *Astron. Astrophys.* **596**, 1

Böhringer, H. et al: 1993, *Mon. Not. R. Astron. Soc.* **284**, L22

Bonafede, A. et al: 2010, *Astron. Astrophys.* **513(5)**, A30

Bonafede, A. et al: 2014, *Mon. Not. R. Astron. Soc. Lett.* **444(1)**, L44

Bondi, H.: 1952, *Mon. Not. R. Astron. Soc.* **112**, 195

Booth, C.M. et al: 2013, *Astrophys. J. Lett.* 777(1)

Botteon, A. et al: 2021, *Astron. Astrophys.* **649**, A37

Bourne, M.A. and Sijacki, D.: 2017, *Mon. Not. R. Astron. Soc.* **472**, 4707

Bourne, M.A. et al: 2021, *Mon. Not. R. Astron. Soc.* **506(1)**, 488

Bourne, M.A., Sijacki, D. and Puchwein, E.: 2019, *Mon. Not. R. Astron. Soc.* **490(1)**, 343

Brüggen, M. and Kaiser, C.R.: 2001, *Mon. Not. R. Astron. Soc.* **325(2)**, 676

Brüggen, M. and Kaiser, C.R.: 2002, *Nature* **418(6895)**, 301

Brüggen, M. et al: 2002, *Mon. Not. R. Astron. Soc.* **331(3)**, 545

Brüggen, M., Scannapieco, E. and Heinz, S.: 2009, *Mon. Not. R. Astron. Soc.* **395**, 2210

Brunetti, G., Zimmer, S. and Zandanel, F.: 2017, *Mon. Not. R. Astron. Soc.* **472(2)**, 1506

Bulbul, G.E. et al: 2012, *Astrophys. J.* **747(1)**, 32

Cantwell, T.M. et al: 2020, *Mon. Not. R. Astron. Soc.* **495(1)**, 143

Capetti, A., Massaro, F. and Baldi, R.D.: 2020, *Astron. Astrophys.* **633**, A161

Cappellari, M. et al: 2012, *Nature* **484(7395)**, 485

Carilli, C.L., Perley, R.A. and Harris, D.E.: 1994, *Mon. Not. R. Astron. Soc.* **270(1)**, 173

Carilli, C.L. and Taylor, G.B.: 2002, *Annu. Rev. Astron. Astrophys.* **40(1)**, 319

Cavagnolo, K.W. et al: 2008, *Astrophys. J.* **683(2)**, L107

Cavagnolo, K.W. et al: 2009, *Astrophys. J. Suppl. Ser.* **182(1)**, 12

Cavagnolo, K.W. et al: 2011, *Astrophys. J.* **732(2)**, 71

Chadayammuri, U. et al: 2021, *Mon. Not. R. Astron. Soc.* **504**, 3922

Chen, Y.H.H., Heinz, S. and Enßlin, T.A.: 2019, *Mon. Not. R. Astron. Soc.* **11(August)**, 1939

Cho, J.: 2014, *Astrophys. J.* **797**, 133

Choudhury, P.P., Sharma, P. and Quataert, E.: 2019, *Mon. Not. R. Astron. Soc.* **488**, 3195

Churazov, E. et al: 2001, *Astrophys. J.* **554(1)**, 261

Churazov, E. et al: 2003, *Astrophys. J.* **590(1)**, 225

Churazov, E. et al: 2012, *Mon. Not. R. Astron. Soc.* **421(2)**, 1123

Churazov, E. et al: 2010, *Space Sci. Rev.* **157**, 193

Cielo, S. et al: 2018, *Astron. Astrophys.* **617**, A58

Clarke, T.E.: 2004, *J. Korean Astron. Soc.* **337**, 337

Colafrancesco, S.: 2005, *Astron. Astrophys.* **435(1)**, L9

Croston, J.H. and Hardcastle, M.J.: 2014, *Mon. Not. R. Astron. Soc.* **438(4)**, 3310

Croston, J.H. et al: 2008, *Mon. Not. R. Astron. Soc.* **386(3)**, 1709

Croston, J.H., Ineson, J. and Hardcastle, M.J.: 2018, *Mon. Not. R. Astron. Soc.* **476**(2), 1614

Dasyra, K.M. et al: 2015, *Astrophys. J.* **815(1)**, 34

David, L.P. et al: 2001, *Astrophys. J.* **557**, 546

de Gasperin, F. et al: 2012, *Astron. Astrophys.* **547**, A56

De Plaa, J. et al: 2012, *Astron. Astrophys.* **539**, A34

De Villiers, J., Hawley, J.F. and Krolik, J.H.: 2003, *Astrophys. J.* **599**(2), 1238

Diehl, S. et al: 2008, *Astrophys. J.* **687(1)**, 173

Dolag, K. et al: 2005, *Mon. Not. R. Astron. Soc.* **364(3)**, 753

Dominguez-Fernandez, P. et al: 2019, *Mon. Not. R. Astron. Soc.* **486(1)**, 623

Donahue, M. and Voit, G.M.: 2022, *Prepr.*

Dong, R. and Stone, J.M.: 2009, *Astrophys. J.* **704**(2), 1309

Donnert, J. et al: 2009, *Mon. Not. R. Astron. Soc.* **392(3)**, 1008

Donnert, J. et al: 2018, *Space Sci. Rev.* **214**, 122

Drake, J.F. et al: 2021, *Astrophys. J.* **923**(2), 245

Dubois, Y. et al: 2009, *Mon. Not. R. Astron. Soc. Lett.* **399(1)**, 49

Dullo, B.T.: 2019, *Astrophys. J.* **886**(2), 80

Duran, R.B., Tchekhovskoy, A. and Giannios, D.: 2016, *Mon. Not. R. Astron. Soc.* **469**(4), 4957

Dursi, L.J.: 2007, *Astrophys. J.* **670(1)**, 221

Dursi, L.J. and Pfrommer, C.: 2008, *Astrophys. J.* **677**(2), 993

Ehlert, K.: 2017, Master thesis, University Heidelberg

Ehlert, K. et al: 2019, *Astrophys. J. Lett.* **872(1)**, L8

Ehlert, K. et al: 2018, *Mon. Not. R. Astron. Soc.* **481(3)**, 2878

Ehlert, K. et al: 2022, *preprint(arXiv:2204.01765)*

Ehlert, K. et al: 2021, *Mon. Not. R. Astron. Soc.* **503(1)**, 1327

Enßlin, T.A. and Brüggen, M.: 2002, *Mon. Not. R. Astron. Soc.* **331**(4), 1011

Enßlin, T.A. et al: 2011, *Astron. Astrophys.* **527**, A99

Fabian, A.C.: 1994, *Annu. Rev. Astron. Astrophys.* **32**, 277

Fabian, A.C.: 2012, *Annu. Rev. Astron. Astrophys.* **50(1)**, 455

Fabian, A.C., Nulsen, P.E.J. and Canizares, C.R.: 1982, *Mon. Not. R. Astron. Soc.* **201**, 933

Fabian, A.C. et al: 2011a, *Mon. Not. R. Astron. Soc.* **418**(4), 2154

Fabian, A.C. et al: 2011b, *Matching X-ray and optical images of the core of the Perseus cluster*, `https://lweb.cfa.harvard.edu/~jzhao/EG/clusters/3C84/`, webpage of Jun-Hui Zhao at Center for Astrophysics Harvard & Smithsonian, Accessed: 2022-05-17

Fabian, A.C. et al: 2003, *Mon. Not. R. Astron. Soc.* **344**, L43

Fabian, A.C. et al: 2000, *Mon. Not. R. Astron. Soc.* **318**(4), L65

Fabian, A.C. et al: 2006, *Mon. Not. R. Astron. Soc.* **366**(2), 417

Fabian, A.C. et al: 2017, *Mon. Not. R. Astron. Soc.* **464**(1), L1

Fanaroff, B.L. and Riley, J.M.: 1974, *Mon. Not. R. Astron. Soc.* **167**, 31P

Farmer, A.J. and Goldreich, P.: 2004, *ApJ* **604**(2), 671

Feretti, L. et al: 2012, *Astron. Astrophys. Rev.* **20**, 54F

Fogarty, K. et al: 2015, *Astrophys. J.* **813**(2), 117

Forman, W. et al: 2007, *Astrophys. J.* **665**(2), 1057

Fujita, Y., Cen, R. and Zhuravleva, I.: 2020, *Mon. Not. R. Astron. Soc.* **494**, 5507

Fujita, Y. et al: 2016, *Mon. Not. R. Astron. Soc.* **455**(3), 2289

Fujita, Y. and Ohira, Y.: 2011, *ApJ* **738**(2), 182

Fujita, Y. and Ohira, Y.: 2012, *Astrophys. J.* **746**(1), 7

Gan, Z. et al: 2017, *Astrophys. J.* **839**(1), 14

Gaspari, M., Brighenti, F. and Temi, P.: 2015, *Astron. Astrophys.* **579**, A62

Gaspari, M. and Churazov, E.: 2013, *Astron. Astrophys.* **559**, A78

Gaspari, M. et al: 2011, *Mon. Not. R. Astron. Soc.* **411**(1), 349

Gaspari, M., Ruszkowski, M. and Oh, S.P.: 2013, *Mon. Not. R. Astron. Soc.* **432**(4), 3401

Gaspari, M., Ruszkowski, M. and Sharma, P.: 2012, *Astrophys. J.* **746**(1), 94

Gaspari, M. and Sądowski, A.: 2017, *Astrophys. J.* **837**(2), 149

Gaspari, M., Temi, P. and Brighenti, F.: 2017, *Mon. Not. R. Astron. Soc.* **466**(1), 677

Gendron-Marsolais, M. et al: 2018a, *Mon. Not. R. Astron. Soc.* **479**, L28, Revealing the velocity structure of the filamentary nebula in NGC 1275 in its entirety, by permission of Oxford University Press, License Number 5311411070696

Gendron-Marsolais, M. et al: 2018b, *Mon. Not. R. Astron. Soc.* **479**, L28

Gendron-Marsolais, M. et al: 2017, *Mon. Not. R. Astron. Soc.* **469**(4), 3872

Gendron-Marsolais, M.L. et al: 2020, *Mon. Not. R. Astron. Soc.* **499**, 5791

Giacintucci, S. et al: 2017, *Astrophys. J.* **841**(2), 71

Gilfanov, M.R., Syunyaev, R.A. and Churazov, E.M.: 1986, *Sov. Astron. Lett.* **13**, 7

Gilkis, A. and Soker, N.: 2012, *Mon. Not. R. Astron. Soc.* **427**(2), 1482

Girichidis, P. et al: 2020, *Mon. Not. R. Astron. Soc.* **491**(1), 993

Gitti, M., Brighenti, F. and McNamara, B.R.: 2012, *Adv. Astron.* 2012

Gitti, M., Brunetti, G. and Setti, G.: 2002, *Astron. Astrophys.* **386**, 456

Gitti, M. et al: 2007, *Astrophys. J.* **660**(**2**), 1118

Gould, R.J.: 1972, *Physica* **58**(**3**), 379

Govoni, F. et al: 2010, *Astron. Astrophys.* **522**(**8**), 1

Govoni, F. et al: 2017, *Astron. Astrophys.* **603**, A122

Graham, J., Fabian, A.C. and Sanders, J.S.: 2008, *Mon. Not. R. Astron. Soc.* **391**(**4**), 1749

Grenier, I.A., Black, J.H. and Strong, A.W.: 2015, *Annu. Rev. Astron. Astrophys.* **53**(**1**), 199

Gronke, M. and Oh, S.P.: 2018, *Mon. Not. R. Astron. Soc.* **480**, L111

Gu, L. et al: 2018, *Space Sci. Rev.* 214(7)

Guidetti, D. et al: 2012, *Mon. Not. R. Astron. Soc.* **423**(**2**), 1335

Guidetti, D. et al: 2008, *Astron. Astrophys.* **483**, 699

Guo, F.: 2015, *Astrophys. J.* **803**(**1**), 48

Guo, F., Duan, X. and Yuan, Y.F.: 2018, *Mon. Not. R. Astron. Soc.* **473**(**1**), 1332

Guo, F. and Mathews, W.G.: 2011, *Astrophys. J.* **728**(**2**), 9

Guo, F. and Oh, S.P.: 2008, *Mon. Not. R. Astron. Soc.* **384**(**1**), 251

Guo, F., Oh, S.P. and Ruszkowski, M.: 2008, *Astrophys. J.* **688**(**2**), 859

Hahn, O. et al: 2017, *Mon. Not. R. Astron. Soc.* **470**(**1**), 166

Han, J.: 2017, *Annu. Rev. Astron. Astrophys.* **55**(**1**), 111

Hanasz, M. et al: 2013, *Astrophys. J. Lett.* 777(2)

Hardcastle, M.J. and Croston, J.H.: 2020, *New Astron. Rev.* **88**, 101539

Heesen, V. et al: 2018, *Mon. Not. R. Astron. Soc.* **474**, 5049

Heinz, S. et al: 2006, *Mon. Not. R. Astron. Soc. Lett.* **373**(**1**), 65

Hillel, S. and Soker, N.: 2014, *Mon. Not. R. Astron. Soc.* **445**(**4**), 4161

Hillel, S. and Soker, N.: 2016, *Mon. Not. R. Astron. Soc.* **455**(**2**), 2139

Hillel, S. and Soker, N.: 2017a, *Astrophys. J.* **845**(**2**), 91

Hillel, S. and Soker, N.: 2017b, *Mon. Not. R. Astron. Soc. Lett.* **466**(**1**), L39

Hillel, S. and Soker, N.: 2018, *Res. Astron. Astrophys.* **18**, 81

Hitomi Collaboration: 2016, *Nature* **535**, 117

Hitomi Collaboration: 2018, *Publ. Astron. Soc. Japan* **70**(**2**), 9

Hogan, M.T. et al: 2017, *Astrophys. J.* **851**(**1**), 66

Hoyle, F. and Lyttleton, R.: 1941, *Mon. Not. R. Astron. Soc.* **101**, 227

Hudson, D. et al: 2010, *Astron. Astrophys.* **513**, A37

Ichimaru, S.: 1977, *Astrophys. J.* **214**, 840

Ichinohe, Y. et al: 2019, *Mon. Not. R. Astron. Soc.* **483(2)**, 1744

Itoh, N., Kohyama, Y. and Nozawa, S.: 1998, *Astrophys. J.* **502**, 7

Ivezić, Ž. et al: 2002, *Astron. J.* **124(5)**, 2364

Jacob, S. and Pfrommer, C.: 2017a, *Mon. Not. R. Astron. Soc.* **467(2)**, 1449

Jacob, S. and Pfrommer, C.: 2017b, *Mon. Not. R. Astron. Soc.* **467(2)**, 1478

Johnson, A.R. et al: 2020, *Astrophys. J.* **888(2)**, 101

Jones, C. et al: 2017, *Astrophys. J.* **842(2)**, 84

Jones, T.W. and De Young, D.S.: 2005, *Astrophys. J.* **624(2001)**, 586

Kale, R. and Parekh, V.: 2016, *Mon. Not. R. Astron. Soc.* **459(3)**, 2940

Kannan, R. et al: 2017, *Astrophys. J. Lett.* **837(2)**, L18

Kazantsev, A.: 1968, *Sov. J. Exp. Theor. Phys.* **26**, 1031

Kellermann, K.I. et al: 2016, *Astrophys. J.* **831(2)**, 168

Kennicutt, R.C.: 1998, *Astrophys. J.* **498(2)**, 541

Kim, W. and Narayan, R.: 2003, *Astrophys. J.* **596(2)**, 889

King, A.: 2016, *Mon. Not. R. Astron. Soc. Lett.* **456(1)**, L109

Kirkpatrick, C.C. and McNamara, B.R.: 2015, *Mon. Not. R. Astron. Soc.* **452(4)**, 4361

Koekemoer, A.M. et al: 1999, *ApJ* **525**, 621

Kuchar, P. and Enßlin, T.A.: 2011, *Astron. Astrophys.* **529(A13)**, 13

Kulsrud, R. and Pearce, W.P.: 1969, *ApJ* **156**, 445

Kulsrud, R.M.: 2005, *Plasma Physics for Astrophysics*, Princeton University Press, Princeton, NJ

Kulsrud, R.M. and Cesarsky, C.J.: 1971, *Astrophys. Lett.* **8**, 189

Kunz, M.W. et al: 2020, *J. Plasma Phys.* **86(6)**, 905860603

Laing, R.A. and Bridle, A.H.: 2013, *Mon. Not. R. Astron. Soc.* **432(2)**, 1114

Laing, R.A. and Bridle, A.H.: 2014, *Mon. Not. R. Astron. Soc.* **437(4)**, 3405

Lakhchaura, K. et al: 2018, *Mon. Not. R. Astron. Soc.* **481(4)**, 4472

Lau, E.T. et al: 2017, *Astrophys. J.* **849(1)**, 54

Leccardi, A. and Molendi, S.: 2008, *Astron. Astrophys.* **486**, 359

Lee, M.A. and Völk, H.J.: 1973, *Astrophys. Space Sci.* **24**, 31

Li, J., Ostriker, J. and Sunyaev, R.: 2013, *Astrophys. J.* **767(2)**, 105

Li, Y. and Bryan, G.L.: 2014, *Astrophys. J.* **789**, 54

Li, Y. et al: 2015, *Astrophys. J.* **811**(2), 73

Li, Y., Ruszkowski, M. and Bryan, G.L.: 2017, *Astrophys. J.* **847**(2), 106

Li, Z. et al: 2020, *Mon. Not. R. Astron. Soc.* **492**, 1841

Lind, K.R. et al: 1989, *Astrophys. J.* **344**, 89

Liska, M. et al: 2019, *Mon. Not. R. Astron. Soc.* **487**, 550

Loewenstein, M., Zweibel, E.G. and Begelman, M.C.: 1991, *Astrophys. J.* **377**, 392

Lyutikov, M.: 2006, *Mon. Not. R. Astron. Soc.* **373**(**1**), 73

Mannheim, K. and Schlickeiser, R.: 1994, *A&A* **286**, 983

Martizzi, D. et al: 2019a, *Mon. Not. R. Astron. Soc.* **483**(2), 2465

Martizzi, D. et al: 2019b, *Mon. Not. R. Astron. Soc.* **483**(2), 2465

Martz, C.G. et al: 2020, *Astrophys. J.* **897**, 57

Massaglia, S. et al: 2016, *Astron. Astrophys* **596**, A12

Mathews, W.G., Faltenbacher, A. and Brighenti, F.: 2006, *Astrophys. J.* **638**(2), 659

Mccourt, M. et al: 2012, *Mon. Not. R. Astron. Soc.* **419**, 3319

McDonald, M. et al: 2019, *Astrophys. J.* **885**(**1**), 63

Mckinley, B. et al: 2022, *Nat. Astron.* **6**, 109

McKinney, J.C.: 2006, *Mon. Not. R. Astron. Soc.* **368**(4), 1561

McNamara, B.R. and Nulsen, P.E.J.: 2007, *Annu. Rev. Astron. Astrophys.* **45**(**1**), 117

McNamara, B.R. and Nulsen, P.E.J.: 2012, *New J. Phys.* **14**, 40

McNamara, B.R. et al: 2005, *Nature* **433**(**7021**), 45

McNamara, B.R. et al: 2006, *Astrophys. J.* **648**, 164

McNamara, B.R., Rohanizadegan, M. and Nulsen, P.E.: 2011, *Astrophys. J.* **727**(**1**), 39

McNamara, B.R. et al: 2014, *Astrophys. J.* **785**, 44

McNamara, B.R. et al: 2016, *Astrophys. J.* **830**(2), 1

Meece, G.R. et al: 2017, *Astrophys. J.* **841**(2), 133

Mehrgan, K. et al: 2019, *Astrophys. J.* **887**(2), 195

Mendygral, P.J., Jones, T.W. and Dolag, K.: 2012, *Astrophys. J.* **750**(2), 166

Miley, G.: 1980, *Annu. Rev. Astron. Astrophys.* **18**, 165

Mingo, B. et al: 2019, *Mon. Not. R. Astron. Soc.* **488**(2), 2701

Miyoshi, T. and Kusano, K.: 2005, *J. Comput. Phys.* **208**(**1**), 315

Mohapatra, R., Federrath, C. and Sharma, P.: 2021, *Mon. Not. R. Astron. Soc.* **500**(4), 5072

Mohapatra, R. and Sharma, P.: 2019, *Mon. Not. R. Astron. Soc.* **484**(4), 4881

Morganti, R. et al: 1988, *Astron. Astrophys.* **189(1-2)**, 11

Morsony, B.J. et al: 2010, *Mon. Not. R. Astron. Soc.* **407(2)**, 1277

Mroczkowski, T. et al: 2018, *Astrophysics with the Spatially and Spectrally Resolved Sunyaev-Zeldovich Effects: A Millimetre/Submillimetre Probe of the Warm and Hot Universe*

Mukherjee, D. et al: 2016, *Mon. Not. R. Astron. Soc.* **461(1)**, 967

Mukherjee, D. et al: 2020, *Mon. Not. R. Astron. Soc.* **499(1)**, 681

Müller, A. et al: 2021, *Nat. Astron.* **5**, 159

Murgia, M.: 2011, *Mem. della Soc. Astron. Ital.* **82**, 507

nasa.gov: 2012, *A Multi-Wavelength View of Radio Galaxy Hercules A*, `https://www.nasa.gov/mission_pages/hubble/science/hercules-a.html`, NASA, ESA, S. Baum and C. O'Dea (RIT), R. Perley and W. Cotton (NRAO/AUI/NSF), and the Hubble Heritage Team (STScI/AURA), webpage of Hubble Space Telescope at NASA, Accessed: 2022-05-17

Navarro, J.F., Frenk, C.S. and White, S.D.M.: 1995, *Mon. Not. R. Astron. Soc.* **275**, 720

Navarro, J.F., Frenk, C.S. and White, S.D.M.: 1996, *Astrophys. J.* **462**, 563

Navarro, J.F., Frenk, C.S. and White, S.D.M.: 1997, *Astrophys. J.* **490(2)**, 493

Newman, W.I., Newman, A.L. and Rephaeli, Y.: 2002, *Astrophys. J.* **575(2)**, 755

Nixon, C. and King, A.: 2013, *Astrophys. J. Lett.* **765(1)**, L7

Nobels, F.S.J. et al: 2022, *preprint(arXiv:2204.02205)*

Nulsen, P.E.J. et al: 2002, *Astrophys. J.* **568(1)**, 163

Ogiya, G. et al: 2018, *Prepr.*

Ogorzalek, A. et al: 2017, *Mon. Not. R. Astron. Soc.* **472(2)**, 1659

Olivares, V. et al: 2019, *Astron. Astrophys.* **631**, A22

O'Neill, B.J. et al: 2019, *Astrophys. J.* **884(1)**, 12

O'Neill, S.M., De Young, D.S. and Jones, T.W.: 2009, *Astrophys. J.* **694**, 1317

O'Neill, S.M. and Jones, T.W.: 2010, *Astrophys. J.* **710(1)**, 180

Ota, N. et al: 2007, *Prog. Theor. Phys. Suppl.* **59(SP1)**, S351

Ota, N. and Yoshida, H.: 2016, *Publ. Astron. Soc. Japan* **68(SP1)**, S19

Owen, F.N., Eilek, J.A. and Kassim, N.E.: 1999, *M87 as a radio galaxy*, `http://www.aoc.nrao.edu/~fowen/M87_halo.html`, webpage of M87 by F. Owen, NRAO, with J. Biretta, STSCI and J. Eilek, NMIMT at National Radio Astronomy Observatory, Accessed: 2022-05-21

Pais, M. et al: 2018, *Mon. Not. R. Astron. Soc.* **478(4)**, 5278

Pais, M. et al: 2020, *Mon. Not. R. Astron. Soc.* **496(2)**, 2448

Pakmor, R. et al: 2016a, *Mon. Not. R. Astron. Soc.* **462(3)**, 2603

Pakmor, R. and Springel, V.: 2013, *Mon. Not. R. Astron. Soc.* **432(1)**, 176

Pakmor, R. et al: 2016b, *Mon. Not. R. Astron. Soc.* **455(1)**, 1134

Pakmor, R.R.R., Bauer, A. and Springel, V.: 2011, *Mon. Not. R. Astron. Soc.* **418**(**2**), 1392

Perucho, M. and Martí, J.M.: 2007, *Mon. Not. R. Astron. Soc.* **382**(**2**), 526

Perucho, M. et al: 2010, *Astron. Astrophys.* **519**, A41

Perucho, M. et al: 2017, *Mon. Not. R. Astron. Soc.* **471**(**1**), L120

Peterson, J.R. and Fabian, A.C.: 2006, *Phys. Rep.* **427**(**1**), 1

Peterson, J.R. et al: 2003, *Astrophys. J.* **590**(**1**), 207

Peterson, J.R. et al: 2001, *Astron. Astrophys.* **365**, L104

Pfrommer, C.: 2008, *Mon. Not. R. Astron. Soc.* **385**(**3**), 1242

Pfrommer, C.: 2013, *Astrophys. J.* **779**(**1**), 10

Pfrommer, C.: 2022, in *The Physics of Galaxy Clusters, lecture notes, The Physics of Galaxy Clusters, delivered winter term 2021/22*, University of Potsdam

Pfrommer, C., Chang, P. and Broderick, A.E.: 2012, *Astrophys. J.* **752**(**1**), 24

Pfrommer, C. and Dursi, J.: 2010, *Nat. Phys.* **6**(**7**), 520

Pfrommer, C. and Enßlin, T.A.: 2004, *Astron. Astrophys.* **413**(**1**), 17

Pfrommer, C., Enßlin, T.A. and Sarazin, C.L.: 2005, *Astron. Astrophys.* **430**, 799

Pfrommer, C. et al: 2017, *Mon. Not. R. Astron. Soc.* **465**(4), 4500

Pillepich, A. et al: 2018, *Mon. Not. R. Astron. Soc.* **473**(**3**), 4077

Pinto, C. et al: 2015, *Astron. Astrophys.* **575**, A38

Pizzolato, F. and Soker, N.: 2005, *ApJ* **632**(2), 821

Powell, K.G. et al: 1999, *J. Comput. Phys.* **154**(2), 284

Prasad, D., Sharma, P. and Babul, A.: 2015, *Astrophys. J.* **811**(2), 108

Prasad, D., Sharma, P. and Babul, A.: 2018, *Astrophys. J.* **863**(**1**), 62

Prasad, D. et al: 2020, *Astrophys. J.* **905**(**1**), 50

Prokhorov, D.A. et al: 2012, *Mon. Not. R. Astron. Soc.* **425**(**3**), 1753

Pulido, F.A. et al: 2018, *Astrophys. J.* **853**(2), 177

Quataert, E.: 2008, *Astrophys. J.* **673**, 758

Rafferty, D.A., McNamara, B.R. and Nulsen, P.E.J.: 2008, *Astrophys. J.* **687**(2), 899

Rafferty, D.A. et al: 2006, *Astrophys. J.* **652**(**1**), 216

Randall, S.W. et al: 2011, *Astrophys. J.* **726**(2), 86

Rebusco, P. et al: 2005, *Mon. Not. R. Astron. Soc.* **359**(**3**), 1041

Reiprich, T.H. and Bohringer, H.: 2002, *Astrophys. J.* **567**(2), 716

Reynolds, C.S., Balbus, S.A. and Schekochihin, A.A.: 2015, *Astrophys. J.* **815**(**1**), 41

Reynolds, C.S., Heinz, S. and Begelman, M.C.: 2001, *Astrophys. J.* **549**, 179

Reynolds, C.S., Heinz, S. and Begelman, M.C.: 2002, *Mon. Not. R. Astron. Soc.* **332(2)**, 271

Reynolds, C.S. et al: 2005, *Mon. Not. R. Astron. Soc.* **357(1)**, 242

Robinson, K. et al: 2004, *Astrophys. J.* **601(2)**, 621

Roh, S. et al: 2019, *Astrophys. J.* **883(2)**, 138

Rossetti, M. et al: 2011, *Astron. Astrophys.* **532**, A123

Rudnick, L. and Blundell, K.M.: 2003, *Astrophys. J.* **588(1)**, 143

Runge, J. and Walker, S.A.: 2021, *Mon. Not. R. Astron. Soc.* **502**, 5487

Russell, H.R. et al: 2015, *Mon. Not. R. Astron. Soc.* **451(1)**, 588

Russell, H.R. et al: 2018, *Mon. Not. R. Astron. Soc.* **477(3)**, 3583

Russell, H.R. et al: 2017, *Mon. Not. R. Astron. Soc.* **472**, 4024

Russell, H.R. et al: 2019, *Mon. Not. R. Astron. Soc.* **490(3)**, 3025

Russell, H.R. et al: 2016, *Mon. Not. R. Astron. Soc.* **458(3)**, 3134

Ruszkowski, M. et al: 2008, *Mon. Not. R. Astron. Soc.* **383(4)**, 1359

Ruszkowski, M. et al: 2007, *Mon. Not. R. Astron. Soc.* **378(2)**, 662

Ruszkowski, M., Yang, H.Y.K. and Reynolds, C.S.: 2017, *Astrophys. J.* **844(1)**, 13

Ruszkowski, M., Yang, H.Y.Y.K. and Reynolds, C.S.: 2018, *Astrophys. J.* **858(1)**, 64

Ryu, D. et al: 2008, *Science (80-.).* **320(5878)**, 909

Ryu, D. et al: 2012, *Sp. Sci Rev* **166**, 1

Salomé, P. et al: 2006, *Astron. Astrophys.* **454**, 437

Sanders, J.S. and Fabian, A.C.: 2007, *Mon. Not. R. Astron. Soc.* **381(4)**, 1381

Sanders, J.S. and Fabian, A.C.: 2008, *Mon. Not. R. Astron. Soc. Lett.* **390(1)**, L93

Sanders, J.S. and Fabian, A.C.: 2013, *Mon. Not. R. Astron. Soc.* **429(3)**, 2727

Sanders, J.S. et al: 2010, *Mon. Not. R. Astron. Soc. Lett.* **402(1)**, L11

Sanderson, A.J., Ponman, T.J. and O'Sullivan, E.: 2006, *Mon. Not. R. Astron. Soc.* **372(4)**, 1496

Sani, E. et al: 2018, *Front. Astron. Sp. Sci.* **5(February)**, 1

Sarkar, K.C., Dey, A. and Sharma, P.: 2021, *preprint(arXiv:2110.12447)*

Savini, F. et al: 2018, *Mon. Not. R. Astron. Soc.* **478(2)**, 2234

Schaal, K. and Springel, V.: 2015, *Mon. Not. R. Astron. Soc.* **446(4)**, 3992

Scharwächter, J. et al: 2013, *Mon. Not. R. Astron. Soc.* **429(3)**, 2315

Schekochihin, A.A. and Cowley, S.C.: 2006, *Phys. Plasmas* 13(5)

Scheuer, P.: 1974, *Mon. Not. R. Astron. Soc.* **166**, 513

Schlickeiser, R.: 1989, *J. Japan Soc. Air Pollut.* **336**, 264

Schober, J. et al: 2015, *Phys. Rev. E - Stat. Nonlinear, Soft Matter Phys.* **92(2)**, 023010

Schuecker, P. et al: 2004, *Astron. Astrophys.* **426**, 387

Shakura, N.I. and Sunyaev, R.A.: 1973, *Astron. Astrophys.* **24**, 337

Sharma, P. et al: 2009, *ApJ* **699(1)**, 348

Sharma, P. and Hammett, G.W.: 2007, *J. Comput. Phys.* **227(1)**, 123

Sharma, P. and Hammett, G.W.: 2011, *J. Comput. Phys.* **230(12)**, 4899

Sharma, P. et al: 2012, *Mon. Not. R. Astron. Soc.* **420**, 3174

Shemmer, O. et al: 2004, *Astrophys. J.* **614(2)**, 547

Sijacki, D. et al: 2008, *Mon. Not. R. Astron. Soc.* **387(4)**, 1403

Sijacki, D. and Springel, V.: 2006, *Mon. Not. R. Astron. Soc.* **371(3)**, 1025

Simionescu, A. et al: 2009, *Astron. Astrophys.* **493(2)**, 409

Simionescu, A. et al: 2008, *Astron. Astrophys.* **482(1)**, 97

Simionescu, A. et al: 2019, *Space Sci. Rev.* **215(2)**, 24

Smith, R.K. et al: 2001, *Astrophys. J.* **556(2)**, L91

Soker, N.: 2003, *Mon. Not. R. Astron. Soc.* **342(2)**, 463

Soker, N.: 2016, *New Astron. Rev.* **75**, 1

Sparre, M., Pfrommer, C. and Ehlert, K.: 2020, *Mon. Not. R. Astron. Soc.* **499(3)**, 4261

Springel, V.: 2010, *Mon. Not. R. Astron. Soc.* **401(2)**, 791

Springel, V. and Hernquist, L.: 2003, *Mon. Not. R. Astron. Soc.* **339(2)**, 289

Sternberg, A., Pizzolato, F. and Soker, N.: 2007, *Astrophys. J.* **656(1)**, L5

Sternberg, A. and Soker, N.: 2008a, *Mon. Not. R. Astron. Soc.* **384(4)**, 1327

Sternberg, A. and Soker, N.: 2008b, *Mon. Not. R. Astron. Soc. Lett.* **389(1)**, 13

Subramanian, K.: 1999, *Phys. Rev. Lett.* **83**, 15

Subramanian, K.: 2016, *Reports Prog. Phys.* **79(7)**, 076901

Sugawara, C., Takizawa, M. and Nakazawa, K.: 2009, *Publ. Astron. Soc. Japan* **61(6)**, 1293

Sunyaev, R.A. and Zeldovich, Y.B.: 1972, *Comments Astrophys. Sp. Phys.* **4**, 173

Talbot, R.Y. et al: 2021, *Mon. Not. R. Astron. Soc.* **504(3)**, 3619

Talbot, R.Y., Sijacki, D. and Bourne, M.A.: 2022, *Mon. Not. R. Astron. Soc.* **514**, 4535

Tamura, T. et al: 2011, *Publ. Astron. Soc. Japan* **63(SP3)**, S1009

Tamura, T. et al: 2001, *Astron. Astrophys.* **365**, L87

Tamura, T. et al: 2014, *Astrophys. J.* **782**, 38

Tang, X. and Churazov, E.: 2017, *Mon. Not. R. Astron. Soc.* **468(3)**, 3516

Taylor, G.B. et al: 2006, *Mon. Not. R. Astron. Soc.* **368(4)**, 1500

Tchekhovskoy, A. and Bromberg, O.: 2016, *Mon. Not. R. Astron. Soc.* **461(2016)**, L46

Tchekhovskoy, A. and McKinney, J.C.: 2012, *Mon. Not. R. Astron. Soc. Lett.* **423(1)**, 55

Thomas, T. and Pfrommer, C.: 2019, *Mon. Not. R. Astron. Soc.* **485**, 2977

Thomas, T., Pfrommer, C. and Enßlin, T.: 2020, *Astrophys. J. Lett.* **890**(2), L18

Thomas, T., Pfrommer, C. and Pakmor, R.: 2021, *Mon. Not. R. Astron. Soc.* **503(2)**, 2242

Tremblay, G.R. et al: 2018, *Astrophys. J.* **865**, 13

Tremblay, G.R. et al: 2016, *Nature* **534(7606)**, 218

Turner, R.J.: 2018, *Mon. Not. R. Astron. Soc.* **476**, 2522

Vacca, V. et al: 2018, *Galaxies* **6(4)**, 1

Vacca, V. et al: 2012, *Astron. Astrophys.* **540**, A38

Van Dokkum, P.G. and Conroy, C.: 2010, *Nature* **468(7326)**, 940

van Leer, B.: 1984, *SIAM J. Sci. Stat. Comput.* **5(1)**, 1

van Weeren, R.J. et al: 2019, *Space Sci. Rev.* **215(1)**, 16

Vantyghem, A.N. et al: 2019, *Astrophys. J.* **870**(2), 57

Vantyghem, A.N. et al: 2014, *Mon. Not. R. Astron. Soc.* **442(4)**, 3192

Vazza, F. et al: 2018, *Mon. Not. R. Astron. Soc.* **474(2)**, 1672

Vazza, F., Roediger, E. and Brüggen, M.: 2012, *Astron. Astrophys* **544**, A103

Vikhlinin, A., Markevitch, M. and Murray, S.S.: 2001, *ApJ* **551(1)**, 160

Vogelsberger, M. et al: 2013, *Mon. Not. R. Astron. Soc.* **436**(4), 3031

Vogt, C. and Enßlin, T.A.: 2005a, *Astron. Astrophys.* **434(1)**, 67

Vogt, C. and Enßlin, T.A.: 2005b, *Astron. Astrophys.* **434(1)**, 67

Voigt, L.M. and Fabian, A.C.: 2004, *Mon. Not. R. Astron. Soc.* **347**, 1130

Voit, G.M.: 2021, *Astrophys. J. Lett.* **908(1)**, L16

Voit, G.M. and Donahue, M.: 2005, *Astrophys. J.* **634**(2), 955

Voit, G.M. and Donahue, M.: 2015, *Astrophys. J. Lett.* **799(1)**, 1

Voit, G.M. et al: 2015, *Nature* **519(7542)**, 203

Voit, G.M. et al: 2017, *Astrophys. J.* **845(1)**, 80

Walker, S.A., Sanders, J.S. and Fabian, A.C.: 2015, *Mon. Not. R. Astron. Soc.* **453(4)**, 3699

Walker, S.A., Sanders, J.S. and Fabian, A.C.: 2018, *Mon. Not. R. Astron. Soc.* **481(2)**, 1718

Wang, C., Li, Y. and Ruszkowski, M.: 2019, *Mon. Not. R. Astron. Soc.* **482**, 3576

Wang, C. et al: 2021, *Mon. Not. R. Astron. Soc.* **504(1)**, 898

Wang, C., Ruszkowski, M. and Yang, H.Y.K.: 2020, *Mon. Not. R. Astron. Soc.* **493**, 4065

Wang, Q.D. et al: 2013, *Science (80-.).* **341(6149)**, 981

Weinberger, R. et al: 2017, *Mon. Not. R. Astron. Soc.* **470(4)**, 4530

Weinberger, R. and Hernquist, L.: 2022, *preprint(arXiv:2204.05316)*

Wentzel, G.W.: 1971, *Astrophys. J.* **163**, 503

Werner, N. et al: 2014, *Mon. Not. R. Astron. Soc.* **439(3)**, 2291

Werner, N. et al: 2013, *Nature* **502(7473)**, 656

Werner, N. et al: 2009, *Mon. Not. R. Astron. Soc.* **398(1)**, 23

Wiener, J., Oh, S.P. and Guo, F.: 2013, *Mon. Not. R. Astron. Soc.* **434(3)**, 2209

Wiener, J., Pfrommer, C. and Peng Oh, S.: 2017, *Mon. Not. R. Astron. Soc.* **467**, 906

Wilman, R.J., Edge, A.C. and Johnstone, R.M.: 2005, *Mon. Not. R. Astron. Soc.* **359**, 755

Wilms, J., Allen, A. and McCray, R.: 2000, *Astrophys. J.* **542**(2), 914

Worrall, D.M.: 2009, *Astron. Astrophys. Rev.* **17(1)**, 1

Wykes, S. et al: 2015, *Mon. Not. R. Astron. Soc.* **447(1)**, 1001

Xu, H. et al: 2002, *Astrophys. J.* **579**, 600

Xu, H. et al: 2009, *Astrophys. J.* **698(1)**, L14

Yang, H.Y. et al: 2012, *Astrophys. J.* 761(2)

Yang, H.Y.K., Gaspari, M. and Marlow, C.: 2018, *Prepr.*

Yang, H.Y.K. and Reynolds, C.S.: 2016, *Astrophys. J.* **829**(2), 90

Yang, H.Y.K. et al: 2016, *Astrophys. J.* **818**(2), 181

Yuan, F. et al: 2015, *Astrophys. J.* **804**(2), 101

Zakamska, N.L. and Narayan, R.: 2003, *Astrophys. J.* **582(1)**, 162

Zhang, C., Churazov, E. and Schekochihin, A.A.: 2018, *Mon. Not. R. Astron. Soc.* **478(4)**, 4785

Zhang, C. et al: 2022, *preprint(arXiv:2203.04259)*

Zhuravleva, I. et al: 2018, *Astrophys. J.* **865(1)**, 53

Zhuravleva, I. et al: 2016, *Mon. Not. R. Astron. Soc.* **458(3)**, 2902

Zhuravleva, I. et al: 2014, *Nature* **515(7525)**, 85

ZuHone, J. et al: 2021a, *Galaxies* **9**(4), 91

ZuHone, J. et al: 2018, *Astrophys. J.* **853**(2), 180

ZuHone, J.A. and Hallman, E.J.: 2016, *Astrophys. Source Code Libr.* (record ascl:1608.002)

ZuHone, J.A. et al: 2021b, *Astrophys. J.* **914(1)**, 73

Zweibel, E.G.: 2013, *Phys. Plasmas* **20(5)**, 055501

Zweibel, E.G.: 2020, *Astrophys. J.* **890**, 67

Acknowledgments

First, I would like to thank my PhD supervisor, Christoph Pfrommer, for his contagious enthusiasm for astrophysics and amazing guidance throughout my PhD. I am very grateful to the support by Rainer Weinberger especially for guiding me back to the essentials when I got lost in the details. Thank you Matthias Steinmetz for useful comments in our thesis committee meetings. I would also like to thank Debora Sijacki and Mateusz Ruszkowski, who kindly agreed to referee this thesis.

I want to thank the Cosmology and High-Energy Astrophysics Section and my collaborators for great moments and discussions, Georg Winner, Philipp Girichidis, Thomas Berlok, Maria Werhahn, Rüdiger Pakmor, Mohamad Shalaby, Ewald Puchwein, Tobias Buck, Timon Thomas, Martin Sparre, Volker Springel and John ZuHone. Special thanks to Matteo Pais especially for our fruitful discussions in park Babelsberg.

Thanks a lot to my parents, Philip and Deborah, for your trusting support and love. Thank you Yulong Zhuang, Sebastian Bustamante, Zenghao Yang and Thomas Noel for all great fun we had and times discussing science.